Determination of the Optimum Metrics for the Characterisation of Scattering Media

by

James Housley, MEng.

Thesis submitted to the University of Nottingham for the degree of Doctor of Philosophy

April 2010

To my parents

Abstract

Determining a scattering medium's absorption and scattering coefficients from measurements of the light reflected or transmitted from the medium is a common problem in various fields. The aim of this thesis was to calculate the errors in the determined coefficients using different combinations of light "metrics" such as reflectance and mean flight time under realistic noise conditions, as a result of which the optimum metric combination could be found.

This was investigated by the forward modelling of various metrics of detected light from a semi-infinite, homogeneous medium using the Diffusion Approximation. The normalised intensity and cumulants of the light's temporal point spread function (TPSF), were investigated as possible metrics and their form over a range of optical coefficients corresponding to *in vivo* human tissue described fully. These metrics were then used to provide simultaneous equations from which the medium's scattering and absorption coefficients could be calculated.

Errors in the metrics will propagate through to errors in the determined coefficients and a general method to calculate the extent of this propagation was described. To

simulate realistic metric errors, a typical streak camera (Hamamatsu C5680) was modelled to determine its effect on the measurements of the metrics. Using this model, "error maps" showing the expected error in each metric's value over the range of absorption and scattering coefficents were produced. These were then applied to the general error analysis method. In full-field detection mode, it was shown that the combination of normalised intensity and first cumulant gave the most accurate answer for the medium's coefficients, while for spatially resolved detection, various combinations of reflectance and the mean time of flight were found to be the optimum metric pairs under different conditions.

Finally, a method of using the known characteristics (either from modelling or experiment) of a detector such as the streak camera to improve the accuracy of the determined coefficients was described.

Acknowledgements

I would like to thank both my supervisors, Prof. John Crowe and Dr. Steve Morgan, for their assistance, knowledge and support throughout my research. This thanks must also be extended to Dr. Ian Stockford who, despite having no official duties concerning my research, quite easily fulfilled the role of a third supervisor. Dr. David Morris also deserves a special mention for his continual assistance and for the height at which he set the proverbial bar.

I would also like to thank Dr. Malcolm Woolfson and Dr. John Walker for their useful discussions at various points throughout this project.

I would like to acknowledge the University of Nottingham's High Performance Computing team, whose facility was essential to the feasibility of some of the methods used in this thesis. I would also like to acknowledge the Engineering and Physical Sciences Research Council for their funding of this research.

I would like to thank those with whom I have shared an office for providing support and amusement.

I would like to thank Cat, for putting up with me for the last four months. Starting

a relationship in the shadow of a looming thesis deadline was never going to be easy, but her patience has been remarkable.

Finally, I would like to thank my family and friends for their constant understanding throughout my research. This applies especially to my parents, without whom I would never have got this far. The dedication of this thesis to them does not even begin to demonstrate the extent of my gratitude for everything they have done for me.

Table of Contents

Chapter 1

Introduction

1.1 Background

The characterisation of a scattering medium through optical methods has applications in many fields such as medicine,[1,2] pharmaceutical manufacturing[3,4] and the food industry.[5,6] These methods involve measurements of the light reflected or transmitted from a scattering medium, from which its optical properties (such as its absorption and scattering coefficients and anisotropy factor) can be determined.

Characterisation of a scattering medium is difficult for two reasons. First, light emerging from the medium will have travelled many different paths resulting in a multitude of different flight times meaning that the relationship between the medium's absorption coefficient and the attenuation of light is therefore no longer linear. Second, depending on the medium and detector geometries, an unknown amount of light will be lost from the medium due to scattering processes without being detected. As a result of these two effects, the determination of the medium's optical properties is

non-trivial.

Many forward models can be used which relate the optical coefficients to the measured light. These can be analytical in nature, such as the Radiative Transport Equation and Diffusion Approximation, or stochastic, such as Monte Carlo modelling. As explained above, however, it is the inverse problem that is of interest: the determination of the medium's optical properties from measurements of the light reflected or transmitted from the medium.

Many solutions to this inverse problem have been described, and a summary of some of these methods is given in Chapter 2. The common process between these methods, however, is the measurement of certain properties (such as the absolute intensity or the mean flight time) of the detected light, from which the optical coefficients of the medium are then determined. The purpose of this thesis is to investigate what combination of these "metrics" will result in the most accurate characterisation of the medium.

1.2 Scattering Media

A homogenous medium is one which is perfectly uniform in composition. A truly homogeneous medium does not exist, however, resulting in small changes in the refractive index throughout the medium. It is these changes that cause the scattering of light: photons passing through the medium are refracted by the boundaries between regions of different refractive indices, thus changing their direction of propagation.

The behaviour of light travelling through scattering media depends on several parameters. These are discussed in the following sections.

1.2.1 Scattering Coefficient

The scattering coefficient, denoted as μ_s, describes the number of scattering events that each photon will experience on average within a certain distance. As such, its units are given as the reciprocal of distance, or more specifically, in this thesis as per micrometre (mm^{-1}). The reciprocal of the scattering coefficient gives the average distance travelled by each photon, and is known as the *mean free path*.

1.2.2 Absorption Coefficient

The absorption coefficient is denoted as μ_a and describes the number of absorption events that photons experience on average over a certain distance. Its units are also given as a reciprocal of distance, or more specifically, in this thesis as per millimetre (mm^{-1}).

Due to the quantum nature of photons, the result of an absorption event is the termination of a photon's propagation. However, the aggregate intensity of a large number of photons in the presence of absorption can be described using the Beer–Lambert law, as covered in §1.4.

1.2.3 Anisotropy Factor

The anisotropy factor, g, defines the average angle of scattering experienced by photons at each scattering event. It is equal to the mean cosine of the angle, and thus can take values between -1 and 1, where -1 results in the reversal of the photon's direction (completely backscattering) and 1 means that the photon's direction is not affected (completely forward scattering). A value of 0 means that the scattering angle is evenly distributed, and the medium is *isotropic*.

1.2.4 Reduced Scattering Coefficient

The values of the scattering coefficient and the anisotropy parameter are often combined (as in the case of the Diffusion Approximation) to give the reduced scattering coefficient, defined as:

$$\mu_{\mathrm{s}}' = \mu_{\mathrm{s}}(1 - g) \tag{1.2.1}$$

Its reciprocal is known as the *transport mean free path* or *effective mean free path* and represents the distance that each photon will travel before its direction is totally randomised.[7]

1.2.5 Medium Geometry

It is clear that a medium's geometry will affect the propagation of photons, and thus the properties of the light detected. For example, photons will, in general, undergo longer pathlengths in a semi-infinite geometry in comparison to slab geometries.

1.2.6 Wavelength

The scattering coefficient, absorption coefficient and anisotropy factor are all dependent on the wavelength of light incident on the medium. The wavelength of light will be assumed to be constant at 633nm throughout this thesis.

1.3 Temporal Point Spread Functions

Due to the scattering experienced within a scattering medium, photons will take different paths and diffuse throughout the medium, and each photon exiting the medium will do so after a different period of time. This temporally resolved information is the medium's impulse response or temporal point spread function (TPSF).

From a quantum point of view, a TPSF consists of a set of photon flight times – the length of time taken by each photon in reaching the detector. This can be represented visually as an irregularly spaced Dirac comb, an example of which can be seen for 50 photons in Figure 1.1.

This "quantum TPSF" can be transformed into a continuous distribution by the summation of the number of photons within each of a set of temporal bins. This is also shown in Figure 1.1.

The normalisation of the area under a TPSF to unity results in a probability density function (PDF), which in this case represents the probability of a photon being detected during a particular time interval. Note that a PDF formed from any

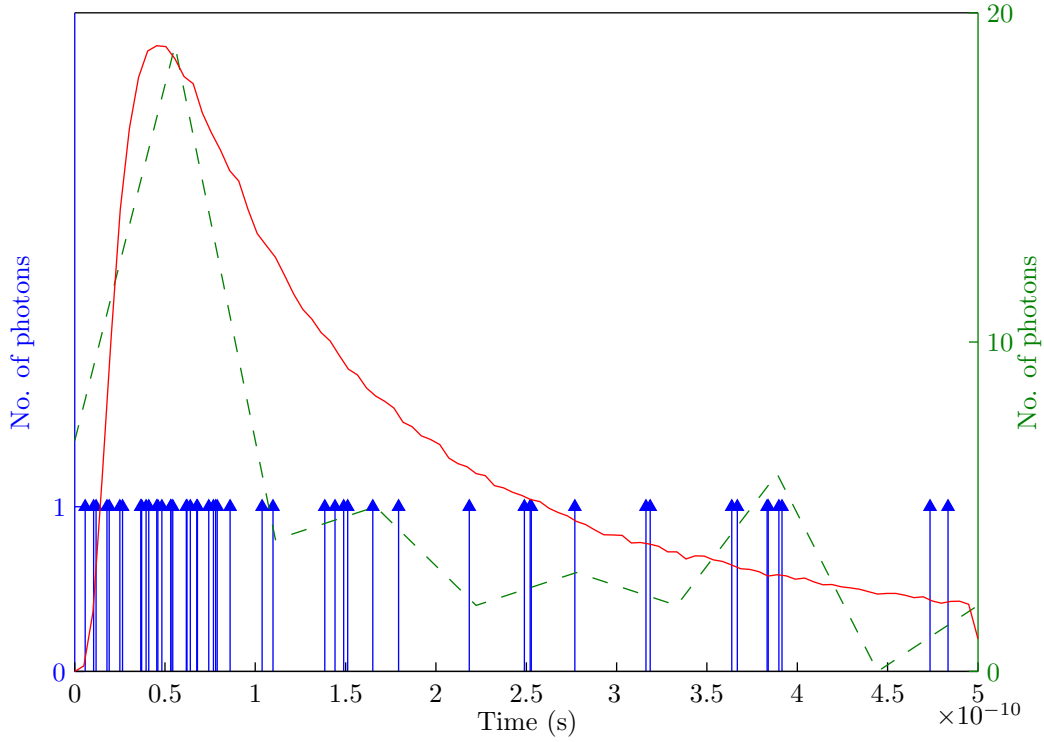

Figure 1.1: A quantum TPSF consisting of 50 photons, as shown in blue, is coarsely binned to produce the green TPSF. The red curve shows a TPSF formed under the same conditions, but using more photons and finer binning.

realistic TPSF, whether binned or not, can only be considered as an estimate of the true probability density function: an exact PDF can only be created from the normalisation of a quantum TPSF containing an infinite number of photons.

1.4 Beer–Lambert Law

The attenuation of light passing through an absorbing medium is described using the Beer–Lambert law, which is defined as:

$$I = I_0 \exp(-\mu_a d) \tag{1.4.1}$$

where I and I_0 are the intensities of light received from and input to the medium respectively, μ_a is the absorption coefficient described in §1.2.2, and d is the optical pathlength.

As explained in §1.2.2, the quantum nature of photons means that it is impossible for part of a photon to be absorbed: absorption is an all-or-nothing process. Therefore, the question of how the Beer–Lambert law relates to a quantum TPSF can be answered in one of two ways:

1. Light particles are not considered to be quantum photons, but light *packets* whose energy can take on a continuous range of values. Thus light particles with fractional values can be detected from an absorbing medium. This method is used extensively in Monte Carlo modelling.

2. The exponential term, $\exp(-\mu_\mathrm{a} d)$, can be considered as the probability of a photon emerging from the absorbing medium. Thus for a μ_a value of zero, the probability of a photon being detected is unity, regardless of the optical pathlength.

Absorption can be added to a TPSF using the Beer–Lambert law by considering an alternative form of Eq. (1.4.1):

$$I = I_0 \exp(-\mu_\mathrm{a} v t) \tag{1.4.2}$$

Here, it can be seen that the optical pathlength has been replaced by the product

of the speed of the light in the medium, v, and the length of time spent within the medium, t. Taking the intensity of the light at each time point of a TPSF to be the initial value I_0, multiplying by $\exp(-\mu_a vt)$ will give the resulting intensity due to added absorption. This is known as the microscopic Beer–Lambert law.[8,9] Applying this over all of a TPSF's time points, it can be seen that the macroscopic addition of absorption to a TPSF is therefore achieved by its multiplication with a decaying exponential of the form $\exp(-\mu_a vt)$.

Note that it is more beneficial to apply the microscopic Beer–Lambert law to a quantum TPSF before binning for its distribution form, rather than afterwards. This is because each photon's contribution will be reduced according to its exact time of arrival, rather than its binned time. One of the two assumptions discussed above must be made when applying the microscopic Beer–Lambert law to a quantum TPSF.

1.5 Metrics

This section will introduce the concepts of probability density functions' moments and cumulants, which are metrics that can potentially be used to describe a TPSF, and therefore the light detected from the medium. The methods used to calculate the moments and cumulants will also be covered.

1.5.1 Moments

A probability density function can be defined uniquely by its *moment generating function*[10] which is an infinite series of the PDF's raw moments; from this point on, these will just be referred to as the 'moments'. The first moment of a PDF is equal to the *expected value* of the distribution. Thus, for a normalised TPSF, the expected value refers to the mean photon flight time, not the mean probability. Despite its name, the expected value is not the most common value, or mode. In fact, in the case of the PDF relating to a discrete quantity such as a number of people, it is likely that the expected value will not be a whole number.

The n^{th} moment of a normalised TPSF, $s(t)$, is defined as:

$$m_n = \int_0^\infty s(t) t^n \, \mathrm{d}t \tag{1.5.1}$$

where t is a photon's time of flight. The zeroth moment is therefore the area under the normalised TPSF, which by definition is equal to unity. Note that the definition of the n^{th} moment for a general PDF calls for the integration to be performed between $-\infty$ and ∞. However, due to the causal nature of a TPSF, the lower integration limit in this case can be made equal to zero.

In the case of a quantum TPSF, the n^{th} moment is defined as:

$$m_n = \sum_{z=1}^{Z} {t_z}^n \tag{1.5.2}$$

where t_z is the z^{th} photon's time of flight, and Z is the total number of photons

detected. It is beneficial to calculate the moments from this discrete data, rather than its PDF, as each photon then contributes to the moment's value at its exact time of arrival and not at an approximation.

From either of these definitions, it can be seen that as the orders of the moments increase, so will the value of the exponent on the photons' times of arrival. As such, for higher-order moments, longer times will contribute more to the moment values than for lower-order moments. Higher-order moments will therefore be more sensitive to the TPSF's tail.

Moments can also be obtained from the normalised TPSF using a PDF's moment-generating function (MGF), M, which is defined as:[11]

$$M = \int_0^\infty s(t) \exp(xt)\, \mathrm{d}t \tag{1.5.3}$$

where x is an arbitrary variable used later in the moments' calculation. Expanding the exponential term as a power series, the MGF becomes:

$$\begin{aligned} M &= \int_0^\infty s(t) \left[1 + xt + \frac{(xt)^2}{2!} + \frac{(xt)^3}{3!} + \cdots\right] \mathrm{d}t \\ &= \int_0^\infty s(t)\, \mathrm{d}t + x \int_0^\infty s(t) t\, \mathrm{d}t + \frac{x^2}{2!} \int_0^\infty s(t) t^2\, \mathrm{d}t + \frac{x^3}{3!} \int_0^\infty s(t) t^3\, \mathrm{d}t + \cdots \end{aligned} \tag{1.5.4}$$

The individual integrals in the above equation have the same form as Eq. (1.5.1), and thus the MGF is an infinite series of the PDF's moments:

$$M = 1 + xm_1 + \frac{x^2}{2!} m_2 + \frac{x^3}{3!} m_3 + \cdots \tag{1.5.5}$$

$$= \sum_{n=0}^{\infty} \frac{x^n}{n!} m_n \tag{1.5.6}$$

The n^{th} moment can then be calculated by differentating the moment-generating function n times with respect to x, and then setting x to zero:

$$m_n = \left.\frac{\mathrm{d}^n M}{\mathrm{d}x^n}\right|_{x=0} \tag{1.5.7}$$

This is demonstrated for m_1 below:

$$\begin{aligned} m_1 &= \frac{\mathrm{d}M}{\mathrm{d}x} \\ &= m_1 + \frac{2x}{2!}m_2 + \frac{3x^2}{3!}m_3 + \cdots \end{aligned} \tag{1.5.8}$$

It can be seen that setting x to zero in the above equation will result in the series reducing to simply the m_1 term.

It can be noted that by setting x to $-\mu_{\mathrm{a}}c$, the subject of the integration in Eq. (1.5.3) has the form of a TPSF with absorption added by the Beer–Lambert law, as described in §1.4. The effect of setting x to zero is therefore to remove the effects of this added absorption. However, this is not the same as removing absorption from the TPSF altogether as the original TPSF, $s(t)$, may have been measured or calculated in the presence of a base level of absorption.

1.5.2 Cumulants

A normalised TPSF can also be defined by the infinite sum of its cumulants. These are related to the moments using the following recursive formula:[12]

$$\kappa_n = m_n - \sum_{k=1}^{n-1} \frac{(n-1)!\kappa_k m_{n-k}}{(k-1)!(n-k)!} \tag{1.5.9}$$

The first three cumulants can therefore be defined as:

$$\kappa_1 = m_1 \tag{1.5.10}$$

$$\kappa_2 = m_2 - {m_1}^2 \tag{1.5.11}$$

$$\kappa_3 = m_3 - 3m_1m_2 + 2{m_1}^3 \tag{1.5.12}$$

It can be seen from Eq. (1.5.10) that the first cumulant is equal to the first moment and thus represents the mean photon flight time. The second cumulant is equal to the variance of the distribution; this represents the spread of different pathlengths that the photons took within the medium. None of the higher-order cumulants, however, have intuitive meanings regarding the shape of the TPSF.

It has already been shown that higher-order moments are more sensitive to a TPSF's tail. The equations above show that, due to the cumulants' dependence on moments of the same order, this property will also apply to cumulants.

The cumulant-generating function (CGF), K, is the natural logarithm of the moment-generating function given in Eq. (1.5.6):

$$\begin{aligned} K &= \ln\left(\sum_{n=0}^{\infty}\frac{x^n}{n!}m_n\right) \\ &= \ln\left(1+\left[xm_1+\frac{x^2}{2!}m_2+\frac{x^3}{3!}m_3+\cdots\right]\right) \end{aligned} \tag{1.5.13}$$

Using the substitution

$$y = xm_1+\frac{x^2}{2!}m_2+\frac{x^3}{3!}m_3+\cdots \tag{1.5.14}$$

it can be seen that:

$$K = \ln(1+y) \tag{1.5.15}$$

Expanding $\ln(1+y)$ as a Taylor series:

$$\begin{aligned}\ln(1+y) &= \sum_{n=1}^{\infty} \frac{-1^{n+1}}{n} y^n \\ &= y - \frac{y^2}{2} + \frac{y^3}{3} - \frac{y^4}{4} + \cdots \end{aligned} \tag{1.5.16}$$

Substituting this series and collecting like-powered terms of x gives:

$$K = xm_1 + \frac{x^2}{2}(m_2 - {m_1}^2) + \frac{x^3}{3!}(m_3 - 3m_1m_2 + 2{m_1}^3) + \cdots \tag{1.5.17}$$

Finally, replacing each set of brackets with its equivalent cumulant form from Eq. (1.5.9), K becomes:

$$K = x\kappa_1 + \frac{x^2}{2}\kappa_2 + \frac{x^3}{3!}\kappa_3 + \cdots \tag{1.5.18}$$

$$= \sum_{n=1}^{\infty} \frac{x^n}{n!}\kappa_n \tag{1.5.19}$$

Note that the sum now begins at $n = 1$, as opposed to $n = 0$ for the MGF.

Like the MGF, the n^{th} cumulant can be found by differentiating K n times with respect to x, and then setting x to zero. The zeroth cumulant can therefore be shown to be equal to zero by merely equating x to zero in the CGF.

1.5.3 Reflectance

The "reflectance" of a medium will be discussed throughout this thesis, and will be derived for a semi-infinite medium with different detectors in the following section.

Various meanings have been bestowed upon the term in previous years,[13–15] making it necessary to explicitly define the term's intended meaning for the purposes of this study.

The reflectance, R, is therefore defined as the energy of the detected emergent light, E_R, normalised by that of the incident light, E_I, as follows:[16,17]

$$R = \frac{E_R}{E_I} \tag{1.5.20}$$

1.6 Streak Cameras

A streak camera allows the measurement of sub-nanosecond events using a standard CCD camera, by transforming the time axis of the TPSF into a spatial deflection. In mechanical streak cameras, this deflection is achieved by a moving mirror or prism setup 'streaking' the image over the surface of the detector.[18] In optoelectronic streak cameras, however, it is achieved by first converting the incident photons into electrons and then using a pair of sweep electrodes to create an electric field to alter the path of the electrons.[19] Mechanical streak cameras, despite their relative simplicity, are inherently limited by the speed at which the mechanical components can be moved, and thus this thesis will concentrate on the more-complicated optoelectronic instrument.

1.7 Applications

One area in which optical methods are frequently used is the characterisation of biological tissue, or more specifically, human skin, which can be useful in cancer diagnosis[20] and the determination of tissue blood oxygenation.[21] One specific use is the non-invasive monitoring of blood glucose levels in diabetic patients by the measurement of a tissue's reduced scattering coefficient. An increase in the blood glucose level will cause an increase in the tissue's extracellular fluid's refractive index, which in turn will cause the reduced scattering coefficient to decrease.[22]

There are significant advantages to the use of optical techniques over other methods. Firstly, the technique is non-invasive and so can be performed *in vivo* with minimal discomfort to the patient. Secondly, optical radiation is non-ionising and therefore can be applied in frequent doses without the risk of damaging healthy tissue. As human skin is a complex structure and therefore difficult to model, this thesis will focus on the characterisation of a single-layered scattering medium with optical coefficients corresponding to the bulk optical properties of human skin.

The aim of this thesis is to improve the accuracy of the characterisation of human skin by determining the optimum metrics that should be used in the process. This will be achieved in this case for a streak camera detection system; however, the methods presented can be applied to any characterisation method.

1.8 Thesis Overview

This thesis describes research into the determination of a medium's scattering and absorption coefficients, or more specifically the optimum metrics to use to minimise the error in these coefficients' values. This will be investigated by the forward modelling of various metrics of detected light from a semi-infinite medium using the Diffusion Approximation. These metrics can then be used to provide simultaneous equations from which the medium's scattering and absorption coefficients can be calculated. However, as it is not possible to measure the metrics exactly, their "detection" by a streak camera will be modelled to give an estimate of the errors in their measured values. With this knowledge, the optimum metrics in characterising a scattering medium under realistic noise conditions can be determined.

A review of the literature relative to this thesis is therefore presented in Chapter 2, thus enabling the methods used within thesis to be put into context with regard to the existing research in this area.

Chapter 3 covers the derivation of the Diffusion Approximation equations used as a forward model to calculate the values of the metrics.

The metrics of interest are chosen and justified in Chapter 4, and their dependence on a medium's optical properties described in detail. In order to do this, the ranges of these properties are also defined by focusing on optical coefficients similar to the bulk properties of human skin.

Chapter 5 achieves a comprehensive and novel model of a typical streak camera's noise sources, allowing the effect of a metric's detection by the camera on its value to be determined. This is achieved in several parts. Firstly, the configuration of the streak camera, along with the associated noise at each of the camera's stages is thoroughly described. The effects of these noise sources on a typical TPSF are then investigated. The model used to describe the streak camera is then detailed and applied to a typical spatially resolved TPSF, and the effects on the metrics discussed at each stage. The same model is then applied to the TPSFs over the entire parameter range described in Chapter 4, allowing "error maps" of each metric to be created.

Equations that relate the errors in the metrics to the errors in the determined scattering and absorption coefficients are derived in Chapter 6. These equations are then applied to the metric surfaces described using the Diffusion Approximation, and the error maps from Chapter 5. This is repeated for both full-field and spatially resolved detection, and the optimum metrics for both detection regimes are determined for which the errors in the determined scattering and absorption coefficients are minimised. A method for using the known characteristics (either by modelling or experiment) of a detector such as the streak camera to improve the accuracy of the determined coefficients is also described.

Finally, the findings of this thesis are summarised and discussed in Chapter 7 in which areas suitable for future research are also highlighted.

Chapter 2

Literature Review

2.1 Introduction

This chapter will serve as a review of the literature concerning the characterisation of scattering media. It provides background information on the current knowledge base in this area, as well as explaining the reasoning for the novel work produced in this thesis.

The review begins with a discussion on various models of photon propagation in use in the optical analysis of scattering media. These are used to relate the value of various quantities concerning the photons passing through a medium as a function of the medium's scattering and absorption coefficients. Numerous models have been used previously, although this review will focus on two of them, the Diffusion Approximation and Monte Carlo modelling, as together these represent a large majority of documented model use.

This is followed by a review of the various techniques used to determine the optical

properties of a medium. These are divided into three types of system: constant intensity, time resolved and frequency modulated. A brief description of the implementation of each system is given, followed by consideration the possible measurements that can be made using each system. The relative advantages of these systems are also covered.

Finally, a brief review is presented of the limited literature concerning the modelling of a streak camera.

2.2 Photon Propagation Models

Photon propagation models are used to relate the properties of light passing through a medium to its optical parameters. The accuracy and limitations of these models are therefore of prime concern when used in the characterisation of scattering media. As a detailed review of propagation models has already been published by Arridge and Hebden,[23] only a brief review of these models is provided here. Furthermore, a full comparison of the two main models of interest, the Diffusion Approximation and the Monte Carlo model, is provided by Flock et al.[24]

2.2.1 The Radiative Transport Equation

Due to the inhomogeneities in a scattering medium, it is beneficial to model the propagation of light using transport theory rather than analytical solutions to Maxwell's equations. The fundamental equation used to define transport theory is the Radiative

Transport Equation (RTE), which is equivalent to Boltzmann's equation used in the kinetic theory of gases and neutron transport theory.[25] It is given by Contini et al. as:[26]

$$\frac{1}{v}\frac{\partial}{\partial t}I(\mathbf{r},t,\hat{\mathbf{s}}) + \hat{\mathbf{s}}\cdot\nabla I(\mathbf{r},t,\hat{\mathbf{s}}) = -(\mu_\mathrm{a}+\mu_\mathrm{s})I(\mathbf{r},t,\hat{\mathbf{s}}) + \frac{\mu_\mathrm{a}+\mu_\mathrm{s}}{4\pi}\int_{4\pi} p(\hat{\mathbf{s}},\hat{\mathbf{s}}')I(\mathbf{r},t,\hat{\mathbf{s}}')d\omega' + \varepsilon(\mathbf{r},t,\hat{\mathbf{s}}) \quad (2.2.1)$$

The equation describes the behaviour of the radiance or specific intensity of the light in the medium, denoted by $I(\mathbf{r},t,\hat{\mathbf{s}})$. This represents the average power flux density at a point $\mathbf{r}$ in the direction of the unit vector $\hat{\mathbf{s}}$, per unit time (t), within a unit solid angle and a unit area perpendicular to $\hat{\mathbf{s}}$. The speed of light in the medium is given by v, and μ_a and μ_s are the medium's absorption and scattering coefficients respectively. The phase function, $p(\hat{\mathbf{s}},\hat{\mathbf{s}}')$, is the probability of a photon moving in the direction of $\hat{\mathbf{s}}$ being scattered into the direction $\hat{\mathbf{s}}'$. Finally, $\varepsilon(\mathbf{r},t,\hat{\mathbf{s}})$ is the source term.

The left-hand side of this equation represents the change in the radiance with respect to both time and space. The first term of the right-hand side equals the loss of radiance due to absorption and the scattering of photons from the direction of interest $\hat{\mathbf{s}}$. The second term represents the gain in radiance caused by the scattering of photons from any other direction $\hat{\mathbf{s}}'$ into the direction $\hat{\mathbf{s}}$. The third term is the increase in the radiance due to the source.

Due to the complexity of the RTE, closed-form solutions do not exist for anything other than very simple medium geometries. As such, approximations must be made

about the nature of the photon propagation to simplify the problem. One such approximation is discussed in the following section.

2.2.2 The Diffusion Approximation

One widely used approximation to the RTE is the Diffusion Approximation which assumes that the scattering of the light within the medium is diffuse. This is valid when the medium's reduced scattering coefficient is much greater than the absorption coefficient, i.e. $\mu_\mathrm{a} \ll \mu_\mathrm{s}(1-g)$, and if the radiance is calculated far from the sources or boundaries of the medium.[27]

Using these assumptions, Eq. (2.2.1) can be simplified greatly to give the diffusion equation:[26]

$$\left(\frac{1}{v}\frac{\partial}{\partial t} - D\nabla^2\right) U_\mathrm{d}(\mathbf{r},t) = Q(\mathbf{r},t) \tag{2.2.2}$$

where $U_\mathrm{d}(\mathbf{r},t)$ is the average diffuse intensity and $Q(\mathbf{r},t)$ is the isotropic source term. D is the diffusion coefficient which can be dependent on the absorption coefficient, scattering coefficient and anisotropy factor. Its correct form is the subject of much debate, especially as regards the nature of its dependence on μ_a. This will be covered in more detail in §3.3.1.

The relative simplicity of Eq. (2.2.2) over (2.2.1) allows analytical expressions to be derived for various medium geometries, as demonstrated by Patterson et al.[27] Contini et al. proposed alternative derivations taking into account the refractive index mismatch between the medium and its surroundings.[26] These expressions are

substantially more complicated than those of Patterson et al. but have been reported to provide more accurate results.[28,29]

The main advantage of the Diffusion Approximation is the speed of calculations that its closed-form expressions provide. However, the assumptions explained above can limit its application.

2.2.3 Monte Carlo Modelling

One solution to modelling light propagation in regions where the Diffusion Approximation is invalid is to use a Monte Carlo model. This can be considered a *conformity* to the RTE in that it satisfies the same theory of propagation, albeit in a numerical fashion.

Monte Carlo modelling is a stochastic technique and so describes light propagation on a photon-by-photon basis. Each photon's path is determined by drawing random numbers from a specific probability distribution (which is related to the medium's scattering coefficient, or more precisely its mean free path) to ascertain the pathlengths between scattering events. At each event, the photon's new direction is determined from a distribution usually based on Henyey-Greenstien[30] or Mie theory.[31] This continues until the photon is scattered out of the medium, or if it reaches a maximum pathlength, as described below.

It is beneficial to add absorption to each photon by the Beer–Lambert law after the simulation, as this allows the results from media with different absorption coefficients

to be determined without repeating the Monte Carlo model. The distance travelled by each photon in the medium must therefore be recorded. Note that by adding absorption in this way to individual photons, the "photons" must in fact be considered as packets of light whose energy can take on a continuous range of values. It is important, especially when modelling large media, to define a cut-off length for the photons as this will prevent the occurrence of lengthy pathlengths that would be absorbed even in low absorption conditions from greatly increasing the length of time required to carry out the simulation.

The above method is repeated many times until the stochastic error in the resulting distribution is low enough so that an accurate picture of the optical response of the scattering medium has been determined. This can obviously be a time-consuming process, especially if the simulation is to be repeated for several different scattering parameters. One solution to this last problem, proposed by Kienle and Patterson[32], is the modelling of a single data set with an arbitrary scattering coefficient. Results corresponding to any scattering coefficient can then be determined by the scaling of this data set. As the dimensions of the medium are also scaled in this process, this approach is suitable for infinite and semi-infinite geometries which are scale invariant. However, in the case of infinite slab geometries, for example, scaling of the results will cause the slab's thickness to also change.

Despite its time-consuming nature, one advantage of Monte Carlo modelling is its

ability to be applied to any geometry. Use of the Monte Carlo model is also considered the "gold standard" in the modelling of light propagation in scattering media due to its accordance with experimental results using phantoms.[24]

2.3 Methods of Examination

The various methods of optical examination of scattering media can be split into the following three types of system: constant intensity, time resolved and frequency modulated. The fundamental principles behind each of these systems will be discussed below. It should be noted that the methodologies used in these three types of system are all linked: integration of the time resolved method over time yields the constant intensity method, while a frequency modulated system is its Fourier Transform.

2.3.1 Constant Intensity Systems

In these systems, a constant intensity light source is used to illuminate the scattering medium, while detection is limited to intensity measurements. Variation in these measurements can therefore come from factors such as the wavelength of light used, providing a spectral analysis of the medium.[33–35] The light source used is therefore of importance, with systems using either a filtered white source or sources of particular wavelengths such as lasers or light emitting diodes.[36] Alternatively, a white light source can be used in conjunction with a grating spectrograph before the detector to select the wavelength of light measured.[37]

Variation in constant intensity measurements can also be observed by the use of spatially resolved detection of the light emitted,[38–40] or a combination of spectral and spatial resolution.[22,37] Further variations due to the angle of incidence of the source can also be added to these systems.[41]

The geometry of the detector is also an important factor in the optical examination of scattering media, with the systems referenced above all employing measurements in reflection mode. Systems based on both reflection and transmission measurements have been described,[42,43] with some also using measurements of the collimated transmittance to provide an estimate of the medium's absorption coefficient.[44,45] It is worth noting, however, that the use of transmission measurements limits the geometries to which the methods can be applied.

The main drawbacks of constant intensity systems occur due to their reliance on measurements of absolute intensity which can be difficult to perform due to problems such as source fluctuations and surface coupling. Despite their relative simplicity, they are therefore often overlooked in favour of time resolved or frequency modulated systems.

2.3.2 Time Resolved Systems

There are two detection schemes related to time resolved measurements. These both revolve around the detection of the temporal point spread function (TPSF) resulting from an ultrashort input pulse.

In the first detection scheme, light is detected through the input slit of a streak camera. The resulting one-dimensional line image is then "streaked" across the surface of a two-dimensional detector such as a CCD array, thus converting the light's temporal information into a second spatial dimension. The study of streak cameras forms a large proportion of this thesis, and as such, literature concerning the modelling of the instrument will be covered in more detail in §2.4.

The second detection scheme is termed Time-Correlated Single Photon Counting (TCSPC) in which photons are detected using a photomultiplier tube or avalanche photodiode.[46] In this method, the intensity of the light entering the instrument is reduced (either by a reduction in the source intensity or with the use of an attenuating stage) until the probability of detecting a single photon from each input pulse is very low. The time of arrival of each photon is then measured using a time-to-amplitude converter (TAC) effectively acting as a stopwatch: the input light pulse triggers its start, while the stop event is triggered by the detection of a photon. As more photons are detected through repetition of this process, the medium's TPSF will be formed. The key to this method is the low probability of the detection of a photon. As the instrument will only record the time position of the first photon to reach the detector, if more than one photon was received for an input pulse, the later photons would not be registered. The reduction of light intensity therefore reduces the probability of multiple photons being received for each input pulse.

The main advantage to a streak camera is its speed, as an accurate representation of the TPSF can be recorded using one input pulse. However, the instrument can be large and expensive as a consequence.[36] In contrast, the TCSPC method is much slower, requiring many thousands of input pulses to detect an adequate representation of the TPSF. Its relative advantage, however, comes from one of the consequences of its method of detection: the time resolution is not dependent on the width of the detector's impulse response. As a result, it can be implemented using smaller and cheaper components.

The wealth of information stored in the TPSF has led to numerous methods of determing a medium's optical properties.[36] These include methods which use the TPSF's tail, methods involving fitting the TPSF to known data, methods involving time gating and methods using various parameters of the TPSF. Short summaries of the literature relating to each of these are given below. Methods which only calculate the change in absorption coefficient do not apply to this thesis and so are not covered here.

Several methods have been described that rely on the knowledge that a TPSF's tail will become increasingly solely reliant on the absorption coefficient.[27,47,48] As a result, it was found that the asymptotic gradient of the logged tail could be directly related to the medium's absorption level. After solving for μ_a, the scattering coefficient can then be calculated from the position of the TPSF's peak in time. The inherent

problem with this technique is that it relies on the measurement of parts of the TPSF where the signal-to-noise ratio is much reduced. Wilson et al. demonstrated that by measuring the gradient earlier on the TPSF, where this limitation was less relevant, the absorption coefficient could still be determined with only a 10% error.[49]

A medium's scattering and absorption coefficients may be determined by the fitting of the TPSF to an analytical expression derived using the Diffusion Approximation.[50–52] Similarly, approaches using equations derived from random walk theory[53] and a database of Monte Carlo results[54] have also been reported. The disadvantage with these methods is that the fitting procedures can be time consuming and so are not suitable for real-time analysis of scattering media.[55]

Using a similar premise as the methods that relate a TPSF's tail to the absorption level, the use of time-gating in transmission mode allows the isolation of early arrival photons having undergone minimal scattering.[56] This approach is limited by the medium's thickness, however, as the number of undeviated photons will decrease sharply as the thickness increases. Techniques which separate early arrival photons that are dependent on both scattering and absorption, and later photons that will be predominantly dependent on absorption have also been described,[57] although they will suffer from signal-to-noise ratio limitations at longer pathlengths.

Methods involving the use of parameters describing a TPSF have been found to

yield more accurate determination of optical coefficients than curve fitting.[58] Solutions to the optical coefficients are determined from measured values of the TPSF's parameters by known relationships between them. In this thesis, these parameters are called "metrics", although the terms "data types"[58] and "analytic descriptors"[59] have also been used previously. There are an infinite number of metrics that can be derived from a TPSF, and an extensive list of examples has been previously published.[60]

One of the most commonly used metrics is the photons' mean time of flight,[38,61] sometimes alongside the TPSF's variance.[55] Other examples of metrics include the moments (which include the mean time of flight) and central moments (which include the variance),[58] the modal average,[29] full width at half maximum (FWHM)[62] and normalised Laplace transforms.[63]

Finally, similar to continuous intensity systems, time resolved instruments can use measurements over different wavelengths. This has been employed in both reflection[64] and transmission.[65]

Time resolved systems have been shown to give the most accurate results for a medium's optical coefficients of the three types of system.[66,67] This thesis will therefore focus on the analysis of such a system.

2.3.3 Frequency Modulated Systems

In frequency modulated systems, the light incident on the medium's surface is modulated, and detection involves the measurement of the resulting light's phase shift

relative to the source (ϕ), the ac amplitude (I_{ac}), dc amplitude (I_{dc}) and modulation depth ($M = I_{\mathrm{ac}}/I_{\mathrm{dc}}$). Characterisation of the medium is then a matter of relating a number of these parameters to the optical coefficients by a known relationship. These relationships are usually analytical solutions to the Diffusion Approximation,[68] although Monte Carlo modelling has also been used for small source–detector separations where these solutions are invalid.[69]

Alternatively, frequency modulated measurements can be related to the cumulants of a medium's TPSF.[70] In this method, the use of N measurements at different frequencies will yield approximations of the first $2N$ cumulants. The accuracy of these approximations, due to the truncation of an infinite series, is discussed in Ref. 71.

The simplest implementation of these systems involves the measurement of light at one source–detector distance and one frequency,[72] although multiple distance methods[73] and multiple wavelength methods[74] have also been demonstrated. Detection using multiple distances or wavelengths can be used to probe different volumes of a medium.[75]

One advantage of frequency modulated systems is their inherent ability to reject non-correlated light sources such as background light, thus making them more practical for use in clinical settings.[76] However, these systems exhibit an increased sensitivity to electromagnetic interference and measures to reduce the effects of this can add to the instruments' complexity.

In general, however, frequency modulated systems are cheaper and faster to implement than time domain systems, making them suitable for real-time analysis, although it has been shown that they do not yield as accurate results as time domain systems.[66]

2.4 Streak Camera Modelling

The development of streak cameras has a long history: the first streak camera was demonstrated in 1882 and consisted of a film fixed to a rotating drum being rotated past a slit.[18] It is perhaps surprising, therefore, that little literature exists concerning the statistics of noise within the instrument. This fact was acknowledged by Secroun et al. in their 1998 conference paper, in which a forward model of a streak camera was described.[77] This model assumed that the input signal was Poisson-distributed and that the sources of noise (namely the photocathode, phosphor screen and input optics) could all be modelled as binomial distributions. Noise from the CCD was initially measured as being negligible and so was ignored in the model. The output signal was then approximated by a "cascade" of Poisson and Binomial laws to equal a Poisson distribution with a mean defined by the product of the initial number of photons in the signal and the probabilities of the noise sources' Binomial distributions. Experimental data was then used to confirm this model. The shot-noise limited nature of the streak camera's measurements was also found in papers characterising existing streak cameras such as that by Donaldson et al.[78] Meanwhile, characterisation of

a different streak camera by Lerche et al. determined that CCD noise was far from negligible and in fact was the major source of noise in the system.[79] It is therefore apparent that different streak cameras will present different noise characteristics.

The shot-noise limited nature of the streak camera's measurements can bring into question this thesis' aim of presenting a detailed streak camera model. However, when describing a streak camera's effects on a TPSF's metrics, rather than merely on its intensity, such a simplistic view does not taken into account processes such as truncation and binning and the effects of the streak camera's noise floor. A detailed model of the streak camera will therefore be necessary to determine the accuracy of a TPSF's metrics and thus the accuracy of a medium's optical coefficients when using such a system.

2.5 Summary

This chapter has presented a review of the literature related to the characterisation of scattering media. First, two different models of photon propagation were reviewed: the Diffusion Approximation and Monte Carlo modelling. One of these must be used to relate the optical properties of a medium to the properties of light passing through the medium, in order to allow for the characterisation of the medium. It is clear that the use of Monte Carlo modelling will result in the determination of more accurate optical coefficients. However, the methods involved in this thesis require the modelling of numerous media of different scattering and absorption coefficients which

will require a great number of Monte Carlo simulations. As the statistics of the TPSFs are of prime concern, and not just its general form, the variance reduction method proposed by Kienle and Patterson[32] (as described in §2.2.3) is not applicable, as each scaled TPSF would exhibit the same statistical properties. As a result, the length of time required to carry out modelling of the entire data set using standard Monte Carlo techniques will be prohibitive. The Diffusion Approximation must therefore be used for its relative speed.

Second, a review of the constant intensity, time resolved and frequency modulated systems that can be used to optically examine scattering media were presented. Consideration was given to both the methodologies of each of these systems, and the types of measurements that could be made using them to determine a medium's properties. Time resolved systems have been shown to provide the most accurate results for a medium's optical coefficients, and hence this thesis will focus on the use of time-domain measurements. Modelling of a streak camera was then chosen over a TCSPC system due to the streak camera's increased speed of detection. This is an important factor in the analysis of media such as human skin to prevent the addition of motion artifacts to the measurements.

Finally, the lack of literature concerning the modelling of a streak camera was investigated, and the need for a detailed streak camera model highlighted.

Chapter 3

The Diffusion Approximation

3.1 Introduction

In this chapter, the limitations of the Diffusion Approximation are discussed, and its use in this thesis justified. The methods used to calculate a TPSF's moments and cumulants, as described in §1.5, are then applied to equations derived from the Radiative Transport Equation using the Diffusion Approximation in order to produce the necessary equations that will be used throughout this study. The appropriate form of the diffusion coefficient is then discussed.

3.2 Limitations

The Diffusion Approximation is based on the fundamental Radiative Transfer Equation. It is an approximation, rather than a solution, of light transport due to the assumptions fully described in Ref. 26. As such, there are limitations to its use, two of which are:[25,27]

1. The absorption coefficient must be much smaller than the reduced scattering coefficient:

$$\mu_{\mathrm{a}} \ll \mu_{\mathrm{s}}(1-g) \tag{3.2.1}$$

2. The point or region at which the reflectance is calculated must be far away from both the source and boundaries.

It is therefore acknowledged that the Diffusion Approximation's use within this thesis is not flawless and that some of the calculated results infringe one or both of the above limitations. However, the major advantage of using the Diffusion Approximation over a stochastic method such as Monte Carlo modelling is its analytical nature, allowing for the production of ideal, noiseless TPSFs to which the exact solutions of the metrics described in §1.5 are known. This allows noise to be added to the TPSF and the resulting effects on these metrics precisely calculated, as is the basis for the methods used to characterise the effects of a streak camera in Chapter 5. In addition to this, knowledge of the analytical forms of the metrics allows for more accurate error analyses to be performed in Chapter 6. Finally, the extensive computer time that would have been required to simulate the numerous results used throughout this thesis by Monte Carlo modelling would have been severely limiting, thus making the detail to which the metrics and errors are analysed in this thesis unfeasible.

3.3 Diffusion Approximation Equations

In order to describe the light transport in a turbid medium, equations based on the Diffusion Approximation were defined for both full-field (over all space) and spatially resolved detection. As explained in §4.3, the geometry of interest is single-layered and semi-infinite in nature.

Full-field Detection

The Diffusion Approximation equations used within this thesis are based on the equation published by Patterson et al. [27, Eq. 7]. This states that, for a semi-infinite geometry, when one joule of light is input as a Dirac delta function to a medium, the light reflected at a point with a source–detector separation, ρ, and after a time, t, is:

$$R_{\text{Patterson}}(\rho, t) = \frac{\exp\left(-\frac{\rho^2 + {z_0}^2}{4Dvt} - \mu_{\text{a}} v t\right) z_0}{(4\pi D v)^{3/2} t^{5/2}} \qquad \text{[Units: Wm}^{-2}\text{]} \tag{3.3.1}$$

where μ_{a} is the medium's absorption coefficient and D is the diffusion coefficient which is dependent on the medium's scattering coefficient, μ_{s}, and is discussed in §3.3.1. The speed of light within the medium, v, is defined by:

$$v = \frac{c}{n} \tag{3.3.2}$$

where c is the speed of light in a vacuum and n is the medium's refractive index.

The z_0 term is the effective mean free path, defined as:[28]

$$z_0 = \frac{1}{\mu_{\text{s}}(1 - g)} \tag{3.3.3}$$

Here it represents the depth at which all the incident photons are assumed to initially scatter.

In order to obtain the equation for the full-field reflectance, Patterson's equation is modified to describe the light detected by an annulus with infinitesimal thickness and a radius of ρ. This is achieved by multiplying the equation by the circumference of the detector, $2\pi\rho$. The resulting equation is then integrated over all radii:

$$\begin{aligned} R(t) &= \int_0^\infty R_{\text{Patterson}}(\rho, t) 2\pi\rho \, \mathrm{d}\rho \\ &= \frac{\exp\left(-\frac{{z_0}^2}{4Dvt} - \mu_\mathrm{a} v t\right) z_0}{2\sqrt{\pi D v t^3/2}} \qquad \text{[Units: W]} \end{aligned} \tag{3.3.4}$$

This equation describes the medium's TPSF for full-field detection. The full-field reflectance is then defined by integrating this over all time:

$$\begin{aligned} R &= \int_0^\infty R(t) \, \mathrm{d}t \\ &= \exp\left(-\sqrt{\frac{\mu_\mathrm{a}}{D}} z_0\right) \qquad \text{[Units: J]} \end{aligned} \tag{3.3.5}$$

The moment-generating function (MGF) can be calculated by first normalising the area under Eq. (3.3.4) in order to give a probability density function, $s(t)$. This is done by dividing the equation through by Eq. (3.3.5):

$$\begin{aligned} s(t) &= \frac{R(t)}{\int_0^\infty R(t) \, \mathrm{d}t} \\ &= \frac{\exp\left(-\frac{{z_0}^2}{4Dvt} - \mu_\mathrm{a} v t + \frac{\mu_\mathrm{a}}{D} z_0\right) z_0}{2\sqrt{\pi D v t^3/2}} \end{aligned} \tag{3.3.6}$$

Multiplying $s(t)$ by $\exp(xt)$ and integrating over all time then gives the MGF, M, as explained in §1.5.1:

$$\begin{aligned} M &= \int_0^\infty s(t)\exp(xt)\,\mathrm{d}t \\ &= \exp\left(\frac{\sqrt{\mu_\mathrm{a} v} - \sqrt{\mu_\mathrm{a} v - x}}{\sqrt{Dv}} z_0\right) \end{aligned} \tag{3.3.7}$$

The first three moments calculated using Eq. (1.5.7) are therefore:

$$m_1 = \frac{z_0}{2v\sqrt{D\mu_\mathrm{a}}} \tag{3.3.8}$$

$$m_2 = \frac{z_0(\sqrt{D\mu_\mathrm{a}} + \mu_\mathrm{a} z_0)}{4v^2 D{\mu_\mathrm{a}}^2} \tag{3.3.9}$$

$$m_3 = \frac{Dz_0(3D + z_0[3\sqrt{D\mu_\mathrm{a}} + \mu_\mathrm{a} z_0])}{8v^3(D\mu_\mathrm{a})^{5/2}} \tag{3.3.10}$$

The cumulants can be calculated either by taking the natural logarithm of the MGF to form the CGF, or by the recursive formula described in Eq. (1.5.9). By the first method, the n^{th} cumulant is derived as follows:

$$\begin{aligned} K &= \ln\left[\exp\left(\frac{\sqrt{\mu_\mathrm{a} v} - \sqrt{\mu_\mathrm{a} v - x}}{\sqrt{Dv}}\, z_0\right)\right] \\ &= \frac{\sqrt{\mu_\mathrm{a} v} - \sqrt{\mu_\mathrm{a} v - x}}{\sqrt{Dv}}\, z_0 \end{aligned} \tag{3.3.11}$$

$$\kappa_n = \left.\frac{\mathrm{d}^n K}{\mathrm{d}x^n}\right|_{x=0} \tag{3.3.12}$$

The first three cumulants are therefore:

$$\kappa_1 = \frac{z_0}{2v\sqrt{D\mu_\mathrm{a}}} \tag{3.3.13}$$

$$\kappa_2 = \frac{z_0}{4v^2\sqrt{D{\mu_\mathrm{a}}^3}} \tag{3.3.14}$$

$$\kappa_3 = \frac{3z_0}{8v^3\sqrt{D{\mu_\mathrm{a}}^5}} \tag{3.3.15}$$

Spatially Resolved Detection

In order to define the TPSF for an annular detector with a finite width, it is necessary to repeat the integration in Eq. (3.3.4). This time, however, the integration is performed between the inner and outer radius of the detector, ρ_1 and ρ_2 respectively:

$$\begin{aligned} R(\rho_1, \rho_2, t) &= \int_{\rho_1}^{\rho_2} R_{\mathrm{Patterson}}(\rho, t) 2\pi\rho \, \mathrm{d}\rho \\ &= \frac{\left(\exp(-\frac{{\rho_1}^2+4Dv^2\mu_\mathrm{a}t^2+{z_0}^2}{4Dvt}) - \exp(-\frac{{\rho_2}^2+4Dv^2\mu_\mathrm{a}t^2+{z_0}^2}{4Dvt})\right) z_0}{2\sqrt{\pi Dv}t^{3/2}} \quad \text{[Units: W]} \end{aligned} \tag{3.3.16}$$

The medium's reflectance for an annular detector is then defined by integrating this equation over all time:

$$\begin{aligned} R(\rho_1, \rho_2) &= \int_0^\infty R(\rho_1, \rho_2, t) \, \mathrm{d}t \\ &= z_0 \left(\frac{\exp\left(-\frac{\sqrt{\mu_\mathrm{a}({z_0}^2+{\rho_1}^2)}}{\sqrt{D}}\right)}{\sqrt{{z_0}^2+{\rho_1}^2}} - \frac{\exp\left(-\frac{\sqrt{\mu_\mathrm{a}({z_0}^2+{\rho_2}^2)}}{\sqrt{D}}\right)}{\sqrt{{z_0}^2+{\rho_2}^2}} \right) \quad \text{[Units: J]} \end{aligned} \tag{3.3.17}$$

The moment-generating function, M, can then be derived as described for full-field detection:

$$\begin{aligned} s(\rho_1, \rho_2, t) &= \frac{R(\rho_1, \rho_2, t)}{\int_0^\infty R(\rho_1, \rho_2, t)\, \mathrm{d}t} \\ M &= \int_0^\infty s(\rho_1, \rho_2, t) \exp(xt)\, \mathrm{d}t \\ &= \frac{\exp\left(\frac{(\sqrt{v\mu_\mathrm{a}} - \sqrt{-x+v\mu_\mathrm{a}})(\beta_1+\beta_2)}{\beta_1\beta_2}\right)\left[\exp\left(\frac{\sqrt{-x+v\mu_\mathrm{a}}}{\beta_2}\right)\beta_1 - \exp\left(\frac{\sqrt{-x+v\mu_\mathrm{a}}}{\beta_1}\right)\beta_2\right]}{\exp\left(\frac{\sqrt{v\mu_\mathrm{a}}}{\beta_2}\right)\beta_1 - \exp\left(\frac{\sqrt{v\mu_\mathrm{a}}}{\beta_1}\right)\beta_2} \end{aligned} \tag{3.3.18}$$

where β_1 and β_2 are defined by:

$$\beta_n = \sqrt{\frac{vD}{{z_0}^2 + {\rho_n}^2}} \tag{3.3.19}$$

3.3.1 The Diffusion Coefficient

The Diffusion Approximation equations derived above all involve the diffusion coefficient, D, which is defined by the original Patterson et al. paper[27] as:

$$D_3 = \frac{1}{3\mu_\mathrm{s}(1-g) + 3\mu_\mathrm{a}} \tag{3.3.20}$$

There have been numerous papers published discussing the validity of this definition, however, with several studies defending Patterson's definition[27,80] and many proposing an alternative derivation excluding the absorption term,[81,82] namely:

$$D_0 = \frac{1}{3\mu_\mathrm{s}(1-g)} \tag{3.3.21}$$

In order to define the optimal diffusion coefficient, Morris [71, § 6.8] compared the errors in the determination of a semi-infinite medium's absorption and scattering

coefficients using the first and second cumulants for both the above definitions. His findings showed that for the first cumulant, the error was smaller when using D_3. Further to this, on solving the equations analytically for an infinite medium, he found that for the first cumulant, the most accurate definition of the diffusion coefficient was:

$$D_4 = \frac{1}{3\mu_\mathrm{s}(1-g)+4\mu_\mathrm{a}} \tag{3.3.22}$$

The appropriate value of the coefficient for the second cumulant was determined, also by Morris, using results from an infinite medium. These results showed that in the absence of scattering ($\mu_\mathrm{s} = 0$), the second cumulant tended to zero when using D_0 and to a non-zero value for D_3 [71, § 5.6.1]. In practice, photons in a scatter-free, infinite medium are said to be *ballistic* and as such the TPSF would resemble a delta function centred on the value of the first cumulant, the mean time of flight. All of the cumulants higher than the first order of such a TPSF will be equal to zero; as the second cumulant tended to zero when using D_0, it can be inferred that this is therefore the most appropriate value for the diffusion coefficient when calculating the second cumulant.

It should be noted that these conclusions were drawn at low scattering levels when the Diffusion Approximation is considered invalid. However, Morris demonstrated that regardless of this fact, a TPSF created using those "hybrid" coefficients almost exactly matched a TPSF generated using Monte Carlo data, whereas TPSFs formed

using either D_0 or D_3 differed from it significantly.

The hybrid definition for the diffusion coefficient is based on an infinite geometry. However, when applied to a semi-infinite geometry, Morris showed that this new definition gave a smaller error in the determination of the absorption and scattering coefficients than both D_0 and D_3.

The question remains, however, of which is the more correct definition to use when calculating the third-order and higher cumulants. Using a similar approach to Morris as the first and second cumulants, Figure 3.1 shows the values of the third, fourth and fifth cumulants calculated using the Diffusion Approximation for an infinite geometry by a detector 10mm from the source. The cumulant values are shown over a range of both scattering and absorption coefficients, using both D_0 and D_3 as the diffusion coefficient. As can be seen, all three cumulants tend to zero for low scattering when using D_0, while measurements using D_3 at lower absorptions tend to a non-zero value. As all the cumulants above the first should be zero for an infinite geometry in the absence of scattering, it is inferred that D_0 is the more appropriate definition of the diffusion coefficient for κ_3, κ_4 and κ_5. From this result, it will be assumed that the more appropriate definition for *all* the cumulants of a higher-order than κ_3 is D_0.

Furthermore, although this assumption is based on the analysis of an infinite geometry, it will be extended to define the diffusion coefficient for a semi-infinite geometry as well. Therefore, the hybrid diffusion coefficient (D_4 for κ_1 and D_0 for all

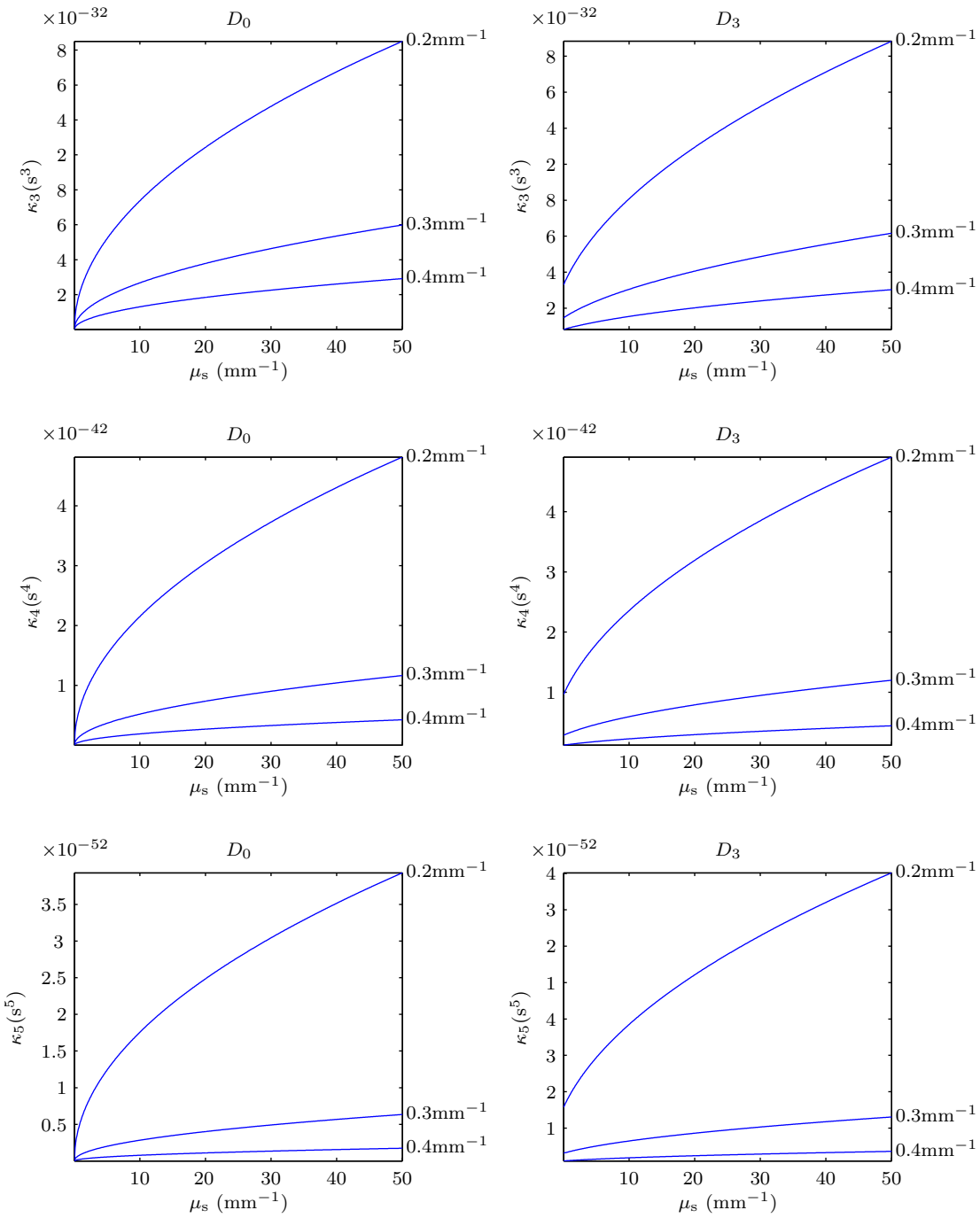

Figure 3.1: The third, fourth and fifth cumulants as calculated using the Diffusion Approximation for an infinite medium using two different diffusion coefficients. The detector is 10mm from the source and the amount of absorption present is displayed next to each plot.

higher-order cumulants) will be used throughout this thesis.

3.3.1.1 Reflectance

The effect of using the hybrid diffusion coefficient in the calculation of a medium's reflectance can be shown to be a simple scaling factor. The relationship between the reflectance calculated using the hybrid coefficient, R^{hybrid}, and that using D_0, R^{D_0}, is defined in Appendix A as:

$$\frac{R^{\text{hybrid}}}{R^{D_0}} = \exp(-\mu_{\text{a}} v \Delta\kappa_1) \tag{3.3.23}$$

where $\Delta\kappa_1$ is defined as the change in the value of the first cumulant from using the two different diffusion coefficients:

$$\Delta\kappa_1 = \kappa_1^{D_4} - \kappa_1^{D_0} \tag{3.3.24}$$

3.3.1.2 TPSFs

The effects of using the hybrid diffusion coefficient instead of D_0 on an unnormalised TPSF are changes in both its expected value and intensity. In order to produce a TPSF using the hybrid definition, D_0 should first be used to calculate an initial TPSF. This can then be shifted in time by the difference between the first cumulants as calculated using both D_0 and D_4, making the TPSF's mean value equal to the first cumulant calculated using D_4 as the diffusion coefficient. By scaling the resulting TPSF by the factor shown in Eq. (3.3.23), the TPSF's intensity will also be equal to that defined by the hybrid reflectance. Therefore, a hybrid TPSF, $R^{\text{hybrid}}(t)$, is

defined by:

$$R^{\text{hybrid}}(t) = \exp(-\mu_{\text{a}} v \Delta\kappa_1)\; R^{D_0}(t - \Delta\kappa_1) \tag{3.3.25}$$

where $R^{D_0}(t)$ is the initial TPSF calculated using D_0 as the diffusion coefficient and $\Delta\kappa_1$ is defined in Eq. (3.3.24).

3.4 Summary

Throughout this thesis, the Diffusion Approximation will be used as a forward model, describing the propagation of light through scattering media. In this chapter, the limitations of this model were discussed briefly, and the model's use in this study justified. Equations describing the light reflected from a semi-infinite medium, dependent on its scattering and absorption coefficients, were then derived for both full-field and spatially resolved detection and for the metrics defined in §1.5.

These equations require the definition of a diffusion coefficent, the exact value of which remains the subject of much debate. In this thesis, different values for the coefficient are used for different cumulants, as suggested by Morris.[71] TPSFs and reflectances calculated using the Diffusion Approximation will also be affected by the use of this "hybrid" coefficient. These effects were described analytically.

Chapter 4

System Metrics

4.1 Introduction

The moments, cumulants and reflectance described in the previous chapter are all metrics from which the medium's scattering and absorption coefficients can be potentially determined. This chapter will describe the relative advantages of the moments and cumulants and will therefore determine the metrics that will be studied in this thesis.

The error analysis performed in Chapter 6, from which the optimum metrics can be determined, requires the knowledge of these metrics' dependence on both the medium's scattering and absorption coefficents. This dependence will therefore be described graphically in this chapter for both full-field and spatially resolved detection. In order to do this, however, the range of skin parameters over which the metrics will be modelled is considered.

4.2 Potential Metrics

A TPSF is described by an infinite number of moments and cumulants, as well as its reflectance – these were defined in §1.5. As analysing all of these possible metrics is inherently impossible, it is necessary to limit the subject of this thesis to a smaller number. The extent of these limitations will be discussed in this section.

4.2.1 Reflectance

The reflectance of a medium is the most intuitive and commonly used metric available and requires only a modest hardware system for it to be measured. For these reasons, it will be one of the metrics investigated in this thesis and will be used as a basis of comparison against the many studies that have previously made use of it.

4.2.2 Moments and Cumulants

A medium's absorption and scattering coefficients could feasibly be calculated using both the infinite sets of the corresponding TPSF's moments and cumulants. There are certain mathematical advantages in using cumulants, however:

- The first and second cumulants of a probability density function equate to the distribution's expected value and variance respectively. In contrast, only the first of the moments (which also represents the expected value) has an intuitive meaning.

- For a distribution, X, and a constant temporal shift, c:

$$\kappa_i[X+c] = \begin{cases} \kappa_1[X] + c & \text{for } i = 1, \\ \kappa_i[X] & \text{for } i \geq 2. \end{cases} \tag{4.2.1}$$

  Thus the effect of the shift on the first cumulant is a simple addition, making the first cumulant *shift-equivariant*, while the second-order and higher cumulants are shift-invariant.[83] This is essential in the calculation of the reflectance and TPSF using a hybrid diffusion coefficient as explained in §3.3.1. Moments greater than the first order, however, do not share this shift invariance.

- Cumulants are additive over convolution. This is important in removing the effects of the shape of the input pulse on the resulting TPSF, as explained later.

For these reasons, it was decided to analyse the cumulants rather than the moments as potential metrics.

4.2.3 Spatial Dependence

As light scatters randomly within a medium, it will exit at different points from the tissue in relation to the position of the incident light. This spatial information can be maintained by spatially binning the light on detection, thus splitting the full-field TPSF into several smaller distributions. This has the advantage of increasing the number of possible metrics. However, this increase also has its disadvantages: the light received in each spatial bin can be significantly less than the amount detected in

a full-field configuration, thus greatly reducing the measurables' signal-to-noise ratios. This could result in greater inaccuracies in the calculated absorption and scattering coefficients. This thesis will therefore look at both full-field and spatially resolved detection as possible regimes when choosing the most appropriate metric pair.

4.3 Tissue Model

The theory presented in Chapter 1 is applicable to any scattering medium. However, in order to discuss the metrics' dependence on the medium's properties – and ultimately to decide on an optimum set of metrics to calculate their values – it is necessary to define a range of values for the scattering and absorption coefficients over which the metrics will be analysed.

The ability to characterise human skin has a number of potential applications as mentioned in Chapter 1. This thesis will therefore focus on human tissue, and thus the ranges of the μ_a and μ_s coefficients will be defined to match those found within skin.

Human skin is a complex, heterogeneous tissue whose exact structure varies considerably between people, as well as over each person's body. However, it is often modelled as consisting of homogeneous layers whose μ_s and μ_a parameters are a measure of the overall scattering and absorption present within each layer. The layers in a simplified version of the model described by Cotton and Claridge[84] are defined as follows:

1. The upper-most layer of the skin is the *stratum corneum* whose thickness varies significantly depending on its position on the body – it is thickest in load-bearing areas such as the soles of the feet. Cotton and Claridge make the assumption that this layer has no scattering or absorption properties and merely acts as a diffuser for the incident light.

2. The second layer of skin is the *epidermis* which, relative to the stratum corneum, has a comparatively constant thickness. It has been shown by Anderson & Parrish[85] that scattering within the epidermis is either negligible or highly forward in nature. They also found that the absorption within the epidermis was predominantly due to the layer's melanin content.

3. Below the epidermis is the *papillary dermis* which consists mainly of blood capillaries and a fine "network" of collagen fibres. These fibres make the papillary dermis highly scattering in nature.

4. The lowest layer of interest within human skin is the *reticular dermis*, consisting of thicker arterial and venous vascular structures, as well as thicker bundles of collagen fibres. As these bundles are large compared to the wavelength of the light, the light will experience highly forward scattering to such an extent that it is assumed that no light will be returned from the reticular dermis. It is therefore unnecessary to investigate the structure of skin below this layer.

Cotton and Claridge later refined their model to separate the papillary dermis into four distinct layers depending on the presence of melanin within the dermis.[86] However, this is not covered here.

The problem with this model, however, is that with each layer having its own scattering and absorption properties, the number of unknowns within the model would be too great to investigate initially. Therefore, a single-layered model was used whose parameters approximated the overall scattering and absorptive effects of human skin.

The model used within this thesis was therefore a semi-infinite, single-layered, absorbing medium containing scattering particles with an anisotropy factor, g, assumed to be constant at a value of 0.9, as stated by Meglinskiĭ and Matcher.[87] A refractive index, n, of 1.4 was modelled indirectly by defining the speed of the light within the medium according to Eq. (3.3.2).

Skin is a complex tissue, and there are large variations in its structure and thickness. This therefore means that it can possess a large range of potential absorption and scattering coefficients, which should be completely covered by the simulations. The findings of several papers[87–89] were therefore compared to find the extent of this range. Simpson et al.[43] found the skin's absorption coefficient to reach as low as 0.01mm^{-1}, whereas Anderson & Parrish[90] stated that it can be as high as 2mm^{-1}. Meanwhile, Jacques[91] recorded a sample of skin's scattering coefficient to be as low as 18.7mm^{-1}, and Anderson & Parrish[90] again found the upper limit to be 140mm^{-1}.

The ranges for the model's scattering and absorption coefficients are therefore shown below:

$$15\text{mm}^{-1} \leq \quad \mu_\text{s} \quad \leq 150\text{mm}^{-1} \tag{4.3.1}$$

$$0.01\text{mm}^{-1} \leq \quad \mu_\text{a} \quad \leq 2\text{mm}^{-1} \tag{4.3.2}$$

In the case of spatially resolved detection, it is also necessary to determine the maximum source-detector distance, ρ_max, up to which the metrics will be investigated. This was achieved by studying the relationship between ρ and the detected intensity – the spatial distribution. As a decrease in the intensity of detected light corresponds to a decrease in the signal-to-noise ratio, the maximum distance can be chosen as the distance beyond which the intensity drops below a threshold level – it would be unlikely that sufficient light would be detected below this threshold to enable accurate measurements of the TPSF's metrics. However, as the spatial distribution is dependent on both the medium's scattering and absorption, this maximum distance will vary for different μ_s and μ_a values. Therefore, in order to maximise the useful range of source-detector distances, the value of ρ_max should be defined for the distribution that minimises the drop in intensity as ρ increases. The lowest absorption coefficient of interest, defined in Eq. (4.3.2) as 0.01mm^{-1}, should therefore be used to produce this distribution. The relevant scattering coefficient is less immediately obvious, however, and so Figure 4.1 shows four spatial distributions over the range of scattering coefficients set in Eq. (4.3.1). The reflectances shown are calculated for a

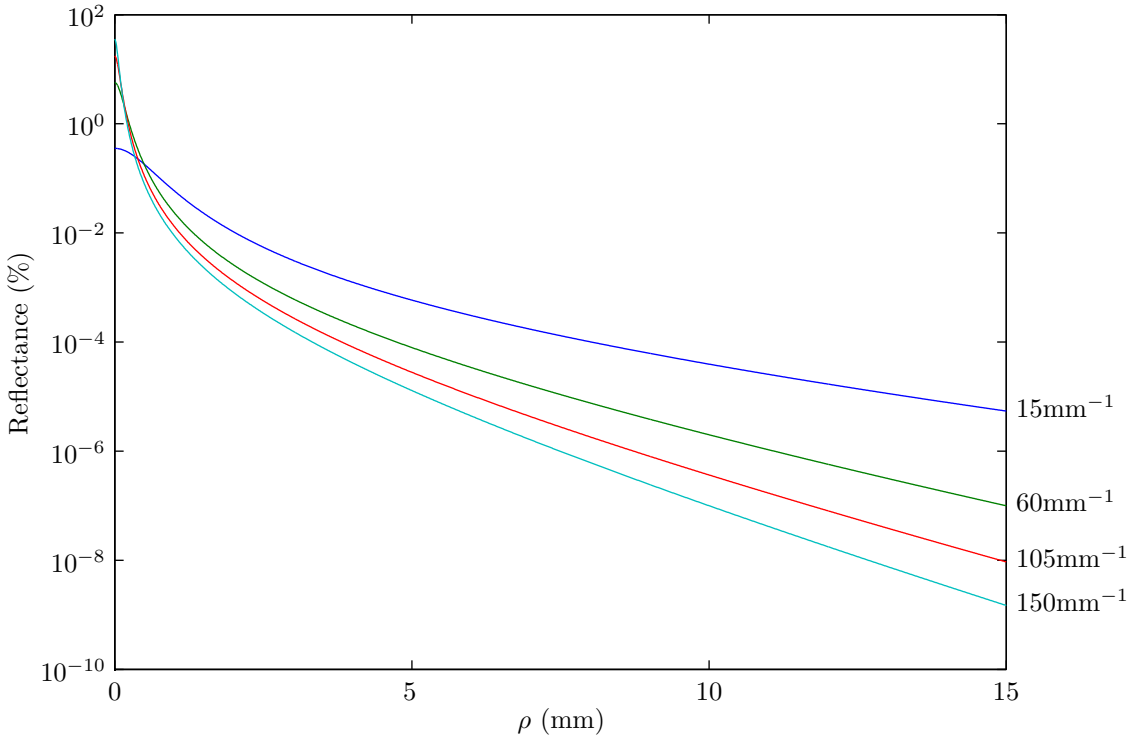

Figure 4.1: The spatial distribution of light reflected from a semi-infinite medium with an absorption coefficient of 0.01mm^{-1} for various scattering coefficients. The value of the scattering coefficient is displayed next to each curve. The reflectances shown are calculated for a detector size of 0.1mm^2, independent of the source–detector distance.

detector size of 0.1mm^2, independent of the source–detector distance.

The variation of the reflectance with source–detector distance will be described fully in §4.4. However, it can be seen from Figure 4.1 that beyond a source–detector distance of 1mm the reflectance decreases as the scattering coefficient, μ_s, increases. The increased scattering causes more photons to be scattered out of the medium near to the source. As well as this, the photons exiting the medium far from the source will have travelled a much longer pathlength, and so will be more affected by the

medium's absorption. In this case, the back-scattered light is therefore maximised (for source–detector distances over 1mm) for the smallest scattering coefficient in Eq. (4.3.1), 15mm^{-1}.

The maximum source–detector distance was therefore chosen to be 10mm, at which point the maximum reflectance over the range of scattering and absorption coefficients defined in Eqs. (4.3.1) and (4.3.2) had dropped to around 4×10^{-5} %.

4.4 Metric Dependence on Scattering, Absorption and Source–Detector Distance

It is now known which metrics are to be examined in this thesis and the ranges of variables over which they will be modelled over. However, before the measurables are investigated for their suitability in determining a medium's absorption and scattering coefficients, it is useful to demonstrate how these metrics vary over the chosen scattering, absorption and, in the case of spatially resolved detection, source–detector distance ranges. This section will therefore describe the metrics' dependence on these parameters.

4.4.1 Full-field Detection

The reflectance and first three cumulants are described for full-field detection using the Diffusion Approximation by Eq. (3.3.5) and Eqs. (3.3.13) to (3.3.15). Substituting the hybrid definition of the diffusion coefficient (D_4 for κ_1 and D_0 for all higher-order

cumulants – as explained in §3.3.1) and the definition of z_0 from Eq. (3.3.3) into these equations, as well as taking into account the corresponding scaling factor for the reflectance (§3.3.1.1), the equations become:

$$R = \exp\left(-\frac{\sqrt{3\mu_\mathrm{a}\mu_\mathrm{s}'} + \sqrt{(3\mu_\mathrm{s}' + 4\mu_\mathrm{a})\mu_\mathrm{a}}}{2\mu_\mathrm{s}'}\right) \tag{4.4.1}$$

$$\kappa_1 = \frac{\sqrt{4 + \frac{3\mu_\mathrm{s}'}{\mu_\mathrm{a}}}}{2v\mu_\mathrm{s}'} \tag{4.4.2}$$

$$\kappa_2 = \frac{\sqrt{3}}{4v^2\sqrt{{\mu_\mathrm{a}}^3\mu_\mathrm{s}'}} \tag{4.4.3}$$

$$\kappa_3 = \frac{3\sqrt{3}}{8v^3\sqrt{{\mu_\mathrm{a}}^5\mu_\mathrm{s}'}} \tag{4.4.4}$$

where μ_s' is the reduced scattering coefficient, defined as:

$$\mu_\mathrm{s}' = \mu_\mathrm{s}(1 - g) \tag{4.4.5}$$

The equation for the TPSF shown in Eq. (3.3.4) can also be altered to use the hybrid definition of the diffusion coefficient – as demonstrated in Eq. (3.3.25) – to give:

$$R(t) = \left(\sqrt{\frac{6}{\pi}}\right) \frac{v\mu_\mathrm{s}' \exp\left(-\frac{3\mu_\mathrm{a}}{2\left(\sqrt{3\mu_\mathrm{a}\mu_\mathrm{s}'} - \sqrt{\mu_\mathrm{a}(3\mu_\mathrm{s}'+4\mu_\mathrm{a})} + 2v\mu_\mathrm{a}\mu_\mathrm{s}'t\right)} - \mu_\mathrm{a}vt\right)}{\left(\frac{\sqrt{3\mu_\mathrm{a}\mu_\mathrm{s}'} - \sqrt{\mu_\mathrm{a}(3\mu_\mathrm{s}'+4\mu_\mathrm{a})} + 2v\mu_\mathrm{a}\mu_\mathrm{s}'t}{\mu_\mathrm{a}}\right)^{3/2}} \tag{4.4.6}$$

The metrics' dependence on the absorption coefficient will be investigated first, with Figure 4.2 showing the effects of the absorption coefficient's value on a TPSF. The TPSFs are shown in terms of power rather than energy as this removes the need to specify a size of time bin. It has been shown in §1.4 that absorption can

be added to a TPSF by its multiplication with a decaying exponential of the form $\exp(-\mu_a vt)$. The attenuation is greater at larger time values as photons arriving later in the TPSF will have travelled further in the medium and so will be more affected by the additional absorption. This has the effect of reducing the TPSF's intensity, width and mean photon flight time. These effects can be seen in more detail in Figure 4.3, which shows the variation of the reflectance and first three cumulants with absorption coefficient for several values of scattering coefficient.

As demonstrated by the TPSFs, Figure 4.3 shows the reflectance decreasing with increasing absorption, with the rate of change being much higher for low values of μ_a: once the TPSF's tail has been attenuated by a small amount of absorption, further increases in absorption will have less effect on the TPSF's overall intensity. This trend is more pronounced for the first cumulant. Despite the tail's relatively low intensity, its photons' long flight times will have a marked influence on the mean flight time. A small increase in the absorption will cause these photons to be strongly attenuated in comparison to the photons arriving earlier in the TPSF, reducing their contribution to the mean time of flight and thus causing the first cumulant to rapidly decrease. In other words, an increase in absorption will reduce the probability of photons with longer pathlengths being detected, and so the mean flight time will reduce.

An increase in absorption has the effect of making a TPSF narrower, as shown in Figure 4.2. The corresponding reduction in probability of photons with longer

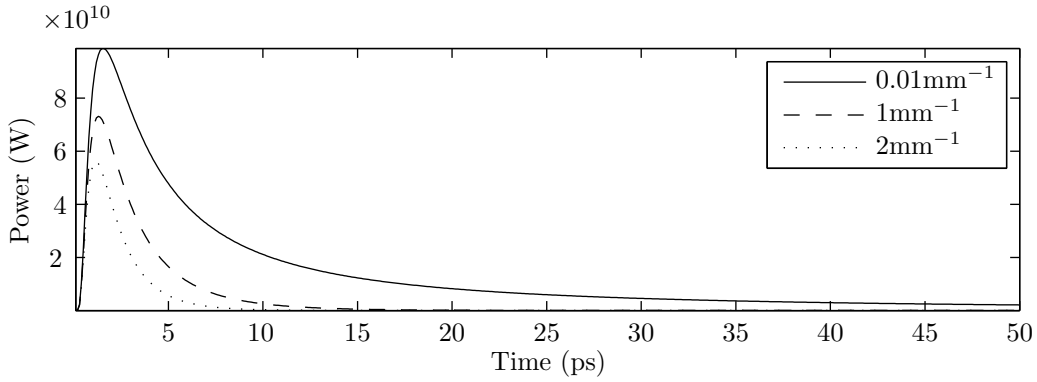

Figure 4.2: The effect of the absorption coefficient's value on a TPSF. The TPSFs shown were calculated using the Diffusion Approximation for full-field detection, using a scattering coefficient of 15mm^{-1}.

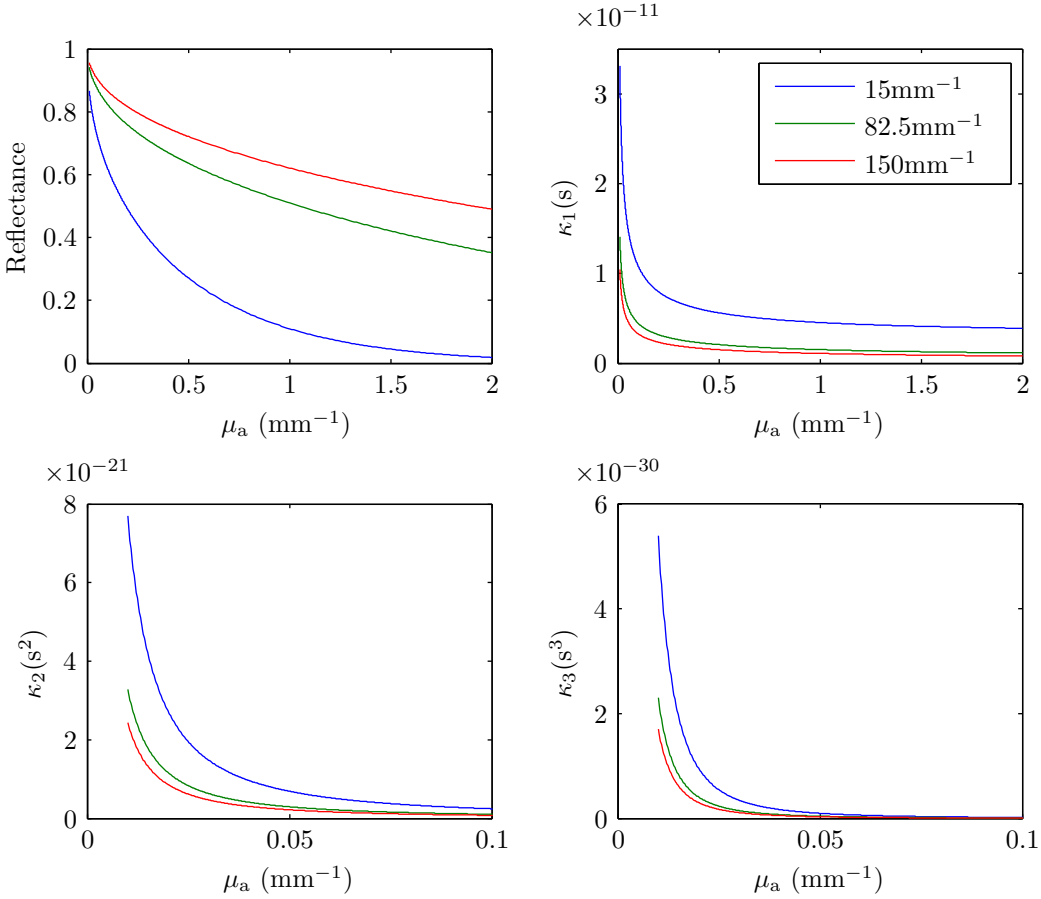

Figure 4.3: Plots of the reflectance and first three cumulants against the absorption coefficient, as calculated using the Diffusion Approximation for full-field detection. The legend shows the value of scattering coefficient for each plot and corresponds to all four graphs. Note that the second and third cumulants are displayed over a smaller range of μ_a values for clarity.

pathlengths results in a smaller range of pathlengths being detected, which in turn causes a reduction in the second cumulant, the variance. Taking this to an extreme, for a very high level of absorption, only photons that are scattered quickly out of the medium will be detected, resulting in a very small variance in photon flight times. The shapes of the second cumulant's plots in Figure 4.3 are determined by the metric's proportionality to $\mu_{\mathrm{a}}^{-3/2}$ as defined in Eq. (4.4.3). Higher-order cumulants follow a similar form, with the power of the absorption coefficient decreasing by one each time, thus giving:

$$\kappa_n \propto {\mu_{\mathrm{a}}}^{\frac{1}{2}-n} \qquad \text{for } n \geq 2 \tag{4.4.7}$$

The gradients of the higher-order cumulants against the absorption coefficient therefore become steeper as the order of the cumulant increases. This is because higher-order cumulants are more dependent on the TPSF's tail, which in turn is more susceptible to attenuation by absorption.

The effect of the value of the scattering coefficient on a TPSF is shown in Figure 4.4. As μ_{s} increases, photons will be scattered out of the medium sooner due to the increased frequency of the scattering events. The decrease in the length of time each photon spends within the medium means that they will be less attenuated due to absorption, thus causing the intensity of light reflected from the medium to increase. As a result of these effects, the TPSF will become narrower and its intensity will increase with increasing scattering.

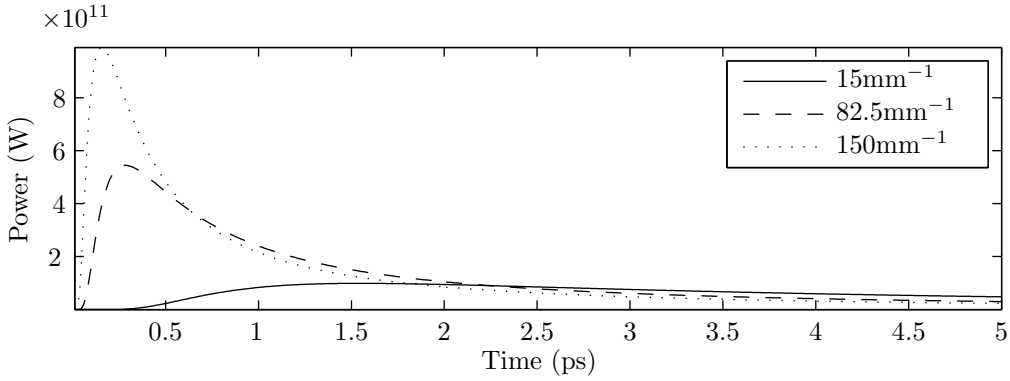

Figure 4.4: The effect of the scattering coefficient's value on a TPSF. The TPSFs shown were calculated using the Diffusion Approximation for full-field detection, using an absorption coefficient of 0.001mm^{-1}.

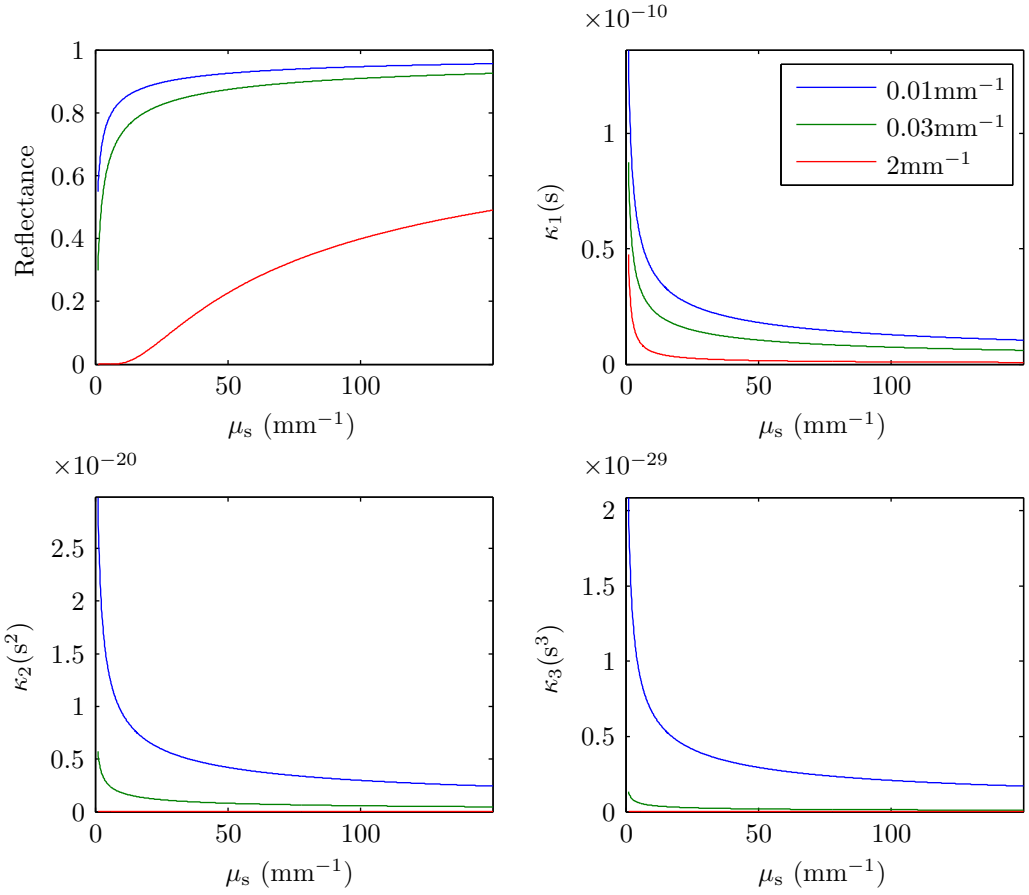

Figure 4.5: Plots of the reflectance and first three cumulants against the scattering coefficient, as calculated using the Diffusion Approximation for full-field detection. The legend shows the value of absorption coefficient for each plot and corresponds to all four graphs. For completeness, a larger range of scattering coefficients than will be used within this thesis is discussed here.

These effects can be seen in more detail in Figure 4.5 which shows a larger range of scattering coefficients than will be used within this thesis, in order to present a complete picture of the metrics' variations with μ_s. The rate of change of the first cumulant, the mean photon flight time, can be seen to be much greater at lower scattering levels than for higher values. The effect can be thought of as obeying the law of diminishing returns: as the scattering level increases, the number of photons not scattered straight out of the medium will decrease, and thus there will be fewer photons remaining that can be affected by further increases in μ_s. The rate of change in the reflectance is steeper for lower scattering levels for similar reasons, except for at high absorption levels: as can be seen by the TPSFs in Figure 4.4, at low scattering levels the eventually back-scattered photons will spend longer in the medium, and so in the case of high absorption will be heavily attenuated.

The second cumulant can be seen to decrease with increasing scattering: the decrease in the probability of photons with longer flight times being detected leads to a decrease in the range of flight times and thus the variance. The third cumulant also follows this form. In fact, in can be seen from Eqs. (4.4.3) and (4.4.4) that all cumulants above the first order are proportional to $\mu_s^{-1/2}$, with only the constant of proportionality changing between orders. Again, this fits with higher-order cumulants relying more heavily on the TPSF's tail which can be seen to decrease with increasing scattering.

As the value of the scattering coefficient tends to zero, the photons entering the medium will experience minimal scattering and so will spend a long time in the medium. As a result, the width of the TPSF, and thus the cumulants, will tend to infinity. The light that is detected will be heavily affected by the medium's absorption and so the reflectance will tend to zero.

Note that in the extreme case of a scatter-free medium, photons will never leave the sample due to its semi-infinite nature. Therefore, the reflectance and cumulants will equal zero.

4.4.2 Spatially Resolved Detection

The TPSF and reflectance of a medium for spatially resolved detection are described using the Diffusion Approximation by Eqs. (3.3.16) and (3.3.17), while the moment generating function is given in Eq. (3.3.18).

The effect of absorption will not be discussed in detail in relation to spatially resolved detection as this has been fully covered during the analysis of the full-field regime; its effects on a TPSF, and therefore the TPSF's metrics, is considered relatively intuitive.

The effect of the scattering coefficient on a TPSF for spatially resolved detection is shown in Figure 4.6 for an annular detector with radius 2.9–3.0mm centred on the source. At low scattering levels, scattering events will occur relatively infrequently, and so photons will spend a long time in the medium. As a result, the corresponding

TPSF will have a relatively low amplitude, due to the increased effect of the medium's absorption, and a high variance due to the large range of flight times of the detected photons. At high scattering levels, photons will undergo frequent scattering events and so will be scattered out of the medium closer to the source. Photons that remain in the medium will also take longer to reach the detection point due to the increased scattering and so will be more susceptible to the medium's absorption. The resulting TPSF will therefore also have a low intensity and high variance, while its mean time of flight will be greatly increased.

For scattering levels between these two values, there is a trade-off between the two effects on the photon transport in the medium. It follows that for any spatial bin off-axis from the source, there should be an optimum level of scattering which will cause the most photons to be scattered sufficiently to reach the point of detection without overly increasing the pathlength and causing excess attenuation by the medium's absorption. (The mid-scattering level in Figure 4.6 does not represent the optimum value of scattering coefficient, merely the middle point between the low and high scattering levels. However, it still shows a large increase in the intensity compared to the low and high scattering level TPSFs.)

The optimum scattering levels can be seen in the reflectance plots in Figure 4.7 for the two more distant spatial bins. The furthest spatial bin shown in the plots corresponds to the TPSF in Figure 4.6, and so by looking at the reflectance plot, it

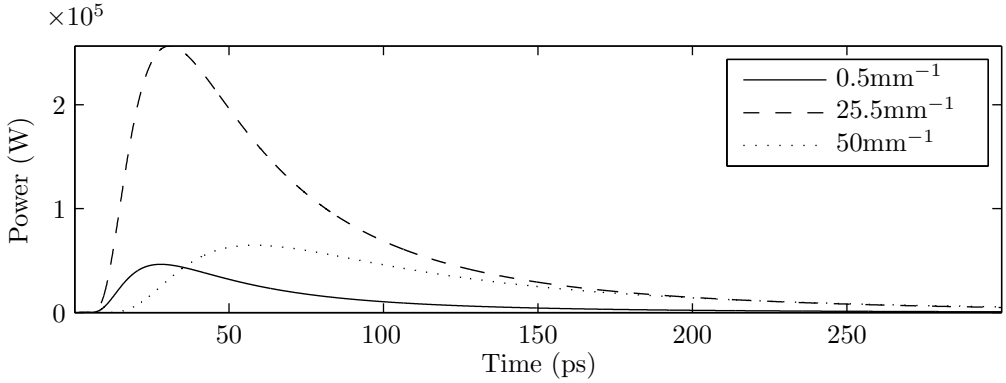

Figure 4.6: The effect of the scattering coefficient's value on a TPSF for spatially resolved detection. The TPSFs shown were calculated using the Diffusion Approximation using an absorption coefficient of 0.001mm^{-1} and an annular detector with radius 2.9–3mm centred on the source. For completeness, the range of scattering coefficients discussed here extends below that which will be used within this thesis.

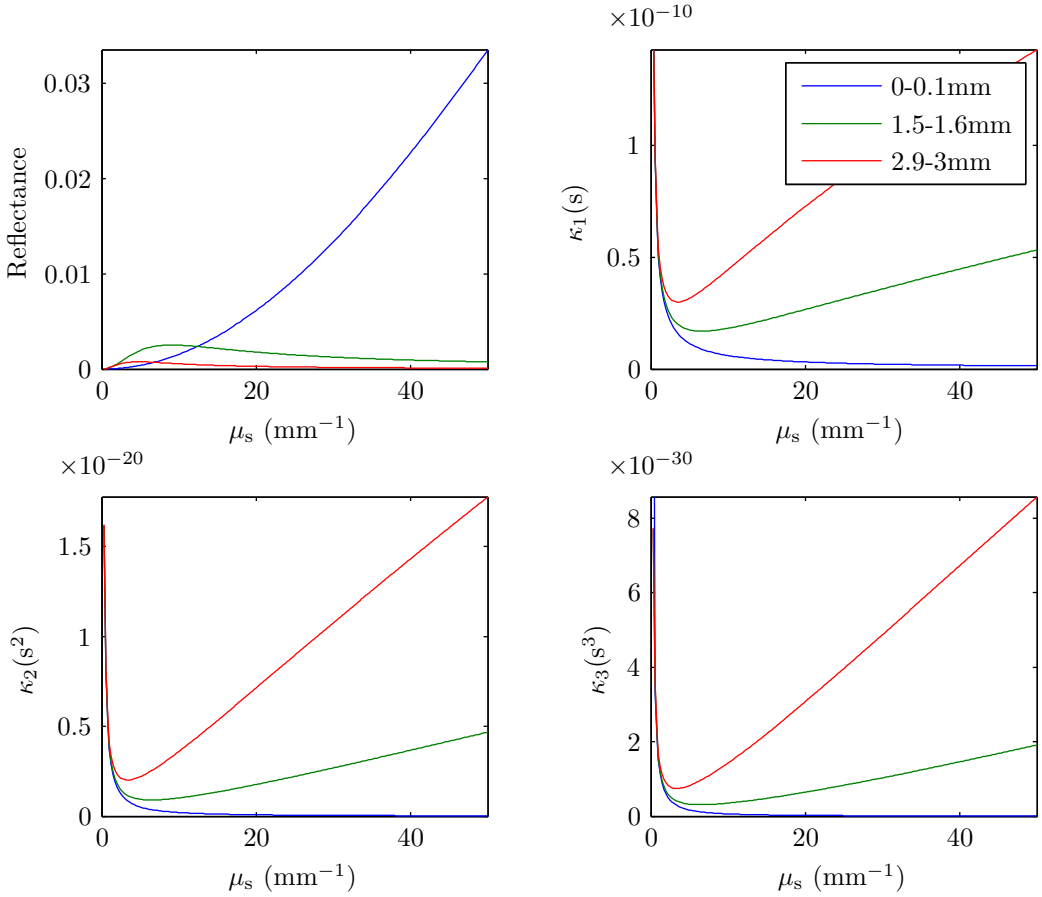

Figure 4.7: Plots of the reflectance and first three cumulants against the scattering coefficient, as calculated using the Diffusion Approximation for spatially resolved detection using an absorption coefficient of 0.001mm^{-1}. The legend shows the inner and outer radii of the annular detector centred on the source and corresponds to all four graphs. For completeness, the range of scattering coefficients discussed here extends below that which will be used within this thesis.

can be seen that the optimum scattering level for the TPSF is around 5mm^{-1}. An optimum level can similarly be seen for the annular detector with radii 1.5–1.6mm. For on-axis (0–0.1mm) detection, however, no such optimum can be seen. In this case, an increase in the scattering levels will merely cause more photons to be scattered out of the medium nearer the source, thereby minimising the time spent within the medium and therefore the attenuation due to the medium's absorption. This will therefore maximise the reflectance on-axis.

In Figure 4.7, both the photons' mean flight time and flight time variance can be seen to tend to infinity as the scattering level tends to zero, regardless of the spatial binning used. This was explained, along with the extreme case of a scatter-free medium at the end of §4.4.1.

As the scattering levels increase, the mean and variance can be seen to increase for off-axis spatial detection as the photons that are not absorbed take longer to scatter out of the medium, and will take a greater range of pathlengths, thus increasing the variance. However, this is not observed for on-axis detection: for high scattering levels, the mean photon flight time will decrease as photons are scattered out of the medium nearer the source. This will also lead to a smaller range of photon pathlengths, thus reducing the variance.

The effect of the source–detector distance on a TPSF can be seen in Figure 4.8. As the radii of the annular detector increase, the photons detected will travel further

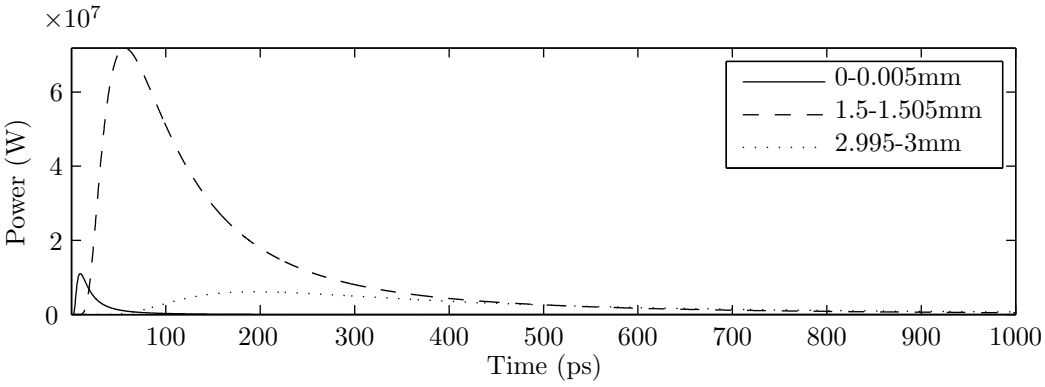

Figure 4.8: The effect of the source–detector distance on a TPSF. The TPSFs shown were calculated using the Diffusion Approximation, using an absorption coefficient of 0.001mm^{-1} and a scattering coefficient of 15mm^{-1}. Note that the full range of source–detector distances used in this thesis are not displayed here for purposes of clarity.

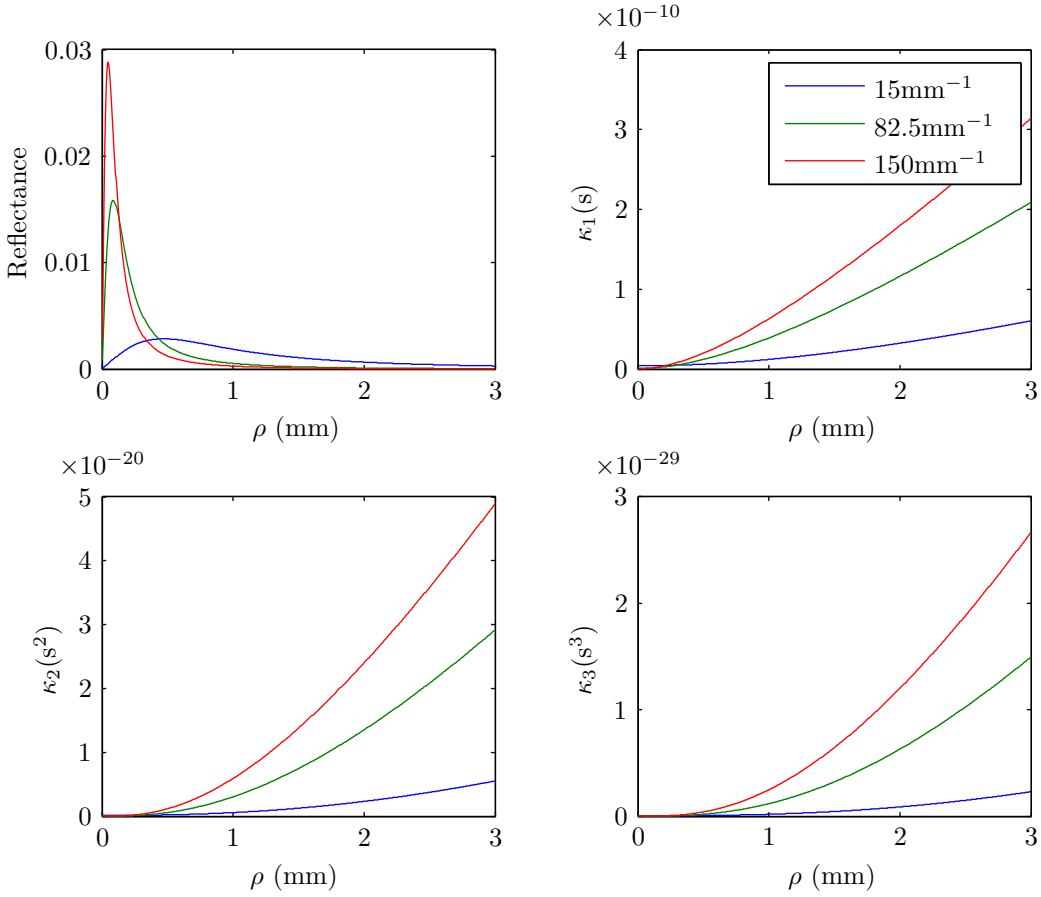

Figure 4.9: Plots of the reflectance and first three cumulants against the source–detector distance, as calculated using the Diffusion Approximation using an absorption coefficient of 0.001mm^{-1}. The legend shows the value of scattering coefficient for each plot and corresponds to all four graphs. Note that the full range of source–detector distances used in this thesis are not displayed here for purposes of clarity.

in the medium and will take a greater range of pathlengths, causing both the peak of the TPSF to be shifted later in time and its width to increase. This corresponds to an increase in both the mean photon flight time and the variance. The change in the reflectance, however, can be seen to be more complex. For a constant detector size, the spatial distribution can be seen to follow the plots in Figure 4.1 on page 53. For a constant level of scattering, the reflectance will naturally decrease as the source–detector distance increases: photons are more likely to scatter out of the medium closer to the source, and photons detected further away will have travelled further in the medium and so will have been attenuated more by the absorption. An increase in scattering will lead to an increase in the number of photons leaving the medium nearer the source, resulting in increased reflectance for low source–detector distances and decreased reflectance for higher values of ρ, which explains the crossing of the plots for different scattering levels near the source.

However, when using annular detectors of a constant width, the areas of the detectors will vary: an annular detector with smaller radii will have a smaller area and so the number of photons it detects will be reduced. This effect can be seen in Figure 4.9 in which the metrics have been calculated against the source–detector distance using an annular detector with a constant width (the distance between the inner and outer radii) of 5μm at each spatial point. The plots of reflectance, although reducing with increasing spatial distance as expected, can be seen to also reduce at

low source–detector distances – this is the effect of the smaller detector area at this distance. Thus, the TPSF for on-axis detection (0–0.005mm) in Figure 4.8 can be seen to be much smaller than that at 1.5mm from the source.

The spatial position of the peak reflectance, below which the detector's smaller size becomes a limiting factor, can be seen to reduce as the scattering level increases. This is because the area over which the majority of the photons are reflected will reduce as the scattering increases and photons are scattered out of the medium sooner. This can be seen by the flattening of the plots at low source–detector distances in Figure 4.1 on page 53. The point below which the rate of change in reflectance begins to decrease for decreasing source–detector distance is approximately the point below which the effect of the reduced detector area will have a marked effect on the reflectance. Therefore, this point will decrease in distance from the source for increased scattering.

As explained for the corresponding TPSFs, the mean photon flight time and variance will increase with both increasing scattering and spatial distance as photons travel further in the medium before being scattered out. It can be seen in Figure 4.9 however, that at small source–detector distances, the first cumulant decreases as μ_s increases. This was demonstrated in Figure 4.7.

4.5 Summary

In this chapter, the metrics that will be analysed in this thesis were determined. The medium's reflectance was chosen for its prevalence in existing characterisation

methods, while the cumulants' intuitive meanings and useful mathematical properties (such as shift-invariance and additivity over convolution) resulted in their choice over the moments. The chapter then described the relative advantages of full-field detection (higher signal-to-noise ratios) and spatially resolved detection (more potential metrics), from which the analysis of both regimes was justified.

The range of scattering and absorption coefficients which the thesis will investigate was determined by focussing on the study of human skin. Possible ranges of the optical coefficients were then determined from existing literature.

Finally, to increase understanding of the results of the error analysis in Chapter 6, the dependence of the metrics in question on a medium's scattering and absorption coefficents were investigated graphically.

Chapter 5

The Streak Camera

5.1 Introduction

After choosing the metrics of interest for the determination of a medium's scattering and absorption properties, the next stage is to investigate how these metrics may be measured using a time resolved system. This comes with its own challenges: since a typical TPSF lasts in the order of nanoseconds, it is essential to record the arrival times of photons with a picosecond resolution, far less than the maximum frame rates associated with a typical CCD camera. One such instrument capable of this high resolution is a streak camera, which this chapter will focus on.

The purpose of this chapter is to ascertain the noise characteristics of a typical streak camera and calculate the effect these will have on the metrics of interest. Using this information, measurements under realistic noise conditions can be modelled. This will be achieved by the analysis of the noise sources within a streak camera. This sequence of noises will then be modelled, allowing its effects on a typical TPSF to be

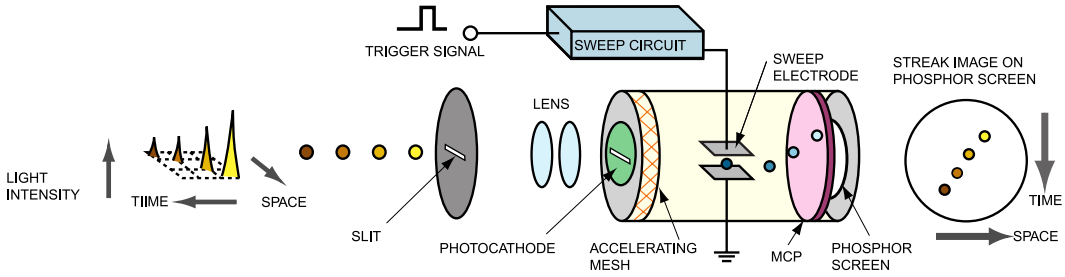

Figure 5.1: The configuration of a standard optoelectronic streak camera.[19] Image reproduced with permission of Hamamatsu Photonics K. K.

investigated. The effects of using a streak camera to attain the potential metrics over the entire parameter range can then be calculated.

The structure of this chapter is as follows. The configuration of a typical streak camera is described in §5.2, and its sources of noise identified. The sources of noise outside the streak camera such as the light source and losses due to scattering and absorption in the medium are also considered here. The generalised effects of each type of noise on TPSFs are covered in §5.5.2. The methods used to model the streak camera are then described in §5.5.3, along with the effects of a typical TPSF's "detection" by the camera on its metrics. This model is then applied to the entire optical coefficient ranges in §5.5.4, to produce a map of errors against the scattering and absorption coefficients for each metric.

5.2 Configuration of a Streak Camera

The configuration of a standard optoelectronic streak camera is described in both Figures 5.1 and 5.2, with the latter also showing the noise distributions for each stage

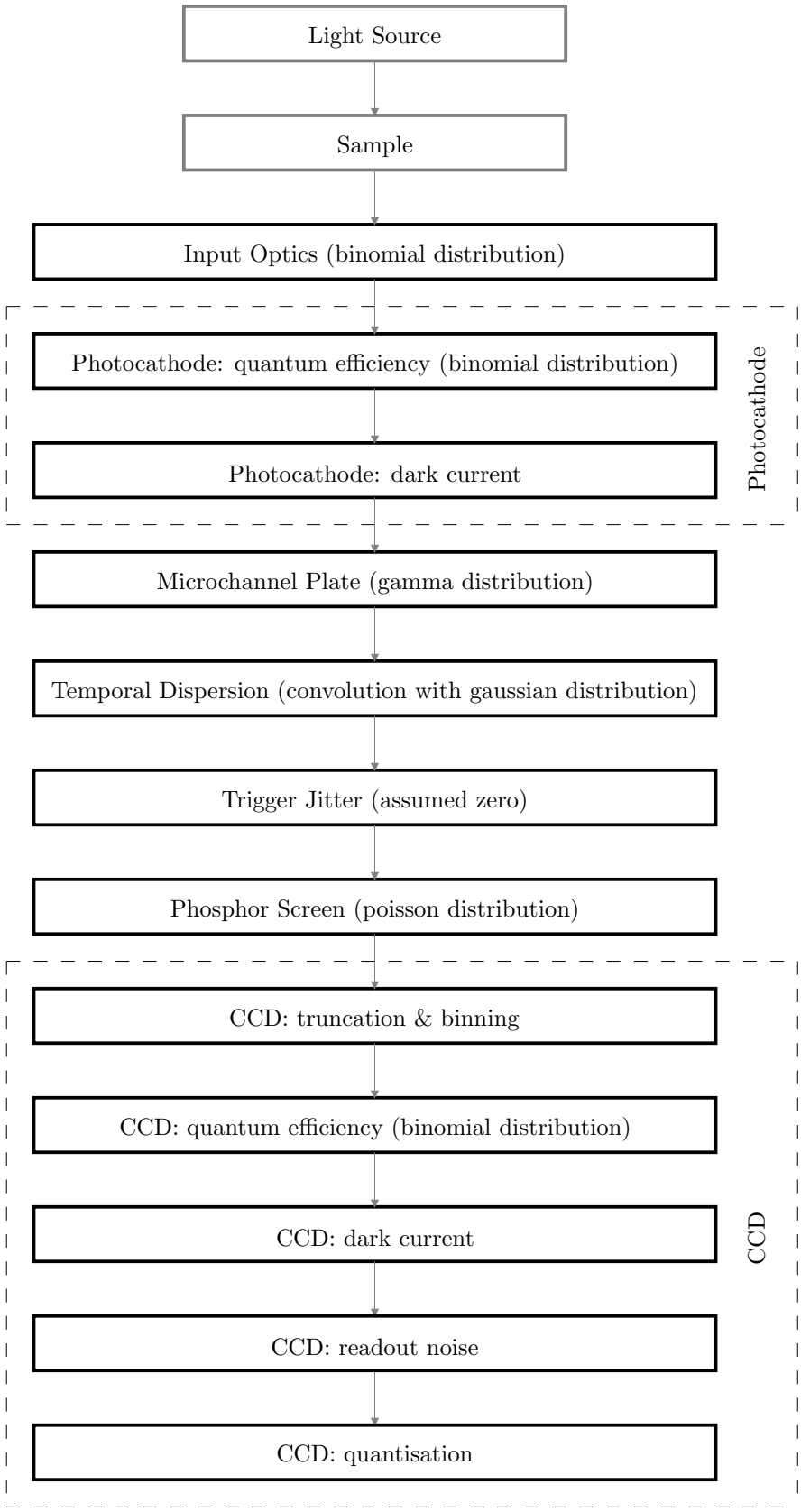

Figure 5.2: The configuration of a standard optoelectronic streak camera in flowchart form, along with the type of noise added at each stage. The first two stages are shown in grey as they occur outside the streak camera.

which will be discussed in §5.5.1. Light first travels through the streak camera's input optics. These consist of a slit, which allows a 1-dimensional line image of the light input to be taken, and a lens to focus these photons onto a photocathode at one end of a streak tube. The photocathode, according to the photoelectric effect, converts the photons to electrons which are then accelerated along the tube by an electrically-charged accelerating electrode.

The accelerated electrons then pass through a pair of sweep electrodes. Variation of the voltage across these plates, and thus the electric field, over time will cause the electrons passing through the electrodes to be deflected by different amounts. Therefore, the application of a linear voltage ramp across the electrodes will cause a deflection linearly proportional to the arrival time of the electrons, thereby sweeping the electrons over one of the CCD's axes.

Before reaching the end of the streak tube, the electrons pass through a microchannel plate (MCP). This electron multiplier increases the number of electrons passing through it via a process which will be explained later. The MCP's gain is dependent on the strength of the electric field applied across it. The electrons emitted from the MCP are then converted back to photons by a phosphor screen. These photons are then focussed onto the surface of a CCD camera.

The result is a two-dimensional image of a one-dimensional line input, with the second dimension containing the temporal information of the detected light. Due

to the finite number of pixels on the CCD, the image will be binned in both the spatial (horizontal) and temporal (vertical) axes, with the resolution of each of the axes dependent on the number of pixels in each direction on the CCD. The result is a binned TPSF for each of the image's spatial bins.

5.3 The Complete System

In order to fully understand the methods used to analyse scattering media, it is necessary to describe the use of the streak camera described above in a complete system. This requires a description of two of the system components, namely the light source and the component used to deliver the emitted light from the surface of the medium to the detector.

Light Source

The light source used in this hypothetical system is modelled as a 633nm laser. It will be shown that the laser must be capable of providing 16nJ pulses (§5.5.3.1 on page 106) within a space of time less than 20% of the shortest streak camera sweep time (§5.5.1). This gives a minimum pulse length of 40ps, giving the laser a power rating of 400W.

Light Delivery Component

It is necessary to consider how to detect light emitted from a medium using a streak camera considering the latter's slit input. In the case of full-field detection, a lens can

be used to focus the incoming light into the streak camera's slit. This will, however, attenuate the light due to the lens' imperfect spectral transmittance: a measure of the intensity of light transmitted through the lens relative to the intensity of incident light as a function of the wavelength of the light. As modern lenses have transmittances of over 95%, this attenutation effect is not considered in this thesis.[92]

The ability to take spatially resolved measurements from a medium using a streak camera is more complicated, however. The simplest method would be to take a radial measurement directly using the streak camera's slit input, as shown in Figure 5.3a. The recorded data could then be split into spatial bins and normalised for area. The simplicity of this method, however, would be outweighed by the relatively small area of the medium's surface "imaged", resulting in low levels of light received by the camera.

It is therefore better to employ annular detection, with which more of the light emitted from the medium's surface can be captured. This can be achieved using a circular bundle of optical fibres placed just above the surface of the medium. The opposite ends of fibres forming an annulus at the medium's surface can then be grouped together and be used to form a linear, spatial bin in the streak camera's slit, as demonstrated in Figure 5.3b. Note that in this figure, only one incomplete set of fibres is shown for simplicity. This method does not come without limitations however: not all emitted light will be accepted into the fibres due to their limited

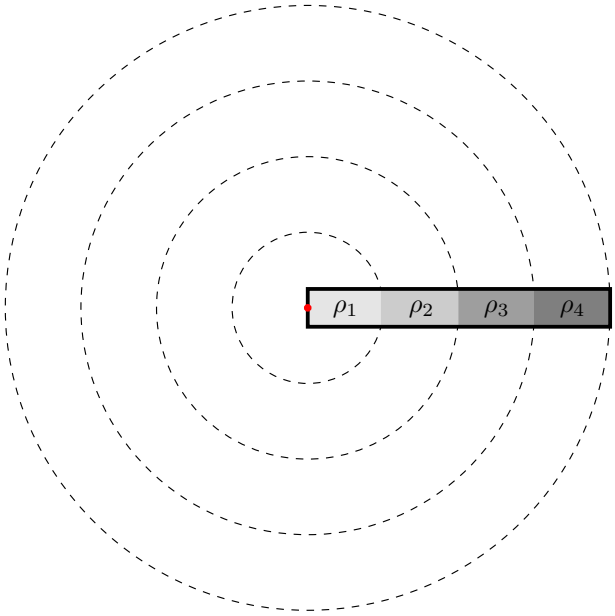

(a)

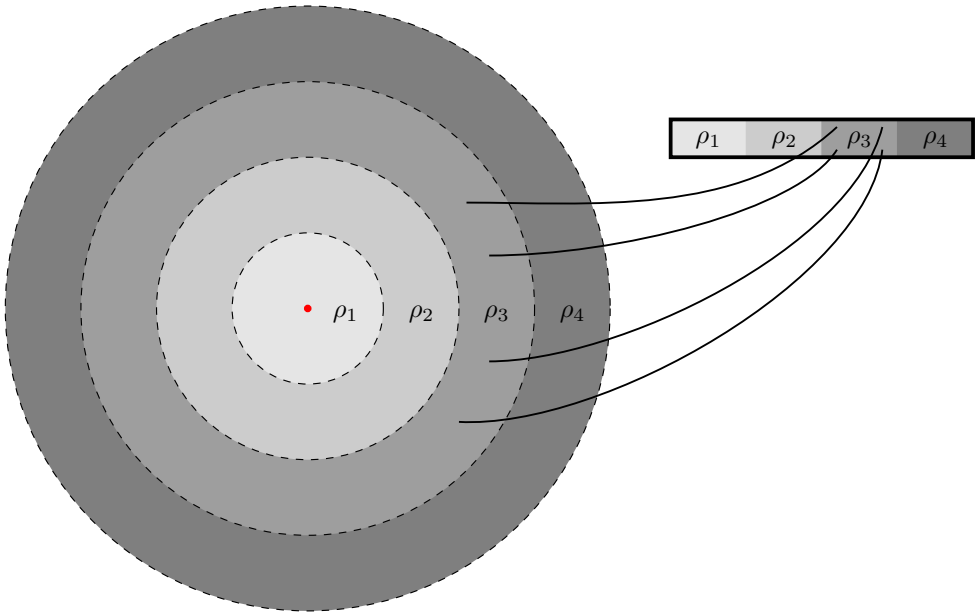

(b)

Figure 5.3: Two methods of light detection using a streak camera. In both figures, the surface of the medium is on the same plane as the paper; the thick black rectangle represents the camera's slit input; and the red dot signifies the position of the light input to the medium. In (a), radial detection is implemented directly into the streak camera's slit, whereas (b) demonstrates the more-complicated case of annular detection. In this latter case, optical fibres are used to deliver the light into the streak camera's slit. In this figure, only a small number of fibres are shown for simplicity.

acceptance angles, and light that is accepted will be attenuated inside the fibres.

The use of fibres, and their attenuating effect on the light emitted from the medium, can be avoided using a mask for each required annular detection. Such a mask would absorb the light emitted from the medium except for in an annular "window". Light passing through this window can then be focussed into the streak camera's slit input using a lens, as for full-field detection. The disadvantages to this method are the time and number of masks required to detect light from each of the annuli. Determination of a small number of annuli of interest, however, as is achieved in this thesis, can limit the extent of these issues.

In order to avoid the complications introduced by the use of optical fibres, this hypothetical system is designed around the use of the mask apparatus as described above.

5.4 Noise on the Initial TPSF

In order to rigorously characterise the errors introduced when using the streak camera, it will be necessary to investigate two potential sources of noise in the signal before it reaches the camera system: the light source and the sample being analysed. These are both shown in Figure 5.2.

Light Source

There will be a distribution in the number of photons emitted by the source of light used to illuminate the sample. Its intensity can therefore be characterised by shot noise.

Note that there is no requirement for the light pulses to be an approximation to a Dirac delta function, as required by the Diffusion Approximation[27] – it can be shown that the effect of the shape of the input pulse on the resulting TPSF (and therefore its cumulants) can be negated by a subtraction of the pulse's cumulants.[93] The limit to the width of the pulses therefore comes from the streak camera's selected sweep time.

Sample Attenuation

Light entering the sample from the source is subject to both scattering and absorption losses. Scattering losses occur when photons leave the medium in a different position to the detector, thereby escaping detection, whereas absorption losses are dependent on the path length of the light through the medium, as described by the Beer–Lambert Law. The effect of these losses is that, even for an ideal light source, the TPSF emitted from the sample will not vary smoothly over time. The corresponding noise can be determined by looking at each of these losses in turn.

As a result of scattering losses, each photon travelling through an absorption-free medium will have a certain probability, p, of reaching the detector, making it

a Bernoulli trial. As this probability does not change between successive photons, and each trial is independent, a sequence of more than one trial can be considered a Bernoulli process. As such, the number of photons detected is given by a binomial distribution, where n, the number of photons entering the sample, is determined for each light pulse by the light source's shot noise. Therefore, the probability of detecting k photons, $\Pr(k)$, when n photons are incident on the sample is:

$$\Pr(k) = \binom{n}{k} p^k (1-p)^{n-k} \tag{5.4.1}$$

where p is the probability of success in each individual trial and

$$\binom{n}{k} = \frac{n!}{k!(n-k)!} \tag{5.4.2}$$

otherwise known as the *binomial coefficent*.

In order to validate this assumption, 10,000 Monte Carlo simulations, each of 2000 photons, were performed for a scattering, absorption-free, medium. The number of photons detected in each simulation was recorded and the mean of these values used to calculate p for the medium simulated:

$$p = \frac{\text{mean number of photons detected}}{n} \tag{5.4.3}$$

where n is the number of photons input to the sample.

Figure 5.4 shows a clear match between the distribution of photons detected from the Monte Carlo simulations and a binomial distribution created using the parameters defined above.

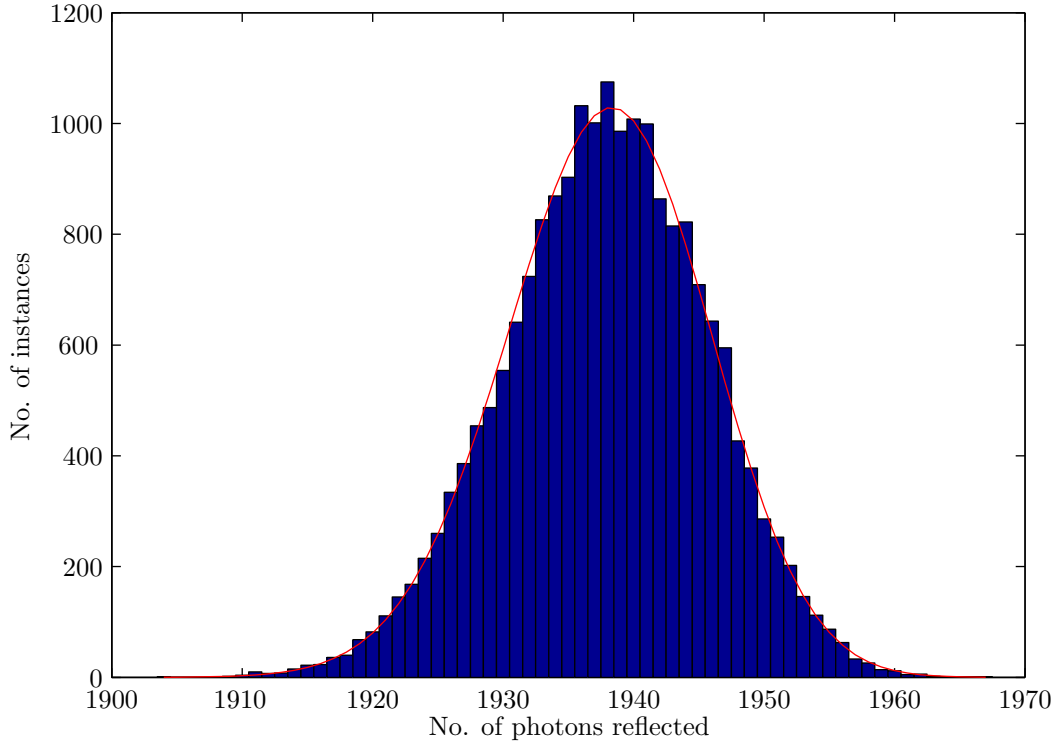

Figure 5.4: A histogram showing the number of photons reflected from a purely scattering, semi-infinite medium over 10,000 simulations of 2000 photons each. A circular detector was modelled in reflection mode with a width of 1000 mean free paths. A binomial distribution using parameters derived in Eq. (5.4.3) is also shown in red.

In order to add noise to an ideal TPSF, the total number of photons in the TPSF was chosen from a binomial distribution, as the same number of photons would not be detected each time. The temporal bin in which each photon appeared was then selected by first converting the ideal TPSF into a cumulative distribution function (CDF). The time of arrival for each photon was then found by selecting a uniformly distributed value between the values of zero and one, and applying this as a probability on the CDF, as can be seen in Figure 5.5. This was repeated for each photon and

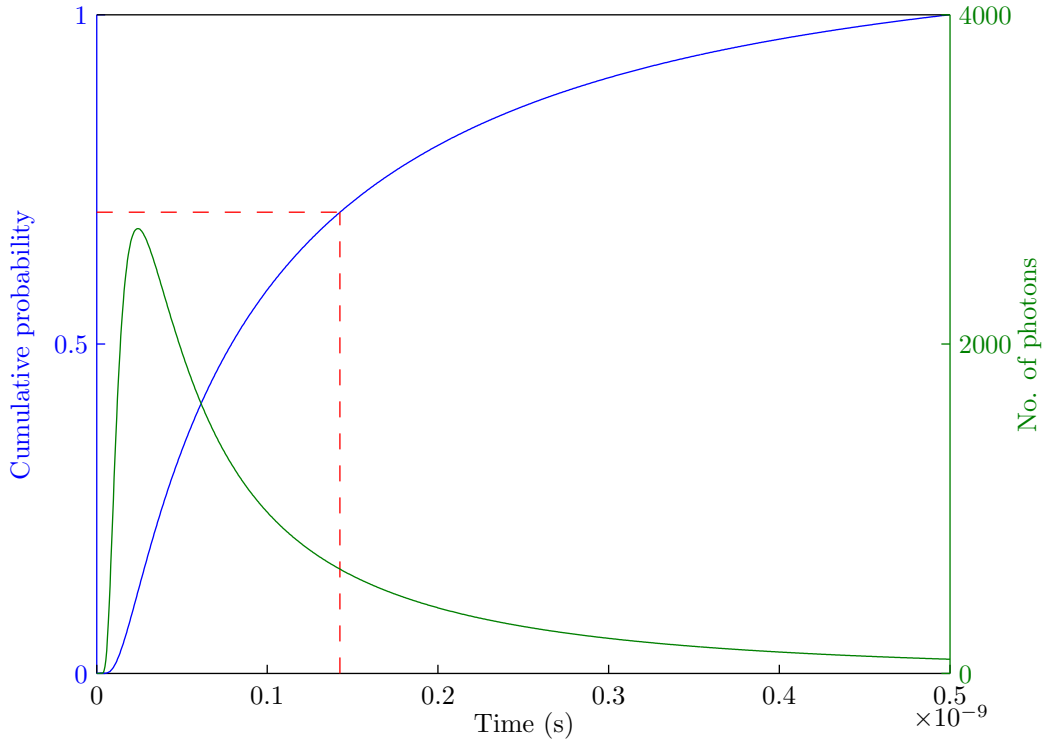

Figure 5.5: A cumulative distribution function in blue, as calculated from a TPSF in green. The red lines show the selection of a uniformly distributed random probability to give a time of arrival for each photon.

the resulting times binned to create a TPSF with noise due to scattering losses.

Absorption can then be added to the TPSF by means of a decaying exponential as explained in §1.4. This attenuation is proportional to the exponential of the pathlength of each photon in the medium. One could presume, therefore, that the absorption process may add further noise to the TPSF, as the attenuation applied to each photon will not be constant. However, the attenuation will reduce the level of both the noise and the signal in equal proportions as shown in Figure 5.6.

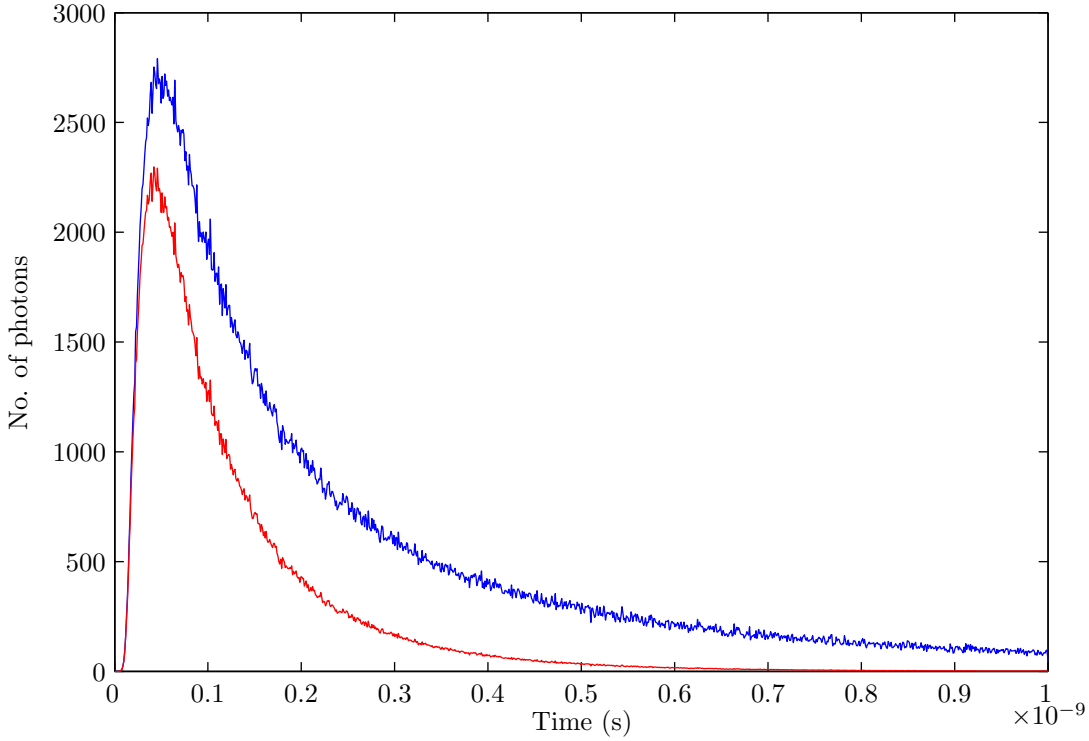

Figure 5.6: A demonstration of the effect of absorption on a typical TPSF. The blue curve shows a TPSF formed under the presence of scattering losses, while the red curve shows the same TPSF with absorption added in the form of a decaying exponential.

5.5 Errors Due to a Streak Camera

At each stage of the streak camera, a different source of error will be added to the incoming TPSF. The modelling of these errors allows the effects of the streak camera on some of the metrics that can be potentially used to calculate the turbid medium's characteristics to be investigated. This section will therefore firstly look at each of the streak camera's different error sources in turn and how each type of noise will affect the metrics. A commercially available streak camera will then be modelled

numerically and its effects on each of the metrics calculated. Finally, this process will be repeated over the entire parameter range. This will eventually allow the optimum pair of metrics in the determination of the absorption and scattering coefficients of a turbid medium to be selected in the case where a streak camera is used.

5.5.1 Sources of Noise

In this section, the sources of noise are described for each stage of a typical streak camera. A summary of the streak camera stages, along with the types of noise caused by each, can be seen in Figure 5.2.

Input Optics

The input optics in a streak camera consist of a slit section and a lens. As well as altering the path of the incoming photons, the lens will have a spectral transmittance. Due to the discrete nature of photons, this transmittance can be considered to be the probability of any single photon passing through the lens. Similar to the effect of the sample attenuation as discussed earlier, this means that each photon is undergoing a Bernoulli trial, and so the number of photons succesfully passing through the lens can be modelled using a binomial distribution, with the binomial parameter p equal to the transmittance at the photons' wavelength.

However, unlike the case of the sample's attenuation, the input optics have no effect on the photons' position in time. The successful transmission of each photon can therefore be treated as independent of each other, and as such, the number of photons

in each temporal bin can be decided according to its own binomial distribution defined by the lens' transmittance.

Photocathode: quantum efficiency

The photocathode converts incident photons into electrons via the photoelectric effect. Within this process, photons incident on the cathode are absorbed and their energies passed onto the electrons within the medium. If the energy of a photon (which is dependent on the wavelength of the light) is enough to overcome the corresponding electron's *work function* – the minimum energy required to free the electron from the medium – it will be ejected from the cathode. This process is called photoemission.[94]

However, not every photon above the threshold frequency incident on the photocathode will cause an electron to be emitted, giving rise to the cathode's *quantum efficiency*. This is defined by the Spicer Three-Step model[95] as the product of three probabilities:

$$\mathrm{QE} = P_\alpha P_T P_E \times 100\% \tag{5.5.1}$$

where P_α is the probability that a photon will successfully yield a free electron from the cathode, P_T the probability that this free electron will reach the surface with sufficient energy to escape and P_E the probability that it will escape. The model is presented here merely as an explanation of the mechanisms behind the photocathode's quantum efficiency; in practice, the properties of the photocathode are not published

in sufficient detail to enable its use. The photocathode's quantum efficiency is instead published as a single probability and so the emission of each photon must be considered as a Bernoulli trial. The number of successful photoemissions is therefore given by a binomial distribution.

Note that the quantum efficiency is sometimes quoted as the *radiant sensitivity*, which is a measure of the current produced by the escaping electrons per watt of incident power on the cathode. It is related to the quantum efficiency by the following equation:[96]

$$\mathrm{QE} = \frac{1.24\ \mathrm{RS}}{\lambda} \times 100\% \tag{5.5.2}$$

where RS is the radiant sensitivity in mAW^{-1} and λ is the wavelength of the incident light in nm.

Photocathode: dark current

Even in the total absence of light, a photocathode will still emit electrons due to the ever-present thermal energy overcoming the cathode's low work function. Dark current can be given in the standard units of current (amperes) or in the number of electrons (counts) per second – the count rate.

Microchannel Plate

The microchannel plate (MCP) is a bundle of long, thin, glass capillaries, the internal surface of each is coated with a secondary electron emitting material. A high voltage is placed across the length of the MCP. After an electron, already accelerated towards

the MCP by electrodes in the photomultiplier tube, enters one of these "channels" it will inevitably strike the inner wall due to each capillary's small diameter. The accelerated electron will contain enough energy to induce the emission of several secondary electrons in a process known as secondary emission. Due to the high voltage across the MCP, these secondary electrons will be accelerated down the channel, producing further collisions with the walls, causing further electrons to be emitted. As the number of electrons emitted during each collision is dependent on the speed of the primary electron in each secondary-emission process, the overall gain can be controlled by the strength of the potential across the MCP.

Due to the random nature of the collisions within the MCP, the overall gain will be different for each primary electron, leading to a distribution in the number of electrons exiting the MCP. This distribution is dependent on the statistics of each of the secondary emission events which in turn are dependent on factors such as the energy of the incident electron and the secondary electron emitting material used, making the final distribution very difficult to deduce. The assumption is often made that the number of electrons emitted from the MCP will follow a Poisson distribution.[97–99] However, it has been shown that the gain has the form of an exponential distribution,[100–102] defined by:

$$f(x) = \begin{cases} \dfrac{1}{\mu_g} \exp\left(-\dfrac{x}{\mu_g}\right), & x \geq 0, \\ 0, & x < 0. \end{cases} \tag{5.5.3}$$

where μ_g is the mean gain value. Due to the negative term within the brackets, this

equation is often described as the *negative* exponential distribution.

Note that this distribution defines the number of photons emitted from the microchannel plate as a result of a single photon input. The distribution of the *total* number of photons emitted from the MCP after an input of n photons is therefore a sum of n exponential distributions. This is equal to a gamma distribution[103] with shape parameter n and scale parameter μ_g. The exponential distribution is in fact a special case of the gamma distribution with a shape parameter $n = 1$.

The output of the MCP will therefore be modelled as a Gamma distribution.

Temporal Dispersion

An impulse of light incident on a streak camera will not correspond to a single point on the camera's phosphor screen: the temporal pulse will spread out as it travels through the instrument. This is due to several reasons:[104, 105]

- Photons entering the streak camera will be diffracted by differing (albeit small) amounts by the input slit. This will cause the photons to travel different distances between the slit and the system's photocathode which will introduce a distribution of flight times for the individual photons.

- Electrons leaving the photocathode are accelerated along the streak tube by an electrode. However, due to their differing initial speeds on emission from the photocathode, the electrons will take different times to reach the system's microchannel plate.

- The electron bunch emitted from the photocathode will broaden due to the Coulomb repulsion experienced between electrons.
- The streak camera's microchannel plate will have a finite temporal response.
- A single electron will not result in a point of light emitted by the streak camera's phosphor screen due to the screen's finite spatial response.

The temporal resolution of the streak camera can therefore be modelled as a Gaussian distribution whose variance is defined by the combination of the effects listed above.[104,106,107]

Trigger Jitter

While discussing the temporal resolution of the streak camera, it is also appropriate to mention the system's other temporal effects: each time an event is repeated and recorded by the streak camera, its image will appear in a slightly different position on the phosphor screen. This is due to slight variations in the timing systems used in the streak camera, such as the sweep circuit, and is known as the trigger jitter.

One solution to this problem is to split the input pulse of light into a reference pulse and a diagnostic pulse.[56,108] The reference pulse is delivered straight to the camera, bypassing the sample with an adjustable time delay, while the diagnostic pulse is incident on the sample as usual. Both pulses then appear on the streak image, with the reference pulse's delay adjusted to make it sufficiently close to the

diagnostic pulse to maximise the image's temporal resolution, but not so close as to affect the shape of the diagnostic pulse. The position of the diagnostic pulse is then known relative to the position of the reference pulse, meaning that by performing cross-correlation on the reference pulse portion of the streak images, the effects of jitter can be ignored for all the moments and hence cumulants.

It will therefore be assumed that this method is used during streak camera detection. This will inherently mean that a proportion of the CCD will be used to image the reference pulse, thus decreasing the number of bins, and therefore temporal resolution, available to the resulting TPSF. However, the length of time required for the reference pulse on the CCD is dependent on the shapes of the reference and diagnostic pulses, both of which will vary greatly according to the experimental setup. Therefore, a further assumption will be made that 20% of the streak camera's image will be "lost" in imaging the reference pulse.

Phosphor Screen

The emission of photons from a phosphor screen is the product of three stages:[109]

1. The absorption of an incident electron within the phosphor material
2. The production of photons due to the energy absorbed from absorbed electrons
3. The escape of the photons from the phosphor material

The variation within these stages will result in a distribution in the number of photons output by the phosphor screen per incident electron. It has been shown that for a phosphor screen of flawless crystals, the variance of this distribution is equal to the mean number of emitted photons, thus making the distribution Poissonian.[110]

Truncation and Binning

The truncation and binning of a TPSF are inherent processes of a streak camera and occur as a result of the system's CCD detector's finite size and resolution.

Truncation of a TPSF has the effect of removing the contribution of the photons beyond the truncation point to the TPSF's cumulants and reflectance. This will affect higher-order cumulants more than lower-order ones, due to higher-order cumulants' increased reliance on the TPSF's tail rather than on the bulk of its mass at the peak. It would therefore be reasonable to assume that longer truncation lengths would always lead to more accurate cumulants. However, in the presence of noise which is independent of the signal level, the tail of a TPSF can be dominated by this noise source, leading to inaccurate results. Therefore, in a noisy system, there is a compromise between maximising the number of photons detected whilst minimising the noise included with the signal.

The binning of a TPSF involves the summation of the number of photons arriving within a certain period of time – a "bin". This has the effect of quantising each photon's time of arrival, giving rise to an error in each photon's contribution to

the TPSF's cumulants. This error in contribution is proportional to the difference between the actual and quantised times of arrival, raised to the power of the order of the cumulant. Larger bins will therefore cause bigger errors due to a greater average correction in the time of arrival, and thus the errors can be minimised by using smaller bins.

However, in the case of a streak camera, the truncation length and bin sizes are inextricably linked, with the number of bins remaining constant over the camera's several possible sweep times. Smaller bins will cause smaller quantisation errors, but will result in the omission of more photons due to the smaller truncation length. Conversely, maximising the truncation length will cause greater quantisation errors due to the larger bins, but will minimise truncation errors due to the inclusion of more photons.

CCD: quantum efficiency

The CCD detector relies on the photoelectric effect of silicon to convert incident photons to electrons in a similar fashion to the streak camera's photocathode. Wells on the CCD then collect the resulting charges before transferring them to a charge amplifier where they are converted to an output voltage.

Due to several losses in the above process,[111] CCD detectors are unable to convert all the photons incident on the screen into electrons, leading to a quantum efficiency. As explained earlier, the discrete nature of the photons gives rise to binomial statistics,

with the quantum efficiency defining the probability of each photon being successfully converted to an electron.

CCD: dark current

Similar to the photocathode, a CCD will still "detect" impulses in the total absence of light. This is due to thermal energy within the CCD's lattice creating free electrons, which are then detected as impulses identical to those caused by incident photons. For this reason, CCD detectors are often cooled in order to reduce the thermal energy present and decrease the number of dark electrons created. The dark count rate is defined by the mean number of impulses detected per second in the absence of light.

CCD: readout noise

The free electrons created by either photons incident on the CCD or the detector's dark current must be converted to a voltage before being converted by an analogue-to-digital converter into a pixel's intensity value. This electron-to-voltage conversion is performed by a charge amplifier which acts as a capacitor according to the following equation:

$$V = \frac{Q}{C} \tag{5.5.4}$$

where V is the resulting voltage as a function of the charge on the electron, Q, and the effective capacitance of the amplifier, C.

Due to the non-ideal nature of the amplifier, noise will be added to each pixel's final value. Despite the output of the charge amplifier being a voltage, this readout

noise is measured in terms of the standard deviation in the number of equivalent electrons measured per pixel per second and is modelled as a Gaussian distribution. For small signal levels, it is possible for the resulting signal to be negative.

CCD: quantisation

As well as adding readout noise to the TPSF, the CCD's analogue-to-digital converter will add further noise by its quantisation of the TPSF's level. Due to the converter's limited bit-depth, the signal level will be approximated by one of 2^N discrete levels, where N is the number of bits. The difference between the signal's true level and its approximation is known as the quantisation noise. The analogue-to-digital converter is assumed to truncate negative analogue signals.

5.5.1.1 Noise on the Input Pulse

In order to measure the reflectance or transmission of a sample, it is necessary to measure the intensity of both the input and output pulses. In practice, this means that the input pulse will also have to pass through the streak camera, thus experiencing the same gain, attenuation and noise transformations as the output signal. The gain and attenuation transformations are essential so as to retain the input pulse's level relative to that of the output pulse. In order to avoid an extra level of complexity within the error calculations, however, the intensity of the input pulse was assumed to be noiseless. This assumption was justified by the following reasons:

- Although the errors due to the streak camera are generally applied on a bin-by-bin basis, the intensity of a pulse is calculated as the sum of the values of all the bins, thereby combining the errors. Due to the symmetrical nature of the majority of the error distributions, the magnitude of the summed error will be smaller than the errors experienced by the individual bins.

- The number of photons in the input pulse will be much larger than in the output pulse due to the lack of sample attenuation. Therefore, the effects of the errors on the input will be greatly reduced compared with those on the output pulse.

An alternative approach, which is not considered here, is the use of a separate time-independent detector to measure the overall intensity of the input and output pulses. Although this would still be a source of error, its relative simplicity would not only result in smaller errors, but also a simpler model in which the effect of the errors on the input pulse could be more-readily calculated.

5.5.2 Generalised Effects of Noise

In this section, the effects of the various different types of noise found in a streak camera are considered on a TPSF. Knowledge of these effects will assist in the explanation of the errors on a typical TPSF's metric calculated in §5.5.3.

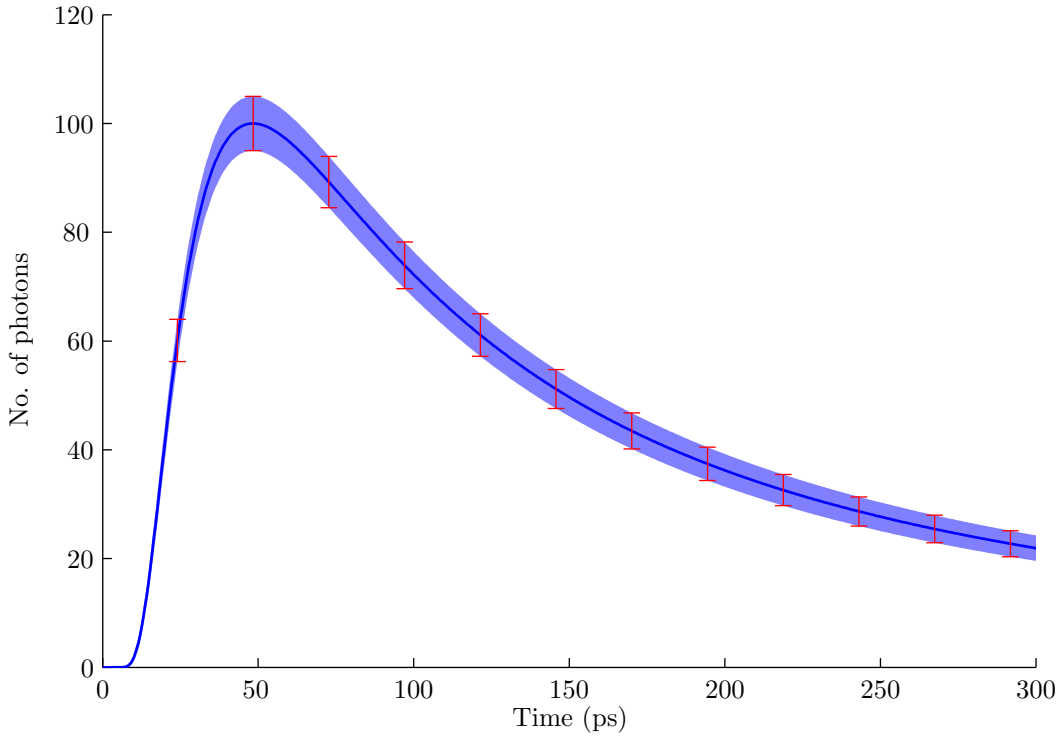

Figure 5.7: The effects of binomially distributed (or gamma-distributed) noise of an arbitrary amplitude on a TPSF. The solid curve shows the original TPSF, while the shaded area and error bars show the noise's standard deviation.

5.5.2.1 Binomially Distributed Noise

The shape of the binomial distribution is dependent on the probability of a photon or electron being output from the stage of the streak camera, p, and the number of photons or electrons input, n. The standard deviation of the distribution, σ, is defined as:

$$\sigma = \sqrt{np(1-p)} \tag{5.5.5}$$

With the stage's probability remaining constant throughout its operation, the standard deviation of the distribution is therefore proportional to $\sqrt{n}$. This can be seen in Figure 5.7, in which the standard deviation of the error is larger at the peak of the TPSF, rather than the tail, as this corresponds to a larger value of n.

The signal-to-noise ratio (SNR) due to binomially distributed noise is given by:

$$\text{SNR} = \frac{n}{\sqrt{np(1-p)}} \tag{5.5.6}$$

It can therefore be seen that the SNR will be low for the TPSF's tail where the value of n is small. As higher-order cumulants rely more on the tail, it is these metrics that will be affected more by binomially distributed noise.

When calculating the noise's effect on the overall reflectance, n is equal to the total number of photons contained in the TPSF. As this number is significantly larger than the number of photons in the TPSF's individual temporal bins, the SNR will be much increased, and thus the effect of binomially distributed noise on the reflectance will be relatively small.

5.5.2.2 Dark Current

Dark current is the addition of photons or electrons to an existing signal and thus can only increase the signal level, as can be seen in Figure 5.8.

The level of the dark current is constant over the whole TPSF and therefore it will have more of an effect on the TPSF's head and tail where it is larger relative to the signal level. The head's contribution to the cumulants is insignificant, however, not

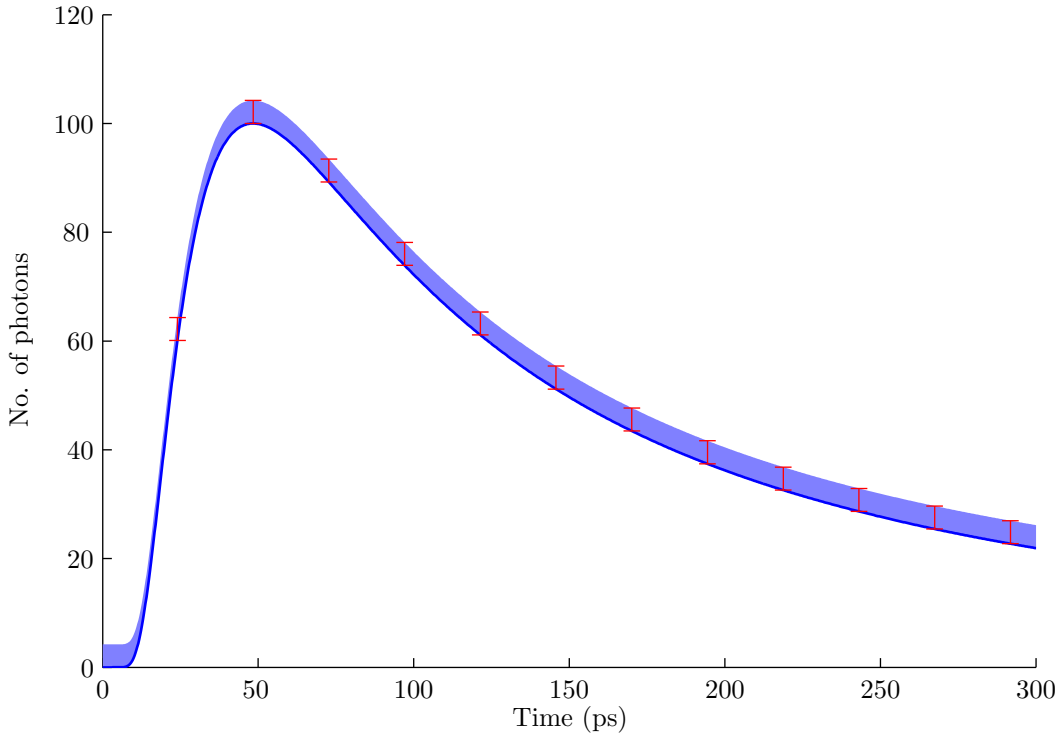

Figure 5.8: The effects of dark current of an arbitrary probability on a TPSF. The solid curve shows the original TPSF, while the shaded area and error bars show the noise's standard deviation.

only due to its small signal level compared to the TPSF's body, but also due to its early times of arrival – the cumulants are increasingly sensitive to longer pathlengths. As a result, the effect of the noise on the TPSF's head on the cumulants will be insignificant.

This does not apply to the TPSF's tail, however. Higher-order cumulants are much more sensitive to the TPSF's tail and so will be increasingly affected by the corresponding dark current.

Dark current will serve as to increase the sample's reflectance by increasing the

TPSF's overall intensity.

5.5.2.3 Gamma-distributed Noise

The variance of a gamma distribution is given as:[112]

$$\sigma = n{\mu_g}^2 \tag{5.5.7}$$

where n is the initial number of photons input to the stage of the streak camera and μ_g is the mean gain for each of the photons. The standard deviation is therefore proportional to $\sqrt{n}$, and so the effects of Gamma-distributed noise on the reflectance and cumulants of a TPSF will follow those of binomially distributed noise.

5.5.2.4 Temporal Dispersion

Temporal dispersion within a streak camera is modelled by convolving the TPSF with a Gaussian distribution. This has the effect of widening the TPSF, as can be seen in Figure 5.9. As the area under a convolution is equal to the product of the two original areas, this widening must also correspond to a drop in the peak amplitude of the TPSF. The overall intensity is unchanged, however, meaning that the reflectance will be unaffected.

It can be shown that the cumulants of two distributions are summed by their convolution.[93,113,114] A Gaussian distribution has only two non-zero cumulants – its expected value and its variance. However, the distribution used to model the streak camera's dispersion has an expected value of zero and as a result, only the TPSF's

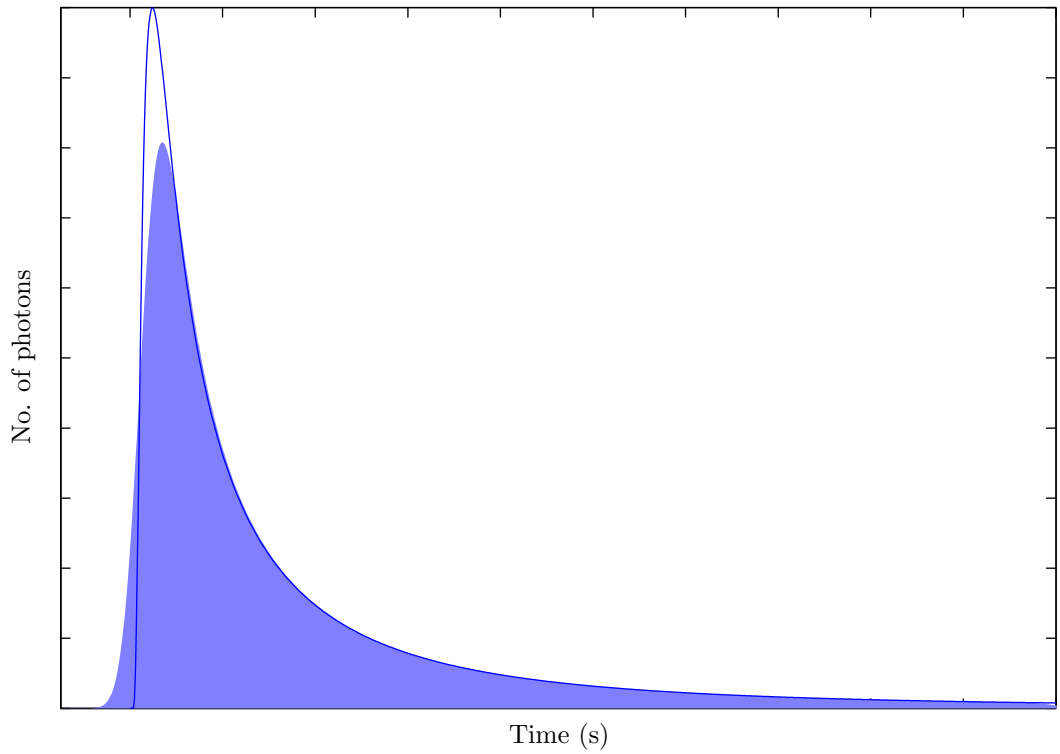

Figure 5.9: The effects of temporal dispersion on a TPSF. The solid curve shows the original TPSF, while the shaded area is the result of its convolution with a Gaussian distribution.

second cumulant will be affected by the temporal dispersion.

5.5.2.5 Poisson-distributed Noise

Poisson-distributed noise has the same form as that due to a binomial distribution, except that its standard deviation is equal to (not proportional to, as in the case of the binomial distribution) $\sqrt{n}$, the square root of the number of photons or electrons. This is shown in Figure 5.10. The relative effects of Poisson-distributed noise on a TPSF's cumulants and reflectance will therefore follow those of binomially distributed noise.

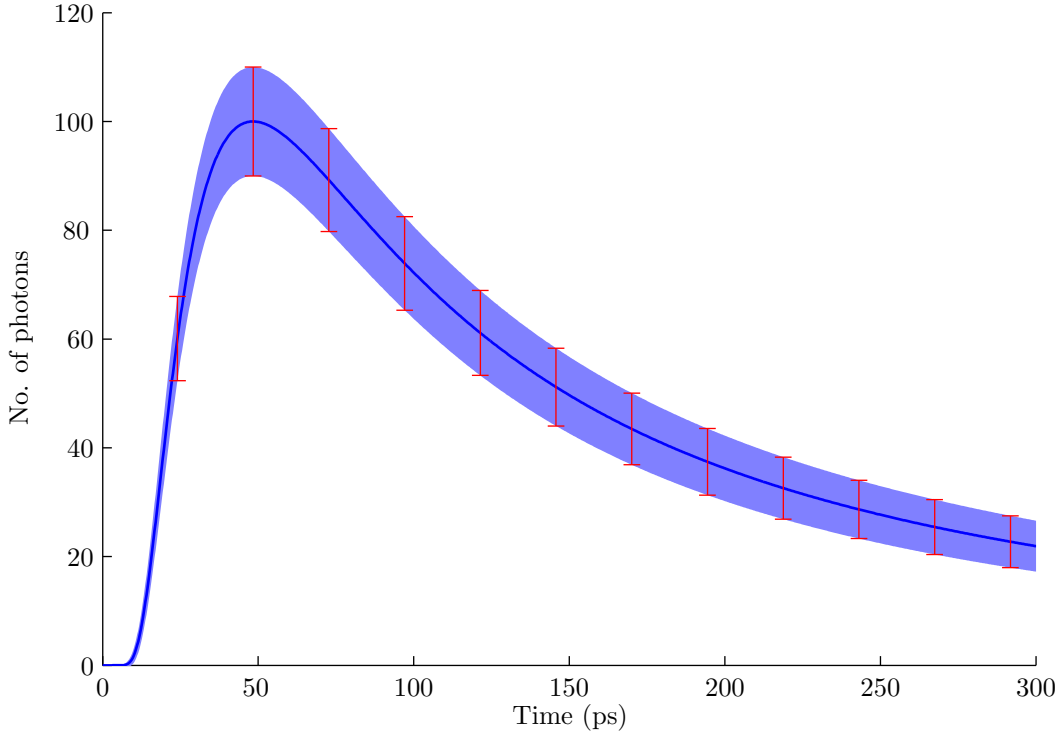

Figure 5.10: The effects of Poisson-distributed noise on a TPSF. The solid curve shows the original TPSF, while the shaded area and error bars show the noise's standard deviation.

5.5.2.6 Readout Noise

As the output from the CCD's charge amplifier is in the form of a voltage, the readout noise corresponds to the addition or subtraction of an equivalent number of electrons from the signal recorded by the camera. This number of electrons is defined by a Gaussian distribution. As a result of the signal's voltage form, the signal can at times be negative at this stage of the streak camera. This can clearly be seen at the beginning of the TPSF shown in Figure 5.11.

As the standard deviation of the readout noise is constant over the whole TPSF,

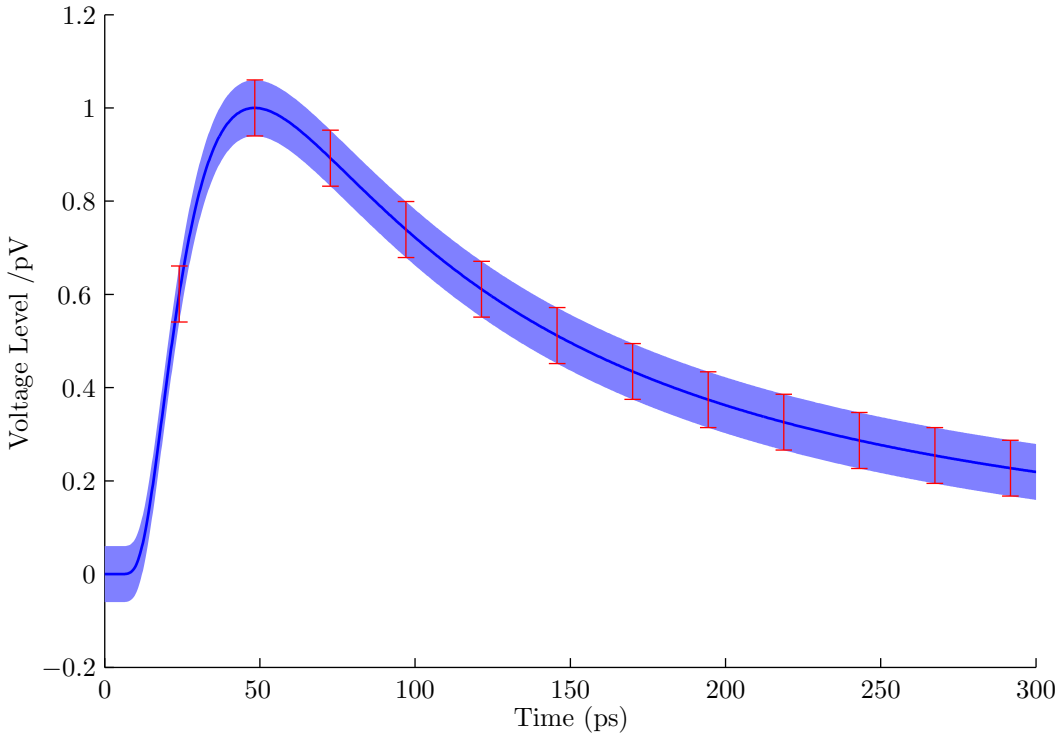

Figure 5.11: The effects of readout noise on a TPSF. The solid curve shows the original TPSF, while the shaded area and error bars show the noise's standard deviation.

the noise will have more of an effect on the TPSF's head and tail, where the noise levels are larger in proportion to the signal level. As for the dark current, therefore, higher-order cumulants will be affected more by readout noise than lower ones.

The reflectance will be largely unaffected by readout noise for the same reasons as binomially distributed noise.

5.5.2.7 Quantisation Noise

Quantisation noise is the approximation of the TPSF by a limited number of signal levels as defined by the CCD's bit-depth. This effect can be seen in Figure 5.12. As

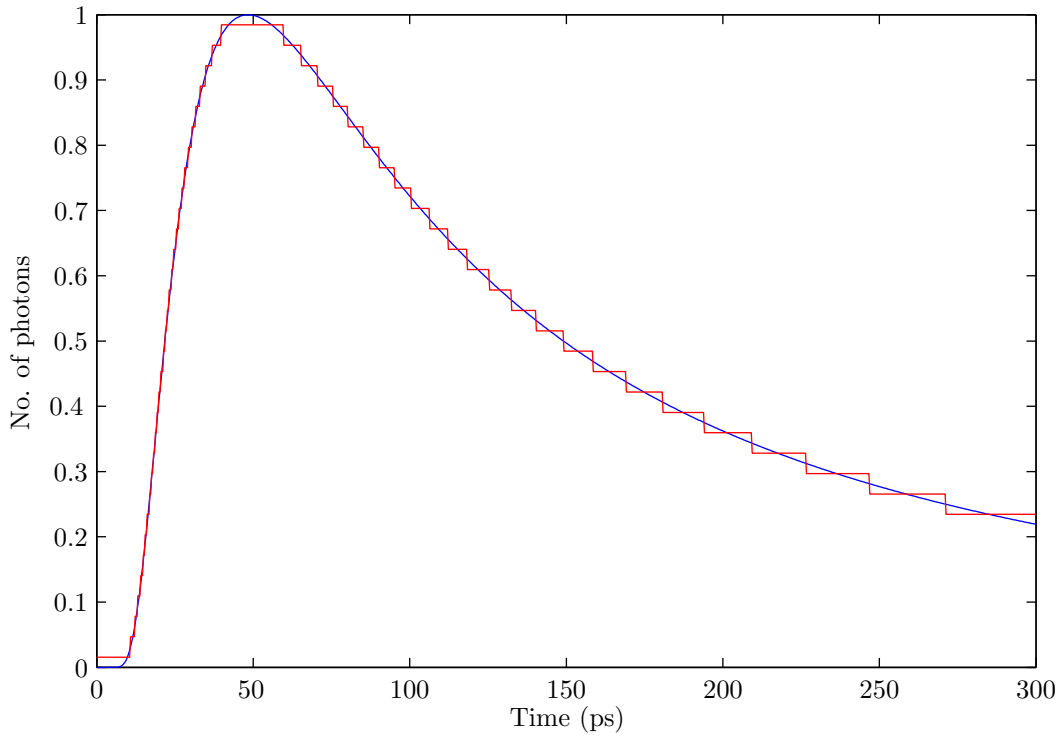

Figure 5.12: The effects of quantisation noise on a TPSF. The blue curve shows the original TPSF, while the red curve shows the TPSF after quantisation.

the levels are linearly spaced, the maximum error due to quantisation is unrelated to the original signal level and so will have a greater effect on the TPSF's head and tail due to their small signal level in comparison with the noise. Quantisation will therefore have a greater effect on higher-order cumulants due to their increasing reliance on the TPSF's tail.

Due to the large number of temporal bins, the overall effect of the summed errors will be much reduced compared to those of the original errors. Therefore, the sample's reflectance will be largely unaffected by quantisation.

However, it should be noted that if the signal to be quantised contains negative values (as will be shown to be possible for a streak camera), these will be truncated by the quantisation process. In this case, the overall level of the TPSF will be increased, increasing the values of both the reflectance and the cumulants. As the TPSF's head and tail are more likely to contain negative values, this effect will be more apparent on higher-order cumulants.

5.5.3 Model of Errors on Metrics for a Typical TPSF

In order to simulate the effects of using a streak camera to record a TPSF, a model of the streak camera was produced. The model was based on a Hamamatsu C5680 streak camera with A1976-01 input optics, an N5716 streak tube and an M5676 fast single sweep unit.

In this section, the parameters and methods used to model this specific streak camera will be described. The model will then be applied to a typical TPSF calculated for a medium representing human skin, and the effects of each stage of the streak camera on its metrics discussed.

5.5.3.1 Model Stages

The structure of the streak camera model can be seen in Figure 5.13. The parameters used in the model are summarised in Table 5.1.

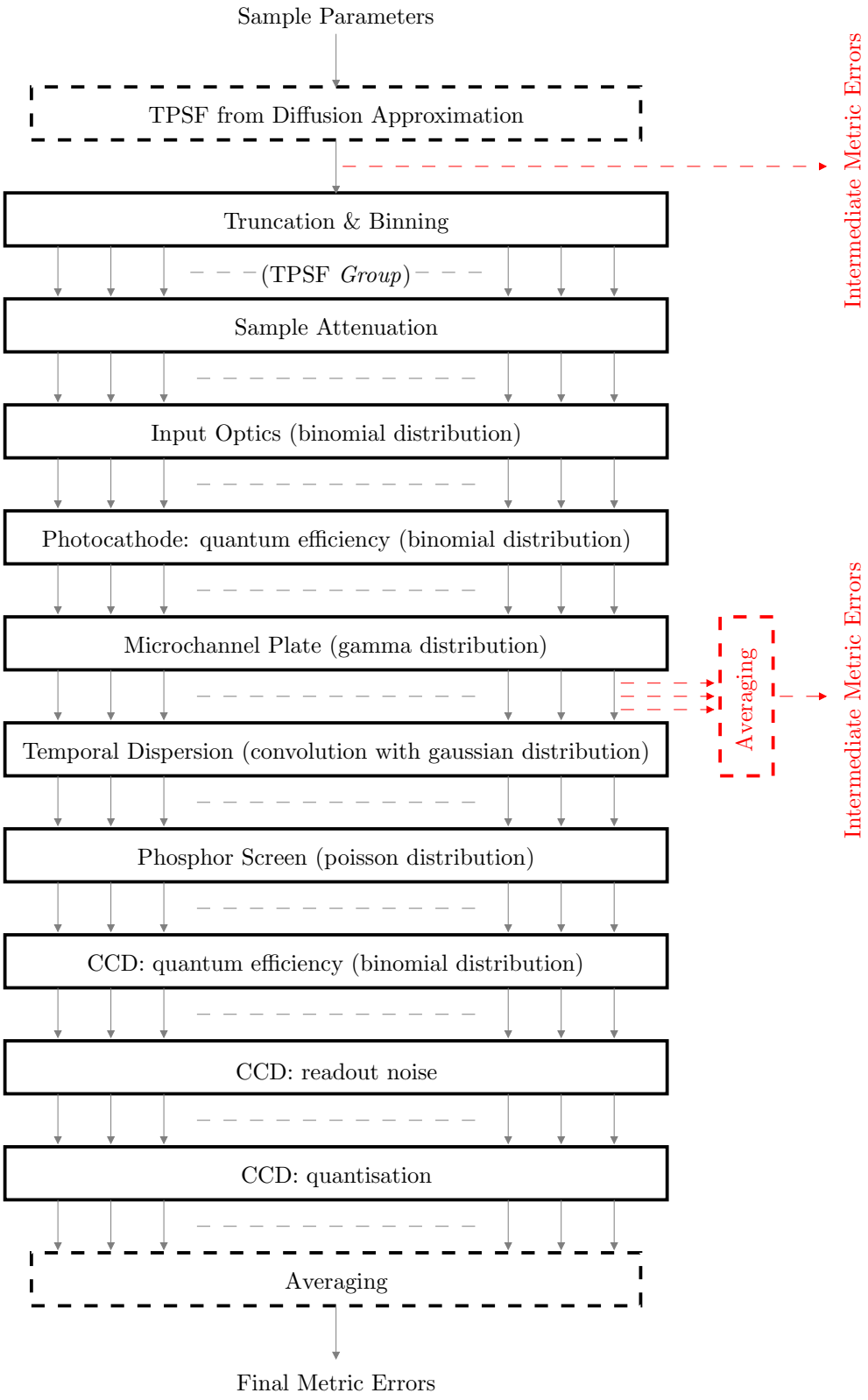

Figure 5.13: Structure of the streak camera model.

Table 5.1: Streak camera model parameters

	Parameter	Value
Source	Wavelength	633nm
	Spot size	10μm
	Pulse length	100ps
Sample	Absorption coefficient, μ_a	0.05mm^{-1}
	Scattering coefficient, μ_s	50mm^{-1}
	Anisotropy factor, g	0.9
	Refractive index, n	1.4
	Sample geometry	semi-infinite
	Annular detector range, ρ	1–1.1mm
	Detector geometry	reflection
TPSF	Truncation length	0.27ns
	No. of bins	554
Streak Camera	Input optics transmittance	68%
	Photocathode quantum efficiency	4.6%
	Photocathode dark current	negligible
	MCP gain	unity
	Temporal dispersion	2ps FWHM
	CCD quantum efficiency	71%
	CCD dark current	negligible
	CCD readout noise	6 electrons r.m.s.
	CCD bit-depth	12 bits

Initial TPSF

Rather than use a Monte Carlo simulation to produce the initial TPSF, an analytical, noiseless TPSF was created using the Diffusion Approximation equations derived in §3.3, to which noise was then added – the method behind this step is decribed in detail in §5.5.3.1. The analytical form of the TPSF meant that exact, analytical solutions to its cumulants could be found, allowing an accurate comparison of the effects of the streak camera to the actual cumulants.

It should also be noted that the equations used to produce the TPSF are correct for a point source – an unrealistic condition in practice. However, no analytical solutions exist for the cumulants of a TPSF created using a source with an intensity profile.[71]

The parameters used with the Diffusion Approximation equations to produce the initial TPSF are shown in Table 5.1.

Input Levels

In order to numerically model the streak camera's effects on the initial TPSF, it is necessary to define the TPSF's absolute level in terms of the number of photons within it.

It is beneficial to keep the signal level of the TPSF as high as possible, as the effect of any errors will therefore be minimised. However, there is a practical limit to the amount of incident light on human skin. This limit comes in the form of

the Maximum Permissible Exposure (MPE) of skin to laser radiation as defined by the International Electrotechnical Commission and approved by the British Standard Institution. The relevant standard[115] states that the MPE of skin to a 633nm laser for a pulse duration of between 1ns and 1ms is 200Jm^{-2}. Assuming a laser spot size of 10μm, the MPE can therefore be calculated to be around 16nJ. As the Diffusion Approximation equations used to produce the model's initial TPSF assume[26] an input of 1J, the TPSF must therefore be scaled down to meet the level of the MPE.

Although the MPE could be increased by using either a larger spot size or a longer pulse length, the spot size must be minimised to best match the Diffusion Approximation equations derived for a point source, and the pulse length must allow for a fast repetition rate in order to use averaging, as discussed later.

A further limit to the level of the TPSF originates in the streak camera: the CCD's *full well capacity*. This is the maximum number of electrons that can be collected by a single pixel on the CCD. To maximise the temporal resolution of the camera, each pixel corresponds to a single time bin. However, depending on the number and size of the spatial bins being measured from the medium, one spatial bin may correspond to several pixels on the CCD. The number of CCD pixels, n, that therefore correspond to each of the medium's spatial bins is:

$$n = \frac{B_i}{B} N \tag{5.5.8}$$

where B_i is the size of the medium's spatial bin, B is the complete spatial range that

will be analysed by the streak camera, and N is the number of pixels in the spatial orientation of the CCD.

The CCD (model C4742-95-12ER) used within the Hamamatsu C5680 system has a full well capacity of 18,000 electrons, and a total of 1344 bins in the spatial orientation.[116] The initial TPSF was created for an annular detector with an inner and outer radius of 1mm and 1.1mm respectively, while in theory the camera would be detecting light up to a radius of 10mm. According to Eq. (5.5.8), a total of 13 CCD bins would therefore be used to capture the signal in each TPSF bin. Thus, the maximum value in any TPSF bin at the point of the detection by the CCD would be 234,000 electrons. This corresponds to a maximum value at the streak camera's input – using the gain and attenuation values as detailed in Table 5.1 for each stage of the system – of approximately 10.5 million photons. If the peak of the TPSF is higher than this value, then the level of the TPSF would need to be reduced accordingly, corresponding to a reduction of the source intensity.

Truncation vs. Binning vs. Noise Floor

Although the truncation and binning of the light input occurs in the final stages of a streak camera system, it is necessary within the modelling process for them to be considered at the beginning of the sequence of errors: it would be unfeasible to carry out the entire model of the streak camera on the billions of individual photons in a TPSF. By binning the TPSF at the beginning, however, the photons can be

considered collectively in bins. Likewise, it is necessary to truncate the infinitely long TPSF produced using the Diffusion Approximation.

Even in a noiseless system, the point at which to truncate a TPSF is not immediately obvious. As the streak camera's CCD has a limited number of bins over which the truncated TPSF must be recorded, truncating after an excessive time period will cause the majority of the TPSF to fall within a small number of bins, leading to errors in the measured cumulants. Likewise, truncating after too small a period will mean that the values of higher-order cumulants will be inaccurate due to their increasing dependence on the TPSF's tail.

Figure 5.14 shows the effect of truncation of an arbitrary TPSF over a small range of time periods on the values of the TPSF's metrics. The reflectance and lower-order cumulants quickly reach their correct values as they rely more heavily on the body of the TPSF. As the order of the cumulant increases, however, more of the TPSF is required for the measured cumulant to match the analytical solution; even when almost 100% of the TPSF is being used, the fourth cumulant has still not reached its correct value.

Note that at the maximum truncation length shown here, none of the metrics show any sign of diverging from their correct value again: the size of the bins – a consequence of the truncation length used – has not yet become a limiting factor.

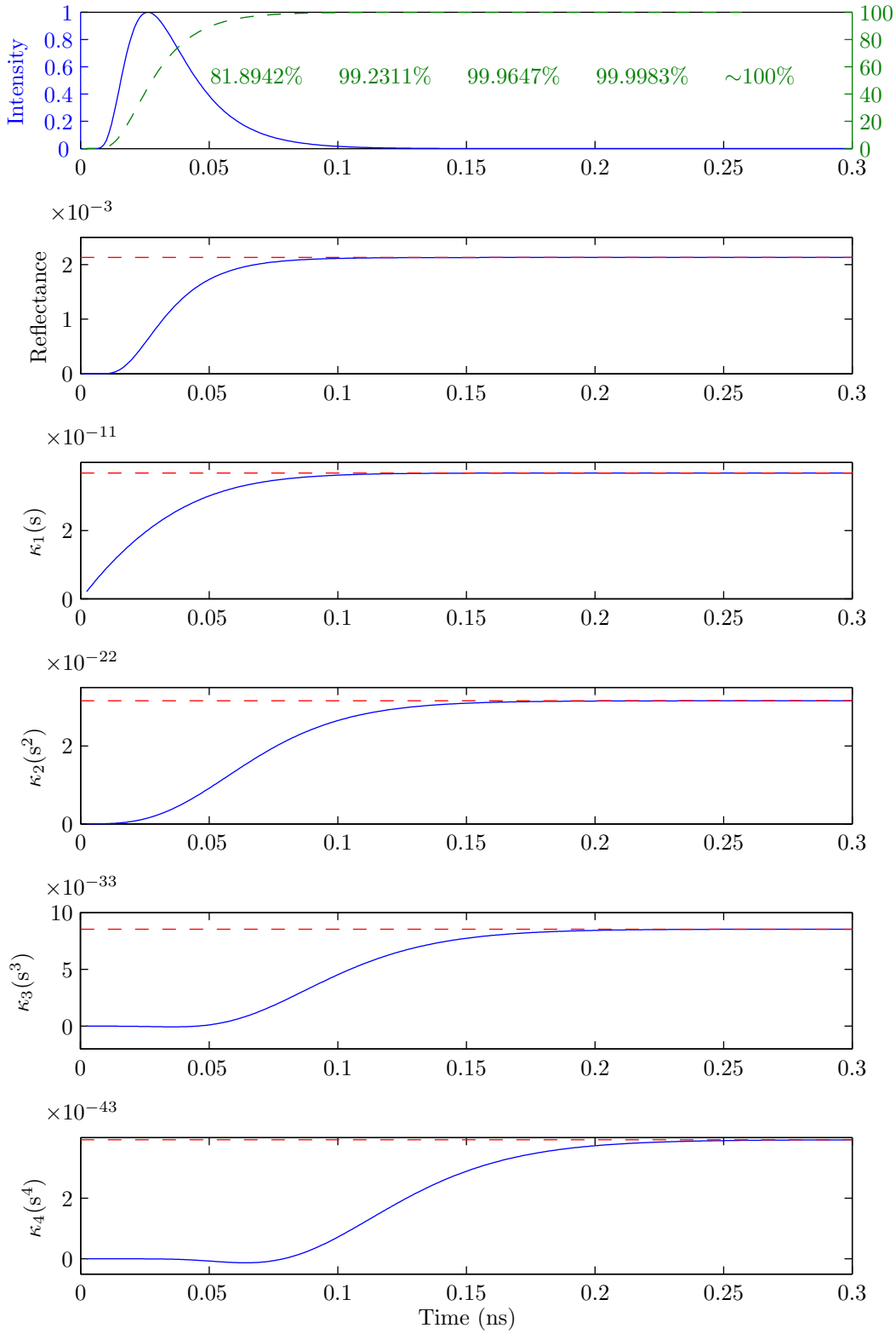

Figure 5.14: The effect of truncation and binning on a TPSF's metrics. The top diagram shows a typical TPSF in blue, as well as its cumulative equivalent in green. The diagrams below then demonstrate the variation in some of the TPSF's metrics against the amount of TPSF used: the height of the curves at each time point represents a metric's value on truncation of the TPSF at that time. The red, dotted lines mark the analytical solution for each of the metrics.

Figure 5.15 therefore shows a similar set of diagrams over a much longer set of truncation lengths, in which a breakdown in the metrics due to excessive bin size can be clearly seen.

Due to the integration within the bins of a streak camera, the reflectance does not rely on how finely the TPSF is binned and so will vary little once the truncation length is long enough to include almost all of the TPSF's weight. This is easily achieved with the truncation lengths displayed in Figure 5.15, thus the reflectance is seen to stay constant at the analytically correct level.

The variations in the first cumulant, the mean time of flight, can be explained by Figure 5.16 which shows the bins used at the beginning of the same TPSF as shown in Figure 5.15 for different truncation lengths. The alternating grey and white areas represent the time bins. With a truncation period of 5ns, the TPSF is sampled sufficiently and the first cumulant is measured as equal to its correct, analytical value. However, after the truncation length increases beyond a certain value, the majority of the TPSF's weight will fall within the first bin, and thus its contribution will appear at the centre of this bin. As the first cumulant is heavily dependent on the position in time of the bulk of the TPSF, it is clear that it will now be heavily dependent on the position of the centre of this first bin. Therefore, at 40ns, when the centre of the first bin is earlier in time than the TPSF's true mean, a slight drop can be seen in the value of the first cumulant. Note there is still a contribution to this value from

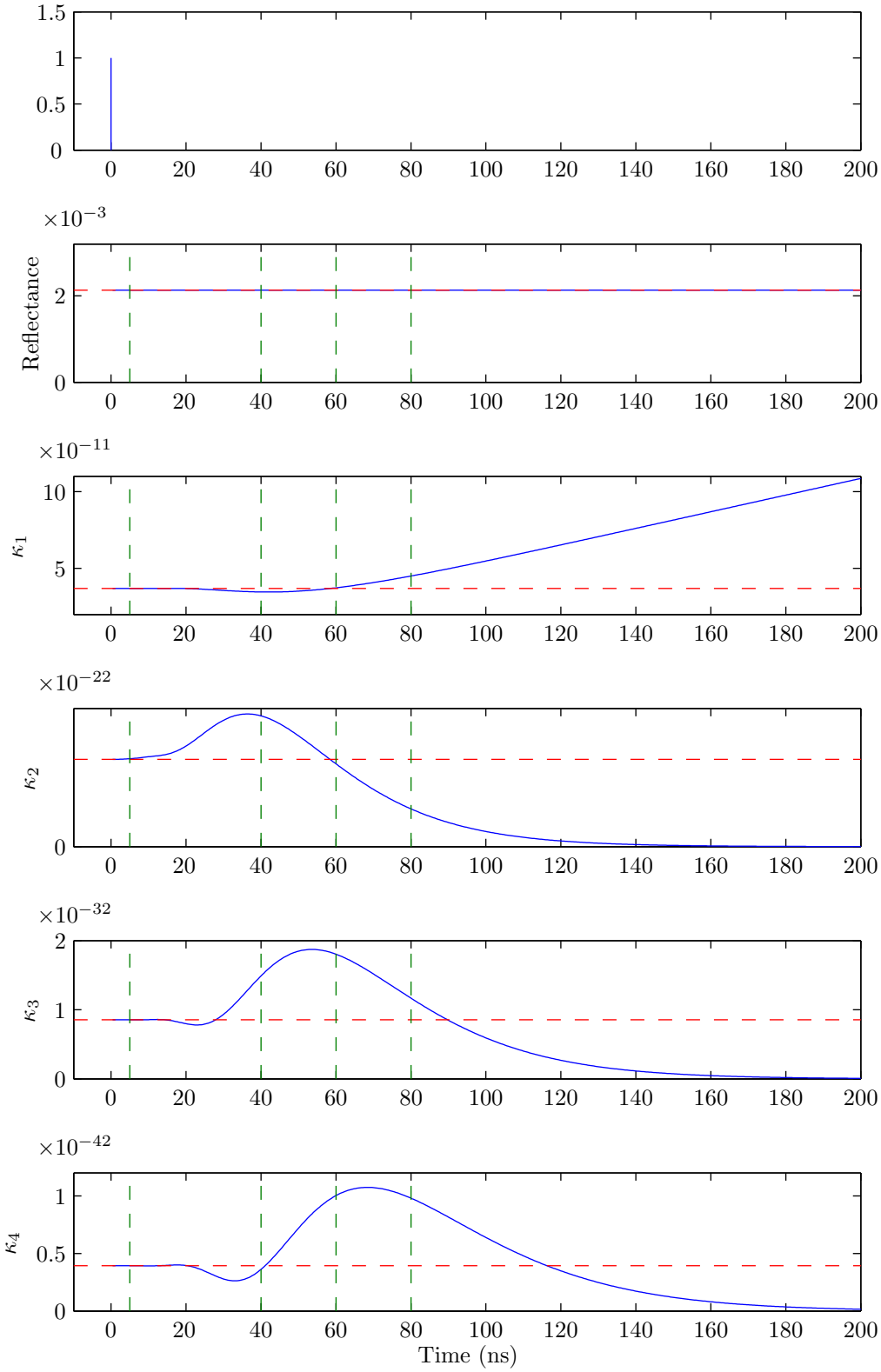

Figure 5.15: The effect of truncation and binning on a TPSF's metrics. The format of the diagrams follows that of Figure 5.14, except that the x-axes begin at a negative time value to enable the TPSF to be seen. The cumulative TPSF is also not shown in this case. The green dotted lines correspond to the truncation lengths used in Figure 5.16.

the second bin, which contains the majority of the rest of the TPSF's weight. This will serve as to increase the value of the first cumulant slightly.

At 60ns the combination of the contributions from the first two bins cause the calculated value of the first cumulant to approximately match the analytical solution. Beyond this point, further increases in the truncation length will increase the first cumulant's dependence on the centre position of the first bin: more of the TPSF's weight will continue to fall within the first bin, increasing its contribution to the value of the first cumulant over that of the second bin. When almost 100% of the TPSF's weight falls in the first temporal bin, the value of the first cumulant can be assumed to rely completely on the centre position of this bin. Therefore, as the relationship between the truncation length and the centre of the first bin is linear, at later truncation lengths the first cumulant can be seen to be varying linearly against the truncation length.

Having considered the effect of truncation length on the metrics, the point at which to truncate a TPSF can be seen to be unclear. However, the addition of a noise floor in the streak camera model can help in defining the most appropriate truncation length for a TPSF, since once the signal drops below the noise floor it is no longer possible to distinguish between the signal and noise. Therefore, truncating the TPSF as it reaches this value would maximise the amount of TPSF that can be analysed without introducing spurious noise to the calculations.

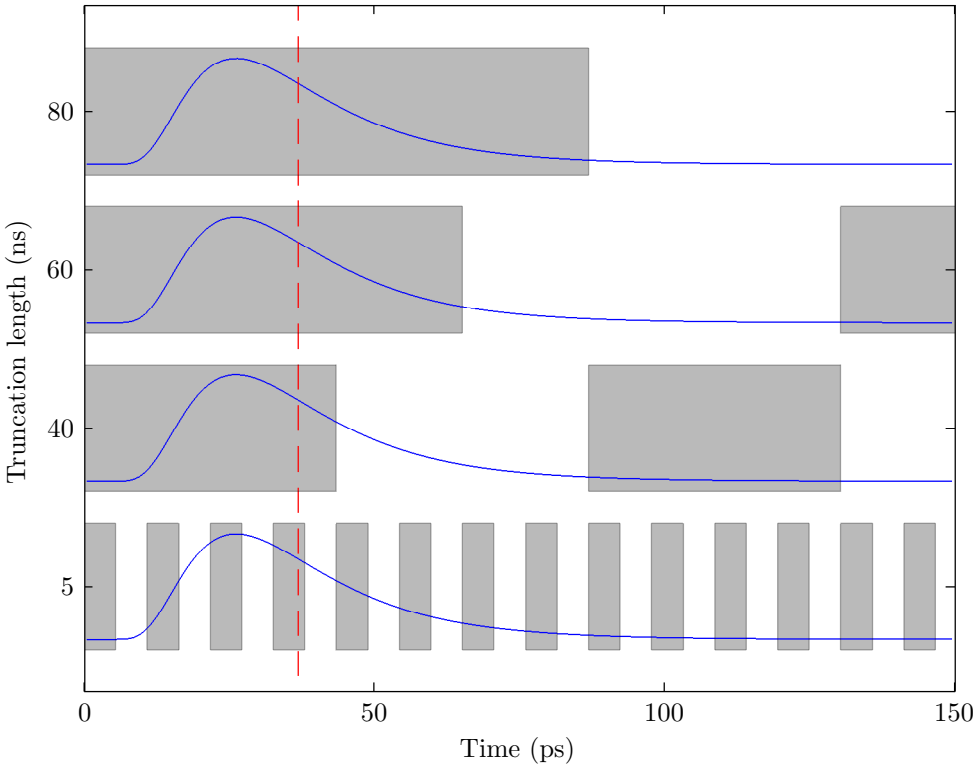

Figure 5.16: The bins used at the beginning of the same TPSF as shown in Figure 5.15 for different truncation lengths, as described by the labels of the y-axis. The alternating grey and white areas represent the time bins. The red, dotted line marks the analytical solution for the TPSF's first cumulant.

The system's noise floor is defined as the signal level recorded by the camera when no light is input, and therefore is made up from the following sources:

- The dark current emitted by the photocathode.
- The dark current emitted by the CCD.
- The readout noise from the CCD.

The noise levels given by the first two sources will be shown to be dominated by that of the CCD's readout noise and so will be ignored in deriving a TPSF's optimal truncation point.

The readout noise from the CCD will be modelled later as a Gaussian distribution with a standard deviation of 6 electrons per pixel, as published by Hamamatsu.[116] It can be shown using the *empirical rule* that over 99.99% of electrons created due to the readout noise will fall within 4 standard deviations of this distribution.[117] A noise floor of 24 electrons per pixel was therefore used within this analysis. This is the noise floor at the stage of the CCD detector; using this figure along with the streak camera's gain and attenuation stages, as given in Table 5.1 gives a noise floor at the input to the camera of 1080 electrons per pixel.

As multiple pixels are used for each temporal bin of the TPSF, as explained in §5.5.3.1 on page 107, multiple measurements of the TPSF are made and then averaged. As all these TPSFs are subject to the noise floor calculated above, the effect of this averaging on its level must be considered. In this case, 13 pixels are used and so 13 times the readout noise is measured and then averaged, giving an overall readout noise level. The standard deviation of this level can be calculated using the *standard error of the mean*, σ_{total}, defined as:[118]

$$\sigma_{\text{total}} = \frac{\sigma_{\text{original}}}{\sqrt{N}} \tag{5.5.9}$$

where σ_{original} is the original standard deviation of the noise floor and N is the number

of measurements averaged. Therefore, the averaged standard deviation of the noise floor is $1080/\sqrt{13}$ which gives a value of around 300 electrons. This is further reduced, however, due to the averaging of groups of 1000 TPSFs, as explained in §5.5.3.2, to give a value of $300/\sqrt{1000} \approx 10$ photons. This value was therefore used as the streak camera's noise floor.

Figure 5.17 shows the position of the most appropriate truncation point for a typical TPSF under exaggerated noise floor conditions. However, it is unlikely that the truncation of the TPSF will be able to be performed at this point: as the streak camera being modelled is only capable of sweeping the input signal over certain pre-determined time periods, the appropriate truncation point will likely fall between two of the camera's possible sweep times – this eventuality is also shown in the figure.

In order to choose a feasible truncation length, it is necessary to follow one of three methods:

1. Select the sweep time below the appropriate truncation length
2. Select the sweep time above the appropriate truncation length
3. Select the sweep time above the appropriate truncation length, but then discard all the bins beyond the truncation point.

The first two methods have the disadvantages of not considering valid parts of the TPSF, and adding noise to the measurements, respectively, as well as depending

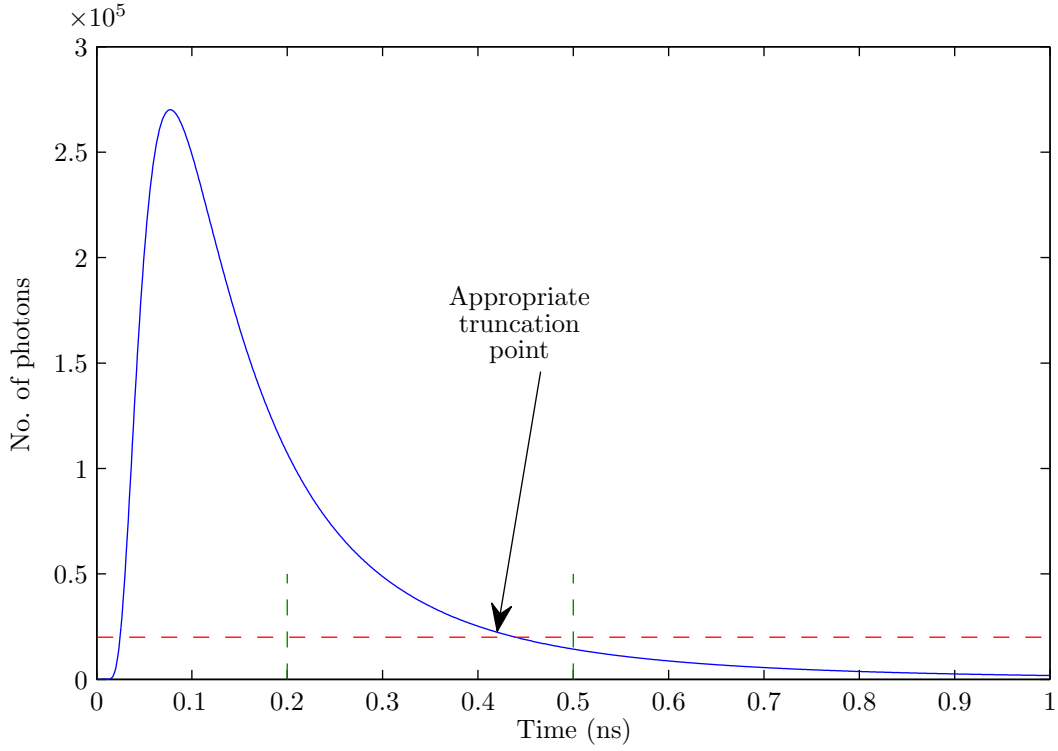

Figure 5.17: The most appropriate truncation length of a TPSF in blue in relation to the system's noise floor in red. The level of the noise floor has been exaggerated for clarity. The green dashed lines show two of the streak camera's possible sweep times.

heavily on the position of the appropriate truncation point between the two sweep times: the errors caused by the first method would be greatly reduced if the truncation length was very close to the lower sweep time.

The third method, however, allows the amount of TPSF used to be maximised whilst minimising the noise added to the signal. The disadvantage, however, is that the number of bins used to record the TPSF may be greatly reduced. The position of the appropriate truncation length within the two sweep times has an obvious effect on the extent of this reduction, with the greatest decrease occuring when the appropriate

truncation length falls infinitesimally above the lower sweep time. The values of the streak camera's pre-determined sweep times mean that, in the worst case, there will be a factor of 2.5 between the two sweep times (for example, 0.2ns and 0.5ns), resulting in only 40% of the available bins being used. However, it can be seen in Figure 5.18 that the number of bins required with which to record a TPSF is quite small to minimise errors in the values of the TPSF's metrics: the maximum number of bins shown, 100, corresponds to around 10% of the number of available bins.

Using this method, the appropriate truncation length below any of the streak camera's sweep times can be found. However, different sweep times will result in different truncation lengths: the difference in bin size between sweep times will affect the TPSF's overall level while the level of the noise floor will stay the same, thus changing the appropriate truncation length. This is shown in Figure 5.19: the blue curve shows a TPSF measured using a sweep time of 0.5ns, while the green curve shows the same TPSF modelled for a sweep time of 1ns. The green TPSF will have bins twice as wide as the blue, and so its intensity will be twice as large, thus giving it a different appropriate truncation length in relation to the noise floor shown in red.

This approach results in a number of possible truncation points for the TPSF using the streak camera's different sweep times. The appropriate length is that for which the noise added by a streak camera has the least effect on the TPSF's cumulants. However, the noise added is dependent not only on the TPSF's truncation length

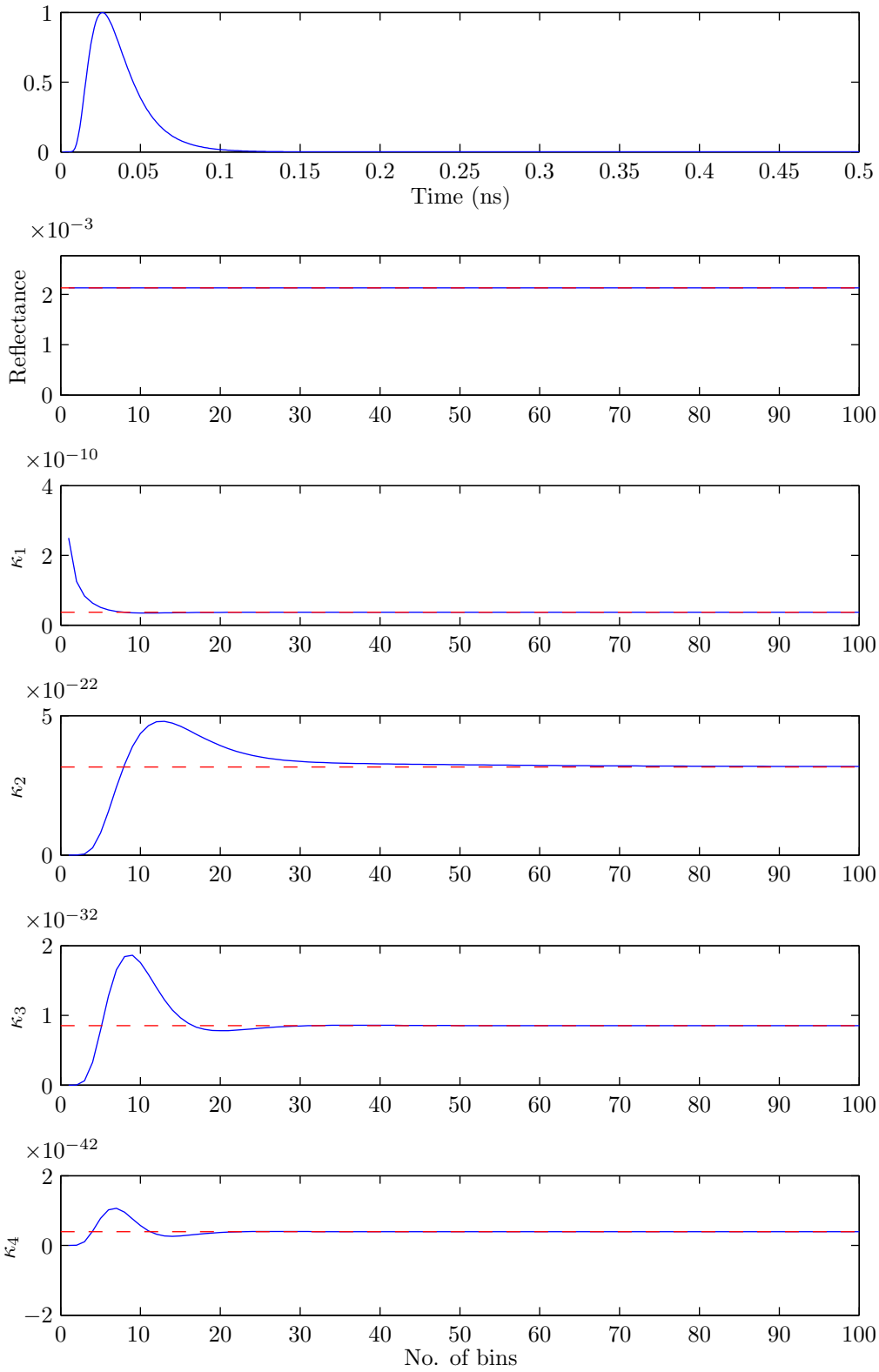

Figure 5.18: The variation of the reflectance and first four cumulants with the number of bins used to sample the TPSF shown in the top diagram. The red, dotted lines mark the analytical solution for each of the metrics.

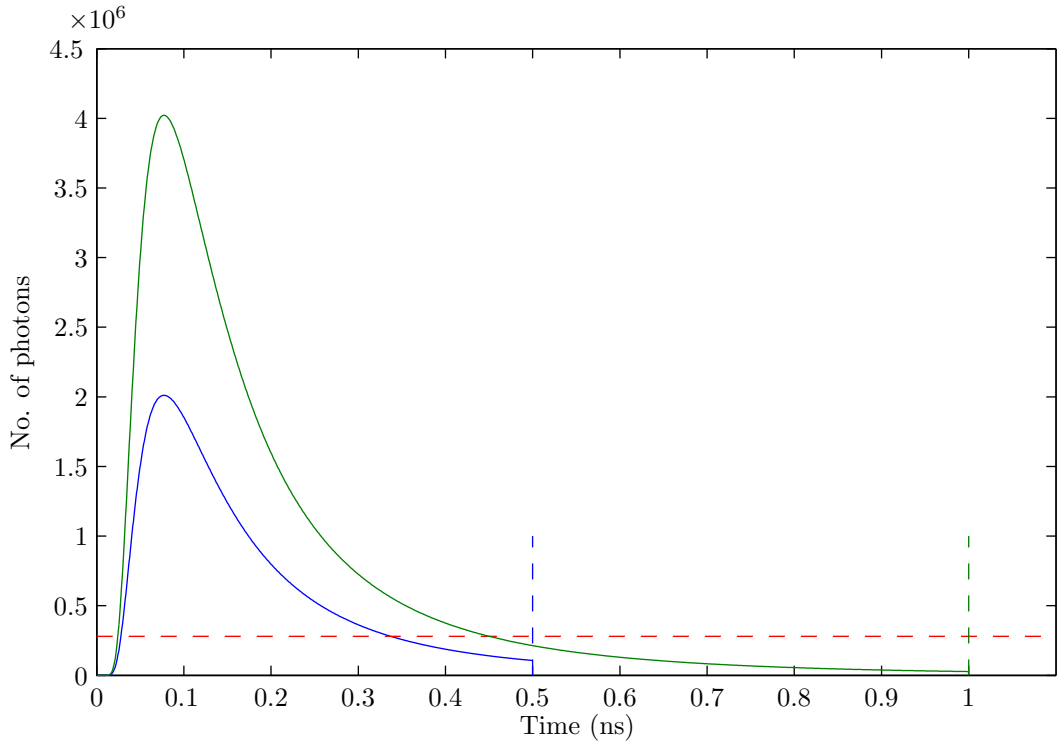

Figure 5.19: An arbitrary TPSF measured using two different sweep times, the value of which is marked by the corresponding dashed, vertical line. The noise floor, the level of which has been exaggerated for clarity, is shown in red.

but also the number of bins used to measure it and its signal level, all of which are inextricably linked. Therefore, using the streak camera model, it is very difficult to determine the appropriate truncation length without modelling all the possible options, which would be prohibitively time-consuming. Furthermore, this would be an unrealistic approach in practice as the true values of the metrics would not be known, and so it would be impossible to know which truncation length gave the best results.

Therefore, for the purposes of this thesis, the following method was used to decide

the appropriate truncation point:

1. Find the best truncation point for each of the streak camera's sweep times.

2. For each of these times, calculate the following ratio:

$$\frac{\text{Truncation length}}{\text{No. of bins used}}$$

3. Rejecting any truncation points that result in fewer than 100 bins being used to capture the TPSF, use the truncation point with the smallest length:bins ratio.

4. If no truncation points using more than 100 bins exist, use the truncation point with the smallest ratio, regardless of the number of bins.

Note that a TPSF's susceptiblity to noise due to its signal level is not considered in this method.

Using the method above, and the parameters set out in Table 5.1, an appropriate truncation length of 390ps was calculated. This corresponded to a sweep time of 500ps; 798 out of the streak camera's 1024 possible time bins[116] were therefore used to model the TPSF.

Sample Attenuation

Noise was to be added to the TPSF via a binomial distribution and a cumulative density function, as explained in §5.4 on page 79.

However, the small p values that can result from a small detector, and the large n values given out by light sources in practice, can mean that selecting a binomially distributed number becomes very computationally intensive. It was therefore necessary to determine a quick and accurate approximation to the binomial distribution.

It is known that for large values of n, a good approximation to a binomial distribution is given by a normal distribution. The smallest value of n for which this approximation still holds is entirely dependent on how close a match between the two distributions is required, but one "rule of thumb" states that the approximation is valid when:[119]

$$np(1-p) > 9 \tag{5.5.10}$$

Use of the parameters listed in Table 5.1 gives the values of n and p for the sample attenuation as 3×10^{10} and 0.0132 respectively, giving a $np(1-p)$ value of around 1.3×10^{8}. In this case, therefore, the approximation should easily hold.

This can be demonstrated by first defining the mean, μ, and variance, σ^2, of a binomial distribution:

$$\mu = np \tag{5.5.11}$$

$$\sigma^2 = np(1-p) \tag{5.5.12}$$

It can then be seen in Figure 5.20 that a normal distribution with these parameters, and with its values rounded to make it discrete, is a good approximation to the binomial distribution.

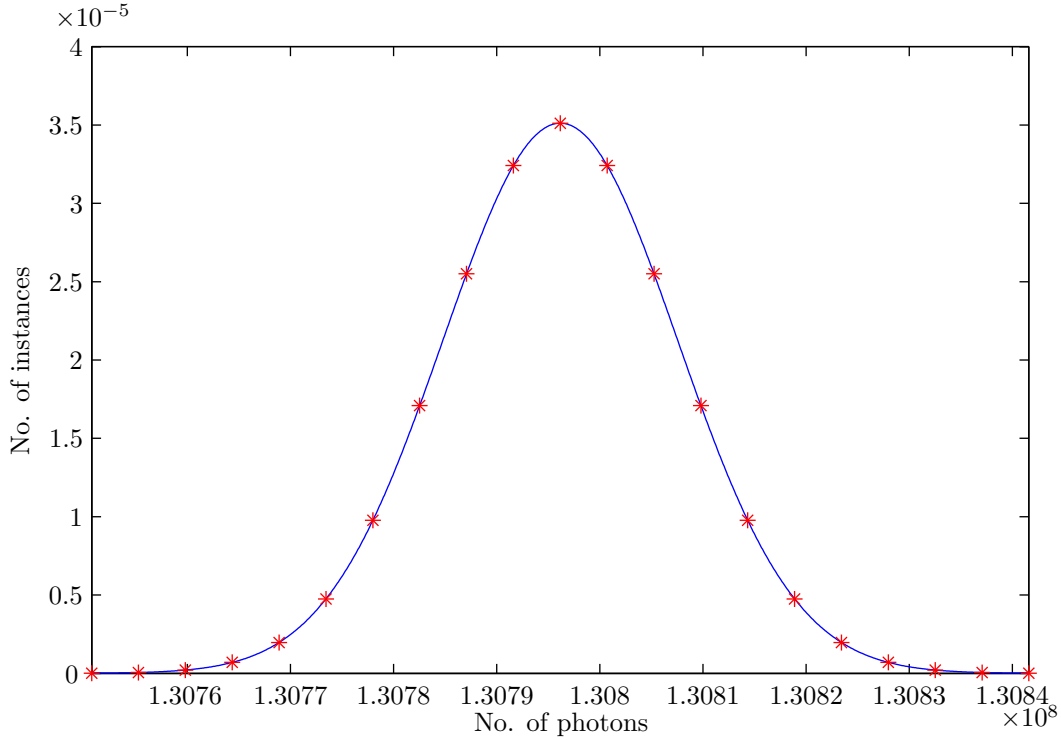

Figure 5.20: The blue curve shows the binomial distribution required to calculate the number of photons exiting the sample. The red stars also show a normal distribution created from the parameters derived in Eqs. (5.5.11) and (5.5.12).

A normal distribution was therefore used in place of the binomial to find the number of photons output from a sample, making the calculations much simpler and quicker.

Input Optics

The A1976-01 input optics used in the streak camera have a transmittance of 68%.[120] Noise from this attenuation could therefore be added by the production of a new TPSF in which each bin's new value was chosen from a binomial distribution with an n parameter equal to the number of photons previously in that bin, and a p value of

0.68.

However, much like the noise caused by the sample attenuation, this would require many computationally intensive binomial distribution calculations, and so the use of normal distribution approximations would be preferable. This was further complicated by the fact that unlike in the case of the sample attenuation, a different distribution was required for each of the TPSF's bins. Due to the different bin's intensity values, this would mean that some of the bins would not satisfy the criterion for the normally distributed approximation as set out in Eq. (5.5.10). Thus, a mixture of the two distributions was used: bins that fulfilled the criterion were approximated using a normal distribution, whereas those that did not were processed using the exact binomial distribution. This meant that binomial distributions were not used for bins containing a large number of photons, where their calculation became unwieldy.

The worst approximation is therefore found at the limit of the the criterion in Eq. (5.5.10). With a p value of 0.68, this occurs for an n value of 42. The approximation at these values can be compared to the actual binomial distribution in Figure 5.21.

Photocathode: quantum efficiency

The photocathode's quantum efficiency is given in the datasheet[120] as a radiant sensitivity of around 23,500μAW^{-1} which corresponds to a quantum efficiency of 4.6%. A p value of 0.046 was therefore used.

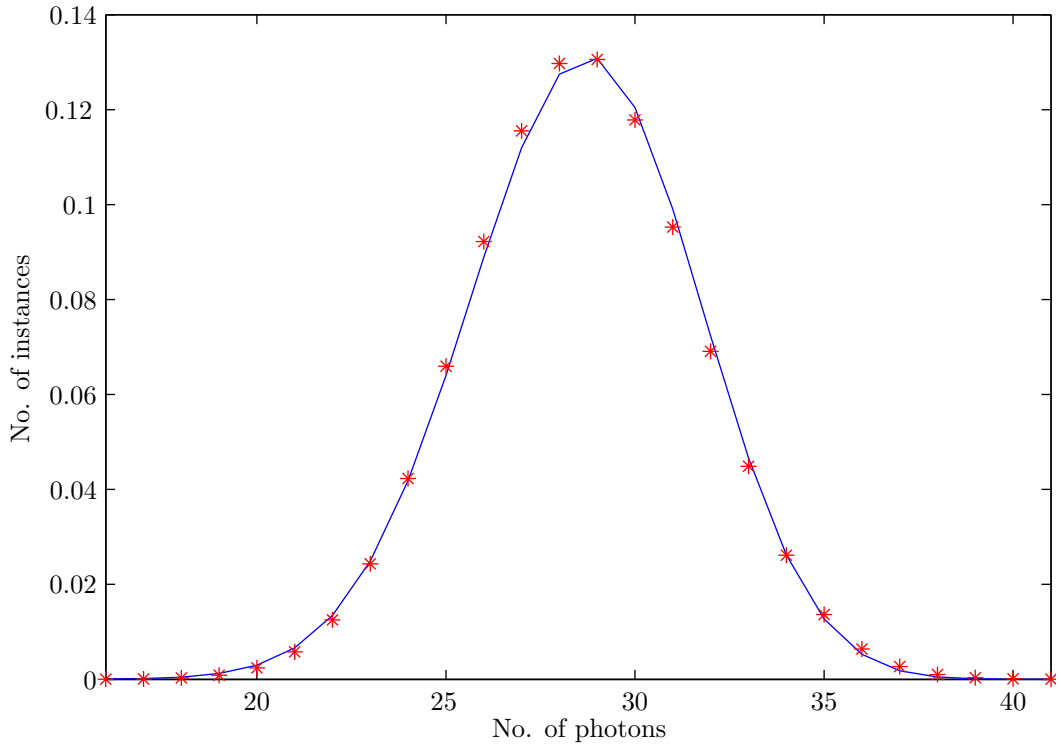

Figure 5.21: The blue curve shows the binomial distribution at the limit of the approximation criterion in Eq. (5.5.10) for the attenuation due to the input optics. The red stars show the normal distribution approximation.

A similar combination of binomial distributions and normal distribution approximations as for the input optics was used to model this attenuation. For the photocathode's p value, the worst approximation occurred at an n value of 206. This approximation can be seen in Figure 5.22.

Photocathode: dark current

The S20 photocathode used in the C5680 streak camera[121] has a dark count rating[122] of $1500\text{s}^{-1}\text{cm}^{-2}$. In the case of a binned signal, this rate is converted into the probability of one or more electrons being added to that bin. As the streak camera's

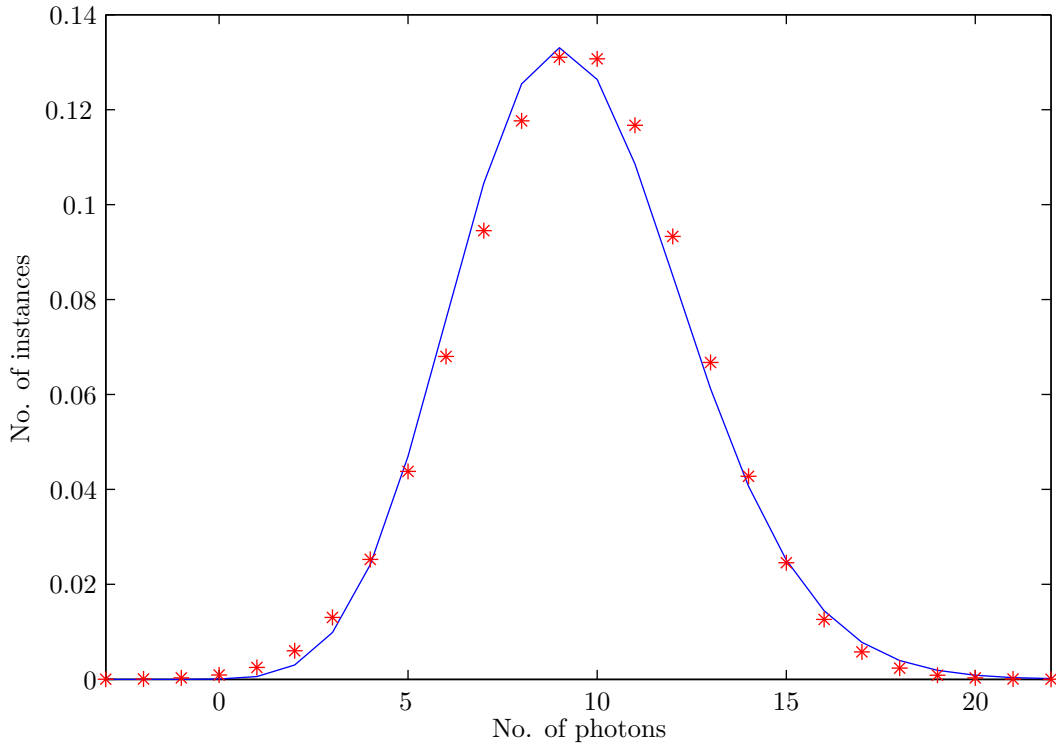

Figure 5.22: The blue curve shows the binomial distribution at the limit of the approximation criterion in Eq. (5.5.10) for the attenuation due to the photocathode. The red stars show the normal distribution approximation.

photocathode size is given[120] as 0.15mm $\times$ 5.4mm, the dark count rate can be calculated to be around 6×10^{-13} electrons per bin. It was therefore decided that the photocathode's dark current could be ignored within this model.

Microchannel Plate

The gain of the microchannel plate (MCP) can be varied[120] up to a value of 3×10^3. This gain is used to maximise the intensity of the TPSF before it reaches the phosphor screen and CCD in order to minimise the effects of the noise added to the signal by these two components. Therefore, for any TPSF with a peak value not close to the

CCD's full well capacity, the MCP's gain was adjusted until the CCD was close to saturation. Although the gain can only be changed in discrete steps, it was therefore necessary to assume that it can be altered smoothly to provide the exact gain required.

Due to the level of the TPSF produced using the parameters in Table 5.1, no gain was necessary in this numerical model. In practice, however, the MCP will have a natural attenuation when it is switched off: electrons will still be lost in collisions with the material. Therefore, a small gain to overcome this attenuation will be required to keep the overall gain at unity. As this level of attenuation is unknown, this effect was ignored for the current TPSF and the gain was set for the specified parameters to be unity. The TPSF entering the stage was therefore replaced with a TPSF with bin values selected from a gamma distribution with a mean gain of unity.

Temporal Dispersion

The effect of the streak camera's temporal dispersion on the TPSF due to the streak camera was achieved by its convolution with a Gaussian distribution. The streak camera is stated[120] to have a temporal resolution of 2ps which is defined by the full width at half maximum of the resulting signal from an input pulse with an infinitesimal temporal width.[19] This was converted to give the distribution's standard deviation, σ, by the following equation:

$$\sigma = \frac{\mathrm{FWHM}}{2\sqrt{2\ln 2}} \tag{5.5.13}$$

Phosphor Screen

The temporal response of the P43 phosphor screen used in the C5680 streak camera system is poorly documented, although a typical decay time[123] to 1% of the maximum intensity is given to be around 3ms. Furthermore, the absolute number of photons that this percentage relates to is dependent on the energy of the incident electrons,[124] ranging from 185 to 550 photons per electron. It is therefore difficult to ascertain the number of photons emitted per incident electron over a particular length of time. However, it is desirable to keep the CCD exposure time as short as possible to reduce the contribution from the CCD's dark current. Therefore, by using the CCD's minimum exposure time[116] 10μs it will be assumed that the average number of photons emitted by the screen in this time will be equal to the number of incident electrons. The phosphor screen, therefore, does not provide any gain within the system, although it will still add noise to the signal. This was modelled by the production of a TPSF with bin values selected from Poisson distributions according to the previous TPSF's intensities.

CCD: quantum efficiency

A P43 phosphor screen has been shown[124] to emit the majority of its light at around 545nm. The CCD's quantum efficiency is given[116] at this wavelength as 71%. The effect of this attenuation was modelled using a combination of binomial distributions and normal distribution approximations as for the input optics and photocathode's

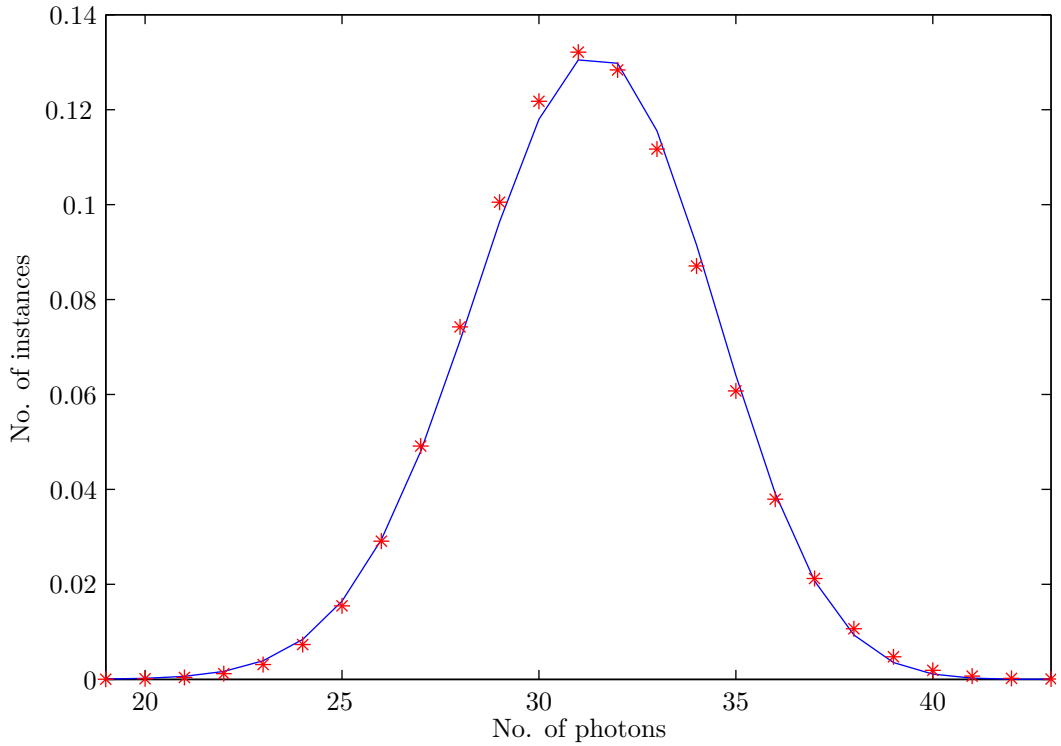

Figure 5.23: The blue curve shows the binomial distribution at the limit of the approximation criterion in Eq. (5.5.10) for the attenuation due to the CCD's quanutm efficiency. The red stars show the normal distribution approximation.

quantum efficiency. For a p value of 0.71, the worst normal approximation occurs for $n = 44$. The match of this approximation to the binomial distribution can be seen in Figure 5.23.

CCD: dark current

The dark current of the CCD is rated[116] as 0.1 pixel^{-1}s^{-1}. As stated in §5.5.3.1 on page 107, 13 bins were used to capture each of the TPSF's bins. Using the CCD's minimum exposure time of 10µs, the total dark current can be calculated as 1.3×10^{-5} electrons per bin. The CCD's dark current was therefore also ignored within this

model.

CCD: readout noise

The CCD's readout noise has a typical value of 6 electrons r.m.s.,[116] which is equal to the standard deviation of the signal. Each bin of the TPSF therefore had a randomly selected value from a Gaussian distribution with a standard deviation of 6 either added to or subtracted from its original value.

CCD: quantisation

The CCD has a bit depth of 12 bits,[116] which corresponds to 4096 different signal levels. With a full well capacity of 18,000 electrons, this will result in a maximum error in each bin of around 2 electrons.

5.5.3.2 Modelling Method

The methodology used in modelling the streak camera can be seen in Figure 5.13. The sample parameters defined in Table 5.1 were applied to the Diffusion Approximation equations derived in §3.3 to create a noiseless TPSF. This TPSF was then truncated and binned, and its amplitude decreased if it exceeded the maximum value determined in §5.5.3.1. Noise due to the sample attenuation was then added to the TPSF, firstly using a binomial distribution (or more specifically a normal distribution approximation) to determine the total number of photons in the noisy TPSF, and secondly using the noiseless, binned TPSF as a cumulative distribution function from

which the photons' arrival times were chosen, as also described in §5.5.3.1. This was repeated several times to create a *group* of TPSFs. In this case, a group of 1000 TPSFs was used, each of which was then passed through the other error steps shown in Figure 5.13.

After the final step, the TPSFs in the group were averaged by summing them and dividing by the number of TPSFs in the group. The reflectance and cumulants were then calculated from the averaged TPSF, the cumulants being determined from the moments using both Eqs. (1.5.1) and (1.5.9). The values of these metrics could then be compared to the analytical solutions calculated using the same sample parameters. Likewise, the *intermediate* errors in the metrics at any point in the model could be determined by the averaging of the group of TPSFs at that point, as shown in red in Figure 5.13.

A complete progression of a group of TPSFs through the error model was termed a *pass*. The errors in the metrics calculated were different after each pass due to the random nature of the model's noise. Therefore, in order to determine the overall distribution of the resulting errors, many passes were repeated so the mean and variances of the errors could be calculated. In this case, 5000 passes of the model were performed – this allowed the mean and variances of both the final and intermediate errors to stabilise.

5.5.3.3 Stage-by-stage Errors

A typical TPSF was passed through the model to simulate the effects of its "detection" by a streak camera, as described in §5.5.3.2. In order to identify the limiting steps within the instrument, it is useful to look at the distributions of the intermediate errors in the detected metrics due to each error step. Each distribution is defined by its mean and coefficient of variation, the latter of which is equal to the standard deviation of the distribution, σ, scaled by its mean, μ, as shown by:

$$CV = \frac{\sigma}{\mu} \tag{5.5.14}$$

The coefficient of variation is equal to the inverse of the signal-to-noise ratio and is used here due to its scale invariance, as explained below.

Firstly, it is important to note that the intermediate errors calculated here are the changes in each metric when compared to its value calculated after the model's previous step (the *differential* errors), and not the errors compared to the initial analytical solutions to the metrics (the *cumulative* errors). These two methods are shown in Eqs. (5.5.15) and (5.5.16) respectively:

$$\text{Differential errors:} \qquad \delta M_j = \frac{M_j - M_{j-1}}{M_{j-1}} \times 100\% \tag{5.5.15}$$

$$\text{Cumulative errors:} \qquad \delta M_j = \frac{M_j - M_0}{M_0} \times 100\% \tag{5.5.16}$$

where M_j is the value of an arbitrary metric after step j in the model and M_0 is the original analytical solution to the metric. δM_j represents the error in the metric.

In order to clarify this distinction, consider the effect of a two-stage error process on a TPSF. In this hypothetical process, the first stage, on average, decreases the value of the TPSF's first cumulant by 10%, whereas the second stage then increases the value by 5% on average. For an original mean time of flight of 100ps, for example, the average change in the first cumulant over the course of the two-stage process can therefore be shown to be:

$$100\text{ps} \quad \longrightarrow \quad 90\text{ps} \quad \longrightarrow \quad 94.5\text{ps}$$

The *cumulative* errors in the first cumulant at each step, calculated using Eq. (5.5.16), are:

$$0\% \quad \longrightarrow \quad -10\% \quad \longrightarrow \quad -5.5\%$$

The effect of the first error step can be seen to be a reduction of the value by 10% (shown as a negative error) as expected, but the value of the second error on the first cumulant (+5%) is not immediately obvious using this method. However, by comparing the values of the first cumulant in the model with the values from the previous step as in Eq. (5.5.15), the *differential* errors are calculated as:

$$0\% \quad \longrightarrow \quad -10\% \quad \longrightarrow \quad +5\%$$

In this case, the effect of increasing the value of the first cumulant by 5% can be clearly seen. The differential errors will therefore be used to analyse the streak camera's performance.

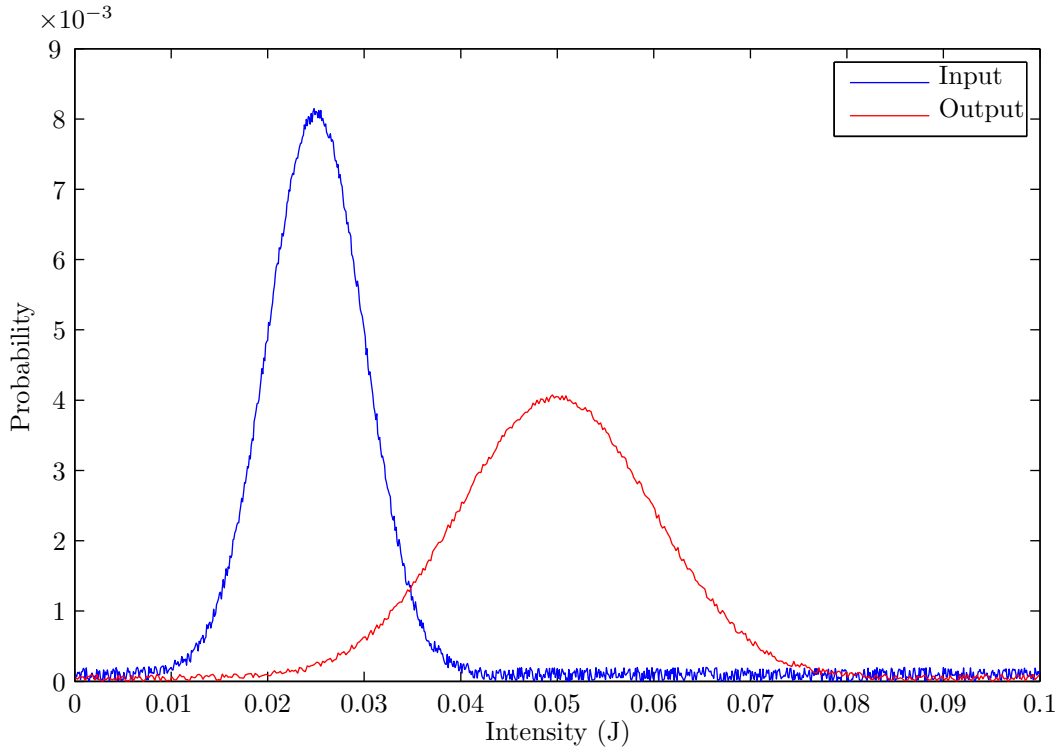

Figure 5.24: An arbitrary distribution of signal intensity is shown in blue. When used as input to a hypothetical error stage that precisely doubles the intensity, the distribution shown in red is produced.

Secondly, the merit of using the coefficient of variation (instead of the distribution's standard deviation or variance) when displaying the differential errors can be seen by considering a model containing a step which *precisely* doubles the intensity of the signal applied to it. If, over the course of several passes, the intensity of the signal input to this step and the resulting output are measured, their distributions can be plotted. An example input distribution formed using arbitrary data can be seen in Figure 5.24, along with the corresponding output distribution from the gain stage. It can be seen that both the mean and variance of the distribution have been doubled by

the stage in the model. However, as the variance will not have changed relative to the mean, the distribution's signal-to-noise ratio will have remained constant. Thus, observing the doubling of the variance separate from the mean is potentially misleading as noise has not been added to the signal. The coefficient of variation, however, due to its dependence on both the distribution's mean and variance will have remained constant. It is more intuitive, therefore, to use the coefficient of variation as its scale invariance determines that it will remain fixed for noise-free gain stages.

The mean and coefficient of variation were therefore used to describe the distributions of the differential errors at each stage of the streak camera model. The equations used were thus:

$$\delta\mu_j = \frac{\mu_j - \mu_{j-1}}{\mu_{j-1}} \times 100\% \tag{5.5.17}$$

$$\delta CV_j = (CV_j - CV_{j-1}) \times 100\% \tag{5.5.18}$$

where μ_j and CV_j are the mean and coefficient of variation respectively of a metric's error distribution after step j in the model, as calculated over several passes. By definition, μ_0 is the original analytical solution to the metric, and CV_0 is zero. $\delta\mu_j$ and δCV_j represent the changes in these variables when compared to the previous step's calculated values.

Note that δCV_j is calculated as a *change in percentage*, rather than a *percentage change*, due to its lack of denominator. This enables the change from zero to a finite value to be calculated as a finite percentage, rather than infinity.

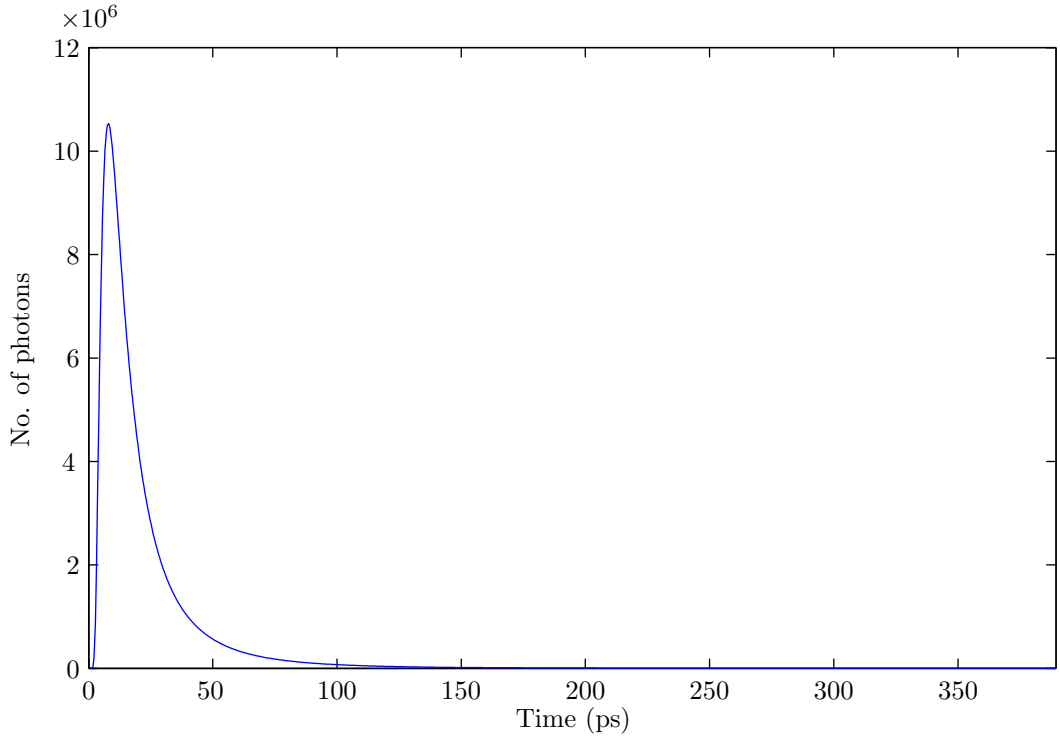

Figure 5.25: The initial noiseless TPSF, calculated using the Diffusion Approximation, which was used to analyse the streak camera model. The TPSF was truncated at approximately 390ps.

The initial noiseless TPSF calculated from the Diffusion Approximation using the parameters in Table 5.1 is shown in Figure 5.25. It was passed through the model in 5000 groups of 1000 TPSFs. The resulting differential errors are shown for the reflectance and first ten cumulants in Figures 5.26 and 5.27. The mean error, $\delta\mu_j$, is marked by a cross for each metric, while the error bars show the coefficient of variation, δCV_j, above and below the mean. The figures are discussed below.

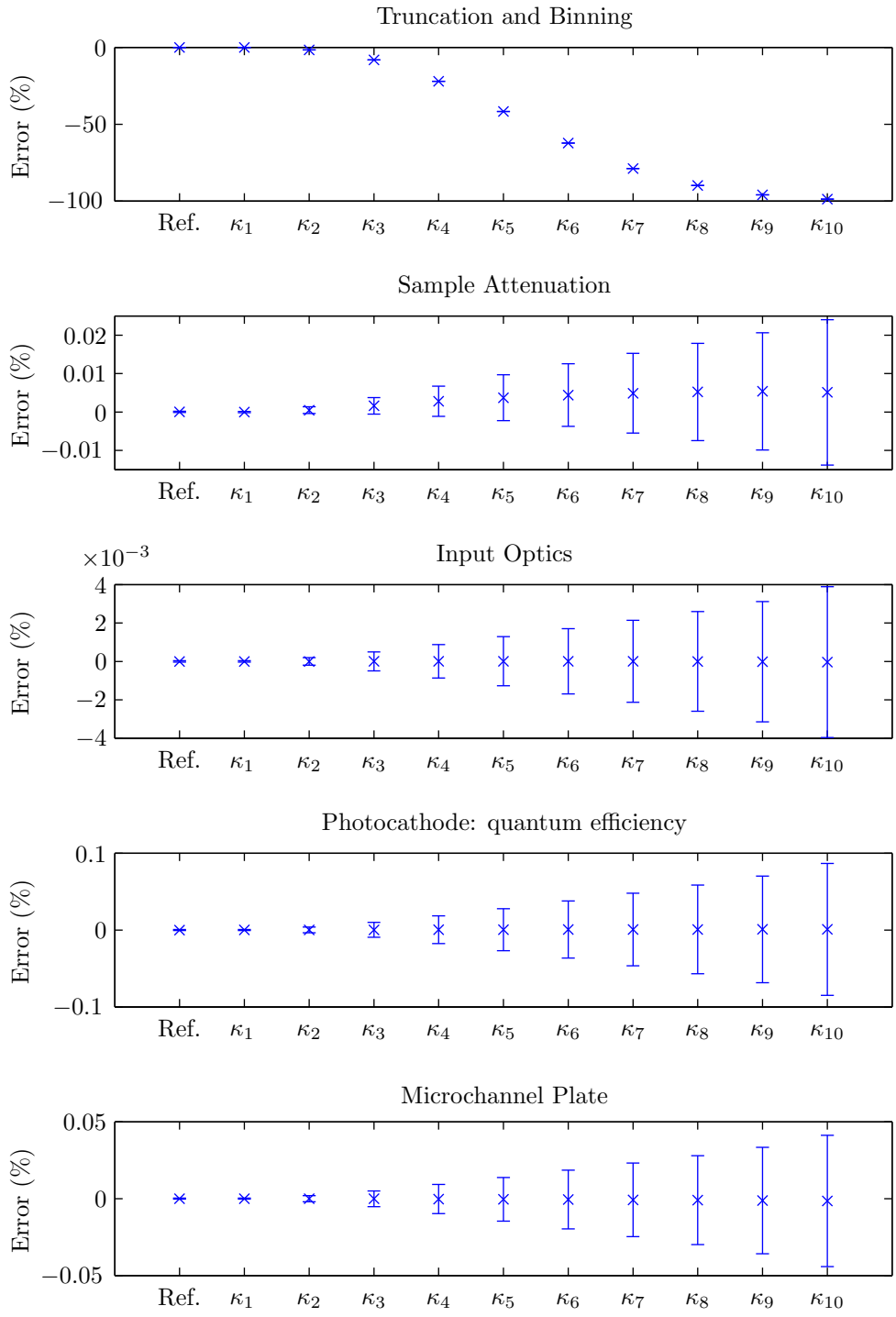

Figure 5.26: The mean and coefficient of variation (marked by the cross and error bars respectively) of the distribution of errors due to the first five stages of the streak camera.

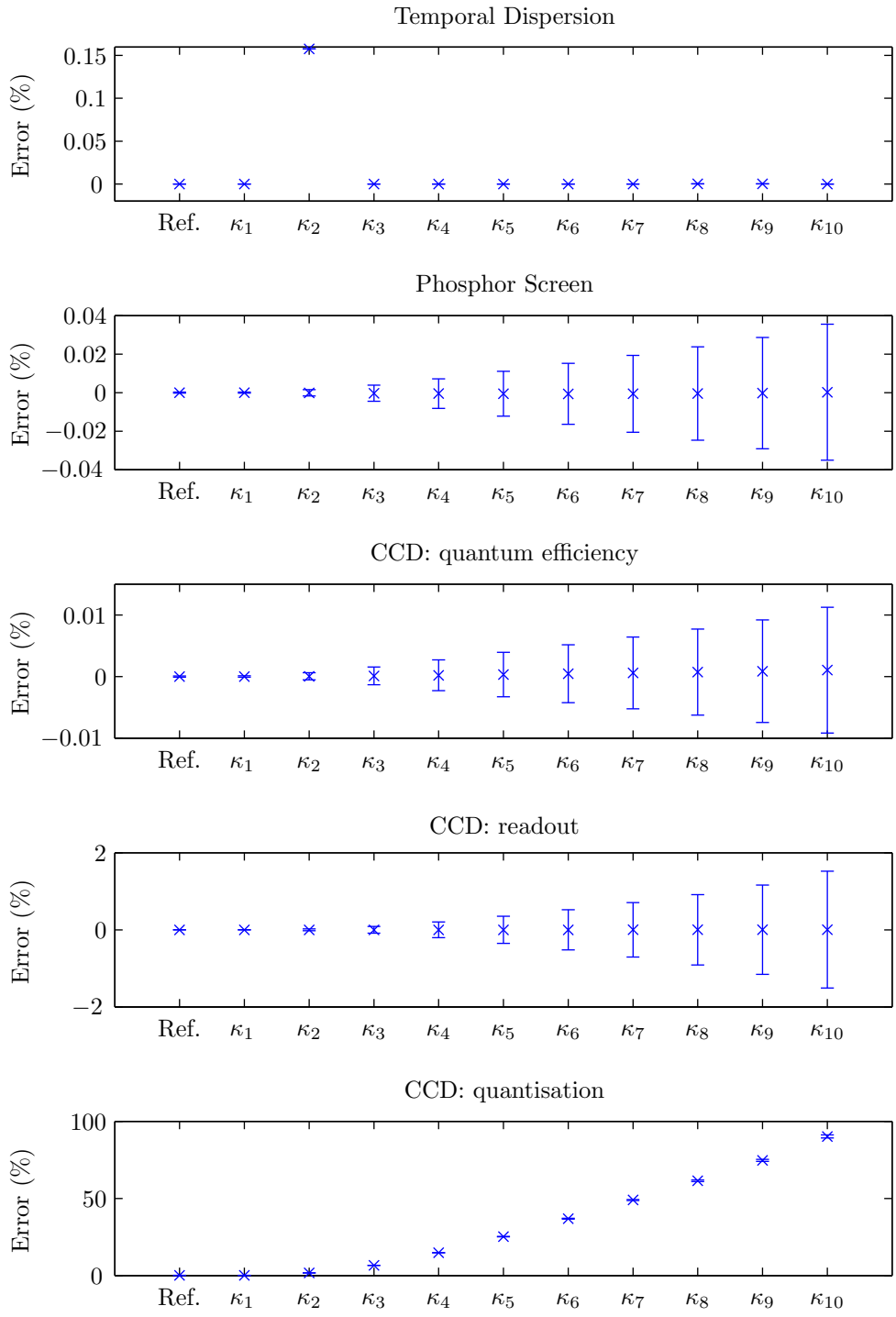

Figure 5.27: The mean and coefficient of variation (marked by the cross and error bars respectively) of the distribution of errors due to the second five stages of the streak camera.

Truncation and Binning

The first stage of the streak camera model is the truncation and binning of the TPSF. As discussed using Figure 5.18, the effect of binning is negligible because this TPSF has been sampled using a sufficient number of bins (798). However, truncation of the TPSF has the effect of completely removing the contribution of photons arriving beyond a certain time. Lower-order cumulants and the reflectance rely on these contributions less than higher-order cumulants and so will be relatively unaffected by this step. As the order of the cumulant increases, however, so does the cumulants' reliance on the TPSF's tail, resulting in a gradual increase in the magnitude of the error. This effect can be seen most clearly with the tenth cumulant, for which the bulk of the non-truncated contributions from the tail have been removed by the truncation, resulting in an error of almost -100%. The errors in this stage will all be negative by definition, as contributions to the cumulants' values have been removed, not added, by the truncation.

The truncation step is not random by nature, and so will have the same effect on the noiseless TPSF for each of its passes through the streak camera. As a result, the coefficients of variation of the error distributions for this step are equal to zero.

Sample Attenuation

The total number of photons in each instance of the noisy TPSF was chosen from a normal distribution. The reflectance will therefore vary around its analytical solution

(the distribution's mean) with a standard deviation, σ_{total}, equal to the standard deviation of the normal distribution, σ_{normal}, adjusted to take into account the averaging over each group of TPSFs. This adjustment can be defined by the *standard error*, as explained in §5.5.3.1 on page 115, as:

$$\sigma_{\text{total}} = \frac{\sigma_{\text{normal}}}{\sqrt{1000}} \tag{5.5.19}$$

The mean and the standard deviation of the normal distribution used to select the number of photons in this case were approximately 3.96×10^8 and 2×10^4 photons respectively. Using Eqs. 5.5.14 and 5.5.19, the coefficient of variation can therefore be calculated as:

$$\begin{aligned} CV = \frac{\sigma}{\mu} &\approx \frac{\left(\frac{2 \times 10^4}{\sqrt{1000}}\right)}{3.96 \times 10^8} \\ &\approx 1.6 \times 10^{-6} \end{aligned} \tag{5.5.20}$$

As the coefficient of variation from the truncation and binning step was equal to zero, δCV for this step is therefore approximately $1.6 \times 10^{-4}\,\%$. The error bar for the reflectance is therefore insignificant.

The errors' coefficients of variation can be seen to increase as the order of the cumulant increases. This is due to the temporal bins for the TPSF's tail – on which higher-order cumulants are more reliant – having less signal level than the bins for the body of the TPSF. As such, a variation in the number of photons detected in the bin will have a larger effect on the bin's final value, thus leading to a larger coefficient

of variation over several passes through the streak camera.

Input Optics & Photocathode: quantum efficiency

The error steps due to the streak camera's input optics and its photocathode's quantum efficiency are both governed by binomially distributed noise. As this has the effect of scaling the TPSF's bins approximately equally, the shape of the TPSF will not be greatly affected and so all of the metrics will vary about their initial values, resulting in the mean errors of the metrics being close to zero. Note that the means will only be equal to zero for an infinite number of passes through the streak camera. Therefore, any small deviations around zero are the result of the limited number of passes carried out.

In the case of the sample attenuation, one binomial distribution was used to find the total number of photons in the TPSF. The large number of photons used in this distribution resulted in a small standard deviation which was then decreased further by the process of averaging, thus resulting in a very small coefficient of variation in the error distribution. In the cases of the input optics and photocathode, however, the reflectance is found as the sum of the binomially distributed numbers from each temporal bin. It is known that the sum of a set of N binomial distributions with equal probability, p, is equal to a binomial distribution with the same probability and with the number of trials, n, equal to the sum of the numbers of trials in the original

set:[125]

$$\sum_{i=1}^{N} \text{Binomial}(n_i, p) = \text{Binomial}\left(\sum_{i=1}^{N} n_i, p\right) \tag{5.5.21}$$

Therefore, the combined distribution resulting from the separate temporal bins will be equivalent to a single distribution corresponding to the total number of photons. As a result, the coefficient of variation in the reflectance's distribution will – as in the case of the sample attenuation – remain small due to the small standard deviation from the binomial distributions used, and the effect of averaging over each group of TPSFs.

The above two effects are common to many of the streak camera's error steps: the gamma, poisson and gaussian distributions also have little effect on the TPSF's shape, as well as sharing the binomial distribution's summation property. Therefore, only effects on the mean errors and the reflectance's coefficient of variation that are not due to these processes will be covered in the rest of this section.

The coefficient of variation of each of the cumulants' error distributions will depend upon the coefficients of variation of the binomial distributions used on each temporal bin which are defined using Eqs. (5.5.11) and (5.5.12) as:

$$CV = \frac{\sigma}{\mu} = \frac{\sqrt{np(1-p)}}{np} \tag{5.5.22}$$

where n is the initial number of photons and p the probabilities of each photon either being transmitted through the input optics or being converted to a photoelectron by the photocathode. As a result, the coefficient of variation is related to the initial

number of photons by:

$$CV \propto \frac{1}{\sqrt{n}} \tag{5.5.23}$$

The coefficient of variation is therefore bigger for smaller values of n. As higher-order cumulants are increasingly dependent on the TPSF's tail, which in turn decreases in values of n as the time of arrival increases, higher-order cumulants' distributions will therefore suffer from increasingly large values of coefficient of variation.

The coefficients of variation for the photocathode stage are larger than for the input optics. This is for two reasons. Firstly, the different values of p for each stage will give rise to larger values of CV for the photocathode stage, according to Eq. (5.5.22). Secondly, as the input optics reduce the number of photons in the signal, the values of n will therefore be smaller for the photocathode stage, resulting in bigger coefficients of variation. This reduction in signal level will also increase the noise effect of individual photons, as explained for the sample attenuation.

Microchannel Plate

The microchannel plate has the effect of adding gamma-distributed noise to the TPSF. The coefficient of variation for this distribution can be calculated using Ref. 112 as:

$$CV = \frac{\sigma}{\mu} = \frac{\sqrt{n}\,\mu_{\mathrm{g}}}{n\,\mu_{\mathrm{g}}} = \frac{1}{\sqrt{n}} \tag{5.5.24}$$

where n is the initial number of photons in each temporal bin and μ_{g} is the mean gain per photon. The change in the coefficients of variation as the order of the cumulant

increase will therefore follow that of the input optics and photocathode. The drop in signal level due to the photocathode's attenuation will result in smaller values of n. This will cause a further drop in the sizes of the coefficients of variation for the same reasons as the photocathode.

Temporal Dispersion

As explained in §5.5.2.4 on page 97, the modelling of the streak camera's temporal dispersion by the convolution of the TPSF with a gaussian distribution will only affect the TPSF's variance. As this effect is the summing of the gaussian distribution's variance to that of the TPSF, the error due to this step will be positive for the second cumulant. Also, as the gaussian distribution's variance is constant, the coefficient of variation of this error will be zero.

Phosphor Screen

The errors on the metrics due to the phosphor screen are governed by poisson-distributed noise. The coefficient of variation for this distribution is given as:

$$CV = \frac{\sigma}{\mu} = \frac{\sqrt{n}}{n} = \frac{1}{\sqrt{n}} \tag{5.5.25}$$

The coefficient of variation of each of the cumulants' error distributions will therefore follow the form of the binomially distributed noise of the input optics and photocathode. As such, the error distributions' coefficients of variation can be seen to increase for higher-order cumulants.

Although the overall signal level output from the phosphor screen will be roughly equal to that input to the microchannel plate, the photons will have been temporally dispersed by their convolution with a gaussian in the previous stage. As a result, the TPSF will consist of a greater number of temporal bins, each containing fewer photons. Due to the nature of the coefficient of variation's dependence on n, namely the square root, this will reduce the coefficients' values compared to the microchannel plate. As the dispersion of the photons due to the streak camera is very slight, so is this reduction.

CCD: quantum efficiency

The CCD's quantum efficiency is subject to binomially distributed noise. As a result, it will also follow the form of the binomially distributed noise of the input optics and photocathode. The different p value will result in the coefficients' smaller values compared to the phosphor screen's.

CCD: readout

Readout noise is added to the TPSF via the addition or subtraction of a number of photons selected from a gaussian distribution. With a standard deviation of 6 electrons, the magnitude of the noise selected from the gaussian distribution has the potential to be large in comparison with later temporal bins' initial values, therefore leading to significant errors. This can be seen especially for higher-order cumulants where the effect will be greatest due to their reliance on the TPSF's tail.

CCD: quantisation

In order to explain the effects of the CCD's quantisation process on the metrics, it is first necessary to consider the output of the previous stage. As photons reach the CCD, they are converted to electrons according to the detector's quantum efficiency. These electrons are then converted to a voltage by a charge amplifier, the non-ideal nature of which adds noise to this voltage. As a result, for pixels containing small numbers of electrons, the final voltage may be a negative value. The quantisation of this signal, however, using an analogue-to-digital converter, does not allow for negative values which will therefore be truncated.

As a result of this, the overall level of the signal will be increased by the quantisation step and there will therefore be an increase in the TPSF's reflectance. The error in the reflectance in Figure 5.27 is approximately 8×10^{-3} %. This appears relatively small, but note that the tail, which is more susceptible to this effect due to its small signal levels, only makes a small contribution to the reflectance in comparison with the main body of the TPSF. The cumulants will also be affected similarly, with the error increasing as the order of the cumulant increases due to its increasing reliance on the TPSF's tail.

Although the quantisation process is not random by nature, its effects on the TPSF will vary due to the variation in the values of the input signal's temporal bins. As a result, the coefficient of variation of the signal will increase. This can be seen

especially for higher-order cumulants, as the tail's small signal level will be more affected by its rounding to the nearest discrete level.

5.5.3.4 Final Errors

As well as looking at the error effects of each stage of the model, it is useful to look at the final error in each metric as a result of the entire model. As the errors therefore need to be considered cumulatively, the standard deviations of the error distributions are used instead of the coefficients of variation.

Figure 5.28 therefore shows the final distribution of the errors in the metrics after their "detection" by the streak camera model. As expected, the mean of each error distribution will increase in magnitude for increasing cumulants due to the effects of the TPSF's truncation.

The standard deviations, however, do not increase as the order of the cumulant increases, as was the general trend for the coefficients of variation for each error stage. Instead, they can be seen to peak at the fifth cumulant, after which they decrease in magnitude. This is due to the loss of contribution to higher-order cumulants as a result of the TPSF's truncation. In general, as the order of the cumulant increases and its value relies more on the TPSF's tail, there will be an increase in standard deviation due to the decrease in signal level. However, this is the standard deviation in the *remaining* contribution to the cumulant after truncation. As this contribution is much smaller than its analytical solution, due to the truncation, the calculated

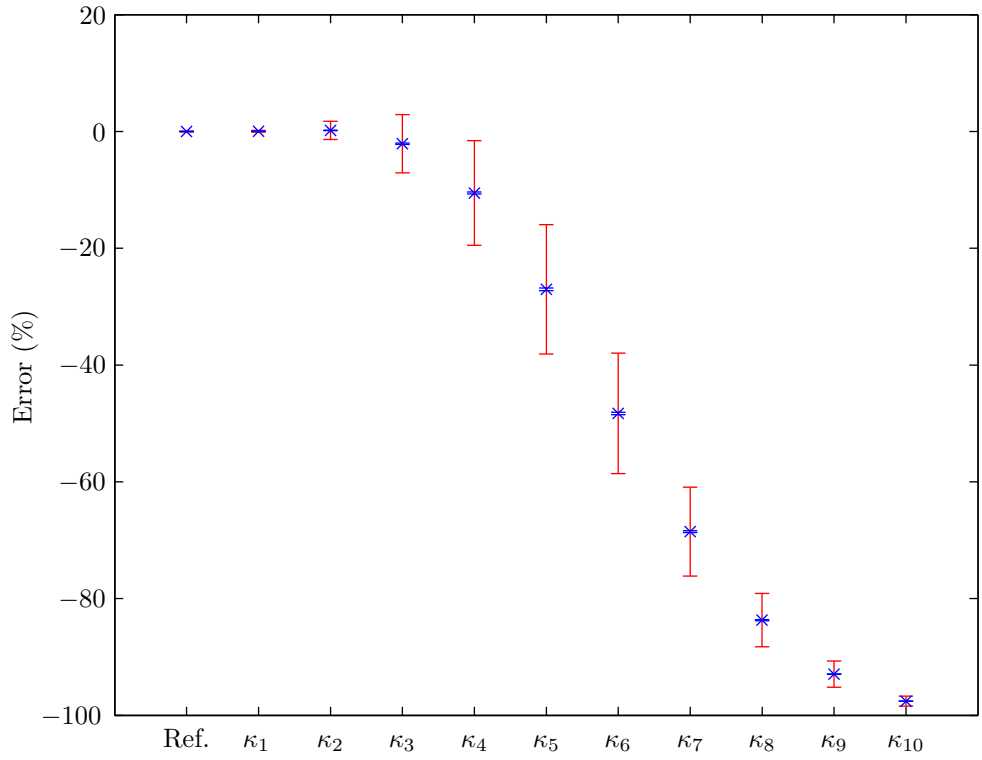

Figure 5.28: The mean and standard deviation (marked by the blue cross and error bars respectively) of the final distribution of the errors in the metrics after their "detection" by the streak camera model. The red error bars show the standard deviations increased by a factor of 50 to allow their levels relative to each other to be seen more clearly.

standard deviation will also be smaller. The form of the standard deviations in Figure 5.28 can therefore be explained by a trade-off between these two effects. Note that this trade-off was not seen in the stage-by-stage errors as the effect of the loss of the signal by truncation was separated from the following errors.

5.5.4 Errors on Metrics over the Entire Parameter Range

Having investigated the errors due to a streak camera for a particular TPSF, the camera model was then applied over the entire range of scattering, absorption and, in the case of spatially resolved detection, source–detector distance parameters, as defined in §4.3. This enabled a map of the total errors in the metrics over the parameter ranges to be produced, which could then be used to determine the optimum metrics for the characterisation of a scattering medium as explained in Chapter 6.

5.5.4.1 Parameter Resolution

The equations derived from the Diffusion Approximation in §3.3 allow for the reflectance and cumulants of a medium to be plotted as a continuous range. However, due to the numerical nature of the streak camera model, the errors must be calculated for discrete values of the input parameters. The question is therefore how finely to sample the input parameters over their respective ranges. A finer resolution would result in a more detailed picture of the errors from a streak camera, but would also require more instances of the model to be carried out. As implementation of the model can be time-intensive, it was therefore necessary to minimise the number of different discrete sets of parameter values.

With this in mind, it was decided to increase the scattering coefficient in steps of 15mm^{-1} resulting in ten discrete μ_s sample points within the chosen range. Likewise, spatial bin widths of 1mm were used, giving ten discrete spatial bins.

It had been observed in preliminary simulations that a medium's reflectance changed very sharply for absorption coefficients less than 0.3mm^{-1}, whereas values above this figure resulted in relatively gradual changes. In order to minimise the number of simulations required for the Monte Carlo method and to allow the initial sharp change in reflectance to be modelled accurately, it was therefore decided to increase the absorption coefficient in steps of around 0.015mm^{-1} for values below 0.3mm^{-1} (21 points), and around 0.1mm^{-1} for values above (17 points).

In total, these resolutions result in 380 parameter pairs for full-field detection, and 3800 parameter triplets for spatially resolved detection.

5.5.4.2 Convergence of the Model

An important factor in the modelling of the errors for these parameter sets was the number of passes through the model that should be performed. This number should be sufficient for the values of the final errors in the metrics to have converged to their mean values. Although this was true of the 5000 passes used for in §5.5.3.3, using this number for every one of the parameter sets would result in the modelling requiring an unfeasible length of time to complete.

Figure 5.29 therefore shows the variation in the final percentage errors in the reflectance and first four metrics against the number of passes through the model. Note that the number of TPSFs in each group was kept constant at 1000. As can be seen, each error converges to its limit as the number of passes increases, with the mean

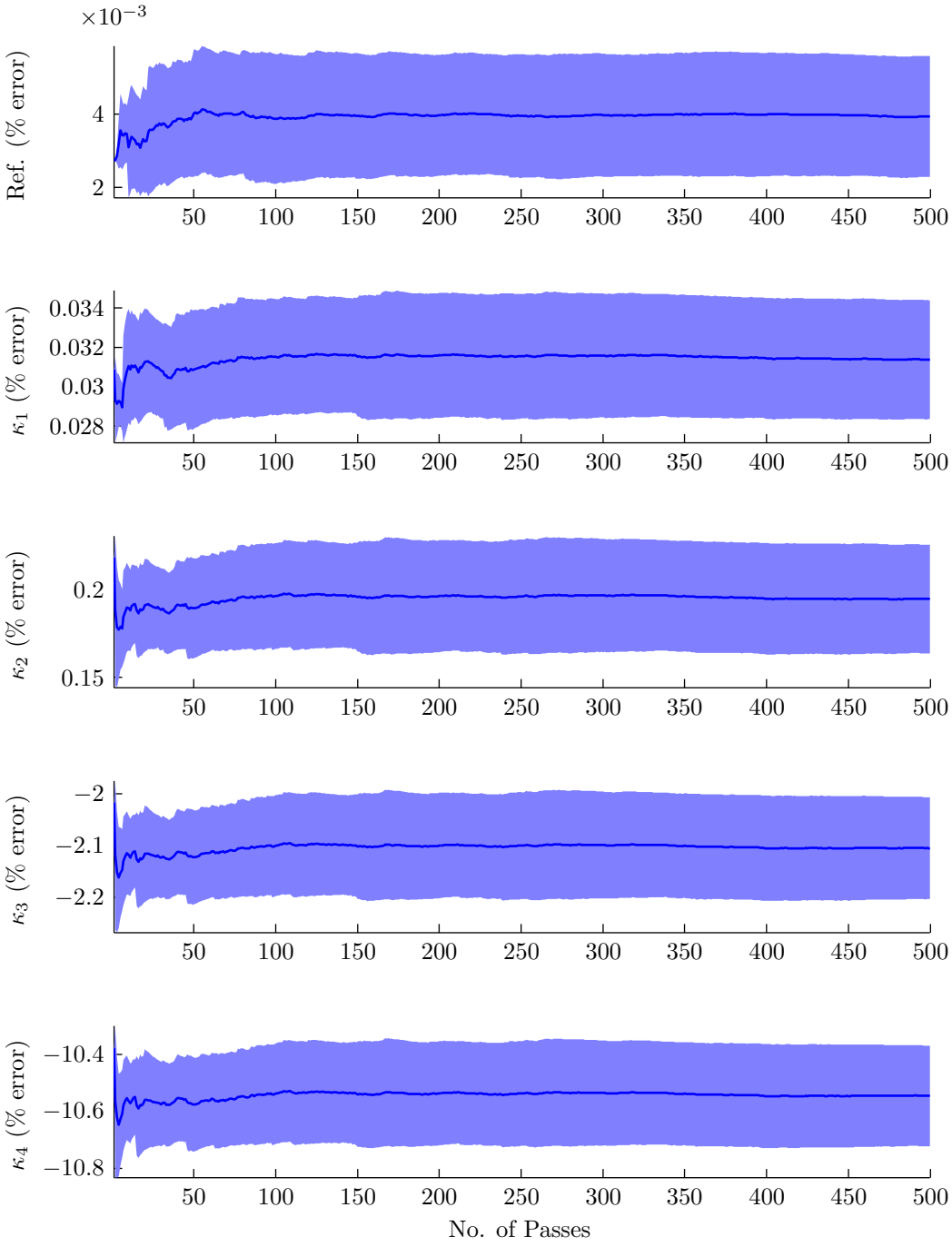

Figure 5.29: The variation in the final percentage errors in the reflectance and first four metrics against the number of passes through the streak camera model. The shaded area shows the size of a standard deviation around each error's mean value, marked by the dark line.

error value remaining consistent after around 500 passes. At 200 passes, however, the mean values of the errors can be seen to be close enough to their limits to give a sufficiently precise error. Therefore, 200 passes will be used for each parameter set.

5.5.4.3 Truncation Length & Signal Level

The method described in §5.5.3.1 was used to define the appropriate truncation length for each of the TPSFs produced. The truncation length will therefore depend on both the intensity and shape of the TPSF, whose variation with the input parameters were fully covered in §4.4. The truncation length for each parameter pair using full-field detection can be seen in Figure 5.30. The black lines mark the boundaries between parameter pairs over which the change in this length resulted in the use of a different sweep time on the streak camera. The value of the truncation length will have a significant influence on the total intensity of the TPSF that will be measured by the streak camera.

The total intensity for each parameter pair is therefore shown in Figure 5.31. The shape of this figure can be explained by looking at the change in both the truncation length and total intensity with μ_a for a constant scattering coefficient of 15mm^{-1} as shown in Figure 5.32. As the absorption increases, both the width and intensity of the TPSF will decrease, as demonstrated in Figure 4.2 on page 57. As a result, the TPSF will reach the noise floor earlier and the truncation length will decrease.

As a general trend, the reduction in truncation length will cause the total intensity

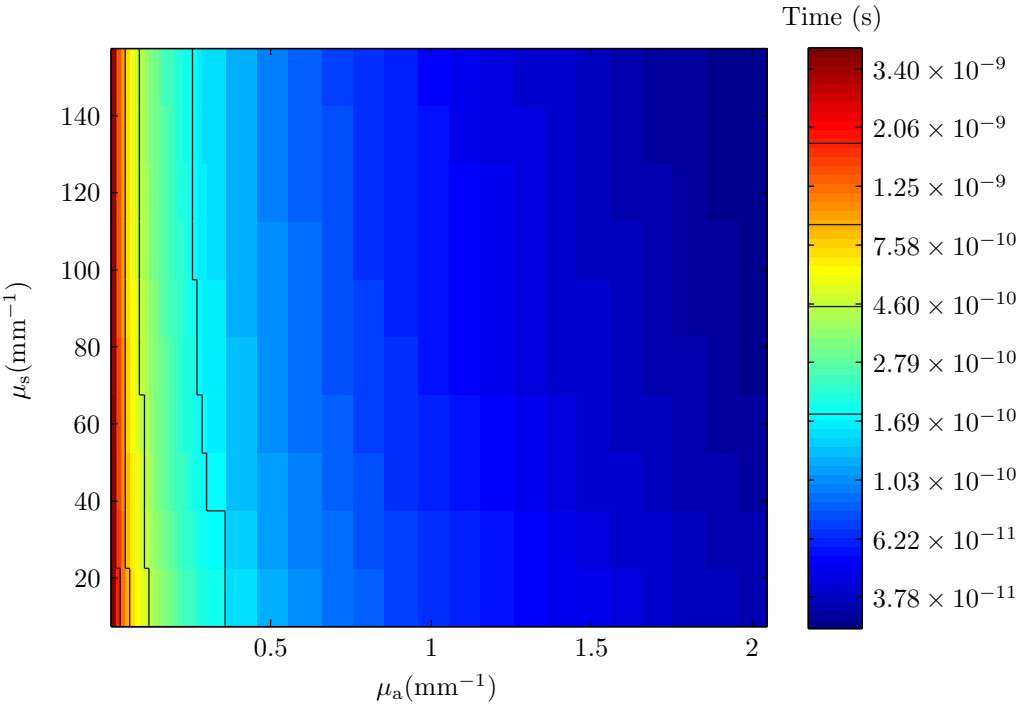

Figure 5.30: The truncation lengths used for each scattering and absorption coefficient pair using full-field detection. The black lines mark the boundaries between parameter pairs over which the change in truncation length resulted in the use of a different sweep time on the streak camera. The figure uses a logarithmic colour axis for clarity.

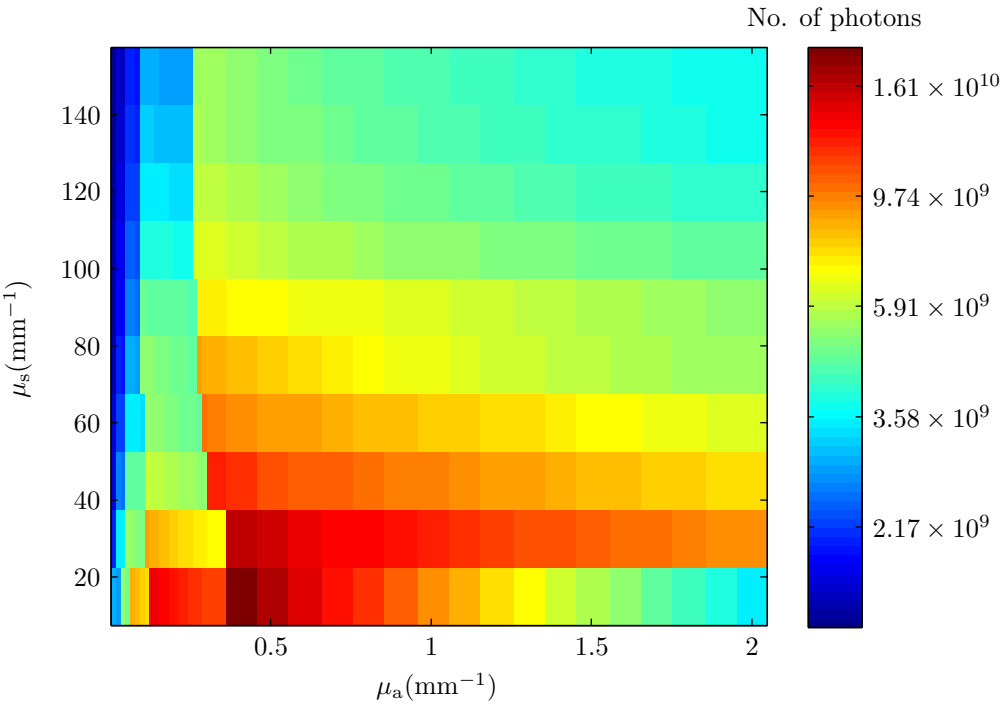

Figure 5.31: The overall intensity of the noiseless TPSFs created for each scattering and absorption coefficient pair using full-field detection. The figure uses a logarithmic colour axis for clarity.

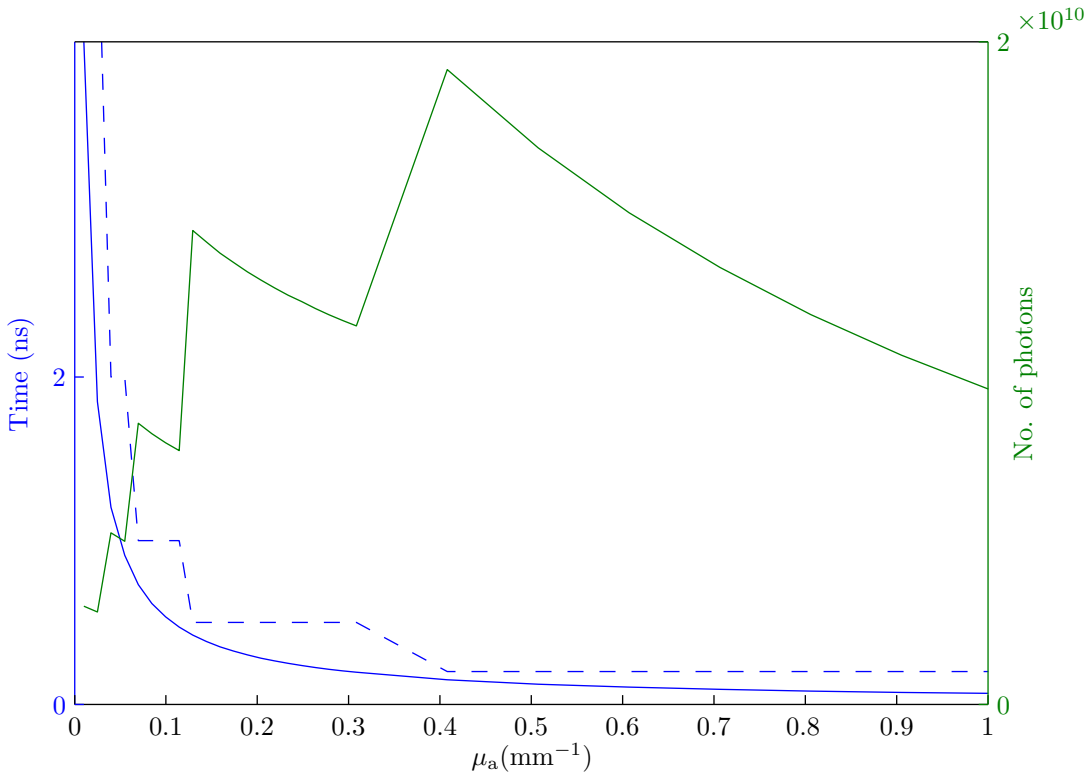

Figure 5.32: The blue lines show the variation of the truncation length of a TPSF (solid line) and the sweep time used to measure it (dashed line) for different values of the absorption coefficient using a constant scattering coefficient of 15mm^{-1}. The variation in the TPSF's total intensity is shown in green.

of the TPSF to decrease: not only will the TPSF's peak intensity decrease, but so will the amount of TPSF that is used. However, by looking at the variation in the streak camera's sweep time as determined using the method described in §5.5.3.1, it can be seen that each time the sweep time reduces there is a corresponding increase in the TPSF's total intensity. In cases where the TPSF's peak value is not large enough to saturate the streak camera's CCD, this effect would not be seen: changing the sweep time, and therefore the binning, would have no effect on the TPSF's overall

intensity. However, the increased intensity due to lack of spatial binning in this case means that the TPSF's peak intensity will be limited to prevent it from saturating the streak camera's CCD. A decrease in sweep time will therefore result in finer temporal bins being used to measure the TPSF, meaning that the peak bin will contain fewer photons. The scaling on the TPSF will therefore be smaller, resulting in a higher overall intensity level.

Figures 5.33 and 5.34 show the truncation length and total intensity for each parameter pair for spatially resolved detection, and demonstrate the case in which a change in the sweep time does not lead to an increase in the reflectance. Due to the spatial binning and the distance of the detector from the light source, insufficient light will be detected to saturate the CCD. The TPSF is therefore not peak-limited and so the reflectance in Figure 5.34 will be relatively unaffected by the change in bin width.

These figures also demonstrate an underlying problem due to the streak camera's noise floor. For large source–detector distances and large scattering and absorption levels, the TPSF's peak light levels will be smaller than the system's noise floor. These TPSFs can therefore not be measured by the streak camera and so they are not plotted here. The consequences of this will be covered in more detail in Chapter 6.

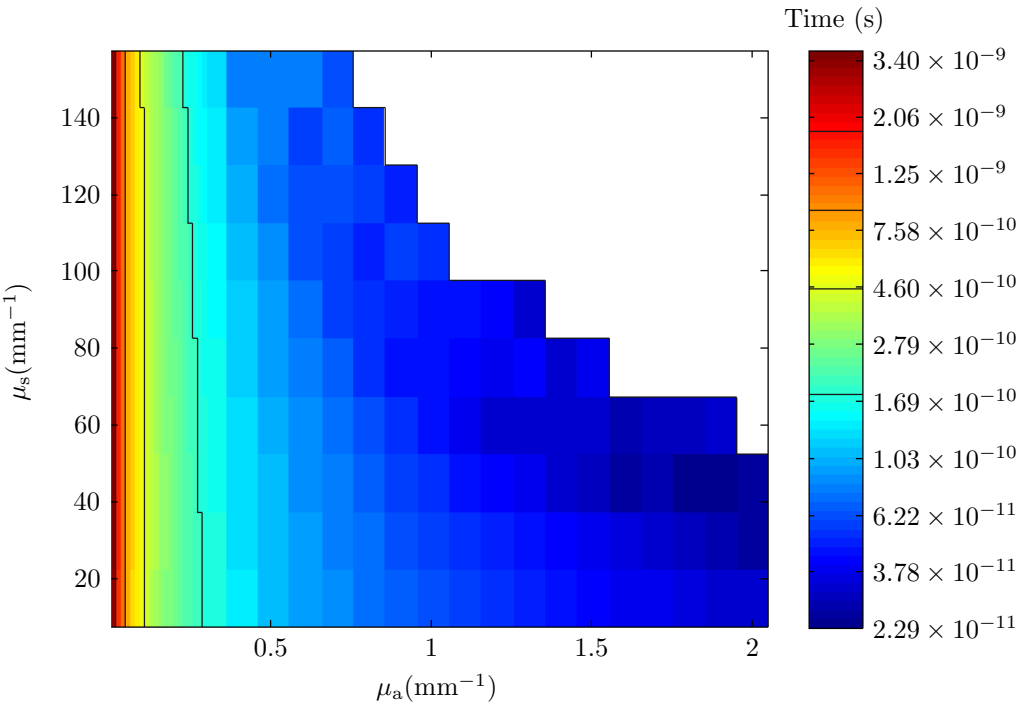

Figure 5.33: The truncation lengths used for each scattering and absorption coefficient pair for an annular detector with radii 3–4mm. The black lines mark the boundaries between parameter pairs over which the change in truncation length results in the use of a different sweep time on the streak camera. The figure uses a logarithmic colour axis for clarity.

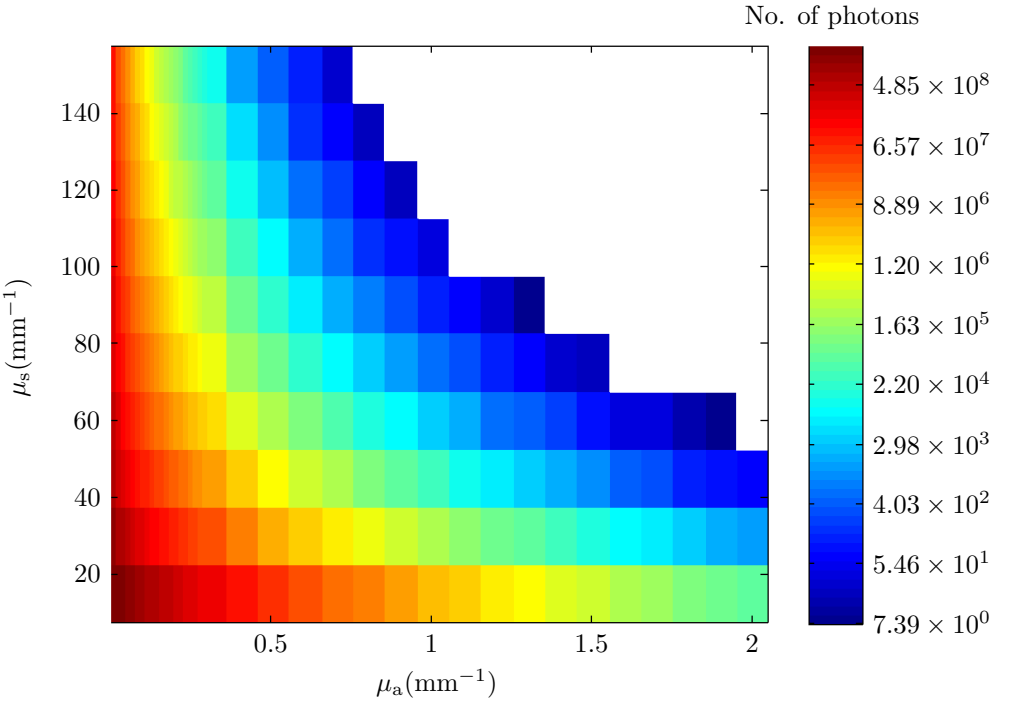

Figure 5.34: The overall intensity of the noiseless TPSFs created for each scattering and absorption coefficient pair for an annular detector with radii 3–4mm. The figure uses a logarithmic colour axis for clarity.

5.5.4.4 Final Error Maps

The mean magnitude (μ) and standard deviation (σ) of the errors in the reflectance and first three cumulants due to the streak camera for full-field detection are shown as "error maps" in Figure 5.35. As the values of the scattering and absorption coefficients and the source–detector distance vary, so will the shape of the TPSF. This will, in turn, affect the following:

1. The truncation length
2. The temporal binning
3. The overall intensity of the TPSF
4. The initial values of the TPSF's metrics

As these are all factors in the distribution of the errors in the metrics due to the streak camera model, the changes in the errors as the input parameters vary are quite complex. However, the general trends will still be discussed here.

The forms of the error maps in Figure 5.35 can be mostly explained by a combination of two effects. Firstly, in general, the TPSF's magnitude will decrease as the absorption increases due to the Beer–Lambert law. This decrease in the number of photons will cause an increase in the effect of noise – the change in the number of photons will have more effect on a small signal level due to its reduced signal-to-noise ratio. As a result of this, the sudden increase in the magnitude of the TPSF caused

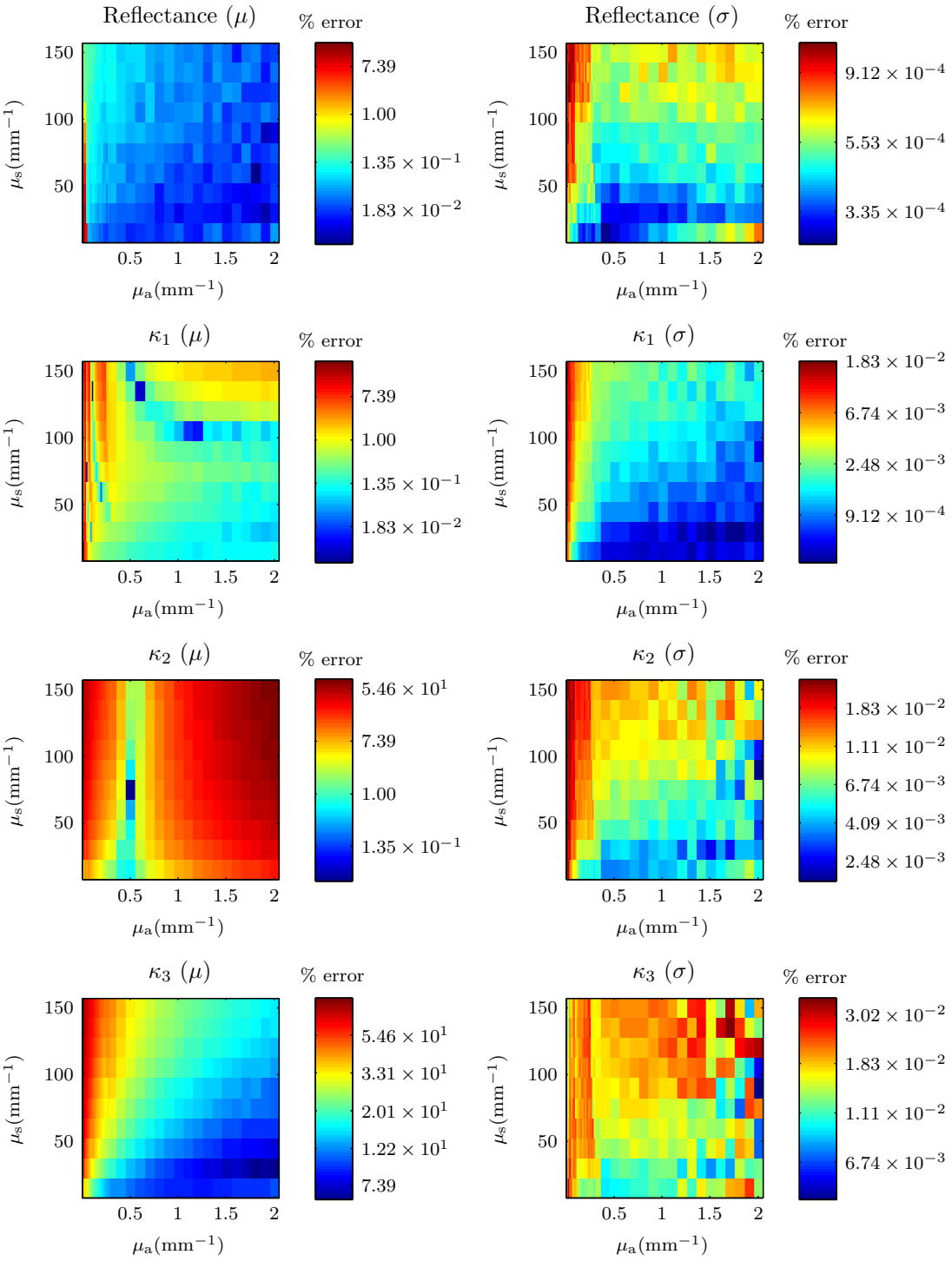

Figure 5.35: The mean magnitude (μ) and standard deviation (σ) of the errors in the reflectance and first three cumulants (shown as a percentage of the analytical metric value) due to the streak camera for full-field detection. The figures use logarithmic colour axes and absolute values of data for clarity.

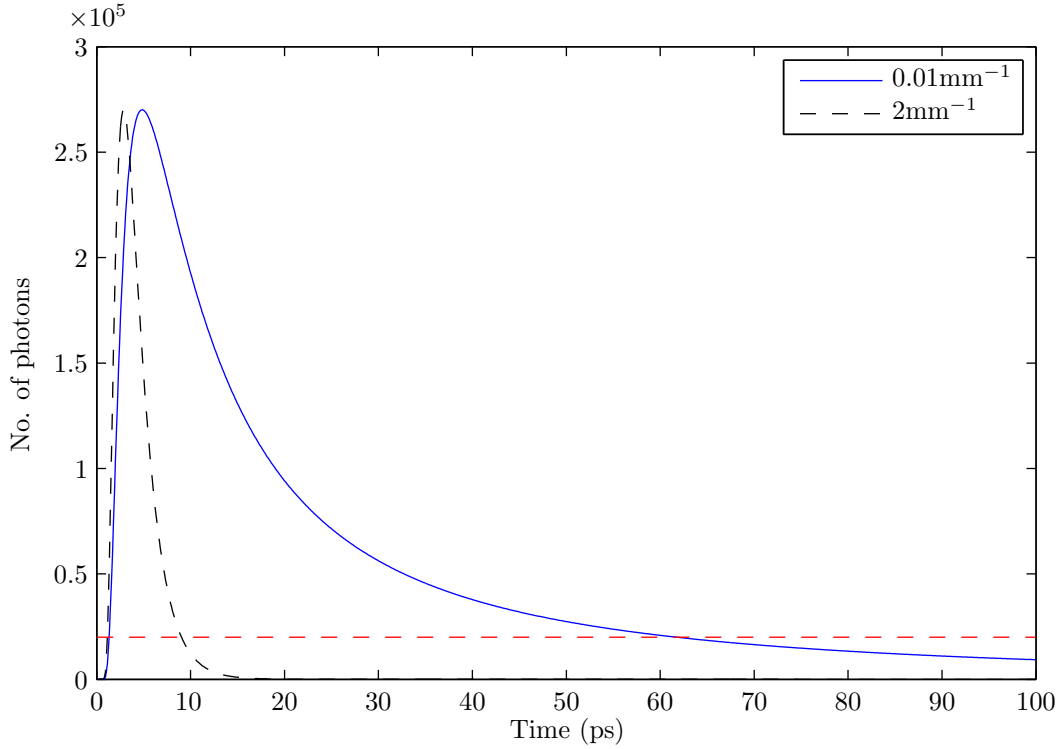

Figure 5.36: The effect of the value of the absorption coefficient (shown in the legend) on the truncation error. The red, dashed line shows the streak camera's noise floor, at which level the TPSFs are truncated.

by a change in the streak camera's sweep time, as demonstrated in Figure 5.32, will therefore cause a sharp decrease in the magnitude of the error. This results in the discontinuities in the error maps for the first cumulant's mean error and the lower-order metrics' standard deviations, which can be seen to correlate with the changes in sweep time shown in Figure 5.30.

Secondly, a change in the value of a medium's absorption coefficient can be seen to have a large effect on the error due to truncation. This can be explained using Figure 5.36. At low absorption levels, the resulting TPSF has a longer tail than at

high absorption levels. This means that the TPSF will cross the level of the noise floor at a shallower angle than the TPSF with high absorption and as a result, a larger proportion of the tail will be lost due to truncation. This effect can be seen in the plot of the mean error in the third cumulant. Higher-order cumulants follow this trend, with the magnitude of the errors increasing as the order increases and the cumulant relies more heavily on the TPSF's tail.

The "valleys" in the mean errors of the first and second cumulant can be explained by the method of presentation of the data. As the plots' colour axes are logarithmic in nature, it is not possible to show negative values and so the values shown are merely the errors' magnitudes. Each valley therefore marks the point at which the errors turn from negative to positive as the absorption increases. In the case of the second cumulant (the variance), this effect is due to the streak camera's temporal dispersion which is modelled by convolving the TPSF with a gaussian distribution, and therefore has the effect of increasing the value of the TPSF's second cumulant. At lower absorption levels, the second cumulant will be reduced heavily by the truncation, as explained above. In this case, the increase in the variance due to the convolution will not be large enough to overcome the truncation's effect and so will merely make the error in the cumulant less negative. As the absorption level increases, however, the error due to truncation will decrease sufficiently for the convolution to first cancel out the error, and then overcompensate by making the error more positive.

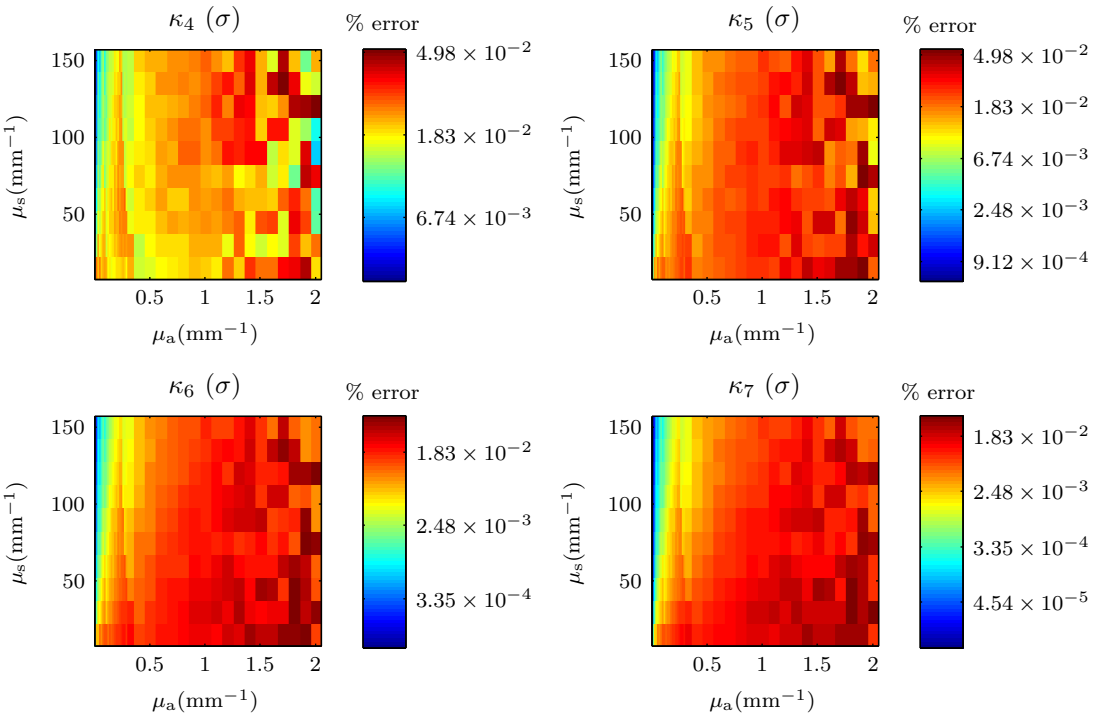

Figure 5.37: The standard deviation (σ) of the errors in the fourth to seventh cumulants (shown as a percentage of the analytical metric value) due to the streak camera for full-field detection. The figures use logarithmic colour axes for clarity.

The standard deviations of the errors in the third order and higher cumulants do not follow the same trend as those of the lower-order cumulants: as the order of the cumulant increases, the standard deviation in the error can be seen to be greater when the mean error is lower. This is shown in Figure 5.37 and is due to a similar effect as seen in Figure 5.28. As the mean error in higher-order cumulants is due to the TPSF's truncation, a large mean error will be the result of the removal of a large proportion of the cumulant's contribution. As such, any noise on this reduced contribution will have a small effect when compared to its cumulant's true, larger

analytical value.

These error maps are an essential part of the determination of the optimum metrics for the characterisation of scattering media and so will be integral in the methods used in the following chapter.

5.6 Model Validation

Having described this novel model of a streak camera, it is important to consider how it could be validated. The foundation of this process is the input of a characterised signal to the streak camera and the measurement of the camera's output. The known characteristics of the input signal allow an identical signal to be applied theoretically to the model and its output calculated. Comparison of the outputs from both the physical camera and the model allow the accuracy of the model in representing the camera to be ascertained.

The question, therefore, is one of the production of a characterised input pulse. Firstly, it would be inappropriate for this pulse to be a TPSF emitted from a tissue sample, as would be the case when taking measurements with the camera – the addition of a tissue sample into the light path would only serve to increase the uncertainty about the input pulse, not only as a result of the model used to describe the light emitted from the tissue sample but also as the sample's optical characteristics used within the model could not be known with 100% accuracy. The input pulse can therefore be that of the system's laser. As a result of the omission of the sample, the

laser should be used at low power levels to simulate the light levels expected from the tissue sample. The laser pulses can be characterised by a technique such as interferometric autocorrelation,[126] although the characteristics must be averaged over a large number of pulses in order to take into account the variation between pulses due to the laser.

Once characterisation of the laser has been completed, the pulses can be applied to both the camera and its model. In both cases, due to the stochastic nature of the camera and its model, this must be averaged over many laser pulses to reduce the uncertainty in the comparison of the camera's and model's outputs. Validation is then achieved by a direct comparison of the resulting TPSFs' cumulants and reflectance, as these are the metrics used in this thesis to ascertain a medium's scattering and absorption properties. The model's accuracy can then be calculated for individual metrics or for a combination. This should be repeated for varying power levels in order to fully validate the streak camera model.

5.7 Summary

Presented in this chapter was a complete model of a streak camera. The configuration of a typical streak camera was discussed, and its sources of noise identified. The noise on the TPSF emerging from the sample due to both the light source and scattering and absorption in the medium were also considered. The effects of the relevant types of noise on a TPSF were then investigated.

This knowledge was then used to produce a model which could be used to simulate the detection of a TPSF by a streak camera. Particular consideration was given to two aspects of this detection. Firstly, the maximum light levels that could safely be used to illuminate human skin were investigated and the resulting intensity of the detected TPSF calculated. Secondly, particular attention was paid to the streak camera's sweep time, as this would determine both the time at which the detected TPSF was truncated, and how finely it was binned. It was found that the TPSF's truncation length had a much larger effect on its calculated metrics than the resolution of its temporal binning, and thus priority was given to calculating the appropriate truncation length. This was determined using the camera's noise floor: once the TPSF dropped below this level, it could no longer be measured accurately. The level of the noise floor was found to be almost entirely dependent on the CCD's readout noise, although it could be significantly reduced by averaging the TPSFs. The camera's sweep time was therefore decided from the TPSF's appropriate truncation length.

A typical TPSF was then "detected" using the streak camera model, and the relative and absolute effects of each of the camera's stages on the TPSF's metrics investigated. It was found that the truncation and quantisation of the TPSF had the largest effect on the metrics' values.

Finally, the streak camera model was applied to TPSFs over the ranges of optical parameters corresponding to human skin, as determined in Chapter 4. From the

results, plots of the errors in each metric measured using the streak camera could be plotted. These "error maps" will be used in the following chapter to determine the accuracy to which a medium's absorption and scattering coefficients can be determined using a streak camera.

Chapter 6

Determination of the Optimum Metrics

6.1 Introduction

In Chapter 4, the dependence of the metrics used within this thesis on a medium's parameters were described. The expected error in the measurement of these metrics due to a streak camera were then discussed in Chapter 5. Using this knowledge, it is now possible to ascertain which of these metrics will allow the determination of a medium's scattering and absorption coefficients with the least errors. These are the optimum metrics for the characterisation of a scattering medium.

In order to determine these optimum metrics, it is first necessary to define how they will be used to characterise the medium. There are two unknowns in the system, namely the medium's scattering and absorption coefficients. (The anisotropy factor is assumed to be constant, as explained in §4.3.) Pairs of metrics must therefore be used to solve for these two unknowns.

The properties that make these metric pairs more suitable for characterisation will be ascertained. Error analysis equations that quantify this suitability are then derived and applied to the values of the metrics and their expected errors. This allows the errors in the calculated values of a medium's scattering and absorption coefficients to be determined for each metric pair, from which the optimum pairing can be selected.

The methods described here for the determination of the optimum metrics can be applied to any system where the errors in the metrics are known. In this case, however, the methods will be used to calculate the optimum metrics for the specific streak camera described in Chapter 5.

6.2 Method of Media Characterisation

In order to determine which are the optimum metrics for the characterisation of a scattering medium, it is necessary to detail the method used in the process. First, consider a noiseless, full-field system with which the reflectance and cumulants of an unknown semi-infinite medium can be measured exactly. Ignoring the inaccuracies that come from using the Diffusion Approximation, these metrics are known to vary with a medium's properties as described by the equations derived in Chapter 3. The reflectance and first cumulant can therefore be seen to vary over the range of absorption and scattering values of interest as shown in Figure 6.1.

The contours on each of the surfaces represent the values of two measurements made with the hypothetical noiseless system. They mark the values of μ_s and μ_a that

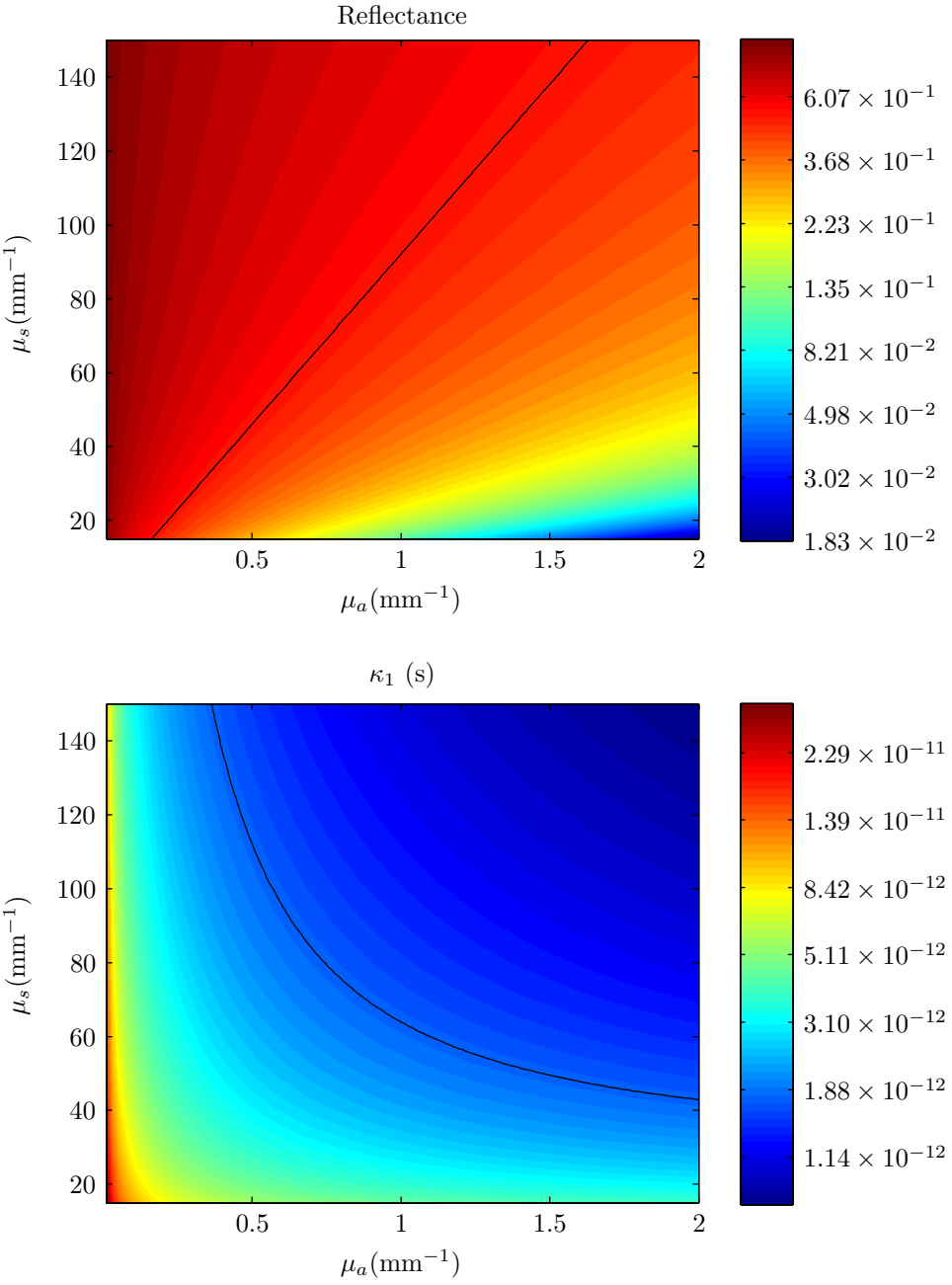

Figure 6.1: The variation of the full-field reflectance and first cumulant with the scattering and absorption coefficients of a semi-infinite medium according to the Diffusion Approximation. The two contours show the positions of an arbitrary measurement on each of the surfaces. The figures use a logarithmic colour axis for clarity.

correspond with each of the measurements. Finding the exact value of the medium's scattering and absorption parameters is therefore a case of finding the position where these contours cross – this is the solution of the two simultaneous equations for the two contours. If the surfaces have been produced analytically, as in this case, these equations are also known analytically. However, if the surfaces have been created either using Monte Carlo modelling or by experiment, curve fitting will have to be applied to each of the contours first to determine their forms.

In practice, it is impossible to take noiseless readings, leading to a small error in the measured value of each metric. This will have the effect of changing the contour of interest on each surface, and thus their crossing point. As a result, there will be an error in the calculated value of the medium's scattering and absorption parameters. This error is an inevitable consequence of noise – it is the magnitude of this error, however, that is of interest.

6.3 Noise Resilience

The optimum metrics can therefore be defined as those that are most resilient to noise, or in other words, those whose surfaces result in the least error in the measured scattering and absorption parameters in the presence of noise. Note that this is a property of metric *pairs*, as it takes two contours to characterise the medium. This will be discussed in more detail in §6.3.2.

6.3.1 Error Analysis

In order to calculate a metric pair's resilience to noise, the change in each of the two metrics, δm_1 and δm_2, is defined in terms of a change in both the medium's scattering and absorption parameters, $\delta\mu_\mathrm{s}$ and $\delta\mu_\mathrm{a}$ respectively:[127]

$$\delta m_1 = \delta\mu_\mathrm{s}\frac{\partial m_1}{\partial\mu_\mathrm{s}} + \delta\mu_\mathrm{a}\frac{\partial m_1}{\partial\mu_\mathrm{a}} \tag{6.3.1}$$

$$\delta m_2 = \delta\mu_\mathrm{s}\frac{\partial m_2}{\partial\mu_\mathrm{s}} + \delta\mu_\mathrm{a}\frac{\partial m_2}{\partial\mu_\mathrm{a}} \tag{6.3.2}$$

The partial derivative terms represent the gradients of each metric surface with the scattering and absorption coefficients and can be calculated either analytically or numerically. However, use of the latter method brings further complications which will be explained in §6.6. Solving Eqs. (6.3.1) and (6.3.2) simultaneously for $\delta\mu_\mathrm{s}$ and $\delta\mu_\mathrm{a}$ gives:

$$\delta\mu_\mathrm{s} = \frac{\delta m_1\dfrac{\partial m_2}{\partial\mu_\mathrm{a}} - \delta m_2\dfrac{\partial m_1}{\partial\mu_\mathrm{a}}}{-J} \tag{6.3.3}$$

$$\delta\mu_\mathrm{a} = \frac{\delta m_1\dfrac{\partial m_2}{\partial\mu_\mathrm{s}} - \delta m_2\dfrac{\partial m_1}{\partial\mu_\mathrm{s}}}{J} \tag{6.3.4}$$

where J is the Jacobian determinant:

$$J = \frac{\partial m_1}{\partial\mu_\mathrm{a}}\frac{\partial m_2}{\partial\mu_\mathrm{s}} - \frac{\partial m_1}{\partial\mu_\mathrm{s}}\frac{\partial m_2}{\partial\mu_\mathrm{a}} \tag{6.3.5}$$

This is discussed in §6.3.2.

The equations shown in (6.3.3) and (6.3.4) represent the error in the medium's

calculated scattering or absorption coefficient in terms of an error in the measured value of each metric, and as such, show the metric pair's resilience to noise.

Note that the equations are also resilient to scaling, as scaling factors on either, or both, of the metrics will appear on both the numerator and denominator and therefore will have no effect on the error in μ_s or μ_a. As scaling factors do not affect a metric's signal-to-noise ratio, this is the desired behaviour of the error analysis equations. This is an important feature, as it also allows metric pairs of different units to be compared.

6.3.2 The Jacobian Determinant

As explained earlier, the resilience of a metric pair to noise is a property of the metric pair and not the individual metrics. The Jacobian determinant is a measure of this resilience, and describes the transformation of data between two parameter spaces. In this case, the transformation is from metric (m_1-m_2) space to coefficient (μ_s-μ_a) space. Rather than considering two surfaces of m_1 and m_2 varying with μ_s and μ_a as in Figure 6.1, this can be visualised as two separate co-ordinate systems, with every point in the m_1-m_2 system mapping to a point in the μ_s-μ_a system. This is demonstrated in Figure 6.2, with arbitrary examples of mappings shown in red.

The figure also shows an area, A_m, in m_1-m_2 space which is defined by the vectors $\mathbf{d}\boldsymbol{m_1}$ and $\mathbf{d}\boldsymbol{m_2}$. This will map onto μ_s-μ_a space as the area A_μ defined by the vectors $\mathbf{d}\boldsymbol{\mu}_s$ and $\mathbf{d}\boldsymbol{\mu}_a$. Vectors $\mathbf{d}\boldsymbol{m_1}$ and $\mathbf{d}\boldsymbol{m_2}$ can be defined in μ_s-μ_a space as the following

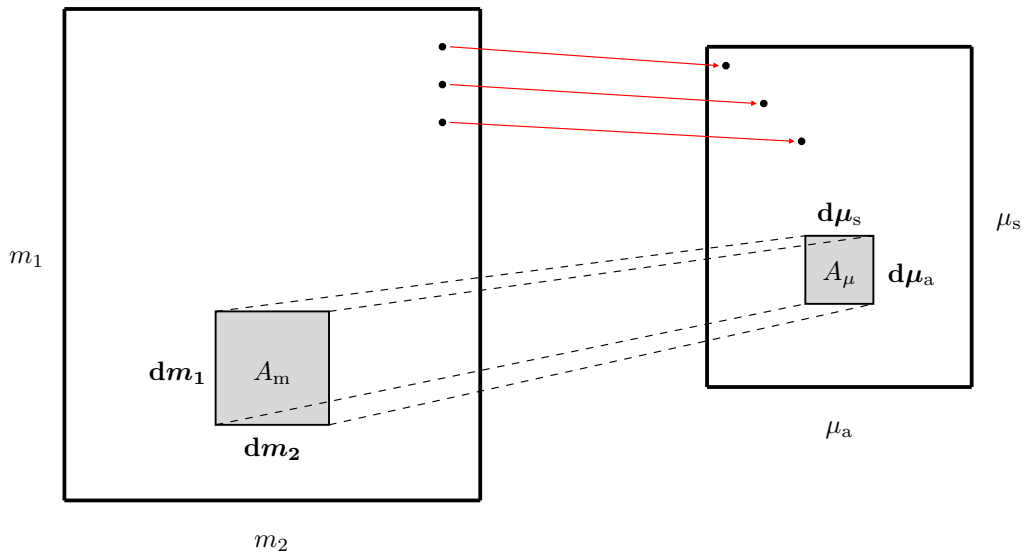

Figure 6.2: A demonstration of the mapping (in red) of points in m_1-m_2 space to μ_s-μ_a space. As a result, areas can also be mapped between the spaces, as shown by A_m and A_μ. This allows the Jacobian determinant to be derived.

vectors:

$$\mathbf{d}\boldsymbol{m_1} = \mathrm{d}m_1\,\hat{\boldsymbol{m}}_\mathbf{1} = \left(\frac{\partial m_1}{\partial \mu_\mathrm{s}}\mathrm{d}\mu_\mathrm{s}\right)\hat{\boldsymbol{\mu}}_\mathrm{s} + \left(\frac{\partial m_1}{\partial \mu_\mathrm{a}}\mathrm{d}\mu_\mathrm{a}\right)\hat{\boldsymbol{\mu}}_\mathrm{a} \tag{6.3.6}$$

$$\mathbf{d}\boldsymbol{m_2} = \mathrm{d}m_2\,\hat{\boldsymbol{m}}_\mathbf{2} = \left(\frac{\partial m_2}{\partial \mu_\mathrm{s}}\mathrm{d}\mu_\mathrm{s}\right)\hat{\boldsymbol{\mu}}_\mathrm{s} + \left(\frac{\partial m_2}{\partial \mu_\mathrm{a}}\mathrm{d}\mu_\mathrm{a}\right)\hat{\boldsymbol{\mu}}_\mathrm{a} \tag{6.3.7}$$

where the terms marked with carets are unit vectors in the direction of the relevant variable.

These can then be used to relate the two areas, A_m and A_μ, as follows. Note that as the vectors defining the areas are not necessarily perpendicular, the areas must be thought of as parallelograms, rather than rectangles. The sizes of the areas are therefore calculated using the magnitude of the cross product, as follows. For the two

vectors:

$$\boldsymbol{a} = a_1\hat{\boldsymbol{\imath}} + a_2\hat{\boldsymbol{\jmath}} \tag{6.3.8}$$

$$\boldsymbol{b} = b_1\hat{\boldsymbol{\imath}} + b_2\hat{\boldsymbol{\jmath}} \tag{6.3.9}$$

where $\hat{\boldsymbol{\imath}}$ and $\hat{\boldsymbol{\jmath}}$ are two arbitrary unit vectors, the cross product is defined as:

$$|\mathbf{a} \times \mathbf{b}| = a_1 b_2 - a_2 b_1 \tag{6.3.10}$$

The result is equal to the area of the parallelogram defined by the two vectors.[128] The area A_m can therefore be calculated as:

$$\begin{aligned}
A_\mathrm{m} &= |\mathbf{d}\boldsymbol{m_1} \times \mathbf{d}\boldsymbol{m_2}| \\
&= \left| \left[\left(\frac{\partial m_1}{\partial \mu_\mathrm{s}} \mathrm{d}\mu_\mathrm{s} \right) \hat{\boldsymbol{\mu}}_\mathrm{s} + \left(\frac{\partial m_1}{\partial \mu_\mathrm{a}} \mathrm{d}\mu_\mathrm{a} \right) \hat{\boldsymbol{\mu}}_\mathrm{a} \right] \times \left[\left(\frac{\partial m_2}{\partial \mu_\mathrm{s}} \mathrm{d}\mu_\mathrm{s} \right) \hat{\boldsymbol{\mu}}_\mathrm{s} + \left(\frac{\partial m_2}{\partial \mu_\mathrm{a}} \mathrm{d}\mu_\mathrm{a} \right) \hat{\boldsymbol{\mu}}_\mathrm{a} \right] \right| \\
&= \left| \left(\frac{\partial m_1}{\partial \mu_\mathrm{a}} \mathrm{d}\mu_\mathrm{a} \frac{\partial m_2}{\partial \mu_\mathrm{s}} \mathrm{d}\mu_\mathrm{s} \right) (\hat{\boldsymbol{\mu}}_\mathrm{s} \times \hat{\boldsymbol{\mu}}_\mathrm{a}) - \left(\frac{\partial m_1}{\partial \mu_\mathrm{s}} \mathrm{d}\mu_\mathrm{s} \frac{\partial m_2}{\partial \mu_\mathrm{a}} \mathrm{d}\mu_\mathrm{a} \right) (\hat{\boldsymbol{\mu}}_\mathrm{s} \times \hat{\boldsymbol{\mu}}_\mathrm{a}) \right| \\
&= \left(\frac{\partial m_1 \partial m_2}{\partial \mu_\mathrm{a}\, \partial \mu_\mathrm{s}} - \frac{\partial m_1 \partial m_2}{\partial \mu_\mathrm{s}\, \partial \mu_\mathrm{a}} \right) \mathrm{d}\mu_\mathrm{s} \mathrm{d}\mu_\mathrm{a} |\hat{\boldsymbol{\mu}}_\mathrm{s} \times \hat{\boldsymbol{\mu}}_\mathrm{a}| \\
&= \left(\frac{\partial m_1 \partial m_2}{\partial \mu_\mathrm{a}\, \partial \mu_\mathrm{s}} - \frac{\partial m_1 \partial m_2}{\partial \mu_\mathrm{s}\, \partial \mu_\mathrm{a}} \right) |\mathbf{d}\boldsymbol{\mu}_\mathrm{s} \times \mathbf{d}\boldsymbol{\mu}_\mathrm{a}| \\
&= J A_\mu
\end{aligned} \tag{6.3.11}$$

The Jacobian determinant therefore relates the two areas, A_m and A_μ, as follows:

$$J = \frac{\partial m_1 \partial m_2}{\partial \mu_\mathrm{a}\, \partial \mu_\mathrm{s}} - \frac{\partial m_1 \partial m_2}{\partial \mu_\mathrm{s}\, \partial \mu_\mathrm{a}} \tag{6.3.12}$$

$$= \frac{A_\mathrm{m}}{A_\mu} \tag{6.3.13}$$

The relevance of this result can be seen by defining the lengths of vectors $\mathbf{d}\boldsymbol{m_1}$ and $\mathbf{d}\boldsymbol{m_2}$ as the magnitude of the errors in each of the metrics. As a result, A_m and

A_μ represent the relative sizes of errors in each co-ordinate system. It can therefore be seen that a large Jacobian determinant will minimise the errors in a medium's calculated scattering and absorption coefficients.

A metric pair's resilience to noise is therefore dependent on the magnitude of their Jacobian determinant. An estimate of this magnitude can be made visually by calculating the Jacobian determinant using a different definition of the cross product as follows. For two vectors, $\mathbf{a}$ and $\mathbf{b}$, the magnitude of their cross product can be defined as:

$$|\mathbf{a} \times \mathbf{b}| = |\mathbf{a}||\mathbf{b}| \sin\theta \tag{6.3.14}$$

where θ is the angle between the two vectors. Defining two metric surfaces' gradients as the vectors $\nabla \boldsymbol{m_1}$ and $\nabla \boldsymbol{m_2}$:

$$\nabla \boldsymbol{m_1} = \frac{\partial m_1}{\partial \mu_\mathrm{s}} \hat{\boldsymbol{\mu}}_\mathrm{s} + \frac{\partial m_1}{\partial \mu_\mathrm{a}} \hat{\boldsymbol{\mu}}_\mathrm{a} \tag{6.3.15}$$

$$\nabla \boldsymbol{m_2} = \frac{\partial m_2}{\partial \mu_\mathrm{s}} \hat{\boldsymbol{\mu}}_\mathrm{s} + \frac{\partial m_2}{\partial \mu_\mathrm{a}} \hat{\boldsymbol{\mu}}_\mathrm{a} \tag{6.3.16}$$

the Jacobian determinant can be calculated using Eq. (6.3.14) as:

$$J = |\nabla \boldsymbol{m_1} \times \nabla \boldsymbol{m_2}| = |\nabla \boldsymbol{m_1}||\nabla \boldsymbol{m_2}| \sin\theta \tag{6.3.17}$$

which is equal to Eq. (6.3.12). It can therefore be seen that the Jacobian determinant is large when the gradients are large and orthogonal. The relevance of this can be seen by considering the contour plots of the two metric surfaces in Figure 6.1. In this form, the magnitude of the gradients can be determined from the proximity of

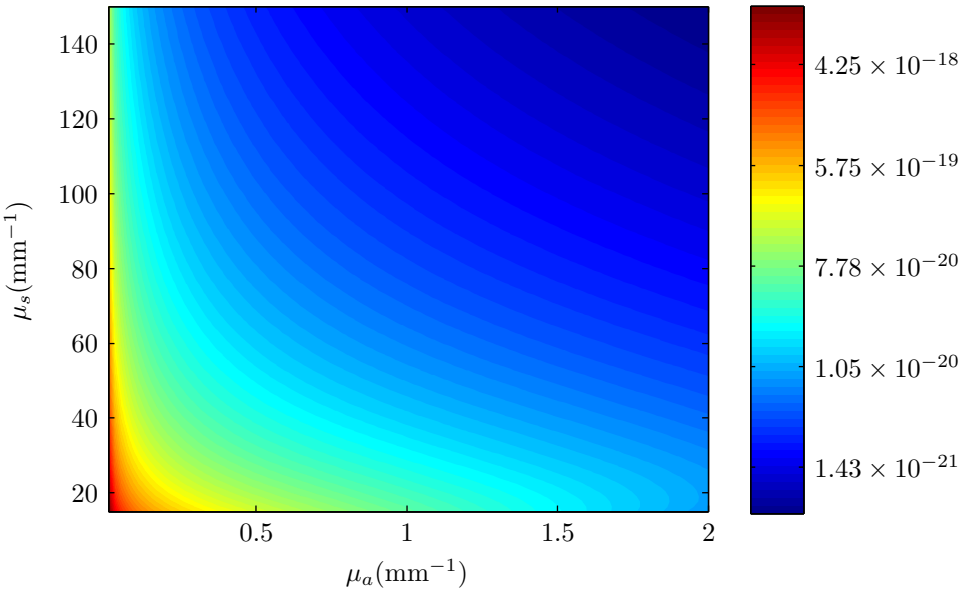

Figure 6.3: The Jacobian determinant surface for the metrics shown in Figure 6.1. The figure uses a logarithmic colour axis for clarity.

consecutive contours. As contours are perpendicular to a surface's gradient, their orthogonality is equal to the orthogonality of the gradients.

The resulting Jacobian determinant surface from these two metric surfaces is shown in Figure 6.3. It is greatest in the bottom left quadrant as the corresponding contours are close together and orthogonal. As a result, a small change in one of the metrics in Figure 6.1 will have a minimal effect on the position of the crossing point and therefore the corresponding values of μ_s and μ_a. The top left and top right regions, however, are limited by near-parallel and shallow gradients respectively, and so a small change in the value of a metric will result in a large error in the coefficients, leading to a smaller value of the Jacobian determinant.

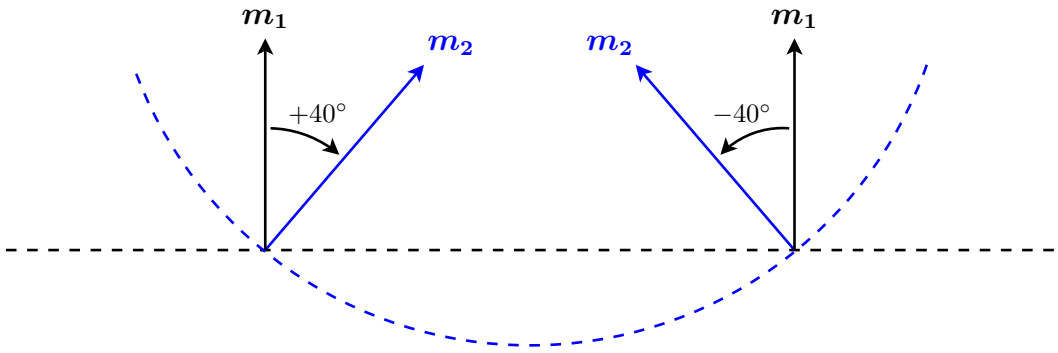

Figure 6.4: Two gradient vectors (as solid lines) for two metrics at two different points. The corresponding contours are shown as dashed lines. The vectors, and therefore the gradients) are chosen to be co-planar for clarity.

6.3.2.1 Solution Uniqueness

Another important factor in determining the optimum metric pair is the uniqueness of the solution to the medium's scattering and absorption coefficients over the range of metric values: a metric pair is unsuitable if there exists a pair of measurements that corresponds to multiple solutions to the medium's coefficients. As a coefficient solution occurs at the crossing point of two surfaces' contours, multiple solutions will therefore occur if any contour pair between the two surfaces cross more than once.

This can be determined using the sign of the Jacobian determinant, as it is a measure of the direction of the surfaces' gradients (or contours) relative to each other at each point on the metric surfaces. As an example, Figure 6.4 shows two gradient vectors (as solid lines) for two metrics at two different points. The corresponding contours are shown as dashed lines. The vectors (and therefore the gradients) are

chosen to be co-planar for clarity. It can be seen that $\boldsymbol{m_2}$ has reversed its horizontal direction relative to $\boldsymbol{m_1}$ between the two points of interest. As a result, the contour corresponding to $\boldsymbol{m_2}$ crosses the contour for $\boldsymbol{m_1}$ twice. This change in direction is marked by a change of sign on the angle between the two vectors, and thus a change of sign on the Jacobian determinant. This change of sign is therefore an indication that unique solutions do not exist for such a metric pair.[129]

6.3.2.2 Resilience to Scaling Factors

In contrast to the error analysis equations, it can be seen from Eq. (6.3.12) that the Jacobian determinant is not resilient to scaling factors, and thus cannot be compared for metrics of different units. As it is not analysed in isolation from the error analysis in this thesis, this feature is unimportant. However, if the Jacobian determinant is to be analysed in more detail, this resilience can be achieved, with no effect on the final calculated error, by performing the error analysis on the logarithm of each metric, as shown in Appendix B.

6.4 Optimum Metrics for Full-field Detection

The error analysis equations defined in Eqs. (6.3.3) and (6.3.4) can now be applied to the case of full-field detection using the streak camera described in Chapter 5. This will result in values for the errors in the scattering and absorption coefficients over the range of the medium's "true" coefficient values. The metric pair's suitability for the

characterisation of a medium is dependent on the error values over the entire range, as will be discussed later.

As explained in §5.5.4.1, it was necessary to calculate the errors in the metric values for discrete values of the medium's coefficients. Therefore, the errors in the coefficients calculated using the error analysis equations are also at discrete points over the surface.

Before calculating the errors in the medium's characterisation, it is first necessary to define the metrics' analytical solutions over the parameter ranges. This was done using the Diffusion Approximation equations from §3.3 to give the metric surfaces shown in Figure 6.5. The forms of these surfaces were discussed in detail in §4.4.

Only the reflectance and first five cumulants are used in this error analysis as it will be shown that these are sufficient to determine the optimum metrics. This also allowed the forms of the metrics and the results of the error analysis to be shown and analysed comprehensively. The six metrics therefore led to a total of 15 metric pair combinations (calculated in combinatorial mathematics using ${}_6C_2$). All these pairs passed the test for uniqueness using the Jacobian determinant as described in §6.3.2.1.

6.4.1 Errors in the Absorption Coefficient

It is possible for each metric pair to give very different results for the errors in the scattering and absorption coefficents of a medium. As specific applications of media

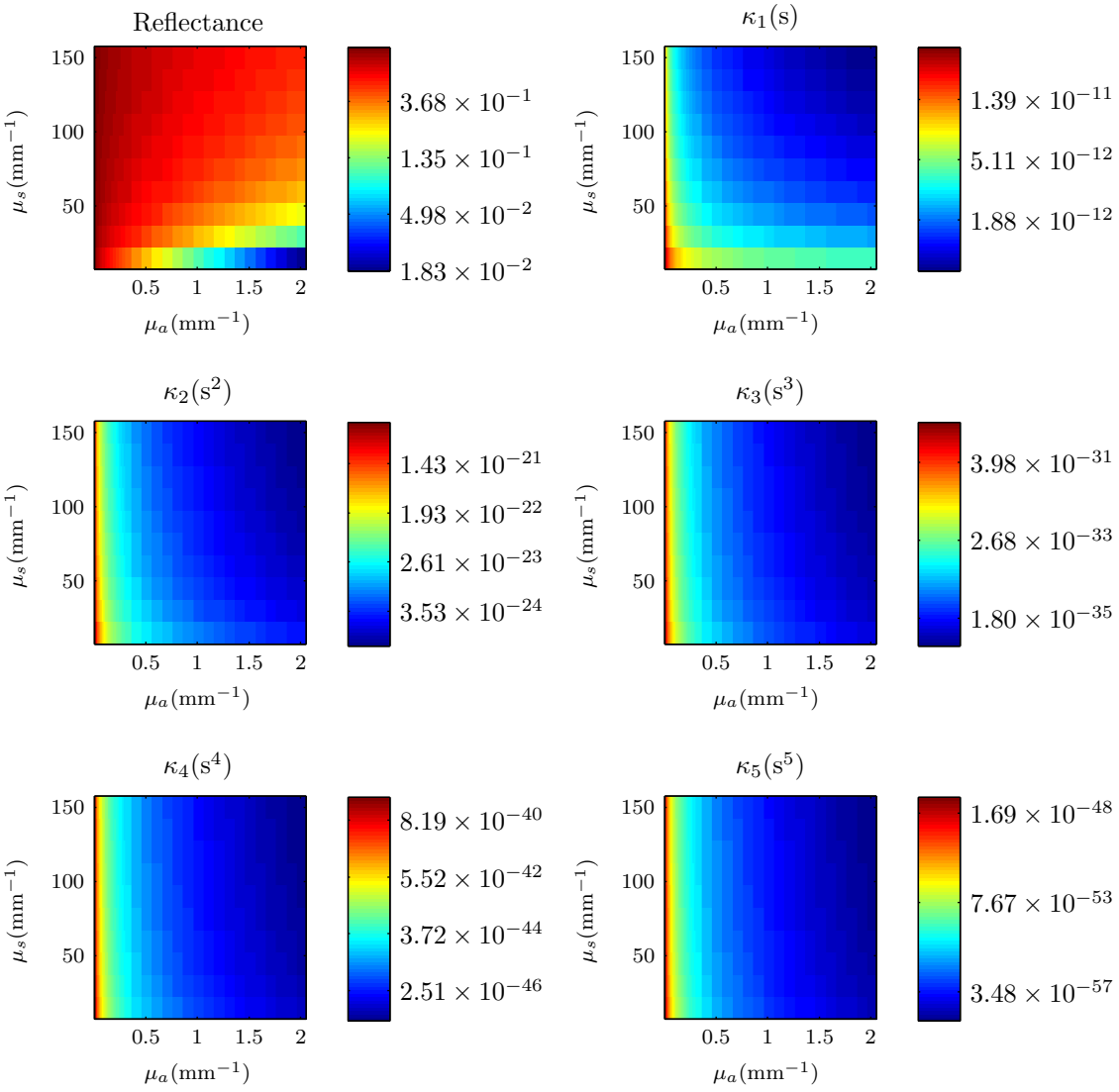

Figure 6.5: Analytical solutions to the metrics of interest as calculated using the Diffusion Approximation for full-field detection. The figures use a logarithmic colour axis for clarity.

characterisation may require varying precisions for these coefficients, it is useful to consider the errors separately. This section will therefore deal with the error in the absorption coefficient.

The errors in the metrics for each metric pair (δm_1 and δm_2 in the error analysis equations) were calculated using the streak camera error maps shown in Figure 5.35. These maps are defined by their mean (μ) and standard deviation (σ) and so the errors used for each metric were calculated as ($\mu + \sigma$) and ($\mu - \sigma$). For each metric pair there are therefore four different combinations of errors:

$$\begin{aligned} \delta m_1 &= \mu_1 + \sigma_1, \quad & \delta m_2 &= \mu_2 + \sigma_2 \\ \delta m_1 &= \mu_1 + \sigma_1, \quad & \delta m_2 &= \mu_2 - \sigma_2 \\ \delta m_1 &= \mu_1 - \sigma_1, \quad & \delta m_2 &= \mu_2 + \sigma_2 \\ \delta m_1 &= \mu_1 - \sigma_1, \quad & \delta m_2 &= \mu_2 - \sigma_2 \end{aligned} \tag{6.4.1}$$

Each of these four combinations was applied to the error analysis equation, and the worst resultant error in the absorption coefficient used for each point in the parameter space.

The values of the partial derivatives in the error analysis equations were calculated analytically from the Diffusion Approximation equations in §3.3.

The errors in the absorption coefficient for the 15 metric pairs are therefore shown in Figures 6.6 and 6.7. It can be seen that these surfaces do not follow the forms of the metric surfaces in Figure 6.5 as it is the differentials of these surfaces that are

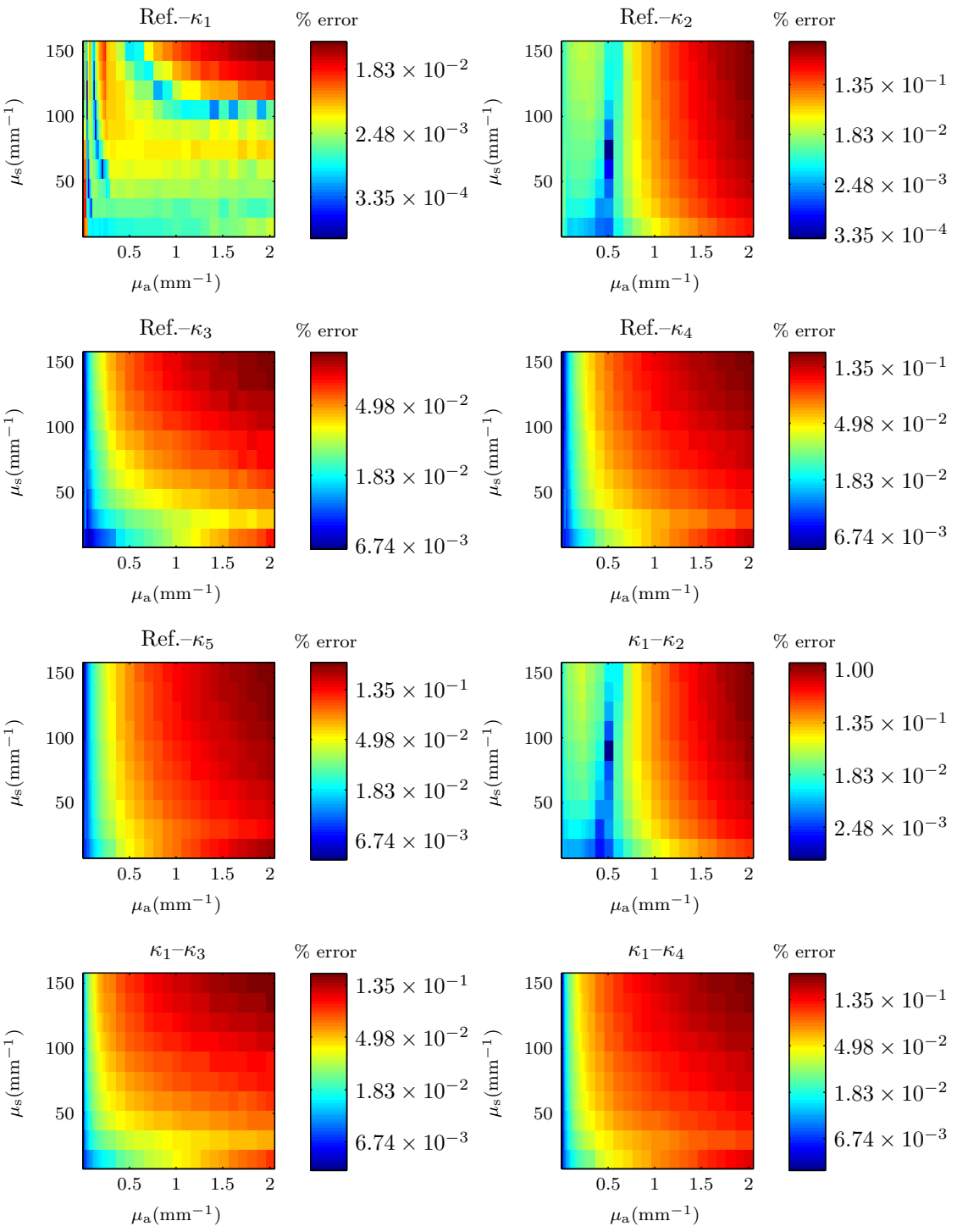

Figure 6.6: The errors in the absorption coefficient determined using the errors in metrics due to a streak camera for eight metric pairs using full-field detection. The figures use a logarithmic colour axis for clarity.

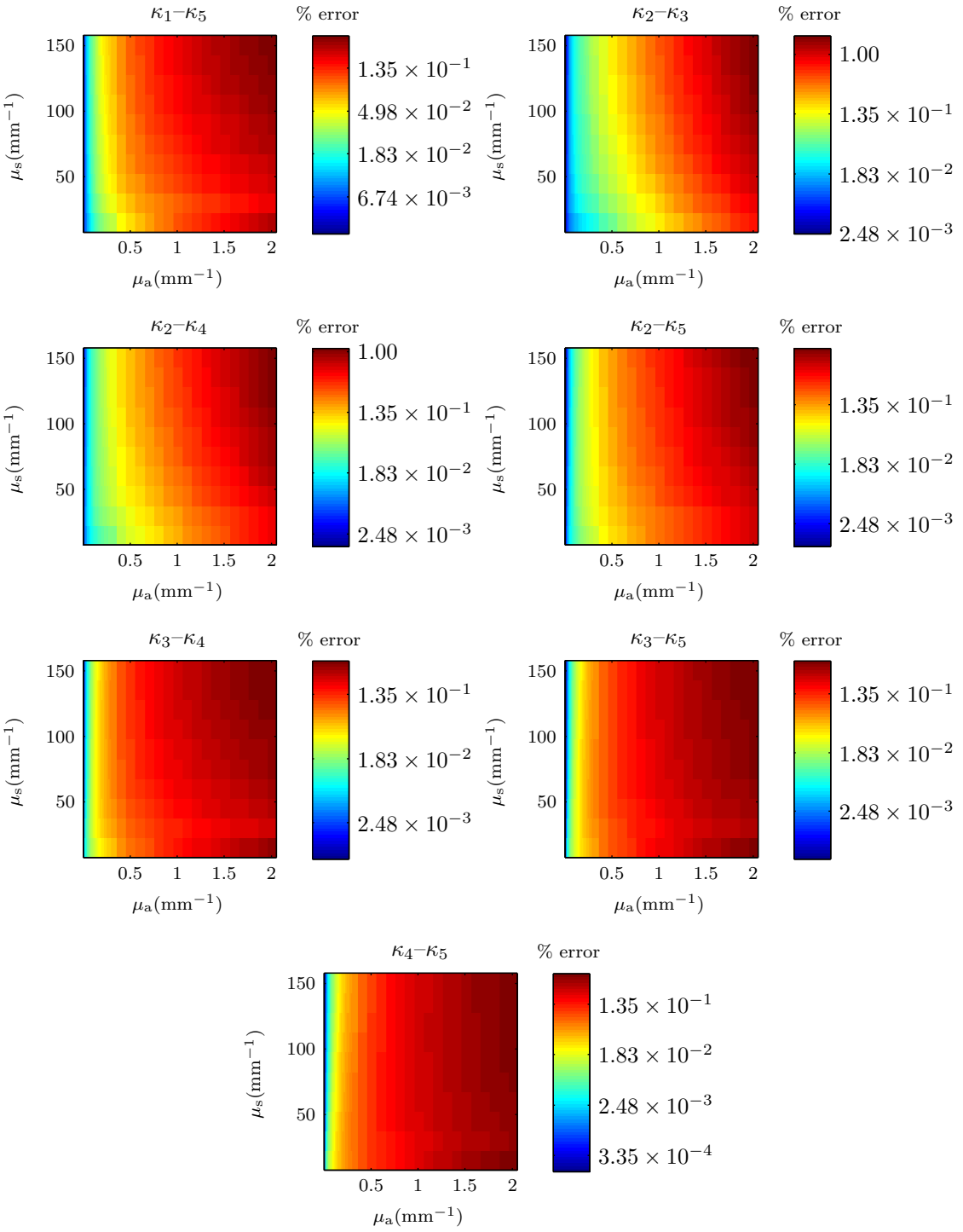

Figure 6.7: The errors in the absorption coefficient determined using the errors in metrics due to a streak camera for a further seven metric pairs using full-field detection. The figures use a logarithmic colour axis for clarity.

relevant to the error analysis. The plots can instead be described due to three effects.

Firstly, the surfaces contain characteristics of the streak camera error maps shown in Figure 5.35. More specifically, each metric pair surface has the characteristics of the error map relating to the metric of the pair with the largest error. Thus the Reflectance–κ_1 surface contains the "valleys" from the error map for the first cumulant as its error map generally has larger values than that of the reflectance.

Secondly, the errors will be much higher in the top right quadrant of the surfaces. This is because, in this region, the Jacobian determinant will be very small due to the shallow gradients of the metric surfaces in Figure 6.5. An example of this can be seen in Figure 6.3. This effect will be more prominent on the Jacobian determinant surfaces of metric pairs that do not involve the reflectance, as the gradients will also lack orthogonality in the top right quadrant.

Thirdly, the error in μ_a is proportional to the differentials of both metrics with μ_s. From the metric surfaces shown in Figure 6.5, the metric pair error surfaces containing the reflectance will therefore show a larger error in the absorption coefficient in the bottom right quadrant. The metric pair error surfaces are therefore explained by a combination of these effects.

In order to determine which of the metric pairs is the optimum over the chosen parameter range, it is necessary to look at the errors over the entirety of each metric pair surface shown in Figures 6.6 and 6.7. This can be done using a histogram of each

surface's errors, as shown in Figures 6.8 and 6.9. The mean error for each metric pair is shown in the top-right corner of the corresponding histogram. It can be seen that different metric pairs result in different error distribution shapes. The Reflectance–κ_2 pairing, for instance, has the bulk of its errors close to one value, with small numbers of instances with a significantly larger error. The Reflectance–κ_3 surface, on the other hand, has a much more even spread of error values with no significant outliers. This can be an important factor in the selection of an optimum pair, as will be discussed in more detail for the errors in scattering coefficient in §6.4.2.

In this case, however, it is clear that the Reflectance–κ_1 pairing gives both the smallest mean (0.005mm^{-1}) and maximum (0.044mm^{-1}) errors out of all the surfaces, thus making the spread of its values less relevant. This is therefore the optimum metric pair for the determination of the absorption coefficient in full-field detection mode using the streak camera described in Chapter 5.

The significance of this result can be assessed by considering an application of this characterisation. One such application is the differentiation of healthy and malignant breast tissues, for which Nair et al.[130] estimated the absorption coefficients of the healthy and malignant tissue to be 0.063mm^{-1} and 0.06mm^{-1} respectively. It is therefore clear that the mean error given by this optimum metric using full-field detection is not small enough to distinguish these two types of tissue, and therefore this approach is inadequate for such an application.

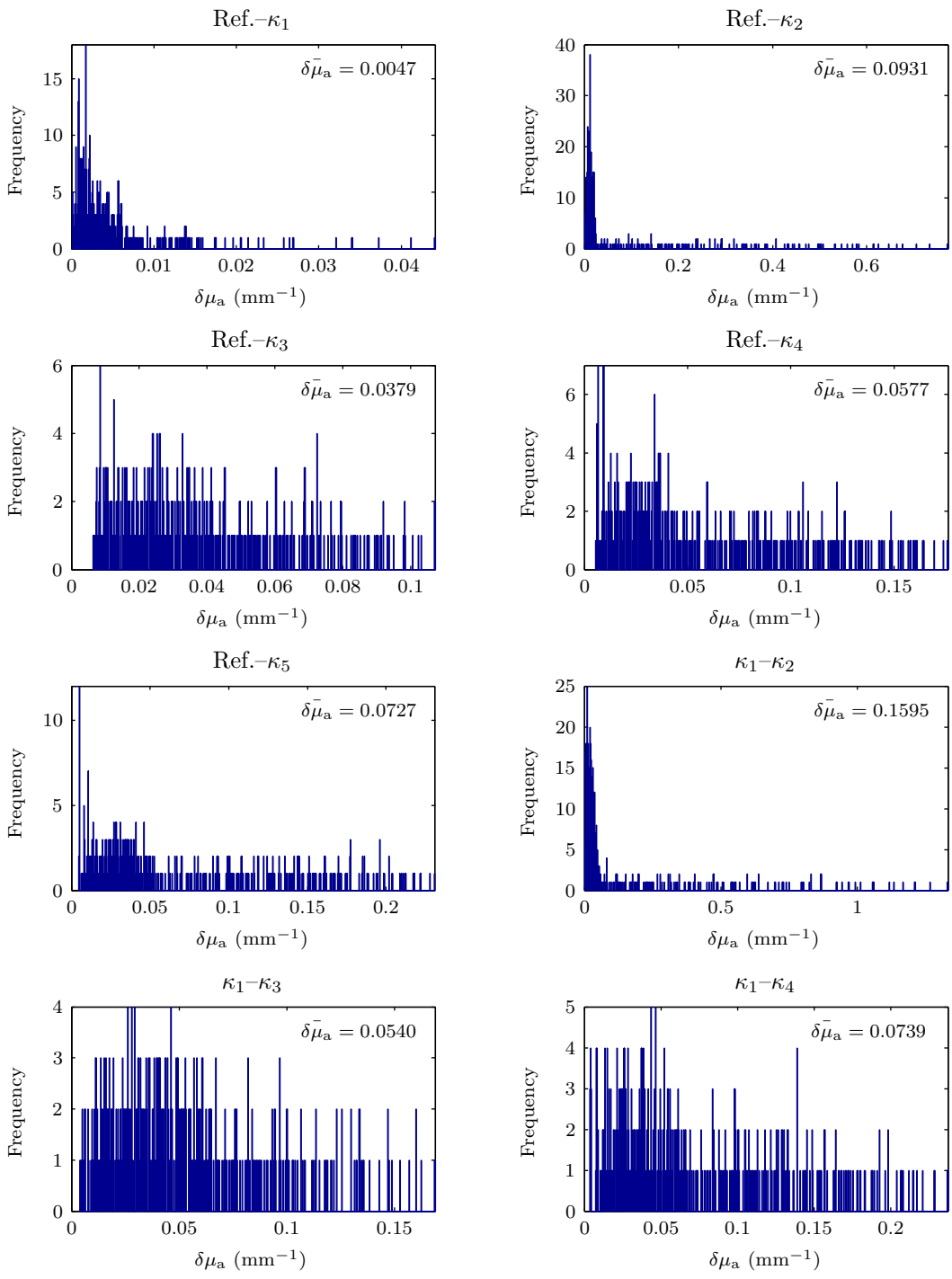

Figure 6.8: Histograms of the errors in the absorption coefficient over each of the metric pair surfaces in Figure 6.6. The limit of the x-axis represents the maximum error for each metric pair. The mean error for each metric pair is shown in the top-right corner of the pair's histogram.

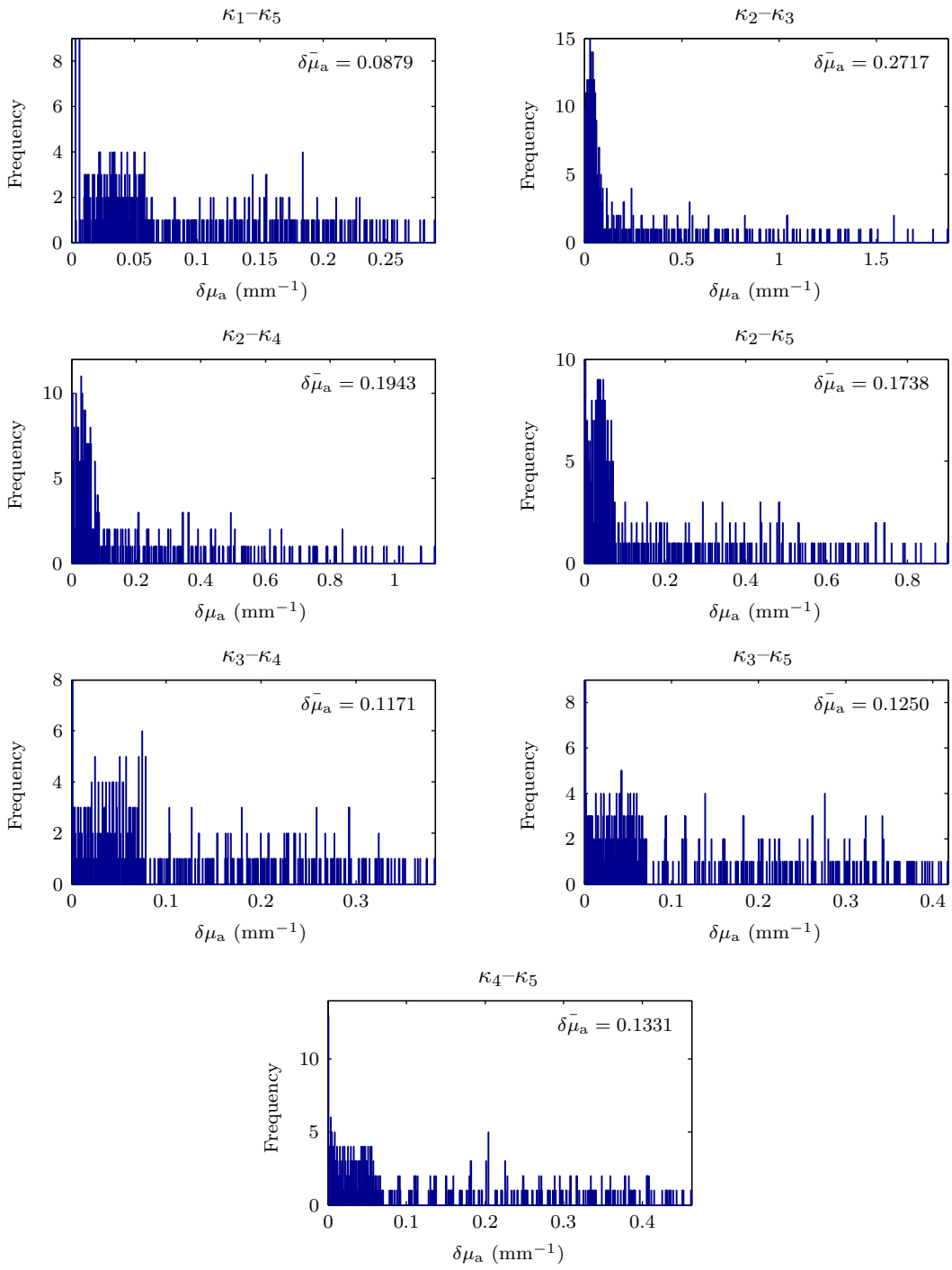

Figure 6.9: Histograms of the errors in the absorption coefficient over each of the metric pair surfaces in Figure 6.7. The limit of the x-axis represents the maximum error for each metric pair. The mean error for each metric pair is shown in the top-right corner of the pair's histogram.

Reflectance measurements can be difficult to perform, however, as they require an exact measurement of the amount of light that physically enters the medium, as opposed to the amount of light merely incident on its surface, as well as measurements of absolute intensity which can be difficult to perform due to problems such as source fluctuations and surface coupling.[60] Therefore, if this metric was discounted for reasons of feasibility, the optimum metric pair would be κ_1–κ_3, with a mean error of approximately 0.05mm^{-1}. As this error is ten times worse than that of the Reflectance–κ_1 pairing, it is possible that steps taken to retain the ability to perform reflectance measurements may be well justified.

Perhaps surprising is the resilience to noise exhibited by the metric pairs containing higher-order cumulants. In general, the error in the absorption coefficient will increase as higher-order cumulants are used, with the κ_1–κ_5 pairing giving a mean error of approximately 0.09mm^{-1}, less than double that of the κ_1–κ_3 metric pair.

The exception to this rule, however, is the second cumulant which is heavily affected by the streak camera's temporal dispersion. At high absorption and scattering levels, the error in this metric is significant, as can be seen in Figure 5.35. As a result, any pairing containing this metric will contain outliers corresponding to this region with high values of error in the absorption coefficient.

6.4.2 Errors in the Scattering Coefficient

The errors in the scattering coefficient for the same 15 metric pairs are shown in Figures 6.10 and 6.11. Their forms can be described by the same three effects as the error in the absorption coefficent. However, in this case, the error result is proportional to the differentials of both metrics with μ_a. As a result, it can be seen from the metric surfaces shown in Figure 6.5, that the metric pair error surfaces will therefore show a larger error in the scattering coefficient on the left hand region of the surface where the metric gradients are larger. This is especially true of the cumulants, due to their significant variation with μ_a at low absorption levels. This explains the large increase in error that can be seen on the very left of the Reflectance–κ_3, Reflectance–κ_4 and Reflectance–κ_5 surfaces.

The higher order metric pairs (κ_2–κ_3 and above) can also be seen to exhibit sharp dips in their errors at low absorption levels. This is, in fact, merely the error in the scattering coefficient changing from positive to negative (as the absorption increases) – due to the logarithmic colour axes, it was necessary to work with the absolute values of the errors.

The histogram of each surface's errors are shown in Figures 6.12 and 6.13. In this case, it can be seen that the shape of the error distributions are particularly relevant in determining the optimum metric pair: the Reflectance–κ_1 pairing gives an error of less than 10mm^{-1} over 95% of the surface. However, there is also a possibility of

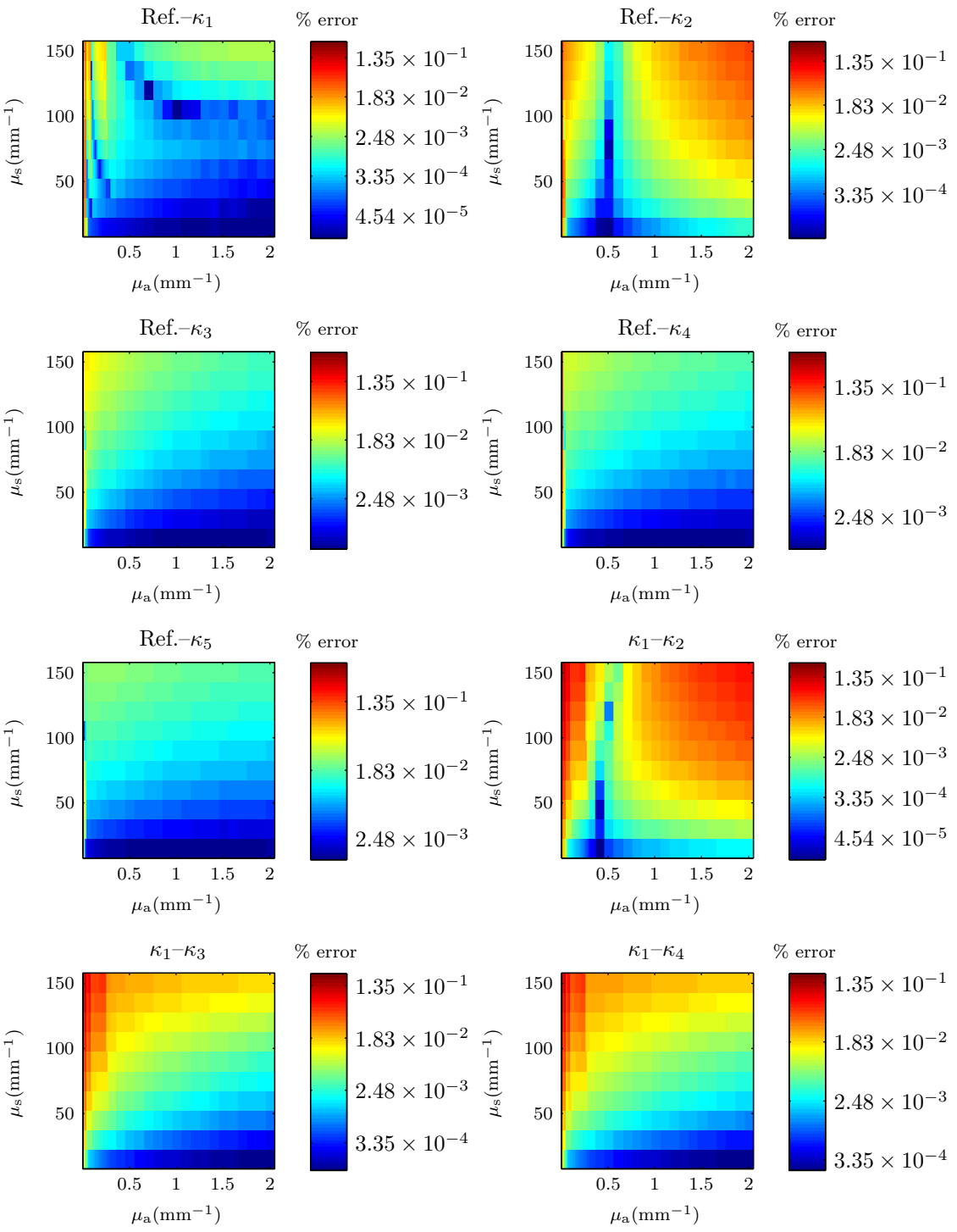

Figure 6.10: The errors in the scattering coefficient determined using the errors in metrics due to a streak camera for eight metric pairs using full-field detection. The figures use a logarithmic colour axis for clarity.

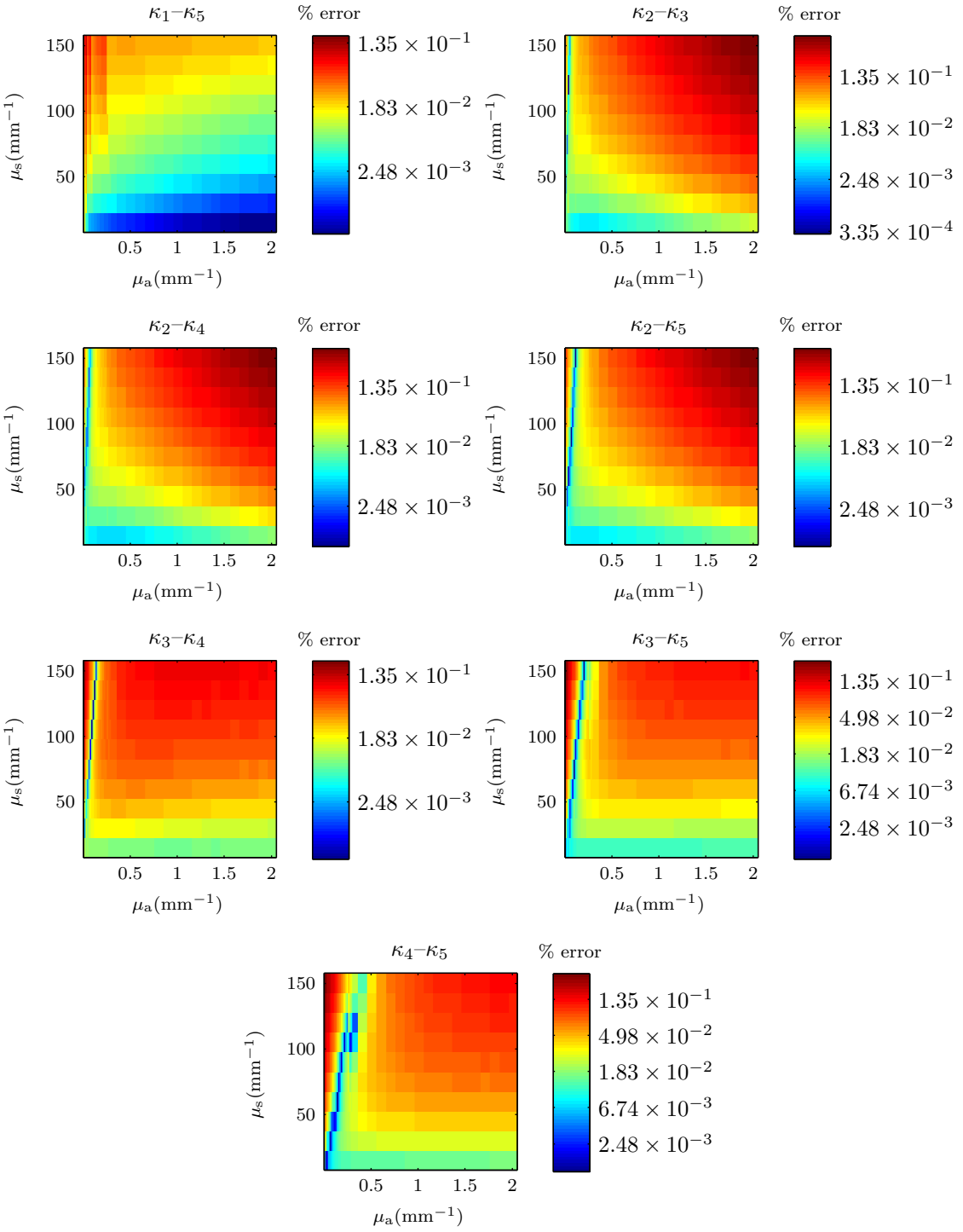

Figure 6.11: The errors in the scattering coefficient determined using the errors in metrics due to a streak camera for a further seven metric pairs using full-field detection. The figures use a logarithmic colour axis for clarity.

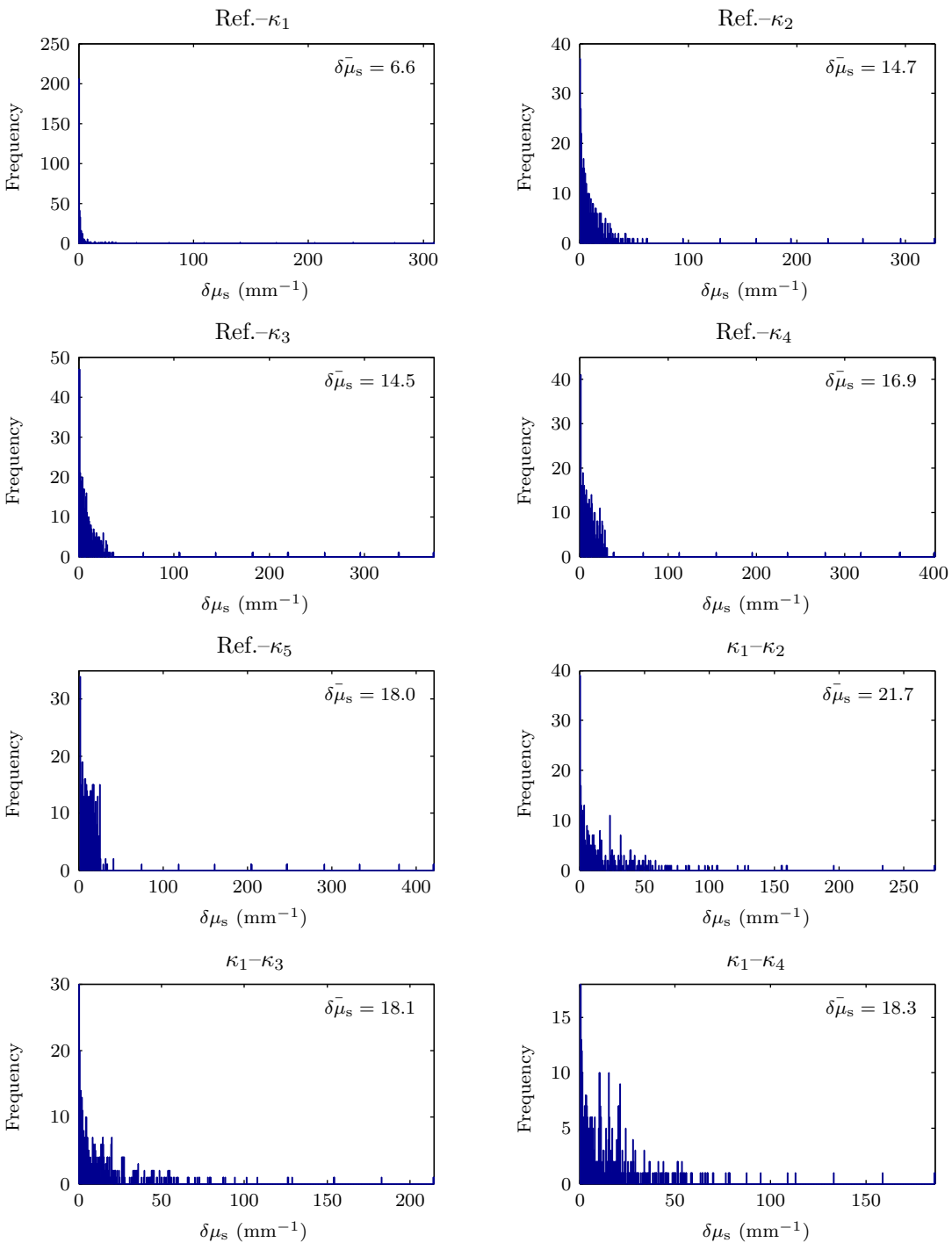

Figure 6.12: Histograms of the errors in the scattering coefficient over each of the metric pair surfaces in Figure 6.10. The limit of the x-axis represents the maximum error for each metric pair. The mean error for each metric pair is shown in the top-right corner of the pair's histogram.

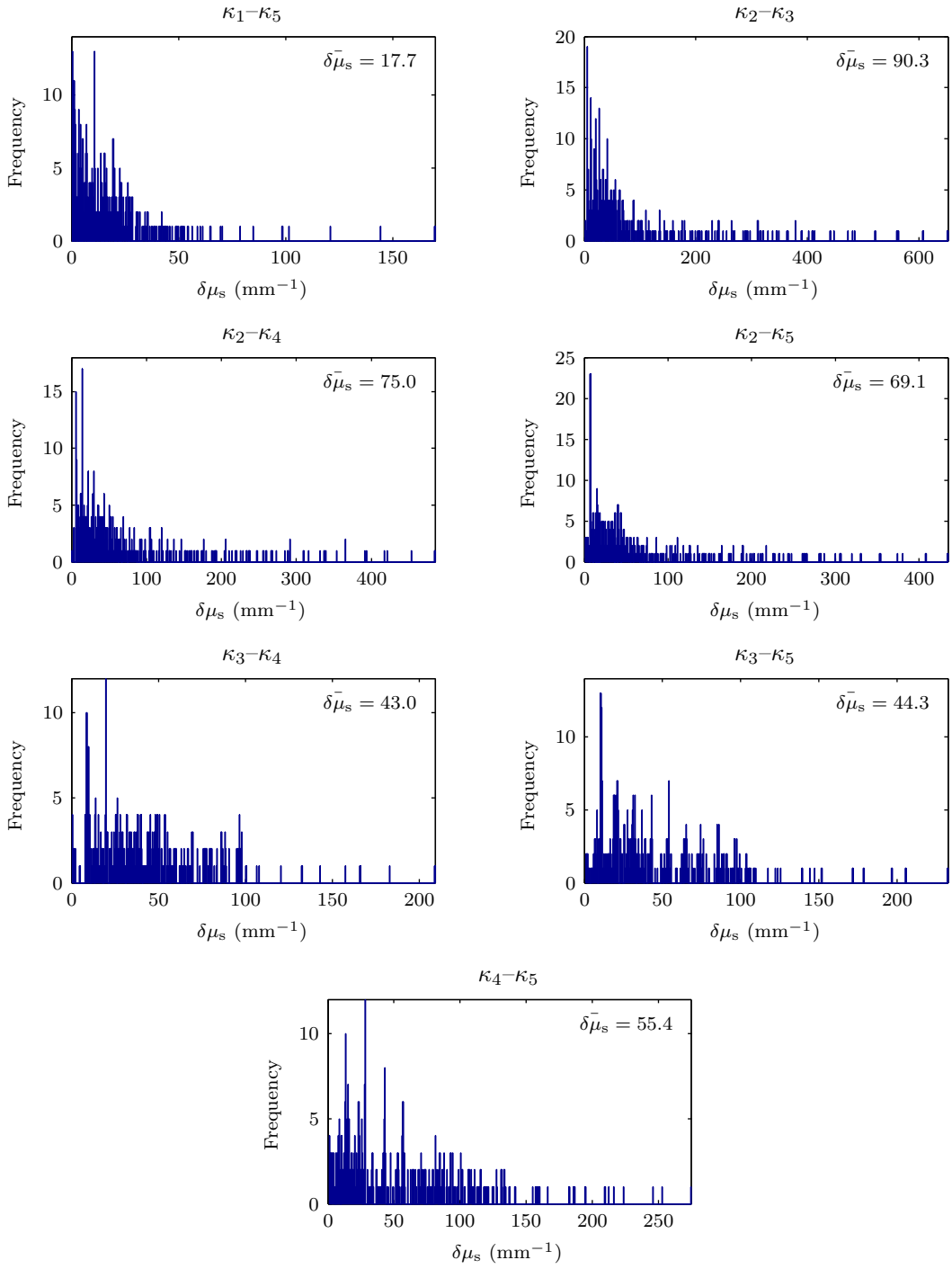

Figure 6.13: Histograms of the errors in the scattering coefficient over each of the metric pair surfaces in Figure 6.11. The limit of the x-axis represents the maximum error for each metric pair. The mean error for each metric pair is shown in the top-right corner of the pair's histogram.

the error being as high as around 310mm^{-1}. The κ_1–κ_5 pairing, meanwhile, gives an error of under 50mm^{-1} over a large majority of the surface, but can give a maximum error of just 170mm^{-1}. The selection of the "optimum" metric pair is therefore a question of application, and whether a larger average error can be tolerated in exchange for a smaller maximum error. In the absence of such an upper limit on the error, it can be seen that once again, the optimum pair for the determination of the scattering coefficient is the Reflectance–κ_1 pairing, with a mean error of around 7mm^{-1}. However, for the application considered earlier – the differentiation of healthy and malignant breast tissue – it can be seen that none of the possible pairings provide enough accuracy: the scattering coefficients of these two tissues, estimated by Nair et al.[130] at 2.3mm^{-1} and 2.8mm^{-1} respectively, cannot be distinguished using any of the possible pairings in full-field detection.

In contrast to the error in the absorption coefficient, metric pairs involving the second cumulant do not produce a large increase in the error in the scattering coefficient: it can be seen from the second cumulant's error map in Figure 5.35 that the error in the metric due to the streak camera is large when both the absorption and scattering levels are high. However, the change in the second cumulant with the absorption coefficient ($\frac{\partial \kappa_2}{\partial \mu_a}$), to which the calculation of the error in μ_s is proportional, is small in this region, as can be seen in Figure 6.5. This therefore limits the maximum error in the scattering coefficient.

It should be noted that if an estimate of the medium's characteristics is already known by an alternative analysis method or *a priori* information, this analysis can be performed on an appropriate region of the metric pair error surfaces, rather than over the entire parameter range. This will result in different histograms, and potentially a different optimum metric pair. As an example of this, consider the $\delta\mu_s$ surfaces in Figures 6.10 and 6.11. If the absorption coefficient is known to be less than 0.5mm^{-1}, the error analysis equations therefore need only to be applied to the left hand sides of the surfaces to produce the histograms in Figures 6.14 and 6.15. As above, the Reflectance–κ_1 pairing gives the smallest mean error, but gives a small probability of an error of 310mm^{-1}. However, in this case, the κ_2–κ_3 metric pair gives a maximum error of only 120mm^{-1}, less than half that of the same metric pair without the use of *a priori* information.

6.5 Optimum Metrics for Spatially Resolved Detection

The methods used in the previous section can now be applied to the case of spatially resolved detection. This raises two issues. Firstly, as demonstrated in Figure 5.34, for large scattering and absorption levels, the TPSF's peak light levels will be smaller than the system's noise floor and as a result, the TPSF will not be detected by the streak camera. This effect will become more substantial as the source–detector distance increases. This is demonstrated by Figure 6.16: the regions in which the

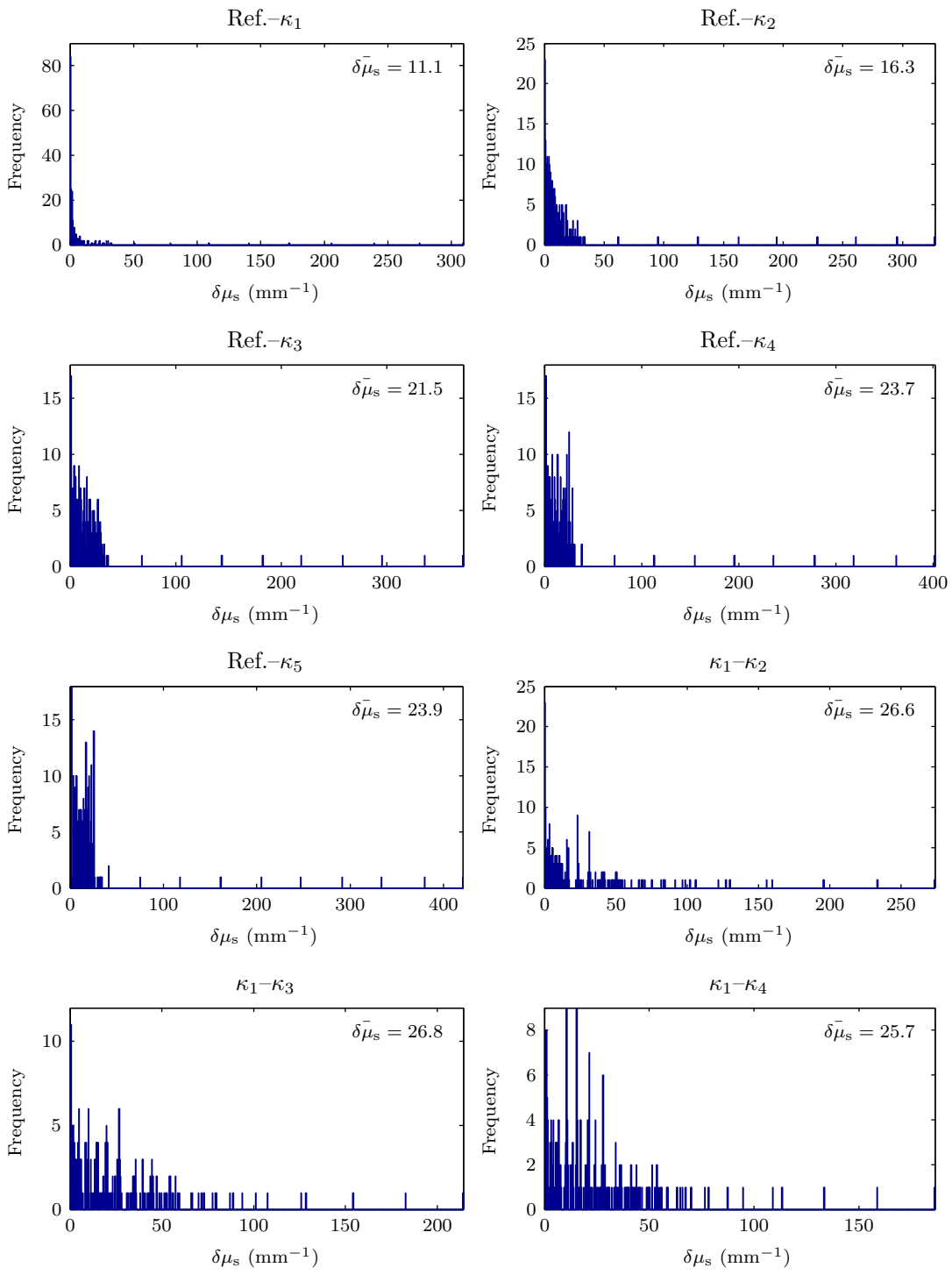

Figure 6.14: Histograms of the errors in the scattering coefficient over the left hand region of each of the metric pair surfaces in Figure 6.10. The limit of the x-axis represents the maximum error for each metric pair. The mean error for each metric pair is shown in the top-right corner of the pair's histogram.

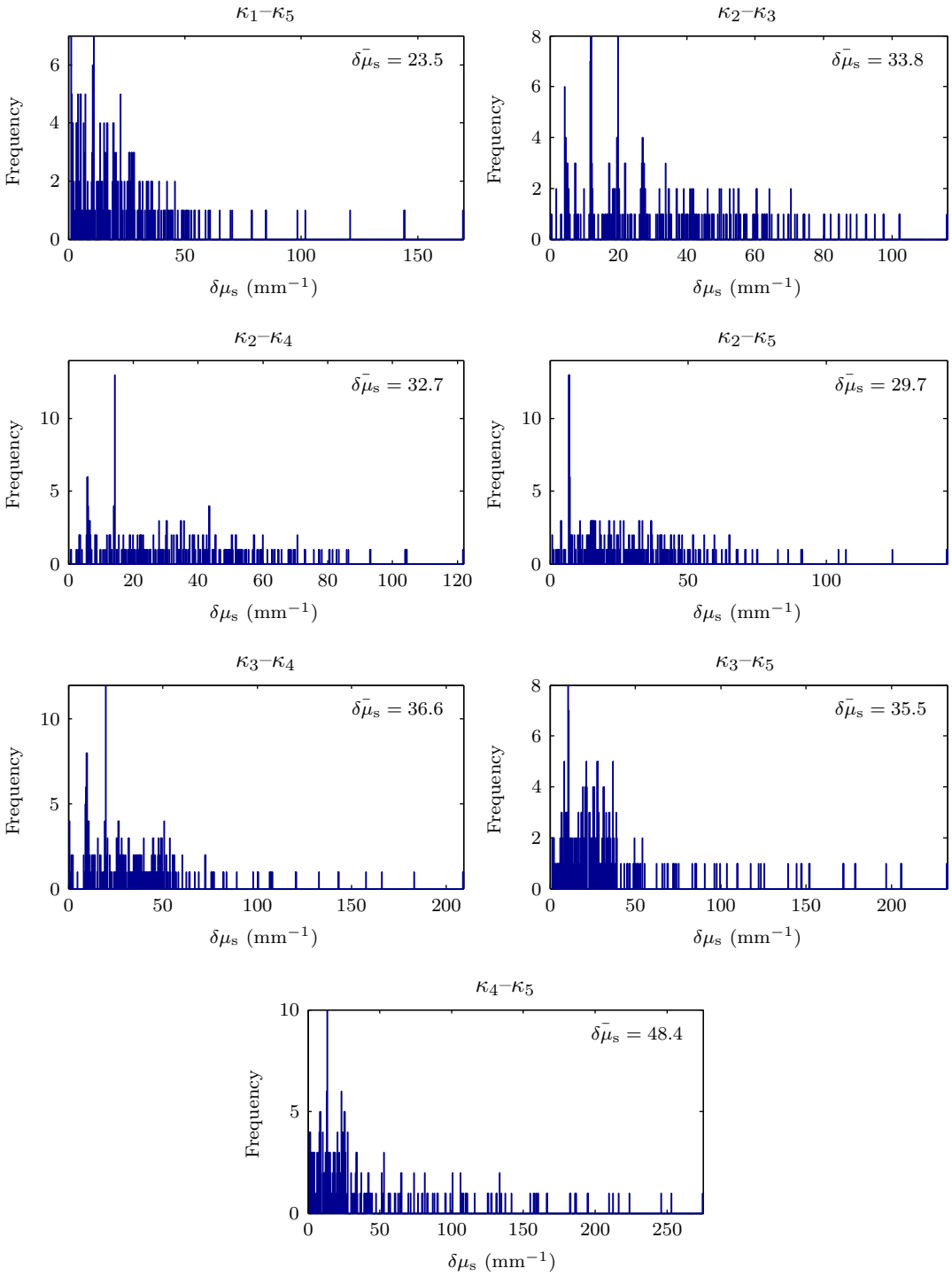

Figure 6.15: Histograms of the errors in the scattering coefficient over the left hand region of each of the metric pair surfaces in Figure 6.11. The limit of the x-axis represents the maximum error for each metric pair. The mean error for each metric pair is shown in the top-right corner of the pair's histogram.

TPSF can not be detected are shown in white for each of the ten annular detector regimes used in this study.

The consequence of this effect is that an assumption can be made about the range of a medium's optical properties as the result of its detection or non-detection using a particular annular detector. Put simply, for each annular detector range, if no TPSF is detected then it can be assumed that the medium's properties fall outside that annular detector's valid range shown in Figure 6.16. The validity of this assumption is dependent on the accuracy of the model used to produce these ranges.

Without an assumption as to the possible range of a medium's optical properties, it is clear from Figure 6.16 that spatially resolved measurements above ρ_1 could potentially lead to an inability to characterise the medium, as the medium's optical coefficients may lie outside that detector's valid range. An assumption about the range of the medium's optical properties, however, allows the use of spatially resolved measurements up to that source–detector distance. For example, the error analysis results for an annular detector of radii 5–6mm (ρ_6) may be compared to those of lower source–detector distances by the truncation of these results to match the valid range of ρ_6 shown in Figure 6.16. This approach cannot be applied the other way round, however: the full valid range of the ρ_2 error analysis cannot be compared to those of larger source–detector distances as they do not contain enough information. Due to the different parameter ranges for each possible assumption, it is therefore

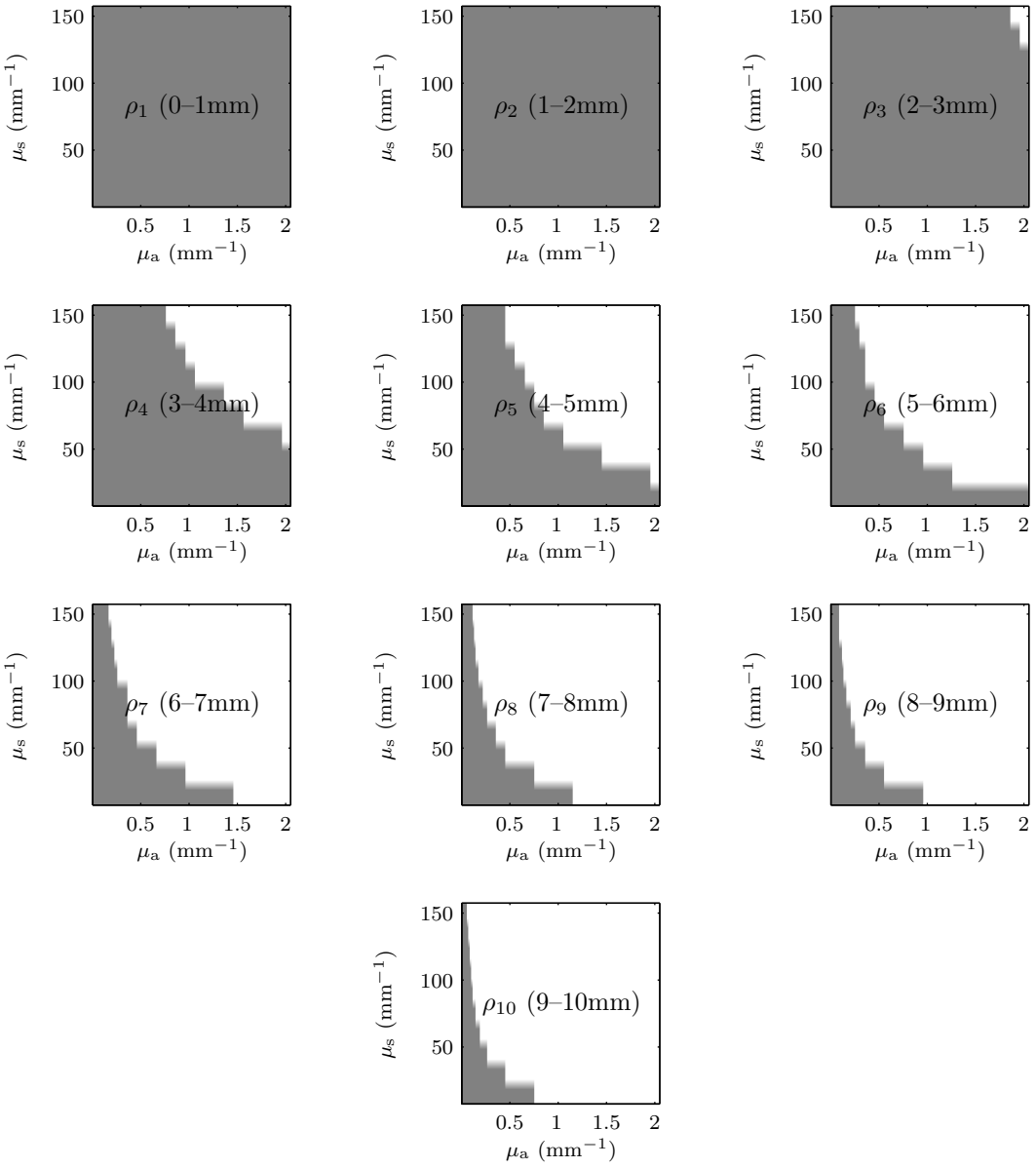

Figure 6.16: Maps of light detection for each annular detector. The regions in white mark the optical coefficients which result in TPSFs which can not be detected over the streak camera's noise floor.

necessary to perform a different error analysis for the valid parameter range of each source–detector distance.

The second issue that arises from the use of spatially resolved detection is the ten-fold increase in the metrics available with which the medium may potentially be characterised. The pairing of the metrics, combined with the need for multiple sets of error analyses as explained above, results in an unwieldy number of metric pair error surfaces to analyse graphically as carried out for full-field detection. The mean error will therefore be used in this case to determine the optimum error pair.

6.5.1 Errors in the Absorption Coefficient

The same methods were used here as for full-field detection: errors on the metrics were calculated using the streak camera model and then propagated through to give an error in the absorption coefficient. In this case, numerous metric pairs failed the test of uniqueness described in §6.3.2.1 and so were discarded as potential optimum pairs.

As previously explained, it is necessary to perform a different error analysis for each of the parameter ranges shown in Figure 6.16. (As ρ_1 and ρ_2 are both valid over the entire metric parameter range, they are considered together.) The results of this are shown in Table 6.1. It can be seen that, with no assumption about the medium's optical properties, the optimum metric pair to determine the absorption coefficient is the reflectance and first cumulant, both measured on-axis.

Table 6.1: Optimum metric pairs for the determination of μ_a

Assumed parameter range (see Fig. 6.16)	Optimum Metric Pair	Mean Error in μ_a (mm^{-1})
ρ_1 or ρ_2	Ref. (ρ_1) – κ_1 (ρ_1)	0.00469
ρ_3	Ref. (ρ_1) – κ_1 (ρ_1)	0.00460
ρ_4	Ref. (ρ_1) – Ref. (ρ_2)	0.00306
ρ_5	Ref. (ρ_1) – Ref. (ρ_2)	0.00231
ρ_6	Ref. (ρ_1) – Ref. (ρ_2)	0.00187
ρ_7	Ref. (ρ_1) – Ref. (ρ_3)	0.00125
ρ_8	Ref. (ρ_1) – Ref. (ρ_3)	0.00080
ρ_9	Ref. (ρ_3) – κ_1 (ρ_3)	0.00057
ρ_{10}	Ref. (ρ_3) – κ_1 (ρ_3)	0.00032

By making an assumption based on the ability of a particular annular detector's ability to detect the TPSF, however, this error can be reduced by the use of two reflectance measurements or reflectance and first cumulant measurements further from the source. The reduction in error in the determined coefficient as the assumption becomes more specific can be explained by the loss of those regions that result in larger errors.

It can be seen that without any assumption about a medium's optical properties, the mean error here is similar to that in the case of full-field detection, and thus there would be no advantage in using spatially resolved detection. However, the advantage of this latter detection regime lies in the use of the different annular detectors to first make assumptions about the medium's optical properties, allowing the mean error in

Table 6.2: Optimum metric pairs for the determination of μ_s

Assumed parameter range (see Fig. 6.16)	Optimum Metric Pair	Mean Error in μ_s (mm^{-1})
ρ_1 or ρ_2	Ref. (ρ_1) – Ref. (ρ_2)	1.42
ρ_3	Ref. (ρ_1) – Ref. (ρ_2)	0.00139
ρ_4	Ref. (ρ_3) – κ_1 (ρ_3)	0.93
ρ_5	Ref. (ρ_3) – κ_1 (ρ_3)	0.78
ρ_6	Ref. (ρ_3) – κ_1 (ρ_3)	0.67
ρ_7	Ref. (ρ_2) – κ_1 (ρ_3)	0.49
ρ_8	Ref. (ρ_2) – κ_1 (ρ_3)	0.31
ρ_9	Ref. (ρ_4) – κ_1 (ρ_3)	0.18
ρ_{10}	Ref. (ρ_4) – κ_1 (ρ_3)	0.10

determining the medium's absorption coefficient to be reduced. This can be demonstrated using the application previously mentioned of the differentiation of healthy and malignant breast tissue. Nair et al.[130] estimated that the absorption coefficients of both these tissues lay below $0.1mm^{-1}$, in which case the tissues would fall within one of the higher parameter ranges in Table 6.1. The mean error in the absorption coefficient would therefore be reduced sufficiently to allow the differentiation of the two tissues – Nair et al. estimated there was a $0.003mm^{-1}$ difference between healthy and malignant breast tissue.

6.5.2 Errors in the Scattering Coefficient

The optimum metrics for the determination of a medium's scattering coefficient can be calculated in a similar fashion to those for the absorption coefficient, and the results of the multiple error analyses are shown in Table 6.2. In this case, it can

be seen that multiple reflectance measurements provide the most accurate determination of the scattering coefficient in the absence of a prior assumption about the medium's properties. Off-axis reflectance and first cumulant measurements are then the optimum pairs for smaller assumed parameter ranges.

In the case of the determination of the scattering coefficient, it can be seen that even without any assumptions about a medium's optical properties, the mean error is still reduced by the use of spatially resolved detection over the full-field regime. This reduction is still not enough to differentiate between healthy and malignant breast tissue, however, which Nair et al.[130] estimated to have a difference of 0.5mm^{-1}. Like in the case of the determination of the absorption coefficient, the mean error is reduced by the use of assumptions made from the different annular detectors, although in this case, the tissue would have to be found to lie in one of the highest parameter ranges for the error to be reduced sufficiently to allow the tissue types to be differentiated.

6.6 Measurement Calibration

If the noise characteristics of a streak camera are known, the measured values of the recorded TPSF's metrics can be calibrated to take into account the known effects of their "detection" by a streak camera. This will have the effect of reducing the errors on the metrics, therefore reducing the error in the determined scattering and absorption coefficients. Due to the random nature of the processes within the camera, the errors in the metrics will have a finite distribution and so can not be calibrated

out exactly. However, the mean of these errors can be removed, leaving the errors on the metrics to be defined purely by their variation about the mean.

In practice, the actual errors in the metrics obtained using a streak camera can be estimated using either a comprehensive model of the camera, as in Chapter 5, or by the characterisation of the camera by performing measurements on test samples of known scattering and absorption parameters to produce the streak camera error maps.

The calibration process is demonstrated here using the streak camera model described in Chapter 5 in full-field detection mode. Part of the calculated errors were used to simulate the *known*, deterministic errors, found through either modelling or sample testing as explained above, while the rest were used as the *unknown*, stochastic errors added to the metrics by the streak camera in experimental use. In this case, the deterministic errors were those due to the truncation of the TPSF. This error is one of the biggest contributions to the errors in the streak camera model, as shown in §5.5.3.3, and so should also provide a large reduction in the errors in the determined scattering and absorption coefficients.

Two problems arise in the calibration process. Firstly, addition of the deterministic errors to the metric surfaces will change the surfaces' contours, thus potentially reducing the number of metric pairs that satisfy the uniqueness criteria described in

§6.3.2.1. Secondly, if the metric surfaces are defined using the Diffusion Approximation, their analytical form is lost by the calibration. The partial differentials of the metrics ($\frac{\partial m_1}{\partial \mu_a}$ etc.) must therefore be defined numerically. This can lead to large inaccuracies if the resolution of the μ_s-μ_a sample points used is low, as the differentials must then be calculated over large ranges of absorption and scattering coefficients (as shown in Figure 6.17) which is inappropriate in regions where the value of the metric changes sharply. One solution to this problem is demonstrated in Figure 6.18 which shows the calculation of each metric and deterministic error at four sub-points around each μ_s-μ_a sample point. This method enables more accurate estimates of the differentials to be calculated, although it requires an increased number of simulations or measurements.

The two problems explained above are made worse when the map of the deterministic errors contains discontinuities, like those seen in Figure 5.35 due to the change in the streak camera's sweep time. The lack of smooth form decreases the likelihood of a metric pair giving unique solutions, and the differentials will decrease in accuracy due to the sudden changes in the values of the calibrated metric between adjacent μ_s-μ_a sample points. In order to combat these effects, the streak camera will be modelled with a constant sweep time of 200ps in this demonstration of the calibration process.

The error maps of the deterministic truncation errors are therefore shown in Figure 6.19. It can be seen that the error increases significantly at low absorption values,

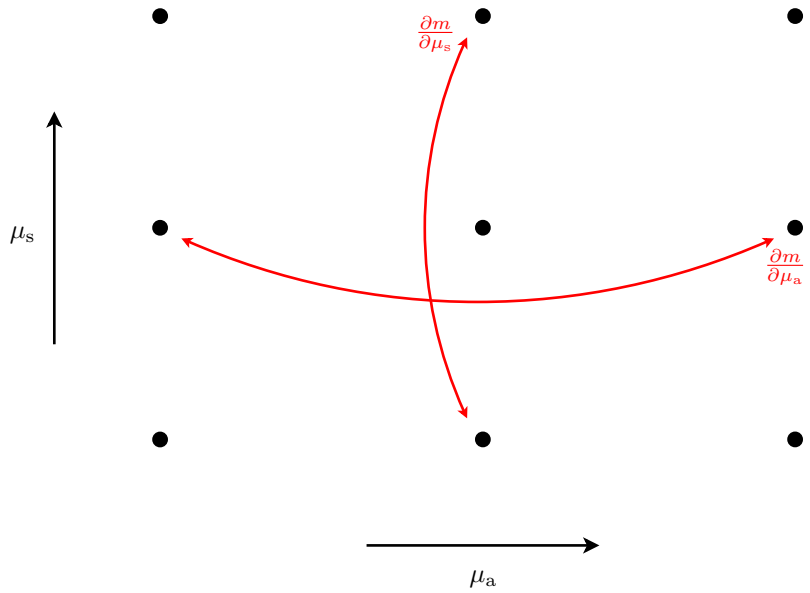

Figure 6.17: The problem of the calculation of a surface's gradients numerically: if the resolution of the μ_s-μ_a sample points used is low, the differentials must be defined over large ranges of absorption and scattering coefficients.

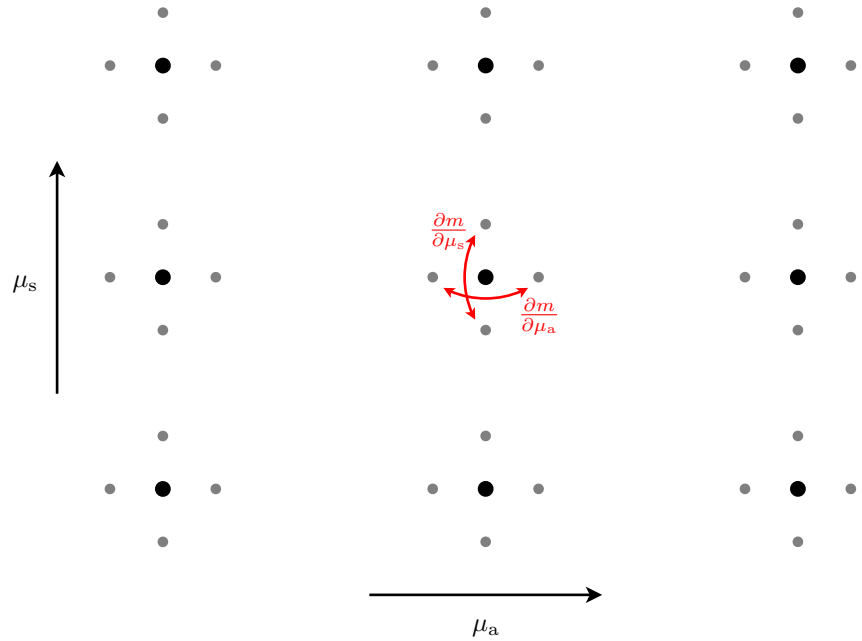

Figure 6.18: One solution involves the calculation of each metric and deterministic error at four sub-points around each μ_s-μ_a sample point.

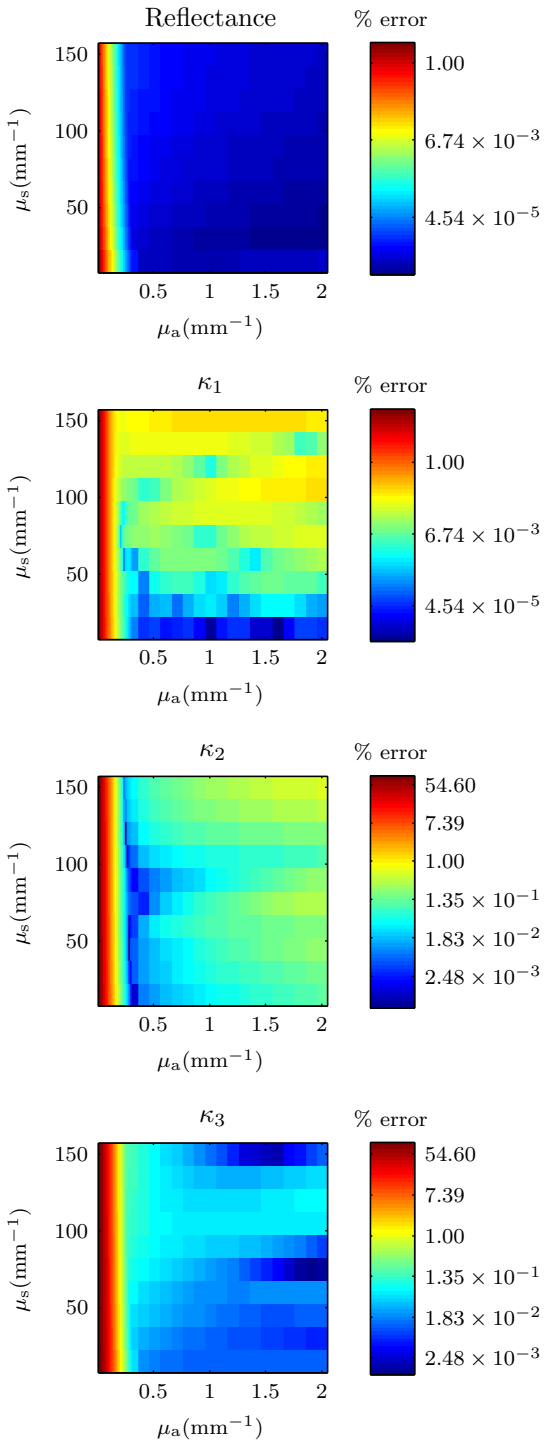

Figure 6.19: The magnitudes of the deterministic errors in the reflectance and first three cumulants (shown as a percentage of the analytical metric value) due to the streak camera for full-field detection. The figures use logarithmic colour axes for clarity.

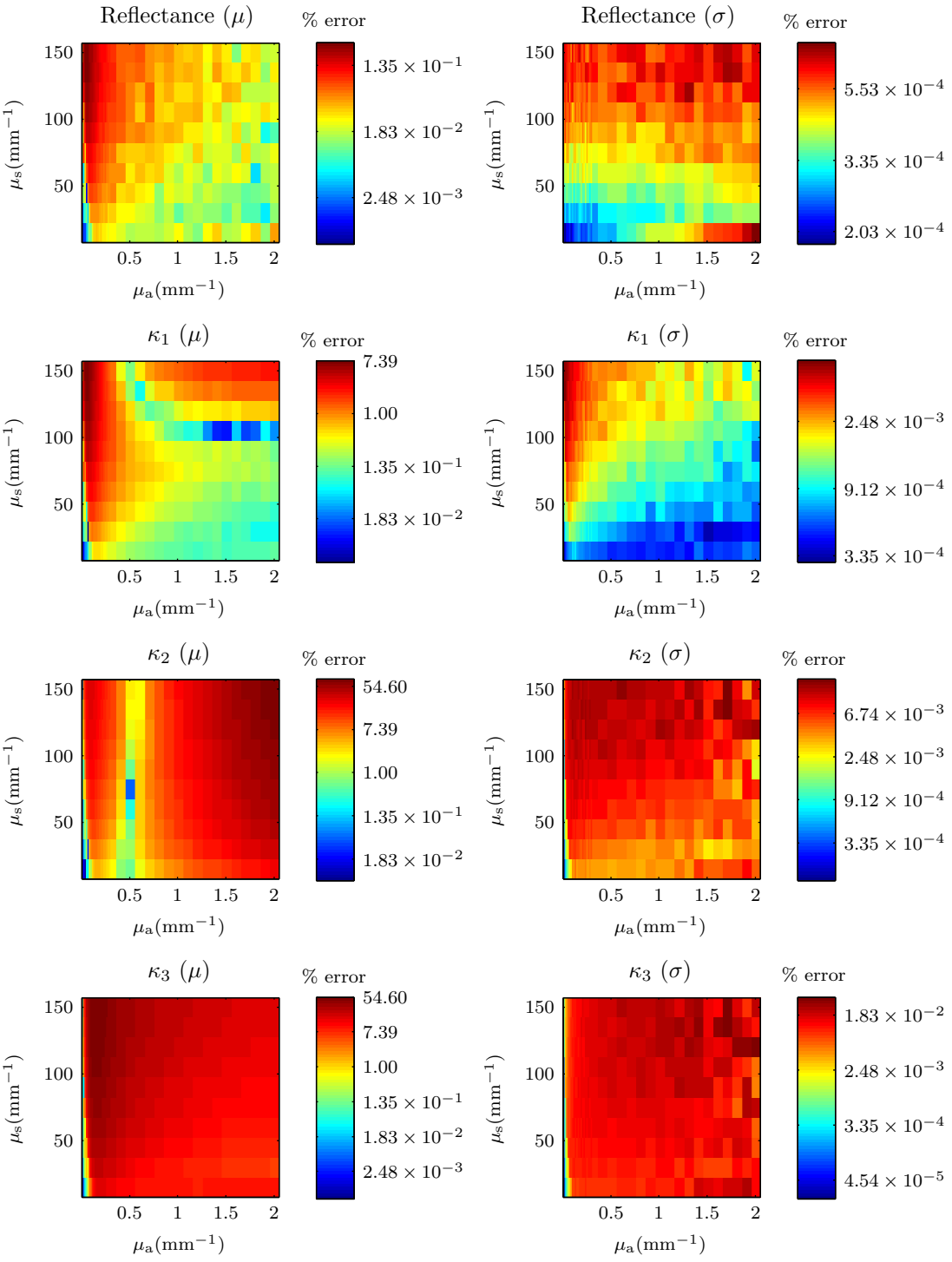

Figure 6.20: The mean magnitude (μ) and standard deviation (σ) of the stochastic errors in the reflectance and first three cumulants (shown as a percentage of the analytical metric value) due to the streak camera for full-field detection. The figures use logarithmic colour axes for clarity.

where the optimum truncation point would normally dictate a much longer sweep time. The perceived "dips" in the error values for the first and second cumulant merely mark the places where the errors change sign. Calibration of the actual measurements was then simulated by applying these error maps to the metric surfaces in Figure 6.5.

Maps of the remaining, stochastic errors are also shown in Figure 6.20. These can be seen to roughly follow the same form as the final error maps for the uncalibrated streak camera in Figure 5.35, but with a region of low error at low absorption levels. This is because in this region, the large intensity of the TPSF makes it less susceptible to the remaining stochastic errors when separated from the large error due to truncation.

The error analyis equations can then be used to calculate the error in the scattering coefficient as in §6.4.2. In this case, however, the error in each metric (δm_1 and δm_2) are calculated from the stochastic error maps, while the differentials of the metrics ($\frac{\partial m_1}{\partial \mu_a}$ etc.) are calculated numerically from the calibrated metric surfaces.

The resulting metric pair error surfaces for the errors in the scattering coefficient are shown in Figures 6.21 and 6.22. As expected, each metric pair surface has the characteristics of the error map relating to the metric of the pair with the largest error. These surfaces are the calibrated equivalent of the those shown in Figures 6.10 and 6.11, from which it can be seen that the errors in the scattering coefficient have been

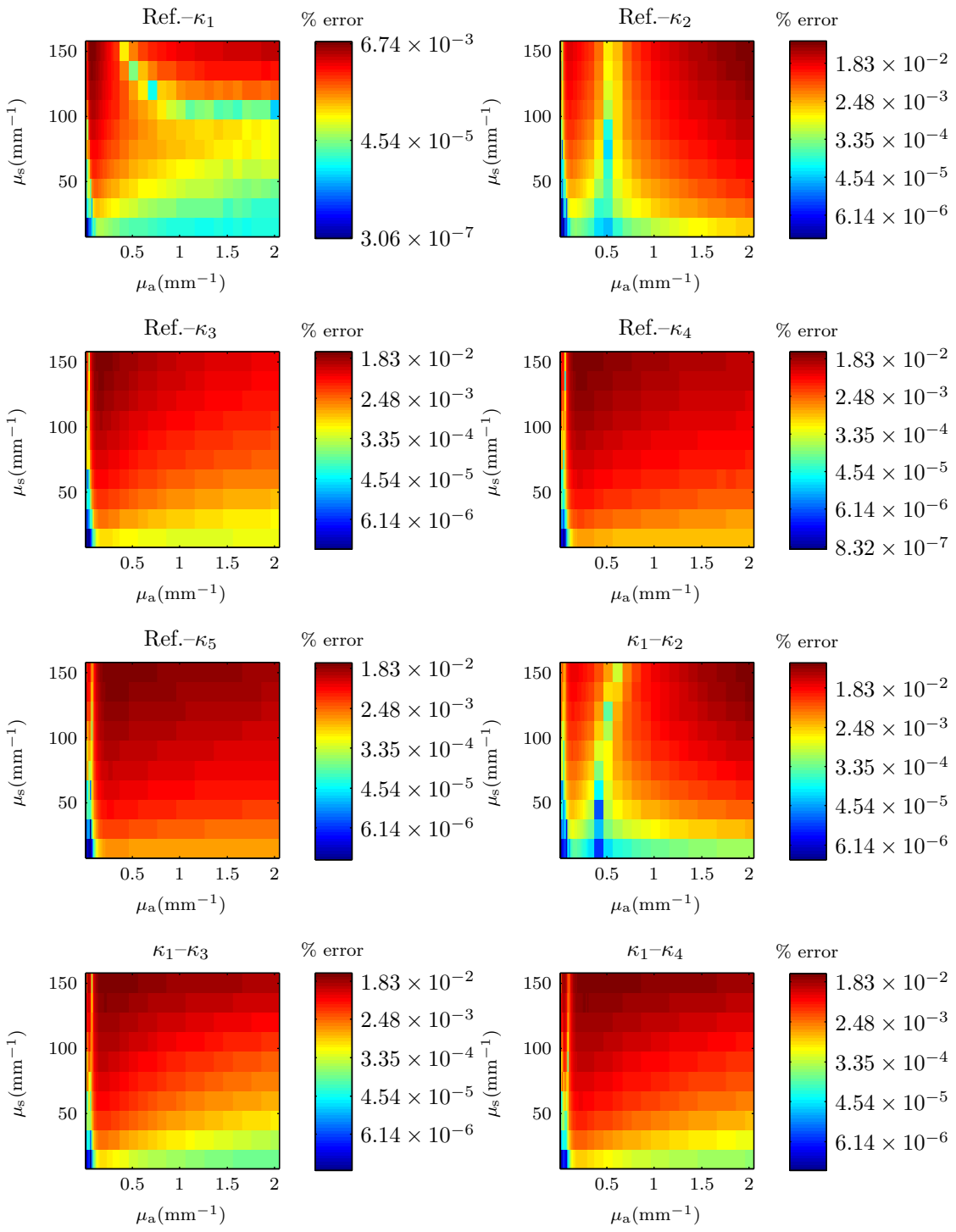

Figure 6.21: The errors in the scattering coefficient determined using measurement calibration for eight metric pairs using full-field detection. The figures use a logarithmic colour axis for clarity.

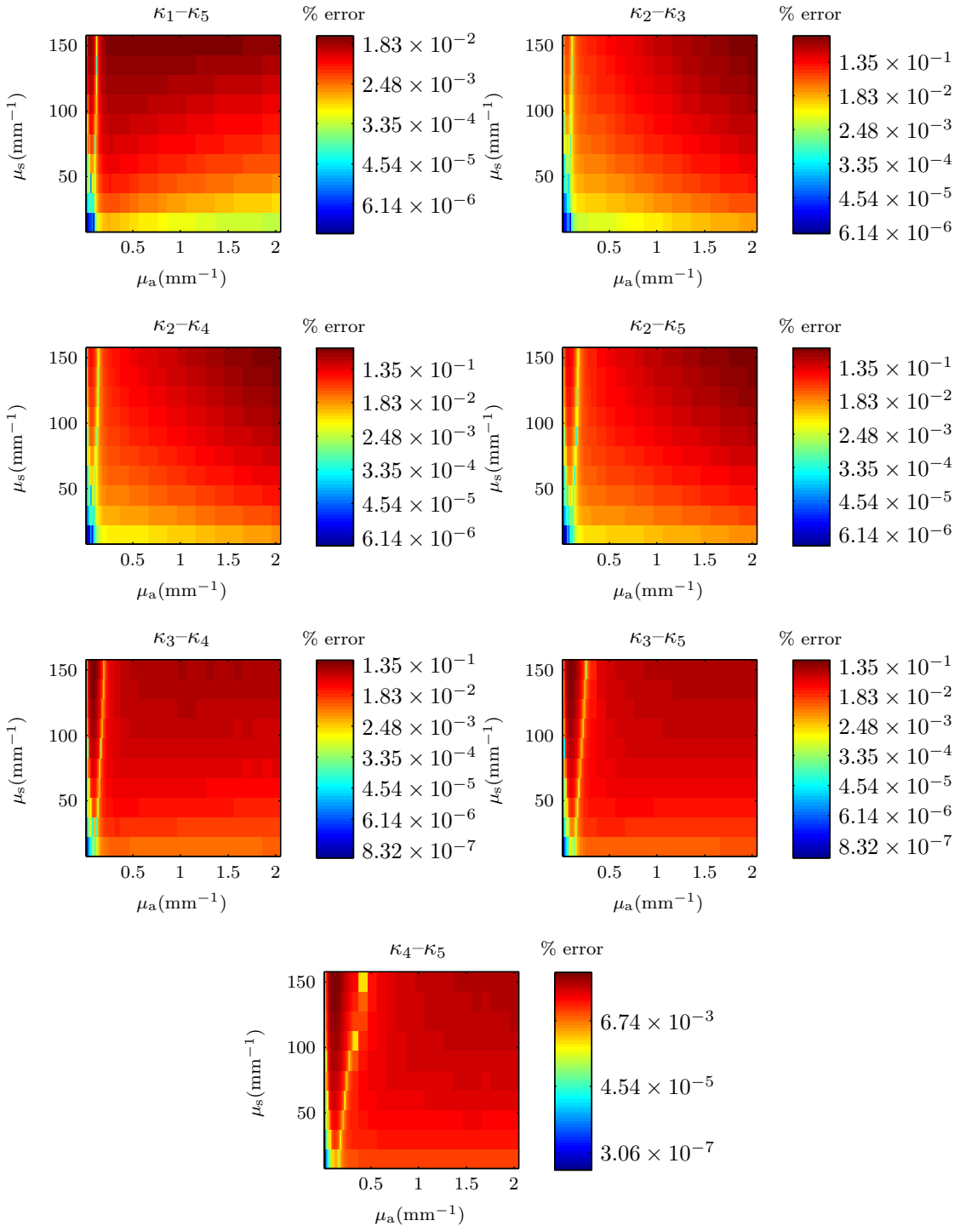

Figure 6.22: The errors in the scattering coefficient determined using measurement calibration for a further seven metric pairs using full-field detection. The figures use a logarithmic colour axis for clarity.

greatly reduced by the calibration process. This is further shown by considering the relevant histograms shown in Figures 6.23 and 6.24. These show that the mean error in the scattering coefficient for the optimum metric pair (Reflectance–κ_1) has dropped to around 1.2mm^{-1} from an original value of 6.6mm^{-1} due to the calibration process, and the maximum has dropped to less than 8mm^{-1} from an original value of 300mm^{-1}. In the case of the differentiation of healthy and breast tissue, as mentioned earlier, this drop is not sufficient to enable calibrated full-field detection to perform such a differentiation. However, due to the magnitudes of these reductions in the errors, it is thought that the application of this calibration method to spatially resolved detection would result in a robust characterisation system, especially considering the current capabilities of the non-calibrated spatially resolved system.

6.7 Summary

Presented in this chapter was a method of determining the optimum metrics for use in the characterisation of a scattering medium. Equations that relate errors on the metrics to error on the medium's optical properties were described. These equations require the knowledge of each metric's dependence on the scattering and absorption coefficients which can be calculated both analytically and numerically. The significance of the Jacobian determinant, on which these equations are based, was also highlighted, as well as its role in determining the uniqueness of the coefficient solution.

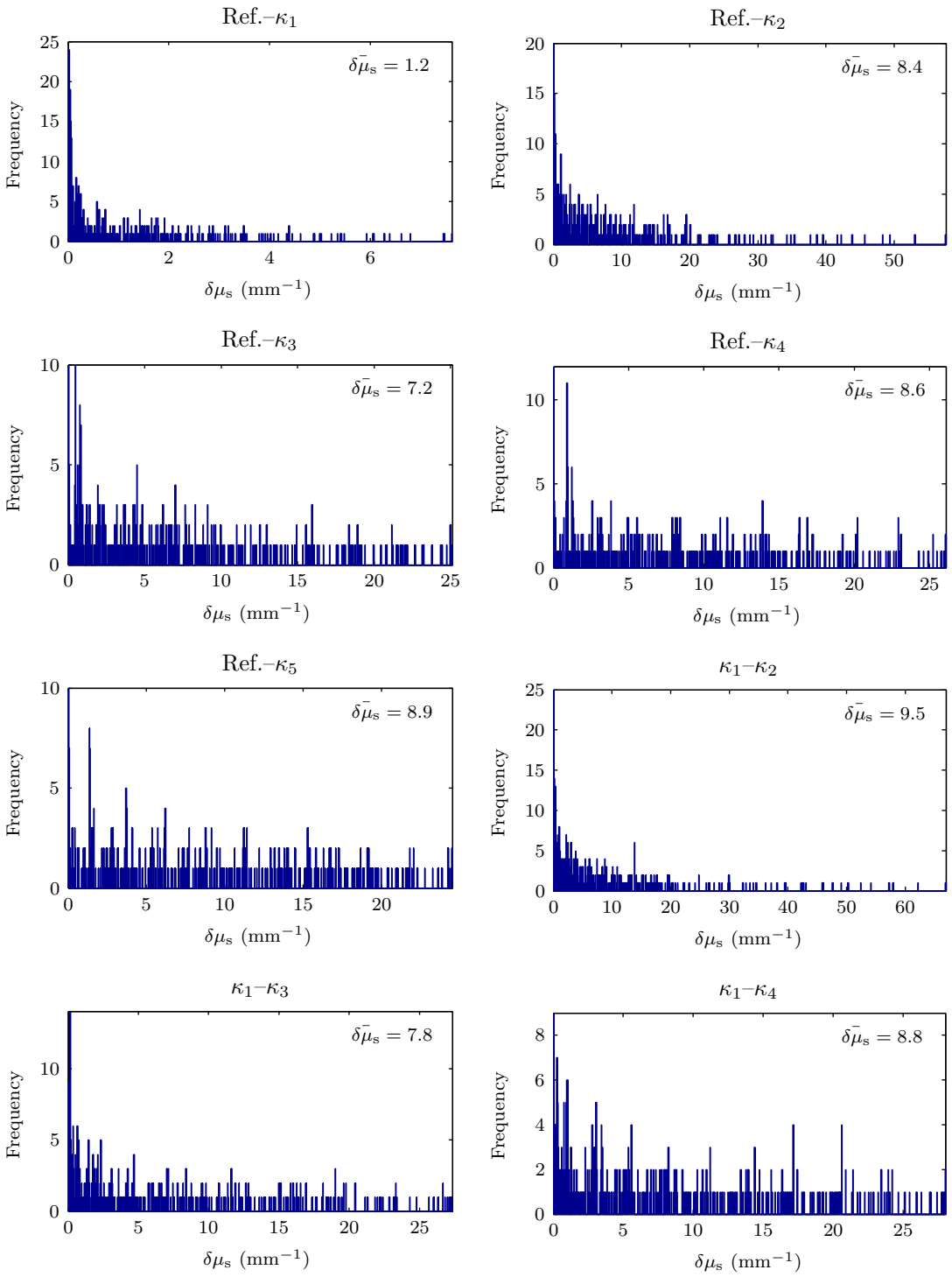

Figure 6.23: Histograms of the errors in the scattering coefficient over each of the metric pair surfaces in Figure 6.21. The limit of the x-axis represents the maximum error for each metric pair.

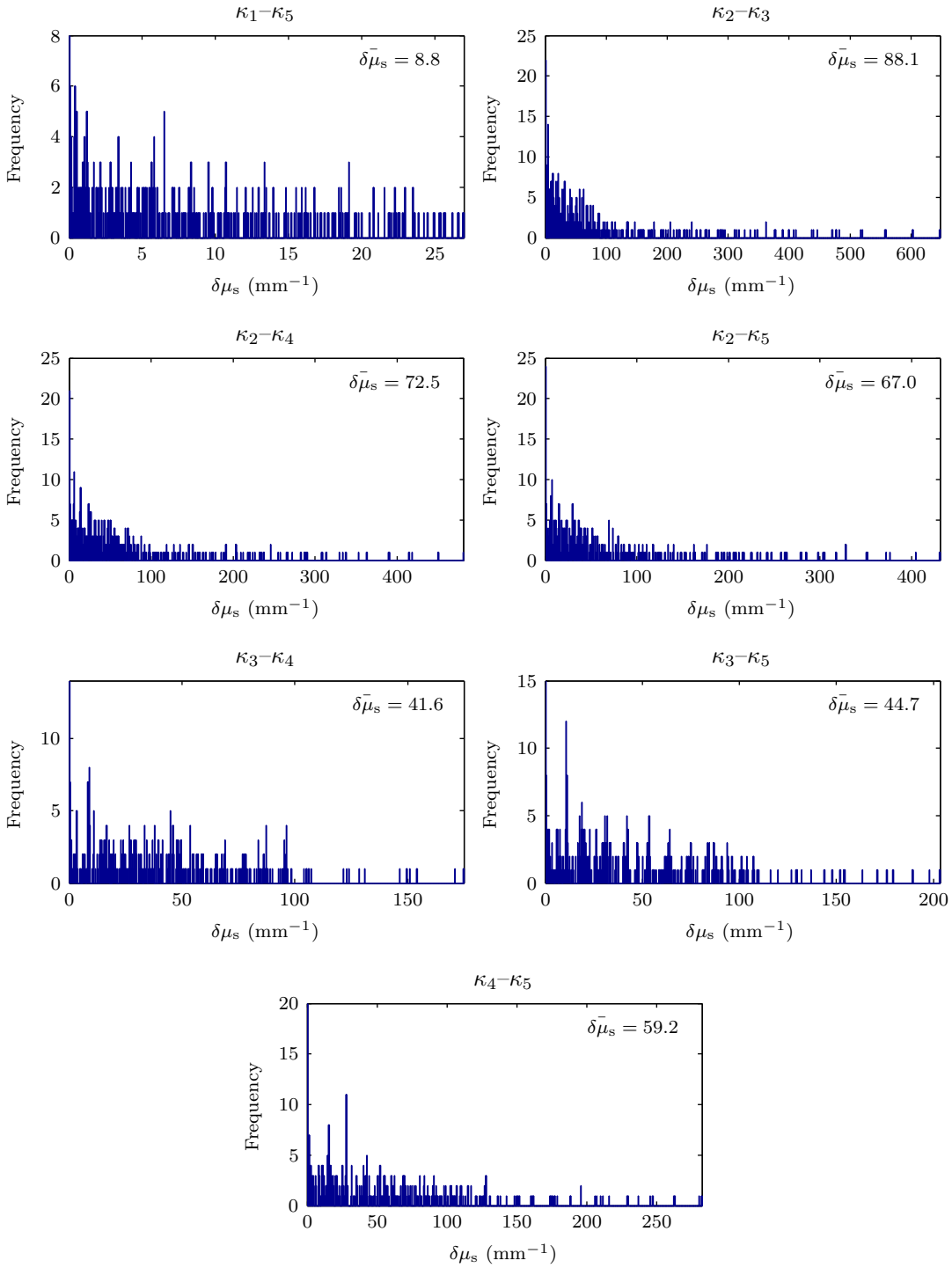

Figure 6.24: Histograms of the errors in the scattering coefficient over each of the metric pair surfaces in Figure 6.22. The limit of the x-axis represents the maximum error for each metric pair.

This method was then applied to the errors in the metrics calculated using the streak camera model in Chapter 5 to determine the resulting errors on the medium's optical properties. Due to the small number of metrics in the case of full-field detection, the analysis could be performed graphically. It was determined that the reflectance and first cumulant metric pair were the optimum metrics for this system.

The method was then applied to spatially resolved detection, and the optimum metric pair determined by the mean error in each of the optical coefficients. Due to the lower light levels measured in this detection regime, the streak camera would be unable to detect TPSFs over its noise floor for media with higher scattering and absorption levels, and for off-axis detection. Providing the model of the detection system is accurate, however, this knowledge could be used to narrow down the range of the medium's optical properties. The error analysis was therefore repeated for the ranges of properties defined by each of the source–detector distances to determine the optimum metric pair to be used for each assumption. The optimum pairings featured the reflectance and first cumulant measurements at a variety of source-detector distances.

Finally, a system of calibrating measurements according to the known noise characteristics of the detector was described. This was applied to the streak camera model measurements, resulting in a significant decrease in the errors in the determined optical coefficients.

Chapter 7

Conclusions & Future Work

7.1 Summary

This thesis has been concerned with the characterisation of scattering media or, more specifically, the errors in this process. The research was carried out with the aim of improving the accuracy of the optical coefficients ascertained by non-invasive, optical means.

Characterisation relies on a forward model which relates a medium's properties to the properties of the light's propagation through it. Measurements of some of these properties, or "metrics", can then be related back to the medium's optical coefficients, thus allowing the medium to be characterised. However, experimental errors on these measurements will also propagate back through the model to cause inaccuracies in the determined coefficients. It is the resilience of these metrics to this propagation that is of interest here. As there are two unknowns in the system (the scattering and absorption coefficients), this resilience is a product of the metric pairs that must be

used to characterise the medium.

In Chapter 1, a medium's temporal point spread function (TPSF) was described. This distribution is formed due to the scattering effects of the medium, and contains a large amount of information about the propagation of the light through the medium, such as its mean time of flight. The Beer–Lambert law, which can be used to add the effects of absorption onto the TPSF was also described. Two examples of metric series that can be calculated from the TPSF are the moments and cumulants, which were covered in detail. The latter of these two series is an established mathematical topic that has only recently begun to be applied to the field of scattering media, and more specfically TPSFs. Certainly, the error analysis performed on the cumulants in this thesis has not been undertaken previously.

Equations describing these metrics were then derived from the Diffusion Approximation to act as a forward model in Chapter 3. This involved an investigation into the most appropriate definition of the diffusion coefficient, from which a novel derivation of the reflectance using a hybrid coefficient value was produced.

In Chapter 4, the mathematical advantages of using the cumulants of the TPSF over the moments were described and it was decided that the applicability of these metrics to the characterisation of scattering media would be researched. The reflectance was also analysed due to its common use in current characterisation methods. Although the methods described in this thesis could be applied to any sort of

scattering media, this study focused on a semi-infinite medium with optical coefficients corresponding to the bulk properties of human skin. The dependence of the metrics of interest on these coefficients was then described, as knowledge of this dependence was integral to understanding the extent of the metrics' resilence to noise later in the thesis.

In order to fully quantify the magnitude of the errors on the determined coefficients of scattering media, it was necessary to ascertain the accuracy to which the metrics used in the characterisation can be measured. In order to achieve this, a typical streak camera was modelled by first identifying its sources of noise. With this knowledge, a model was produced which seeked to precisely simulate the detection of light. This model was much more detailed than any previously described, which have tended to conclude that streak cameras were merely shot-noise limited. As a result of this model, it was then possible to determine the effects of a TPSF's "detection" by the camera, and thus the effects on the metrics in question. It was shown that the truncation of a TPSF by the streak camera is one of the greatest sources of noise due to the streak camera and so particular consideration was given to determining the most appropriate point at which to truncate. Ultimately, this is dependent on the streak camera's noise floor, although this can be reduced by the effects of averaging.

Once the effects of the streak camera on a typical TPSF had been described, the model was applied to TPSFs formed under the scattering and absorption levels

found in human tissue. Maps of the errors in each of the metrics as a function of the medium's optical properties were therefore calculated.

In Chapter 6, equations were described which could be used to relate the error on the metrics to an error on the determined optical properties of the medium. Using the knowledge of the metrics' dependence on the medium's scattering and absorption coefficients from Chapter 4, and the values of the metric errors due to their detection by a streak camera from Chapter 5, it was then possible to calculate which metric pair would result in the smallest error in the optical properties of the medium being characterised.

In the case of full-field detection, measurements of the reflectance and first cumulant provided the optimum metric pair, although it was shown that even using this pairing, the accuracy of the measurements using the streak camera was not sufficient for differentiating between healthy and malignant breast tissue, as an example. It was also shown that the omission of reflectance measurements for reasons of feasiblity would have severely detrimental effects on the accuracy to which a medium could be characterised.

For spatially resolved detection, the ability of different annular detectors to detect a TPSF over the streak camera's noise floor could be used to make assumptions about a medium's optical properties. More specific assumptions led to more accurate measurements of the medium's optical properties, to the point where such a system

could feasibly be used in the the differentiation of healthy and malignant breast tissue.

Finally, a method for reducing the errors in the determined coefficients by using knowledge of the noise characteristics of the detection system was described. This was then applied to the streak camera model in full-field detection mode, resulting in a substantial decrease in the error in the characterisation of the medium. It is assumed that application of this calibration method to the case of spatially resolved detection would lead to a significantly more robust characterisation system.

This thesis made use of several simplifying assumptions, namely the use of a semi-infinite geometry, a single wavelength, and fixed values of the media's anisotropy factor and refractive index. It is therefore necessary to consider the effects of these assumptions on the completed work. Put simply, a change in any of these assumptions would result in a change in both the reflectance and TPSFs produced by the Diffusion Approximation. As a result, the values of the metrics calculated from these will change, also affecting their propagation through the streak camera model and the errors produced therein. It is therefore clear that the results of the error analysis will certainly change quantitatively, although how much this will affect the ordering of the metric pairs is unclear. Use of the current assumptions, however, allows estimates of how robust certain metric pairs are in comparison with each other to be made. It should also be noted that the model of the streak camera and the error analysis methods, which form the bulk of this thesis, will be unaffected by changes in these

assumptions, and so these can be applied regardless of what assumptions are made.

7.2 Future Work

There are numerous opportunities for further work related to this thesis. Firstly, the streak camera model presented in Chapter 5 would benefit from being validated experimentally. This would require the measurement of a known time distribution using the Hamamatsu streak camera on which the model is based, as explained in §5.6. In order to fully validate the system's modelled noise characteristics, this would need to be repeated for a range of input intensities. The calibration of the measurements described in §6.6 could also be tested using this setup. The calibration method should be applied to the case of spatially resolved detection, and these results also validated using the same method.

The methods used in this thesis made extensive use of the Diffusion Approximation as the analytical expressions allowed for quick calculations of the TPSFs and their metrics. One obvious opportunity for future work is therefore the use of Monte Carlo modelling in place of the Diffusion Approximation, as this would reduce the inaccuracies associated with the assumptions made in the approximation's derivation. This step should not be undertaken lightly however, as the intensity of the light simulated as being input to the medium is, at a wavelength of 633nm, the equivalent of over 50 billion photons for each TPSF.

It is speculated that the use of more than two metrics can be used to determine

a medium's optical coefficients with an increase in the accuracy of the determined values. This problem is said to be overdetermined as there are more metrics than unknowns. If three metrics are used, for example, the solution to the medium's optical coefficients is now given by the point of intersection of three contours. It is clear that, in the presence of noise, it is unlikely that there will be a shared crossing point for all three contours, in which case the solution is now given by the point which minimises the errors in the three metric equations.

Finally, it would be interesting to produce similar models of frequency modulated and TCSPC systems, as this would allow a direct comparison of all three systems' performance for the characterisation of a scattering medium using a TPSF's cumulants and reflectance.

Appendix A

Reflectance using a Hybrid Diffusion Coefficient

A.1 Derivation

The hybrid diffusion coefficients discussed in §3.3.1 (D_4 for κ_1 and D_0 for all higher-order cumulants) would suggest that the use of a single definition in the calculation of the reflectance will lead to inaccurate results. However, it is also possible to determine the reflectance using the hybrid coefficients. Firstly, a medium's attenuation, A, is defined in terms of its reflectance, R, and by the use of Eq. (1.5.20):

$$A = -\ln(R) = -\ln\left(\frac{E_{\mathrm{R}}}{E_{\mathrm{I}}}\right) \tag{A.1.1}$$

where E_{R} and E_{I} are the energies of the emergent and incident light respectively. This total attenuation can then be split into two parts: the attenuations caused by the medium's scattering and absorption processes, A_{s} and A_{a}:

$$A = A_{\mathrm{s}} + A_{\mathrm{a}} \tag{A.1.2}$$

The attenuation due to scattering is simply a measure of the loss of signal brought about by photons leaving the medium in a different position to the detector. It can be defined using the reflectance of the medium calculated with no absorption, $R_{\mu_\mathrm{a}=0}$:

$$A_\mathrm{s} = -\ln(R_{\mu_\mathrm{a}=0}) = -\ln\left(\frac{E_{\mu_\mathrm{a}=0}}{E_\mathrm{I}}\right) \tag{A.1.3}$$

where $E_{\mu_\mathrm{a}=0}$ is the energy of the light after scattering losses. By definition, the input intensity, E_I, for the Diffusion Approximation is one joule. Note that as A_s is calculated in the absence of absorption, it is unaffected by a change in the absorption contribution within the diffusion coefficient: as the diffusion coefficients under investigation in this case vary solely in their contributions from the medium's absorption, it is irrelevant which coefficient is used to calculate A_s.

The attenuation due to absorption in Eq. (A.1.4), A_a, can then be defined in terms of the emergent light from the medium, E_R, and $E_{\mu_\mathrm{a}=0}$:

$$A_\mathrm{a} = -\ln\left(\frac{E_\mathrm{R}}{E_{\mu_\mathrm{a}=0}}\right) \tag{A.1.4}$$

If the TPSF of the medium in the absence of absorption is given as $S(t)$, then $E_{\mu_\mathrm{a}=0}$ can be defined as:

$$E_{\mu_\mathrm{a}=0} = \int_0^\infty S(t)\,\mathrm{d}t \tag{A.1.5}$$

Absorption can be added to this TPSF using the Beer–Lambert law, as explained in §1.4:

$$E_\mathrm{R} = \int_0^\infty S(t)\exp(-\mu_\mathrm{a}ct)\,\mathrm{d}t \tag{A.1.6}$$

Substituting Eqs. (A.1.5) and (A.1.6) into Eq. (A.1.4):

$$\begin{aligned} A_{\mathrm{a}} &= -\ln\left(\frac{\int_0^\infty S(t)\exp(-\mu_{\mathrm{a}}ct)\,\mathrm{d}t}{\int_0^\infty S(t)\,\mathrm{d}t}\right) \\ &= -\ln\left(\int_0^\infty s(t)\exp(-\mu_{\mathrm{a}}ct)\,\mathrm{d}t\right) \end{aligned} \tag{A.1.7}$$

where $s(t)$ is the normalised TPSF. A_{a} is therefore related to the natural logarithm of a moment-generating function, as shown in Eq. (1.5.3), and so has the form of a cumulant-generating function with $x = -\mu_{\mathrm{a}}c$:

$$\begin{aligned} A_{\mathrm{a}} = -K &= -\sum_{n=1}^{\infty}\frac{x^n}{n!}\kappa_n \\ &= \mu_{\mathrm{a}}c\kappa_1 - \frac{(\mu_{\mathrm{a}}c)^2}{2}\kappa_2 + \ldots \end{aligned} \tag{A.1.8}$$

It is therefore possible to define A_{a} as an infinite sum of scaled cumulants. As a result, the hybrid diffusion coefficients can be used to define the reflectance as follows. Firstly, using D_0 as the diffusion coefficient, the attenuation due to absorption is calculated analytically using Eq. (A.1.4), where E_{R} and $E_{\mu_{\mathrm{a}}=0}$ can be determined using the analytical solutions to the reflectance in the presence and absence of absorption respectively. In other words, using Eqs. (A.1.1) and (A.1.3), and the knowledge that by definition, the input intensity, E_{I}, for the Diffusion Approximation is equal to one joule:

$$R = E_{\mathrm{R}} \tag{A.1.9}$$

$$R_{\mu_{\mathrm{a}}=0} = E_{\mu_{\mathrm{a}}=0} \tag{A.1.10}$$

The resulting attenuation formed using D_0 as the diffusion coefficient, $A_{\mathrm{a}}^{D_0}$, is equal to an infinite sum of its cumulants. If the first cumulant is then calculated using D_0 (denoted by $\kappa_1^{D_0}$), its contribution can be subtracted from the attenuation and replaced by the contribution of the first cumulant calculated using D_4 (shown as $\kappa_1^{D_4}$). The resulting attenuation, $A_{\mathrm{a}}^{\mathrm{hybrid}}$, is therefore the attenuation calculated using the hybrid diffusion coefficients:

$$A_{\mathrm{a}}^{\mathrm{hybrid}} = A_{\mathrm{a}}^{D_0} - \mu_{\mathrm{a}} c \kappa_1^{D_0} + \mu_{\mathrm{a}} c \kappa_1^{D_4} \tag{A.1.11}$$

The hybrid reflectance, R^{hybrid}, can then be calculated using Eqs. (A.1.1) and (A.1.2):

$$A^{\mathrm{hybrid}} = A_{\mathrm{s}} + A_{\mathrm{a}}^{\mathrm{hybrid}} \tag{A.1.12}$$

$$R^{\mathrm{hybrid}} = \exp(-A^{\mathrm{hybrid}}) \tag{A.1.13}$$

A.2 Overall Effect

The calculation of R^{hybrid} shown above is a long process. However, the overall effect of using a hybrid diffusion coefficient in the calculation of a medium's reflectance can be shown to be a simple scaling factor, as demonstrated below.

Substituting Eq. (A.1.11) into (A.1.12):

$$\begin{aligned} A^{\mathrm{hybrid}} &= A_{\mathrm{s}} + A_{\mathrm{a}}^{D_0} - \mu_{\mathrm{a}} c \kappa_1^{D_0} + \mu_{\mathrm{a}} c \kappa_1^{D_4} \\ &= A_{\mathrm{s}} + A_{\mathrm{a}}^{D_0} + \mu_{\mathrm{a}} c \Delta\kappa_1 \end{aligned} \tag{A.2.1}$$

where $\Delta\kappa_1$ is the change in the value of the first cumulant from using the two different diffusion coefficients:

$$\Delta\kappa_1 = \kappa_1^{D_4} - \kappa_1^{D_0} \tag{A.2.2}$$

Substituting Eq. (A.2.1) into (A.1.13):

$$\begin{aligned} R^{\text{hybrid}} &= \exp(-A_\text{s} - A_\text{a}^{D_0} - \mu_\text{a} c \Delta\kappa_1) \\ &= \exp(-A_\text{s}) \exp(-A_\text{a}^{D_0}) \exp(-\mu_\text{a} c \Delta\kappa_1) \end{aligned} \tag{A.2.3}$$

Finally, comparing the reflectance calculated using the hybrid diffusion coefficients, R^{hybrid}, and the original reflectance, R^{D_0}:

$$\begin{aligned} \frac{R^{\text{hybrid}}}{R^{D_0}} &= \frac{\exp(-A_\text{s}) \exp(-A_\text{a}^{D_0}) \exp(-\mu_\text{a} c \Delta\kappa_1)}{\exp(-A_\text{s}) \exp(-A_\text{a}^{D_0})} \\ &= \exp(-\mu_\text{a} c \Delta\kappa_1) \end{aligned} \tag{A.2.4}$$

The change in reflectance due to the use of hybrid diffusion coefficients is therefore a scaling factor of the form $\exp(-\mu_\text{a} c \Delta\kappa_1)$, where $\Delta\kappa_1$ is defined in Eq. (A.2.2).

Appendix B

Logged Error Analysis

By performing the error analysis described in Eqs. (6.3.3) and (6.3.4) on the logarithm of two metrics, the Jacobian determinant can be made resilient to scaling factors. This can be useful when analysing the determinant in isolation from the error analysis equations.

B.1 Effect on the Jacobian Determinant

Taking the logarithms of two metrics, m_1 and m_2, Eqs. (6.3.3) and (6.3.4) become:

$$\delta\mu_{\mathrm{s}} = \frac{\delta(\ln m_1)\dfrac{\partial(\ln m_2)}{\partial\mu_{\mathrm{a}}} - \delta(\ln m_2)\dfrac{\partial(\ln m_1)}{\partial\mu_{\mathrm{a}}}}{-J_{\log}} \tag{B.1.1}$$

$$\delta\mu_{\mathrm{a}} = \frac{\delta(\ln m_1)\dfrac{\partial(\ln m_2)}{\partial\mu_{\mathrm{s}}} - \delta(\ln m_2)\dfrac{\partial(\ln m_1)}{\partial\mu_{\mathrm{s}}}}{J_{\log}} \tag{B.1.2}$$

where:

$$J_{\log} = \frac{\partial(\ln m_1)}{\partial\mu_{\mathrm{a}}}\frac{\partial(\ln m_2)}{\partial\mu_{\mathrm{s}}} - \frac{\partial(\ln m_1)}{\partial\mu_{\mathrm{s}}}\frac{\partial(\ln m_2)}{\partial\mu_{\mathrm{a}}} \tag{B.1.3}$$

From the chain rule:

$$\frac{\partial(\ln m)}{\partial \mu} = \frac{\left(\frac{\partial m}{\partial \mu}\right)}{m} \tag{B.1.4}$$

Using this identity, Eq. (B.1.3) becomes:

$$J_{\log} = \frac{\left(\frac{\partial m_1}{\partial \mu_{\mathrm{a}}}\right)\left(\frac{\partial m_2}{\partial \mu_{\mathrm{s}}}\right)}{m_1 \quad m_2} - \frac{\left(\frac{\partial m_1}{\partial \mu_{\mathrm{s}}}\right)\left(\frac{\partial m_2}{\partial \mu_{\mathrm{a}}}\right)}{m_1 \quad m_2} \tag{B.1.5}$$

It can therefore be seen that the logged Jacobian determinant is resilient to scaling factors, and thus can be compared for metrics of different units.

B.2 Effect on the Calculated Error

Eqs. (B.1.1) and (B.1.2) require the error in a logged metric, $\delta(\ln m)$. However, due to the natural logarithm's lack of additivity, it is not possible to separate the error, δm, from the original value, m:

$$\ln(m + \delta m) \neq \ln(m) + \ln(\delta m) \tag{B.2.1}$$

However, using the chain rule, it can be shown that:

$$\delta(\ln m) = \frac{\delta m}{m} \tag{B.2.2}$$

Therefore, the error in a logged metric is simply defined as its error divided by its error-free value.

Substituting Eqs. (B.2.2) and (B.1.5), Eq. (B.1.1) becomes:

$$\delta\mu_{\mathrm{s}} = \frac{\dfrac{\delta m_1 \left(\frac{\partial m_2}{\partial \mu_{\mathrm{a}}}\right)}{m_1 \quad m_2} - \dfrac{\delta m_2 \left(\frac{\partial m_1}{\partial \mu_{\mathrm{a}}}\right)}{m_2 \quad m_1}}{-\dfrac{\left(\frac{\partial m_1}{\partial \mu_{\mathrm{a}}}\right)\left(\frac{\partial m_2}{\partial \mu_{\mathrm{s}}}\right)}{m_1 \quad m_2} + \dfrac{\left(\frac{\partial m_1}{\partial \mu_{\mathrm{s}}}\right)\left(\frac{\partial m_2}{\partial \mu_{\mathrm{a}}}\right)}{m_1 \quad m_2}} \tag{B.2.3}$$

By removing common factors, this equation can be seen to be identical to Eq. (6.3.3). Therefore, performing the error analysis on logged metrics has no effect on the calculated error and yet provides a Jacobian that is resilient to scaling factors.

Bibliography

[1] V. Quaresima, S. Romina, A. Pizzi, and M. Ferrari, "Measurement of the muscle optical properties on muscular dystrophy patients by a frequency-domain photometer," in *Biomedical Optical Spectroscopy and Diagnostics*, p. AP15 (Optical Society of America, 1996).

[2] M. Kohl, M. Essenpreis, and M. Cope, "The influence of glucose concentration upon the transport of light in tissue-simulating phantoms," Physics in Medicine and Biology **40**, 1267–1287 (1995).

[3] A. Eustaquio, M. Blanco, R. D. Jee, and A. C. Moffat, "Determination of paracetamol in intact tablets by use of near infrared transmittance spectroscopy," Analytica Chimica Acta **383**(3), 283–290 (1999).

[4] M. Blanco, J. Coello, A. Eustaquio, H. Iturriaga, and S. Maspoch, "Analytical control of pharmaceutical production steps by near infrared reflectance spectroscopy," Analytica Chimica Acta **392**(2–3), 237–246 (1999).

[5] H. E. Snyder and D. J. Armstrong, "An Analysis of Reflectance Spectrophotometry as Applied to Meat and Model Systems," Journal of Food Science **32**(3), 241–245 (1967).

[6] H. B. Ding and R. J. Xu, "Differentiation of Beef and Kangaroo Meat by Visible/Near-Infrared Reflectance Spectroscopy," Journal of Food Science **64**(5), 814–817 (1999).

[7] F. C. MacKintosh and S. John, "Diffusing-wave spectroscopy and multiple scattering of light in correlated random media," Phys. Rev. B **40**(4), 2383–2406 (1989).

[8] Y. Hasegawa, Y. Yamada, M. Tamura, and Y. Nomura, "Monte Carlo simulation of light transmission through living tissues," Appl. Opt. **30**(31), 4515–4520 (1991).

[9] Y. Tsuchiya and T. Urakami, "Frequency Domain Analysis of Photon Migration Based on the Microscopic Beer-Lambert Law," Japanese Journal of Applied Physics **35**(Part 1, No. 9A), 4848–4851 (1996).

[10] M. J. Hassett and D. Stewart, *Probability for risk management*, 1st ed. (ACTEX Publications, 1999).

[11] S. M. Ross, *Introduction to Probability and Statistics for Engineers and Scientists*, 4th ed. (Academic Press, 2009).

[12] P. J. Smith, "A Recursive Formulation of the Old Problem of Obtaining Moments from Cumulants and Vice Versa," The American Statistician **49**(2), 217–218 (1995).

[13] G. Schaepman-Strub, M. Schaepman, T. Painter, S. Dangel, and J. Martonchik, "Reflectance quantities in optical remote sensing—definitions and case studies," Remote Sensing of Environment **103**(1), 27–42 (2006).

[14] F. E. Nicodemus, J. C. Richmond, J. J. Hsia, I. W. Ginsberg, and T. Limperis, "Geometrical considerations and nomenclature for reflectance," Tech. rep., Inst. for Basic Standards, National Bureau of Standards, Washington, DC. (1977).

[15] F. E. Nicodemus, "Reflectance Nomenclature and Directional Reflectance and Emissivity," Appl. Opt. **9**(6), 1474–1475 (1970).

[16] R. Siegel and J. R. Howell, *Thermal Radiation Heat Transfer*, 4th ed. (Taylor & Francis, 2002).

[17] R. L. Cook and K. E. Torrance, "A reflectance model for computer graphics," SIGGRAPH Comput. Graph. **15**(3), 307–316 (1981).

[18] T. Nordlund, *Topics in Fluorescence Spectroscopy* (Springer US, 2002).

[19] *Guide To Streak Cameras* (Hamamatsu Photonics K. K., 2008).

[20] J. B. Fishkin, O. Coquoz, E. R. Anderson, M. Brenner, and B. J. Tromberg, "Frequency-domain photon migration measurements of normal and malignant tissue optical properties in a human subject," Appl. Opt. **36**(1), 10–20 (1997).

[21] E. M. Sevick, B. Chance, J. Leigh, S. Nioka, and M. Maris, "Quantitation of time- and frequency-resolved optical spectra for the determination of tissue oxygenation," Anal. Biochem. **195**(2), 330–351 (1991).

[22] J. T. Bruulsema, J. E. Hayward, T. J. Farrell, M. Essenpreis, and M. S. Patterson, "Optical properties of phantoms and tissue measured in vivo from 0.9 to 1.3 um using spatially resolved diffuse reflectance," in *Optical Tomography and Spectroscopy of Tissue: Theory, Instrumentation, Model, and Human Studies II*, B. Chance and R. R. Alfano, eds., vol. 2979, pp. 325–334 (SPIE, 1997).

[23] S. R. Arridge and J. C. Hebden, "Optical imaging in medicine: II. Modelling and reconstruction," Physics in Medicine and Biology **42**, 841–853 (1997).

[24] S. Flock, B. Wilson, and M. Patterson, "Monte Carlo Modeling of Light Propagation in Highly Scattering Tissues—-I: Model Predictions and Comparison with Diffusion Theory," Biomedical Engineering, IEEE Transactions on **36**(12), 1169–1173 (1989).

[25] A. Ishimaru, *Wave Propagation and Scattering in Random Media. Volume 1: Single Scattering and Transport Theory* (Academic Press, 1978).

[26] D. Contini, F. Martelli, and G. Zaccanti, "Photon migration through a turbid slab described by a model based on diffusion approximation. I. Theory," Applied Optics **36**(19), 4587–4599 (1997).

[27] M. S. Patterson, B. Chance, and B. C. Wilson, "Time resolved reflectance and transmittance for the noninvasive measurement of tissue optical properties," Applied Optics **28**(12), 2331–2336 (1989).

[28] F. Martelli, D. Contini, A. Taddeucci, and G. Zaccanti, "Photon migration through a turbid slab described by a model based on diffusion approximation. II. Comparison with Monte Carlo results," Applied Optics **36**(19), 4600–4612 (1997).

[29] I. Delfino, M. Lepore, and P. L. Indovina, "Experimental Tests of Different Solutions to the Diffusion Equation for Optical Characterization of Scattering Media by Time-Resolved Transmittance," Appl. Opt. **38**(19), 4228–4236 (1999).

[30] L. G. Henyey and J. L. Greenstein, "Diffuse radiation in the Galaxy," Astrophys. J **93**, 70–83 (1941).

[31] H. C. van de Hulst, *Light scattering by small particles* (Courier Dover Publications, 1981).

[32] A. Kienle and M. S. Patterson, "Determination of the optical properties of turbid media from a single Monte Carlo simulation," Physics in Medicine and Biology **41**, 2221–2227 (1996).

[33] V. J. Anselmo and B. E. Zawacki, "Multispectral photographic analysis: a new quantitative tool to assist in the early diagnosis of thermal burn depth," Annals of Biomedical Engineering **5**(2), 179–193 (1977).

[34] M. Afromowitz, J. Callis, D. Heimbach, L. DeSoto, and M. Norton, "Multispectral imaging of burn wounds: a new clinical instrument for evaluating burn depth," Biomedical Engineering, IEEE Transactions on **35**(10), 842–850 (1988).

[35] S. J. Matcher and C. E. Cooper, "Absolute quantification of deoxyhaemoglobin concentration in tissue near infrared spectroscopy," Physics in Medicine and Biology **39**(8), 1295–1312 (1994).

[36] D. T. Delpy and M. Cope, "Quantification in tissue near-infrared spectroscopy," Phil. Trans. R. Soc. Lond. **352**, 649–659 (1997).

[37] M. G. Nichols, E. L. Hull, and T. H. Foster, "Design and testing of a white-light, steady-state diffuse reflectance spectrometer for determination of optical properties of highly scattering systems," Appl. Opt. **36**(1), 93–104 (1997).

[38] S. F. Baker, J. G. Walker, and K. I. Hopcraft, "A dual thickness spatial system for determining optical coefficients from scattering media," Measurement Science and Technology **15**(3), 501–508 (2004).

[39] H. Liu, D. A. Boas, Y. Zhang, A. G. Yodh, and B. Chance, "Determination of optical properties and blood oxygenation in tissue using continuous NIR light," Physics in Medicine and Biology **40**, 1983–1993 (1995).

[40] B. Chance, H. L. Liu, T. Kitai, and Y. T. Zhang, "Effects of Solutes on Optical Properties of Biological Materials: Models, Cells, and Tissues," Analytical Biochemistry **227**(2), 351–362 (1995).

[41] G. Marquez, L. V. Wang, S.-P. Lin, J. A. Schwartz, and S. L. Thomsen, "Anisotropy in the Absorption and Scattering Spectra of Chicken Breast Tissue," Applied Optics **37**, 798–804 (1998).

[42] V. G. Peters, D. R. Wyman, M. S. Patterson, and G. L. Frank, "Optical properties of normal and diseased human breast tissues in the visible and near infrared," Physics in Medicine and Biology **35**(9), 1317–1334 (1990).

[43] C. R. Simpson, M. Kohl, M. Essenpreis, and M. Cope, "Near-infrared optical properties of ex vivo human skin and subcutaneous tissues measured using the Monte Carlo inversion technique," Phys. Med. Biol. **43**, 2465–2478 (1998).

[44] C. J. Hourdakis and A. Perris, "A Monte Carlo estimation of tissue optical properties for use in laser dosimetry," Physics in Medicine and Biology **40**, 351–364 (1995).

[45] J. Pickering, S. Prah, N. Vanwieringen, J. Beek, H. Sterenborg, and M. Gemert, "Double-integrating-sphere system for measuring the optical properties of tissue," Applied Optics **32**, 399–410 (1993).

[46] M. Miwa, Y. Ueda, and B. Chance, "Development of time-resolved spectroscopy system for quantitative noninvasive tissue measurement," in *Optical Tomography, Photon Migration, and Spectroscopy of Tissue and Model Media: Theory, Human Studies, and Instrumentation*, B. Chance and R. R. Alfano, eds., vol. 2389, pp. 142–149 (SPIE, 1995).

[47] S. Jacques, "Time-resolved reflectance spectroscopy in turbid tissues," Biomedical Engineering, IEEE Transactions on **36**(12), 1155–1161 (1989).

[48] J. M. Tualle, B. Glbart, E. Tinet, S. Avrillier, and J. P. Ollivier, "Real time optical coefficients evaluation from time and space resolved reflectance measurements in biological tissues," Optics Communications **124**(3-4), 216–221 (1996).

[49] B. Wilson, E. Sevick, M. Patterson, and B. Chance, "Time-dependent optical spectroscopy and imaging for biomedical applications," Proceedings of the IEEE **80**(6), 918–930 (1992).

[50] S. J. Madsen, B. C. Wilson, M. S. Patterson, Y. D. Park, S. L. Jacques, and Y. Hefetz, "Experimental tests of a simple diffusion model for the estimation of scattering and absorption coefficients of turbid media from time-resolved diffuse reflectance measurements," Appl. Opt. **31**(18), 3509–3517 (1992).

[51] G. Mitic, J. Kölzer, J. Otto, E. Plies, G. Sölkner, and W. Zinth, "Time-gated transillumination of biological tissues and tissuelike phantoms," Appl. Opt. **33**(28), 6699–6710 (1994).

[52] R. Cubeddu, M. Musolino, A. Pifferi, P. Taroni, and G. Valentini, "Time-resolved reflectance: a systematic study for application to the optical characterization of tissues," Quantum Electronics, IEEE Journal of **30**(10), 2421–2430 (1994).

[53] R. Cubeddu, A. Pifferi, P. Taroni, A. Torricelli, and G. Valentini, "Experimental test of theoretical models for time-resolved reflectance," Medical Physics **23**(9), 1625–1633 (1996).

[54] A. Pifferi, P. Taroni, G. Valentini, and S. Andersson-Engels, "Real-Time Method for Fitting Time-Resolved Reflectance and Transmittance Measurements with a Monte Carlo Model," Appl. Opt. **37**(13), 2774–2780 (1998).

[55] A. Liebert, H. Wabnitz, D. Grosenick, M. Möller, R. Macdonald, and H. Rinneberg, "Evaluation of Optical Properties of Highly Scattering Media by Moments of Distributions of Times of Flight of Photons," Appl. Opt. **42**(28), 5785–5792 (2003).

[56] J. C. Hebden, R. A. Kruger, and K. S. Wong, "Time resolved imaging through a highly scattering medium," Appl. Opt. **30**(7), 788–794 (1991).

[57] D. Grosenick, K. T. Moesta, H. Wabnitz, J. Mucke, C. Stroszczynski, R. Macdonald, P. M. Schlag, and H. Rinneberg, "Time-Domain Optical Mammography: Initial Clinical Results on Detection and Characterization of Breast Tumors," Appl. Opt. **42**(16), 3170–3186 (2003).

[58] J. C. Hebden, S. R. Arridge, and M. Schweiger, "Investigation of alternative data types for time-resolved optical tomography," in *Advances in Optical Imaging and Photon Migration*, p. ATuC1 (Optical Society of America, 1998).

[59] L. Leonardi and D. H. Burns, "Quantitative constituent measurements in scattering media from statistical analysis of photon time-of-flight distributions," Analytica Chimica Acta **348**(1-3), 543–551 (1997).

[60] S. R. Arridge, "Optical tomography in medical imaging," Inverse Problems **15**, R41–R93 (1999).

[61] M. Schweiger, S. R. Arridge, M. Hiraoka, M. Firbank, and D. T. Delpy, "Comparison of a finite-element forward model with experimental phantom results: application to image reconstruction," in *Photon Migration and Imaging in Random Media and Tissues*, B. Chance and R. R. Alfano, eds., vol. 1888, pp. 179–190 (SPIE, 1993).

[62] P. Marquet, F. P. Bevilacqua, C. D. Depeursinge, and E. B. de Haller, "Determination of reduced scattering and absorption coefficients by a single charge-coupled-device array measurement, part I: comparison between experiments and simulations," Optical Engineering **34**(7), 2055–2063 (1995).

[63] M. Schweiger and S. R. Arridge, "Optimal Data Types in Optical Tomography," in *IPMI '97: Proceedings of the 15th International Conference on Information Processing in Medical Imaging*, pp. 71–84 (Springer-Verlag, London, UK, 1997).

[64] A. Torricelli, A. Pifferi, P. Taroni, E. Giambattistelli, and R. Cubeddu, "In vivo optical characterization of human tissues from 610 to 1010 nm by time-resolved reflectance spectroscopy," Physics in Medicine and Biology **46**, 2227–2237 (2001).

[65] A. Pifferi, P. Taroni, A. Torricelli, F. Messina, R. Cubeddu, and G. Danesini, "Four-wavelength time-resolved optical mammography in the 680-980-nm range," Optics Letters **28**, 1138–1140 (2003).

[66] S. F. Baker, J. G. Walker, and K. I. Hopcraft, "Comparison of optical arrangements for determining the optical coefficients of a scattering medium," in *Optical Tomography and Spectroscopy of Tissue IV*, B. Chance, R. R. Alfano, B. J. Tromberg, M. Tamura, and E. M. Sevick-Muraca, eds., vol. 4250, pp. 239–250 (SPIE, 2001).

[67] V. Ntziachristos and B. Chance, "Accuracy limits in the determination of absolute optical properties using time-resolved NIR spectroscopy," Medical Physics **28**(6), 1115–1124 (2001).

[68] S. J. Madsen, P. Wyss, L. O. Svaasand, R. C. Haskell, Y. Tadir, and B. J. Tromberg, "Determination of the optical properties of the human uterus using frequency-domain photon migration and steady-state techniques," Physics in Medicine and Biology **39**(8), 1191–1202 (1994).

[69] A. Kienle and M. S. Patterson, "Determination of the optical properties of semi-infinite turbid media from frequency-domain reflectance close to the source," Physics in Medicine and Biology **42**, 1801–1819 (1997).

[70] J. Crowe, D. Morris, M. Woolfson, P. Rodmell, and J. Walker, "Quantitative spectrophotometry of scattering media via frequency-domain and constant-intensity measurements," J. Opt. Soc. Am. A **24**(7), 1969–1974 (2007).

[71] D. E. Morris, "Quantitative Spectrophotometry on Scattering Media," Ph.D. thesis, School of Electrical & Electronic Engineering, The University of Nottingham (2009).

[72] M. S. Patterson, J. D. Moulton, B. C. Wilson, K. W. Berndt, and J. R. Lakowicz, "Frequency-domain reflectance for the determination of the scattering and absorption properties of tissue," Appl. Opt. **30**(31), 4474–4476 (1991).

[73] S. Fantini, M.-A. Franceschini, J. S. Maier, S. A. Walker, B. B. Barbieri, and E. Gratton, "Frequency-domain multichannel optical detector for noninvasive tissue spectroscopy and oximetry," Optical Engineering **34**(1), 32–42 (1995).

[74] B. J. Tromberg, O. Coquoz, J. B. Fishkin, T. Pham, E. R. Anderson, J. Butler, M. Cahn, J. D. Gross, V. Venugopalan, and D. Pham, "Non-Invasive Measurements of Breast Tissue Optical Properties Using Frequency-Domain Photon Migration," Royal Society of London Philosophical Transactions Series B **352**, 661–668 (1997).

[75] M. W. Hemelt and K. A. Kang, "Determination of a Biological Absorber Depth Utilizing Multiple Source-Detector Separations and Multiple Frequency Values of Near-Infrared Time-Resolved Spectroscopy," Biotechnology Progress **15**(4), 622–629 (1999).

[76] A. P. Gibson, J. C. Hebden, and S. R. Arridge, "Recent advances in diffuse optical imaging," Physics in Medicine and Biology **50**(4), R1–R43 (2005).

[77] A. Secroun, A. Mens, D. Gontier, P. Brunel, J.-C. Rebuffie, and C. Goulmy, "Experimental and theoretical characterization of noise in a streak camera," in *Current Developments in Optical Design and Engineering VII*, R. E. Fischer, L. M. Germann, A. E. Hatheway, M. McConnell, and W. J. Smith, eds., vol. 3429, pp. 32–38 (SPIE, 1998).

[78] W. R. Donaldson, R. Boni, R. L. Keck, and P. A. Jaanimagi, "A self-calibrating, multichannel streak camera for inertial confinement fusion applications," Review of Scientific Instruments **73**(7), 2606–2615 (2002).

[79] R. A. Lerche, J. W. McDonald, R. L. Griffith, G. V. de Dios, D. S. Andrews, A. W. Huey, P. M. Bell, O. L. Landen, P. A. Jaanimagi, and R. Boni, "Preliminary performance measurements for a streak camera with a large-format direct-coupled charge-coupled device readout," Review of Scientific Instruments **75**(10), 4042–4044 (2004).

[80] S. R. Arridge, M. Cope, and D. T. Delpy, "The theoretical basis for the determination of optical pathlengths in tissue: temporal and frequency analysis," Physics in Medicine and Biology **37**(7), 1531–1560 (1992).

[81] T. Durduran, A. G. Yodh, B. Chance, and D. A. Boas, "Does the photon-diffusion coefficient depend on absorption?" J. Opt. Soc. Am. A **14**(12), 3358–3365 (1997).

[82] M. Bassani, F. Martelli, G. Zaccanti, and D. Contini, "Independence of the diffusion coefficient from absorption: experimental and numerical evidence," Opt. Lett. **22**(12), 853–855 (1997).

[83] A. Wierman, "Revisiting the performance of large jobs in the M/GI/1 queue," in *Proceedings of the Forty-Fifth Annual Allerton Conference On Communication, Control, and Computing*, pp. 607–614 (2007).

[84] S. Cotton and E. Claridge, "Developing a predictive model of human skin coloring," in *Medical Imaging 1996: Physics of Medical Imaging*, R. L. V. Metter and J. Beutel, eds., vol. 2708, pp. 814–825 (SPIE, 1996).

[85] R. R. Anderson and J. A. Parrish, "The optics of human skin," Journal of Investigative Dermatology **77**(1), 13–19 (1981).

[86] S. Cotton, E. Claridge, and P. Hall, "Noninvasive Skin Imaging," in *IPMI '97: Proceedings of the 15th International Conference on Information Processing in Medical Imaging*, pp. 501–506 (Springer-Verlag, London, UK, 1997).

[87] I. V. Meglinskiĭ and S. D. Matcher, "Analysis of the Spatial Distribution of Detector in a Multilayer Randomly Inhomogeneous Medium with Strong Light Scattering and Absorption by the Monte Carlo Method," Optics and Spectroscopy **91**(4), 654–659 (2001).

[88] W.-F. Cheong, S. A. Prahl, and A. J. Welch, "A Review of the Optical Properties of Biological Tissues," Quantum Electronics, IEEE Journal of **26**(12), 2166–2185 (1990).

[89] M. J. C. V. Gemert, S. L. Jacques, H. J. C. M. Sterenborg, and W. M. Star, "Skin Optics," Biomedical Engineering, IEEE Transactions on **36**(12), 1146–1154 (1989).

[90] R. R. Anderson and J. A. Parrish, "Optical Properties of Human Skin," in *The Science of Photomedicine*, J. D. Regan and J. A. Parrish, eds., pp. 147–194 (Plenum Press, New York, 1982).

[91] S. L. Jacques, C. A. Alter, and S. A. Prahl, "Angular dependence of HeNe laser light scattering by human dermis," Lasers Life Sci. **1**, 309–333 (1987).

[92] *Optics Catalog*, vol. 20 (Thorlabs). pp. 590–591.

[93] E. T. Jaynes and G. L. Bretthorst, *Probability Theory: The Logic of Science* (Cambridge University Press, 2003).

[94] C. N. Berglund and W. E. Spicer, "Photoemission Studies of Copper and Silver: Theory," Phys. Rev. **136**(4A), A1030–A1044 (1964).

[95] W. E. Spicer and A. Herrera-Gómez, "Modern Theory and Applications of Photocathodes," in *Proc. SPIE*, vol. 2022, pp. 18–35 (1993).

[96] C. D'Ambrosio and H. Leutz, "Hybrid Photo Detectors," Nuclear Instruments and Methods in Physics Research A **501**, 463–498 (2003).

[97] A. Brunelle, P. Chaurand, S. Della-Negra, Y. L. Beyec, and E. Parilis, "Secondary Electron Emission Yields from a CsI Surface Under Impacts of Large Molecules at Low Velocities (5×10^3 – 7×10^4 ms^{-1})," Rapid Communications In Mass Spectrometry **11**, 353–362 (1997).

[98] G. Westmacott, M. Frank, S. E. Labov, and W. H. Benner, "Using a superconducting tunnel junction detector to measure the secondary electron emission efficiency for a microchannel plate detector bombarded by large molecular ions," Rapid Communications In Mass Spectrometry **14**, 1854–1861 (2000).

[99] I. S. Gilmore and M. P. Seah, "Ion detection efficiency in SIMS: Dependencies on energy, mass and composition for microchannel plates used in mass spectrometry," International Journal of Mass Spectrometry **202**, 217–229 (2000).

[100] A. J. Guest, "A computer model of channel multiplier plate performance," Acta Electronica **14**(1), 79–97 (1971).

[101] G. Eschard and B. W. Manley, "Principle and characteristics of channel electron multipliers," Acta Electronica **14**(1), 19–39 (1971).

[102] V. Chalmeton and P. Chevalier, "Pulse height distribution for single electron input," Acta Electronica **14**(1), 99–106 (1971).

[103] N. Balakrishnan and A. P. Basu, *The Exponential Distribution: theory, methods and applications* (CRC Press, 1995).

[104] P. Gallant, P. Forget, F. Dorchies, Z. Jiang, J. C. Kieffer, P. A. Jaanimagi, J. C. Rebuffie, C. Goulmy, J. F. Pelletier, and M. Sutton, "Characterization of a subpicosecond x-ray streak camera for ultrashort laser-produced plasmas experiments," Review of Scientific Instruments **71**(10), 3627–3633 (2000).

[105] R. L. Shepherd, R. Booth, D. F. Price, M. W. Bowers, D. A. Swan, J. D. Bonlie, B. K. Young, J. Dunn, W. E. White, and R. E. Stewart, "Characteristics of an Ultrafast X-ray Streak Camera," in *X-Ray and UV Detectors*, vol. 2278, pp. 78–84 (SPIE, 1994).

[106] A. Klisnick, J. Kuba, D. Ros, R. Smith, G. Jamelot, C. Chenais-Popovics, R. Keenan, S. J. Topping, C. L. S. Lewis, F. Strati, G. J. Tallents, D. Neely, R. Clarke, J. Collier, A. G. MacPhee, F. Bortolotto, P. V. Nickles, and K. A. Janulewicz, "Demonstration of a 2-ps transient x-ray laser," Phys. Rev. A **65**(3), 033,810 (2002).

[107] M. Drabbels, G. Lankhuijzen, and L. Noordam, "Demonstration of a far-infrared streak camera," Quantum Electronics, IEEE Journal of **34**(11), 2138–2144 (1998).

[108] D. T. Delpy, M. Cope, P. van der Zee, S. Arridge, S. Wray, and J. Wyatt, "Estimation of optical pathlength through tissue from direct time of flight measurement," Physics in Medicine and Biology **33**(12), 1433–1442 (1988).

[109] N. Kalivas, I. Kandarakis, D. Cavouras, L. Costaridou, C. D. Nomicos, and G. Panayiotakis, "Modeling quantum noise of phosphors used in medical X-ray imaging detectors," Nuclear Instruments and Methods in Physics Research Section A: Accelerators, Spectrometers, Detectors and Associated Equipment **430**(2–3), 559–569 (1999).

[110] P. W. Roberts, "Some Comments on the Resolution of Scintillation Spectrometers," Proceedings of the Physical Society. Section A **66**(2), 192–194 (1953).

[111] J. Janesick and T. Elliott, "History and Advancement of Large Array Scientific CCD Imagers," in *Astronomical CCD Observing and Reduction Techniques*, S. B. Howell, ed., vol. 23 of *Astronomical Society of the Pacific Conference Series*, p. 6 (1992).

[112] H. C. S. Thom, "A Note on the Gamma Distribution," Monthly Weather Review **86**(4), 117–122 (1958).

[113] M. P. Morrissey and E. I. Shakhnovich, "Design of proteins with selected thermal properties," Folding and Design **1**(5), 391–405 (1996).

[114] J.-P. Bouchaud and M. Potters, *Theory of Financial Risk and Derivative Pricing*, 2nd ed. (Cambridge University Press, 2003).

[115] *BS EN 60825-1:2007: Safety of laser products — Part 1: Equipment classification and requirements* (BSi, 2007).

[116] *High Resolution Digital B/W CCD Camera ORCA-ER [C4742-95-12ER] (Data Sheet)* (Hamamatsu Photonics K. K., 2003).

[117] D. P. Foster, R. A. Stine, and R. P. Waterman, *Basic business statistics: a casebook* (Birkhäuser, 1998).

[118] D. S. Paulson, *Biostatistics and Microbiology: A Survival Manual* (Springer, 2008).

[119] M. Schader and F. Schmid, "Two Rules of Thumb for the Approximation of the Binomial Distribution by the Normal Distribution," The American Statistician **43**(1), 23–24 (1989).

[120] *Universal Streak Camera C5680 Series (Product Sheet)* (Hamamatsu Photonics K. K., 2008).

[121] J. Hinkson, R. Keller, J. Byrd, and A. Lumpkin, "Commissioning of the Advanced Light Source dual-axis streak camera," in *Particle Accelerator Conference, 1997. Proceedings of the 1997*, vol. 1, pp. 775–777 (1997).

[122] *DiCam-PRO – Intensified CCD Imaging System (Product Sheet)* (The Cooke Corporation, 2008).

[123] A. R. Faruqi and S. Subramaniam, "CCD detectors in high-resolution biological electron microscopy," Quarterly Reviews of Biophysics **33**(1), 1–27 (2000).

[124] *Phosphor Screens (Data Sheet)* (Proxitronic, 2000).

[125] R. H. Chitale, *Random Processes* (Technical Publications, 2008).

[126] J.-C. M. Diels, J. J. Fontaine, I. C. McMichael, and F. Simoni, "Control and measurement of ultrashort pulse shapes (in amplitude and phase) with femtosecond accuracy," Appl. Opt. **24**(9), 1270–1282 (1985).

[127] S. F. Baker, "Optimal Determination of the Optical Coefficients from Scattering Media," Ph.D. thesis, School of Electrical & Electronic Engineering, The University of Nottingham (2002).

[128] H. P. Greenspan and D. J. Benney, *Calculus: An Introduction to Applied Mathematics*, 3rd ed. (H. P. Greenspan, 1997).

[129] E. Claridge and S. J. Preece, "An inverse method for the recovery of tissue parameters from colour images," in *Information Processing in Medical Imaging: 18th International Conference*, C. Taylor and J. A. Noble, eds., vol. 2832 of *Lecture notes in computer science*, pp. 306–317 (Springer, 2003).

[130] M. S. Nair, N. Ghosh, N. S. Raju, and A. Pradhan, "Determination of optical parameters of human breast tissue from spatially resolved fluorescence: a diffusion theory model," Appl. Opt. **41**(19), 4024–4035 (2002).